

Summer 2007

Optimization Methods of Laser Induced Breakdown Spectroscopy (LIBS) and the Self-Absorption Problem

Olodia Ayed Taha Nassef
Old Dominion University

Follow this and additional works at: https://digitalcommons.odu.edu/ece_etds

 Part of the [Electrical and Computer Engineering Commons](#)

Recommended Citation

Nassef, Olodia A.. "Optimization Methods of Laser Induced Breakdown Spectroscopy (LIBS) and the Self-Absorption Problem" (2007). Doctor of Philosophy (PhD), dissertation, Electrical/Computer Engineering, Old Dominion University, DOI: 10.25777/c13v-2889
https://digitalcommons.odu.edu/ece_etds/105

This Dissertation is brought to you for free and open access by the Electrical & Computer Engineering at ODU Digital Commons. It has been accepted for inclusion in Electrical & Computer Engineering Theses & Dissertations by an authorized administrator of ODU Digital Commons. For more information, please contact digitalcommons@odu.edu.

**OPTIMIZATION METHODS OF LASER INDUCED BREAKDOWN
SPECTROSCOPY (LIBS) AND THE SELF-ABSORPTION**

PROBLEM

By

Olodia Ayed Taha Nassef

A Dissertation Submitted to the Faculty of Old Dominion University
in Partial Fulfillment of the Requirement for the Degree of

DOCTOR OF PHILOSOPHY

ELECTRICAL AND COMPUTER ENGINEERING

OLD DOMINION UNIVERSITY

AUGUST 2007

Approved by:

Hani E. Elsayed-Ali (Director)

Sacharia Albin (Member)

Mude Erten-Unal (Member)

Juergen F. Kolb (Member)

Linda Vahala (Member)

ABSTRACT

OPTIMIZATION METHODS OF LASER INDUCED BREAKDOWN SPECTROSCOPY (LIBS) AND THE SELF-ABSORPTION PROBLEM

Olodia Ayed Taha Nassef

Old Dominion University, 2007

Director: Hani E. Elsayed-Ali

Laser Induced Breakdown Spectroscopy (LIBS) is a well-established technique for determining elemental composition. Compared to conventional methods, its ability to analyze solids, liquids, and gases with little or no sample preparation makes it more versatile and ideal for field, multi-element, and in-situ analysis. The method can be certified for analytical applications of interest in environmental monitoring and quality control processes. Previous work has demonstrated that several different experimental parameters (e.g. laser wavelength, repetition rate, interaction geometry, surface conditions) may affect the effective analytical possibilities of the method. Therefore, many studies have been devoted to optimize such parameters in a way to enhance its figure of merits. In this thesis, LIBS is combined with a spark discharge to operate in a laser triggered spark discharge mode. This Spark Discharge Laser Induced Breakdown Spectroscopy (SD-LIBS) is evaluated for Al and Cu targets in air under atmospheric pressure. Significant enhancement in the measured line intensities and the signal-to-background ratios, which depends on the spark discharge voltage and the laser fluence, is observed in SD-LIBS when compared to LIBS alone for similar laser conditions. The measured line intensities increase with the applied voltage for both targets, and the ratio of the measured line intensity using SD-LIBS to that using LIBS is found to increase as the laser fluence is decreased. For Al II 358.56, such intensity enhancement ratio

increases from ~ 50 to ~ 400 as the laser fluence is decreased from 48 to 4 J/cm² at an applied voltage of 3.5 kV. Thus, SD-LIBS allows for using laser pulses with relatively low energy to ablate the studied material, causing less ablation, and hence, less damage to its surface. Moreover, applying SD-LIBS gives up to 6-fold enhancement in the S/B ratio, compared to those obtained with LIBS for the investigated spectral emission lines.

Self-Absorption Laser Induced Breakdown Spectroscopy (SA-LIBS) of compacted brass samples was introduced as a new approach whose principle stems from the well-known Atomic absorption Spectroscopy (AAS) technique. Two closely produced plasmas were generated; one acts as the light source analogous to AAS while the other acts as the analyte thus we let the plasma probe itself. Temporal development of Cu spectral lines was initially obtained in order to examine the lines which are more susceptible to self-absorption. SA-LIBS showed that Cu 324 and 327 nm are significantly subject to self-absorption while Cu 330 nm is not, a result that agrees with those reported in literature. Non-linear calibration curves were also obtained, a problem which was previously demonstrated in several reports for brass samples and was attributed to the difference in ablation rate. Internal standardization of emission lines is a method that results in linear calibration curves. Assuming that the concentration of the absorbing species follows a Gaussian distribution, we tried to solve the familiar Beer-Lambert's law for our specific experimental condition. Linear calibration curves of the logarithm of the absorption and absorbing species concentration or equivalently exponential relationship between them have been obtained. The plasma temperature was about the same for both Zn and Cu species, which is reasonably accepted under the assumption of LTE.

This thesis is dedicated to my father.

ACKNOWLEDGMENTS

This thesis would not have been possible without the support of many people. I wish to express my deep and sincere gratitude to my research advisor, Dr. Hani Elsayed-Ali, for his enthusiastic supervision, constructive comments, and his support. His wide knowledge, logical way of thinking and his true scientist intuition have been of great value to me. His understanding, encouragement, and guidance have provided a good basis for the present dissertation. I also would like to thank the members of my PhD committee, Dr. Linda Vahala, Dr. Sacharia Albin, Dr. Juergen F. Kolb, and Dr. Mujde Erten-Unal for their help and support.

During this work, I have collaborated with many colleagues for whom I have great regard and respect. I also wish to extend my warmest thanks to all those who have shared their knowledge, helped me with my work in the Physical Electronics Research Institute (PERI), Old Dominion University, and spread some funny moments on those scientifically dark days.

I am forever indebted to my late father who formed part of my vision and taught me the good things that really matter in life. The memory of my father still provides a persistent inspiration for my journey in this life. I am grateful for my mother for her loving support and prayers. She also endured a lot of this effort, but always found a way to encourage me. I owe my loving thanks to my whole family, without their encouragement and understanding, it would have been impossible for me to finish this work.

Words fail me to express my appreciation to my husband, for his understanding and patience during the PhD period. I owe him for unselfishly letting his intelligence,

passions, and ambitions collide with mine. One of the best experiences that we lived through in this period was the birth of our kids Eleanor and Mahmoud, who provided an additional and joyful dimension to our life mission.

The chain of my gratitude would be definitely incomplete if I would forget to express my deepest and sincere gratitude to "The Great Creator" for inspiring, supporting, and guiding me; this humble being.

My thanks and appreciations also go to the Egyptian government for giving me the scholarship that enabled me to undertake this study. The financial support I received from Old Dominion University at the latter part of my study is also highly appreciated. I am very grateful to Dr. Stephen Zahorian and Dr. Hani Elsayed Ali for their kind consideration and support.

Finally, I would like to thank everybody who was important to the successful realization of this thesis, as well as express my apology that I could not mention them each.

TABLE OF CONTENTS

	Page
List of Figures	
List of Tables	
CHAPTER I INTRODUCTION.....	1
1.1 Basic setup.....	8
1.1.1 Laser source.....	8
1.1.2 Sample under investigation.....	9
1.1.3 Detection.....	11
1.2 Advantages and disadvantages of LIBS.....	12
References of Chapter I.....	15
CHAPTER II OPTIMIZATION OF LASER INDUCED BREAKDOWN SPECTROSCOPY (LIBS)	24
2.1 LIBS Sensitivity.....	25
2.1.1 Double pulsation.....	25
2.1.2 Choice of wavelength.....	29
2.1.3 Pulse duration effects.....	33
2.1.4 Background pressure and ambient gas.....	36
2.1.5 Experimental Geometry.....	41
2.1.6 Additional excitation source	45
2.2 Self-absorption problem in LIBS.....	51
2.2.1 Experimental treatment.....	51
2.2.2 Theoretical correction.....	53
References of Chapter II.....	56
CHAPTER III PRINCIPLES OF LASER INDUCED BREAKDOWN SPECTROSCOPY (LIBS)	65

3.1	Laser-target interaction.....	66
3.2	Plasma formation.....	69
3.3	Plasma characterization.....	72
3.3.1	Temperature determination using spectral line ratios.....	73
3.3.2	Temperature determination using Boltzmann plots.....	74
3.3.3	Temperature determination using Saha- Boltzmann plots.....	76
3.3.4	Temperature determination using line to continuum ratio.....	78
3.3.5	Electron density measurements.....	79
3.4	Plasma propagation.....	80
3.5	Spectrum analysis.....	83
3.5.1	Line emission	83
3.5.2	Background continuum radiation.....	86
3.5.2. a	The free-bound radiation (f-b).....	87
3.5.2. b	The free-free transitions (f-f).....	88
3.6	Sample concentration measurement.....	89
3.6.1	Calibrated standard.....	90
3.6.2	Calibration-free laser induced breakdown spectroscopy (CF-LIBS)	91
	References of Chapter III.....	94
CHAPTER IV	INSTRUMENTATION AND EXPERIMENTAL PARAMETERS	103
4.1	Nanosecond LIBS setup.....	104
4.1.1	Laser characterization and pulse width.....	106
4.1.2	Integrated spectra.....	107
4.1.3	Time-resolved line emission.....	110
4.2	Single-element experiments Cu, Al, C.....	111
4.2.1	Experiment.....	111
4.2.2	Blackbody calibration method.....	114
4.2.3	Laser fluence effect.....	118
4.2.4	Boltzmann Plot.....	119
4.2.5	Pulse accumulation effect.....	121
4.2.6	Spatially resolved spectra-expansion mechanism	122

	4.2.7 Pressure effect.....	124
	4.2.8 Single pulse spectrum.....	127
	4.3 Multi-element experiments	128
	4.4 Picosecond LIBS.....	128
	References of Chapter IV.....	130
CHAPTER V	Spark Discharge Laser Induced Breakdown Spectroscopy (SD- LIBS)	133
	5.1 Introduction.....	133
	5.2 Experiment.....	135
	5.3 Results and discussion.....	138
	5.3.1 Electric circuit characteristics.....	139
	5.3.2 Plasma emission.....	141
	5.3.3 Plasma characterization.....	151
	5.3.4 Sample ablation.....	158
	5.4 Summary.....	160
	References of Chapter V.....	161
CHAPTER VI	Self-Absorption Induced Breakdown Spectroscopy (SA-LIBS)	167
	6.1 Theory of emission and absorption.....	172
	6.2 Optical Absorption Technique.....	175
	6.3 Experiment.....	177
	6.4 Modification of previous experiment.....	181
	6.5 Theory.....	184
	6.6 Results and discussion.....	186
	6.7 Summary.....	205
	References of Chapter VI	207

CHAPTER VII	Conclusion and Future perspectives.....	210
APPENDIX	215
VITA	231

List of Figures

Figure		Page
1.1	A schematic diagram of LIBS illustrates the different components of a typical experiment studying LIBS.	4
3.1	Schematic illustration of Inverse Bremsstrahlung absorption, IB.	69
3.2	Schematic illustration of multiphoton ionization.	70
3.3	Schematic energy level diagram for a hydrogenic species of charge $Z-1$.	85
4.1	Schematic diagram of the experimental setup.	105
4.2	Laser pulse shape as detected with a diode detector.	106
4.3	FWHM of the laser beam as a function of position of the focusing lens to the target surface.	106
4.4	Hg lamp spectrum detected by CVI spectrometer.	107
4.5	Measured detector wavelength shift error.	107
4.6	Schematic diagram of time-integrated LIBS experiment.	108
4.7	Time-integrated LIBS spectrum of Cu in air.	109
4.8	Time-integrated LIBS spectrum of Al in air.	109
4.9	Time-integrated LIBS spectrum of C in air.	110
4.10	Schematic diagram of the time-resolved LIBS experiment.	110
4.11	Time-resolved Al line 358 nm intensity.	111
4.12	Time-resolved of Al line 309 nm intensity.	111
4.13	Time-integrated spectrum of Cu in air.	112
4.14	Grotrian energy level diagram of Copper; Cu given by B. Nemet and L. Kozma [8].	113
4.15	Blackbody calibration method used to correct for the detector intensity response.	115
4.16	Cu spectrum with calibrated blackbody emission at different temperatures.	116

4.17	Calibrated Cu spectrum at different laser fluences using blackbody emission calibration [(*)]: Saturated lines have not been analyzed].	118
4.18	Cu line emission as a function of laser fluence for different Cu lines.	119
4.19	Boltzmann plots used for plasma temperature determination.	121
4.20	Cu line emission as a function of number of laser shots (one frame is equivalent to 3 pulses).	122
4.21	Cu line emission as a function of axial position measured from the sample surface	123
4.22	Cu plasma temperature as a function of axial position measured from the sample surface	124
4.23	Schematic diagram for the experimental setup for LIBS using a vacuum chamber.	125
4.24	Spectra of Cu, both at atmospheric pressure and ~100 mtorr.	126
4.25	Spectrum of Al, at ~100 mtorr.	126
4.26	Single pulse integrated spectrum of Cu in air.	127
4.27	Spectral line identification of Ni alloy.	128
4.28	Picosecond laser focused on Al sample. It is clear that using the picosecond laser with high repetition rate results in low background and high S/B ratio.	129
5.1	The experimental setup used for LIBS and spark discharge assisted LIBS (SD-LIBS).	137
5.2	(a) The temporal shape of the discharge voltage and current; (b) the time evolution of the deposited electric power in the plasma and the emitted integrated light intensity for a laser fluence of 48 J/cm ² and an applied voltage of 3.25 kV.	140
5.3	The integrated spectra for Al, W and Cu under a background of partial vacuum of 50 mTorr (a, c, e) and at atmospheric pressure (b, d, f).	142
5.4	Al spectral lines Al II 281, Al I 309, Al II 358, Al I 394, and Al I 396 nm observed in conventional LIBS (I _{LIBS}) and spark discharge assisted LIBS with an applied voltage of 3.25 kV (I _{SD-LIBS}).	145
5.5	Intensity of the Al spectral emission lines Al I 309 and Al II 358 nm as a function of the applied voltage (Laser fluence ~4 J/cm ² and ~48 J/cm ²).	147

5.6	Signal-to-background ratio S/B of Al spectral emission lines Al I 309 and Al II 358 nm as a function of the applied voltage (Laser fluence ~ 4 and ~ 48 J/cm ²).	149
5.7	Comparison of the Al time profile spectral lines Al II 358 nm (a) and Al I 309 nm (b) using both LIBS and SD-LIBS with 48 J/cm ² laser fluence and 2 kV-applied voltage.	151
5.8	The time resolved temperature of (a) conventional LIBS; and (b) spark discharge assisted LIBS (SD-LIBS) using 8-averaged scans of Cu I 510, Cu I 515 and Cu I 521 nm (Applied voltage = 3 kV and laser fluence of 48 J/cm ²).	153
5.9	Temporal behavior of electron density n_e (cm ⁻³) of Cu plasma induced by spark discharge assisted LIBS (SD-LIBS), 4 μ s after the laser pulse.	155
5.10	Comparison table of the size of the plasma produced by SD-LIBS compared to that produced by conventional LIBS.	156
5.11	Line profile of LIBS produced plasma compared to that produced by SD-LIBS.	157
5.12	Optical microscopy images and depth profiles of Al samples as a result of accumulated 5 laser shots for both modes of operation.	159
6.1	Schematic diagram of a typical atomic Absorption Spectroscopy (AAS) experiment.	168
6.2	Schematic diagram of a technique for measuring optical absorption using the plasma's own emission light as the optical source.	176
6.3	Schematic diagram of the configuration applied in our experiment using the plasma's own emission light as a broadband light source which probes itself to measure the optical absorption.	178
6.4	Temporal development of Cu 330 and 327 nm with no mirror (red line) and when reflected by applying the mirror (black line) [a and b].	180
6.5	Schematic diagram of Self-Absorption LIBS (SA-LIBS) experimental setup.	182
6.6	Schematic diagram of the idea of SA-LIBS configuration.	185
6.7	(a) Integrated spectra of pure Zn, Cu and 5.36/94.64 Cu/Zn samples. (b) Calibration curves resulted from Self-absorption-LIBS technique using the integrated intensities of different spectral lines of Zn.	187
6.8	The emission intensity for the spectral lines; CuI 522 and ZnI 481 nm as a function of the laser fluence for the 47.95/52.05 Cu/Zn sample.	188

6.9	Temporal development of some spectral lines Cu 324, 327 and 330 nm (a) at laser pulse energy = 5 and 13 J/cm ² for the light source spot and the analyte spot, respectively.	190
6.10	The emission intensity resulting from the three acquired measurements for the spectral lines; Cu I 324 and 327 and Zn I 481 nm as a function of the time for the 0.66/99.34 Cu/Zn sample.	193
6.11	The emission intensity resulting from the three acquired measurements for the spectral lines; Cu I 324 and 327 and Zn I 481 nm as a function of the time for the 1.47/ 98.34 Cu/Zn sample.	194
6.12	The emission intensity resulting from the three acquired measurements for the spectral lines; Cu I 324 and 327 and Zn I 481 nm as a function of the time for the 8.31/91.69 Cu/Zn sample.	195
6.13	The emission intensity resulting from the three acquired measurements for the spectral lines; Cu I 324 and 327 and Zn I 481 nm as a function of the time for the 13.47/86.53 Cu/Zn sample.	196
6.14	Calibration curves for different Cu and Zn emission lines resulted from Self-absorption-LIBS technique (SA-LIBS) using the integrated intensities of those spectral lines over a time period of 2 μs (from 1.2 to 3.2 μs).	197
6.15	Calibration curves for Zn signal normalized to the Cu line intensity resulted from SA-LIBS technique.	199
6.16	The average transmission for the spectral lines of Cu (a) 324 nm, (b) 327 nm and (c) 522 nm as a function of the Cu wt %.	200
6.17	The average transmission for the spectral lines of Zn (a) 481 nm, (b) 471 nm and (c) 468 nm as a function of the Zn wt %.	201
6.18	Grotrian diagram of Zn showing the different prominent spectral lines of Zn [15].	203
6.19	Grotrian diagram of Cu that shows the possible atomic transition of its spectral lines [17].	204
6.20	Temporal development of plasma temperature for Cu which was calculated using the spectral lines Cu I 510, 515 and 522 nm while the plasma temperature for Zn the Zn I 334 and 481 nm were used at laser fluence of ~14.5 J/cm ² for the light source spot and ~5.9 J/cm ² for the analyte spot.	205

List of Tables

Table		Page
4.1	List of LIBS component.	105
4.2	Comparison of calibrated intensity values at different temperatures and the obtained experimental values.	117
4.3	Spectroscopic parameters for Cu lines.	120
5.1	Cu spectroscopic parameters used for the determination of plasma temperature.	152
6.1	Comparison of the integrated line and background intensities of CuI 324 and CuI 327 nm with and without the metallic mirror at fluence 3.5 mJ/cm ² .	179
6.2	Composition of brass samples used in this study.	184
6.3	Cu and Zn spectral line parameters used for the determination of plasma temperature.	202

CHAPTER I

INTRODUCTION

One of the most critical environmental concerns nowadays is the problem of waste and pollution produced by human actions. The problem grows with man's increasing impact on the environment. Additionally, accumulated toxic waste from the past few decades of industrial and military production have already reached critical local mass in a number of areas, prompting concentrated detection and cleanup efforts. Most available methods utilize expensive equipment or consist of time-consuming laboratory analysis. Thus, an integral approach for multi-element screening and waste management is gaining favor and a developing demand for effective, economic, and simple pollution-control methods has become a global interest, particularly for the detection of soil and ground water contamination.

Plasma and plasma-based systems offer a number of advantages for pollution detection, waste disposal, and treatment. The remote action characteristic of plasma interactions is well suited to handling toxic materials at a distance. Plasmas, particularly hot ones, are high-temperature systems that can be produced using electrical, optical, microwaves, or other sources that offer efficient ways to couple energy directly to selected charged particles, which can then initiate breakdown or transformation chemical reactions. Comparisons of different plasma-based analytical techniques are illustrated by several authors [1-5]. Generally, the basic principles of spectroscopic techniques are related to

The reference model of this work follows the SPIE format.

the electronic, atomic, and molecular structure and also to gas discharge physics. The oldest elemental analysis technique is atomic spectroscopy, which goes back to the work of Bunsen and Kirchoff in the mid 19th century [6]. They showed how the optical radiation emitted from flames is characteristic of the elements present in the flame or introduced into the flame by various means. It has also been observed that the intensity of element-specific features in the spectra, namely the atomic spectral lines, changed with the amount of elemental species present. This was the basis of the discovery of Atomic Emission Spectroscopy (AES). Parallel to that work, it was found that radiation of the same wavelength as the emitted lines are absorbed by a cold vapor of the same particular element, which was the discovery of Atomic Absorption Spectrometry (AAS). Thus, the type of spectroscopy depends on the physical quantity measured. For instance, AES and AAS focus on the intensity of radiation emitted or absorbed from the analyte, while other techniques, such as mass spectrometry, are based on the measurement of the charge to mass (e/m) ratio. This technique was also found to be applicable to the plasma sources developed in the case of flame, inductively coupled plasma, microwave plasma, and arc discharge plasma where they have shown to be sufficient ion sources for the analysis. Although most of these techniques offer high performance in terms of high power of detection, precision, and accuracy, they need high cost sophisticated equipment and time-consuming sample preparation procedures that do not allow for in situ on-line field applications.

Since the advent of lasers in the early 1960s, spectroscopic techniques, which are based on laser-induced plasmas (LIP), have been recognized as one of the most versatile techniques that continued to develop especially for environmental analysis due to their

advantages; they offer real-time in situ monitoring and multi-element screening capabilities with high analytical sensitivity and selectivity [7,8]. These encouraged researchers to continue their efforts to study the plasma processes, dynamics, and characterization and to develop handable sensors based on LIP to be applied for elemental analysis in different applications such as heavy metal detection in soils [9], biomolecules detection [10], and on-line control over different laser processes [11]. One challenging LIP-based technique with minimum sample preparation and in-situ measurements is Laser Induced Plasma Spectroscopy or commonly known as Laser Induced Breakdown Spectroscopy (LIBS). A schematic diagram of a LIBS experiment is illustrated in Figure 1. This technique is considered one of the most vital techniques with respect to its analytical performance compared to other atomic emission elemental standard techniques, which need the sample to be vaporized and sprayed into the plasma source such as LA-ICP, flame, and graphite furnace spectroscopic techniques. In LIBS, when a powerful-pulsed laser is focused on a gas, liquid, or solid target, a high ionized expanding plasma is generated. The mechanisms involved in the laser-induced plasma depend on both the particular target irradiated and the nature of the laser pulse (duration, frequency, wavelength, and energy). In the first stage of plasma formation, mechanisms involving free-electrons, such as photoionization, radiative recombination, and inverse Bremsstrahlung, govern the plasma emission as a continuum spectrum. When the laser pulse is off, the plasma parameters vary dramatically as a function of time due to the rapid cooling of the plasma. In this stage, ionic and atomic lines rise-up from the continuum and decrease exponentially in intensity and broadening. The internal temperature of species was determined to be in the range of 8000-20,000 K, while the

electron densities were found to be $\sim 10^{16}$ - 10^{19} cm^{-3} . The first applications of LIBS as a quantitative method were proposed in 1980s [12-16]. Since then, many diagnostic LIBS-based systems have been developed for different medical and environmental applications [17-29] and extend to space exploration [30]. The experimental and theoretical studies of this spectroscopic technique and its applicability in different fields have been reviewed by several papers [31-33].

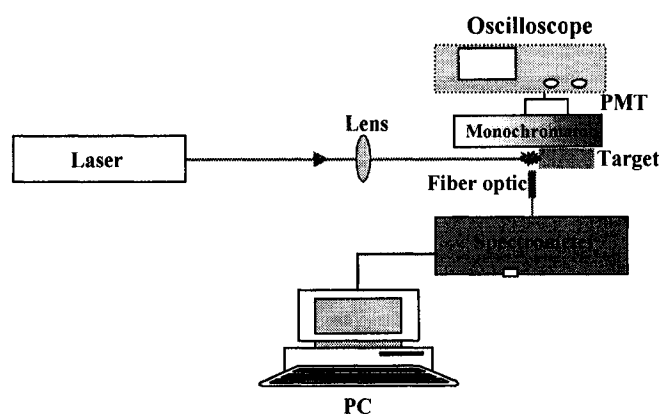


Fig. 1.1 A schematic diagram of LIBS illustrates the different components of a typical experiment studying LIBS. A laser beam is directed and focused on a target by a series of mirrors and a lens. Temporal and integral spectra are acquired for qualitative and/or quantitative analysis.

For many years, efforts were devoted to establish the validity of LIBS measurements for elemental analysis. However, the analytical results are not often satisfactory in terms of accuracy, repeatability, and detection limits. It has been demonstrated that the effective analytical capabilities of the method is affected by different experimental parameters such as laser power and repetition rate, interaction geometry, surface conditions, the amount of ablated and vaporized material, the ability of

plasma to absorb or reflect the delivered energy, the degree of ionization that can change as a function of laser wavelength and irradiance, the nature of ambient gas and pressure, the sample surface morphology, and the collecting optics geometry. Moreover, the laser ablation processes, the overall sample composition, the thermal and optical properties of the sample through the ablation rate, and the assumption of a stoichiometric process all affect the accuracy of the quantitative analysis. Although there have been numerous papers published over the last few years to improve the capabilities of the technique, considerable research is still continuing in order to further develop the method with the optimization of the various aforementioned experimental parameters. Recently, some commercial LIBS instruments offered the possibility of direct measurements without any assembly of single instrumental components. However, even these commercial instruments are still not sufficient to guarantee the achievement of reproducible and precise quantitative results. Thus, LIBS has not yet overcome the experimentation stage to become a routine methodology, which is indicated by the variety of experimental configurations reported in the literature. Each arrangement is the answer to a different analytical problem. Although this confirms the versatility of the LIBS technique, the use of many experimental conditions makes it difficult to carry out a meaningful comparison between results obtained in different laboratories. If all the parameters affecting LIBS are set and a careful consideration is paid for the laser shot-to-shot variations in terms of laser beam energy and spatial profile, the spectral line intensities will generally be proportional to the elemental concentration and reproducible and stable measurements could be obtained. However, the choice of these different parameters is critical and depends on the application.

In the same sense, emphasis is given to solve the problems resulting from the self-absorption of the emitted spectral lines in the produced plasma, which is a crucial problem that highly affects the quantitative analysis of LIBS. The more electron density that is in the laser produced plasma, the more probable the self-absorption phenomena occurs. This in turn affects the spectral line intensities leading to the non-linearity of the calibration curves (Ideally, line emission intensity should be linearly proportional to the concentration) and/or a poor precision of the quantitative analysis. In order to surmount this problem, time-resolved spectroscopy and/or performing LIBS under reduced pressure atmospheres, particularly inert gases, have enhanced the effect of self-absorption in constructing the calibration curves [34]. However, from the viewpoint of field-based and industrial applications, performing experiments in air at atmospheric pressure is more practical to help improve the capability and the ease of the on-line sample analysis. For this reason, many studies have been performed on elemental analysis using laser induced plasma in air at atmospheric pressure [35-38]. Grant et al. [39] used an excimer laser (40 mJ, 28 ns) to analyze several elements of iron ores in air at atmospheric pressure using time-resolved spectroscopy. Gornushkin et al. [40] studied the growth curve method applied to laser-induced plasma emission spectroscopy. In their results, it was indicated that the higher the laser energy, the higher the plasma temperature, resulting in a high degree of ionization and a smaller number of ground state neutral atoms responsible for self-absorption. Omenetto et al. experimentally studied the self-absorption phenomenon in Inductively Coupled Plasma (ICP) [41] and discussed the main equations describing the self-absorption process in a flame [42]. The results were interpreted by means of the Curve of Growth (COG) method [43, 44] which later has been applied to Laser Induced

Breakdown Spectroscopy (LIBS) by Gornushkin et al. [22]. The same COG method was also used by Bulajic et al. [45] and Corsi et al. [46] for correcting self-absorption effects in calibration-free LIBS (CF-LIBS) [47]. Lazic et al. [48] presented a simple model for constructing calibration curves of intensity from a thick homogenous plasma. Aragon et al. [49] studied the influence of the optical depth on spectral line emission from laser-induced plasmas. More recently, several authors also faced the problems of modeling laser-induced plasma inhomogeneities to account for self-reversal phenomena [50-52] produced by the presence of cold absorbing atoms in the periphery of the plasma. All the aforementioned approaches rely on some modeling of the laser-induced plasma parameters (size, temperature, electron density) for obtaining information about the effect of self-absorption on the emission lines. However, the complexity of the laser-target interaction mechanism and the fastness of the plasma evolution reduce the applicability of most of these models, in real situations, to quantitative analytical LIBS measurements.

In this study, we are contributing to the progressing work dedicated to refine the analytical capabilities of LIBS. Bearing in mind that the increase of laser ablation energy can be a way to improve the emission intensities through an increase of the ablated matter, the plasma temperature is not notably increased and the distribution of the excited population over the different excitation energy levels is unchanged [53]. For instance, carrying out LIBS experiment on aluminum samples at atmospheric pressure [9], when the laser ablation energy was doubled, the emission intensity increased by no more than a factor of 2, whatever the excitation energy level of the element contained in the matrix. Furthermore, the increase of laser ablation energy leads to a pronounced self-absorption of the emission lines for elements contained in high concentrations in samples [54].

Additionally, the feasibility of employing inexpensive and portable equipment for in situ field applications will be absent. Thus, we reconfigured an optimization method for LIBS that dealt with the amount of power deposited in the plasma, keeping in mind that increasing the intensity and the signal to background S/B ratio enhances the LIBS results which consequently enhances LIBS figure of merits. Since LIBS is based on the spectral analysis of atomic emission from laser-induced plasma, obtained by focusing a pulsed laser beam onto the sample, once the atomic and/or ionic emission lines are assigned to a specific transition, they allow for a qualitative identification of the species present in the plasma, while their relative intensities can be used for the quantitative determination of the corresponding elements. In our first optimization method, attention was paid toward the enhancement of signal and signal-to-background ratio of the detected spectral lines. In our second attempt of optimizing LIBS, a development of an approach that combines the principles of optical emission spectroscopy along with those of atomic absorption spectroscopy aimed to achieve quantitative analysis with higher analytical performance. In the following section, we introduce the main components needed for the conventional LIBS experiments.

1.1 Basic setup

1.1.1 Laser source

Previously, different kinds of lasers have been used for LIBS experiments. The LIBS experimentalists could not choose any laser sources but just those that generate pulses of sufficient power to produce the plasma and those that the technology allowed. For initial LIBS developments in 1962, Brech and Cross [55] described a LIBS experiment using a ruby laser at 694 nm with 50-ns pulse duration. Then in the 70s, three

commercially manufactured LIBS microanalyzers (Mark III Jarrell–Ash, LMA 10 VEB Carl Zeiss, and JLM 200 JEOL) were proposed that used a Q-switched ruby laser [56]. However, because of the difficulty to control the pulse-to-pulse stability, the technique was not viewed as a technique of reference for the analysis of solids; the pulsed-laser technology was not sufficiently developed. The next phase of LIBS development started with the advent of the Nd:YAG and excimer lasers in the 80s [57]. Since then, many UV, visible, and near-IR laser wavelengths have been made available, making it possible to vary the wavelength and to study how it can affect LIBS measurements [58-60]. With the wide variety of laser systems available in terms of wavelength [61,62] and pulse duration [63], one is able to study and investigate more systematically the best conditions for LIBS implementation. However, the choice of laser wavelength is certainly dependent on the analytical task and/or the aim of the research.

The most widely used lasers include: (1) the Q-switched Nd:YAG laser with output wavelengths (λ) of 1064 nm and 532 nm (second harmonic) and pulse duration of 5-10 ns; (2) the ruby laser ($\lambda = 693$ nm and pulse length = 20 ns); (3) various gas lasers, including CO₂ ($\lambda = 10.6$ μ m and pulse length = 100 ns) and N₂ ($\lambda = 337$ nm and pulse length = 10 ns); and (4) excimer lasers with pulse lengths of 10-20 ns, including ArF ($\lambda = 193$ nm), KrF ($\lambda = 248$ nm) and XeCl ($\lambda = 308$ nm). These lasers have peak power outputs ranging from 1-100 MW. When these laser pulses are focused by an appropriate lens to submicron-sized spots, the resulting energy fluence is in the order of 10^{10} - 10^{12} Wcm⁻². This energy fluence is sufficient to produce plasma on solid samples.

1.1.2 Sample under investigation

The history of the LIBS technique proves its flexibility to be applied to all types

and states of materials. In 1963, spectrochemical analysis of surfaces using lasers was first presented, followed by the observation of optical induced breakdown in a gas in 1964. Then, during the 1970s, development continued in several directions. In 1972, Felske et al. described the analysis of steel by means of a Q-switched laser. In the early 1980s, there was a renewed interest in spectrochemical applications of LIBS, driven by its unique advantages and applications in different media. Important applications were the detection of hazardous gases and vapors in air and small amounts of beryllium in air or on filters. A repetitively pulsed Nd:YAG laser at 1.06 μm was used to excite effluent gases from an experimental fixed-bed coal gasifier. Although alkalis at the parts per billion levels were not detected, the major constituents, including sulfur, were easily seen and quantified. Liquids were analyzed either by excitation at the surface or in the volume. Solutions of ten different elements were analyzed and atomic and ionic uranium spectra were seen by exciting a flowing solution of uranium in nitric acid. Uranium could not be detected by focusing into the liquid, only through focusing on the liquid-air interface. As a progressing technique, LIBS was used by Poulain and Alexander [64] to measure the salt concentration in seawater aerosol droplets. Then, Aguilera [65] applied LIBS to determine carbon content in molten and solid steel, while the elemental analysis of aluminum alloy targets was studied by Sabsabi and Cielo. [66]. During the 1990s, the applications turned to very practical problems, such as monitoring environmental contamination, control of materials processing, and sorting of materials to put them in proper scrap bins. More concentrated work was directed to develop a rugged, moveable instrumentation. Optical fibers were built into LIBS systems, primarily for carrying the spark light to the spectrometer and occasionally for the delivery of the laser pulse as well.

As early as 1988, a moveable beryllium monitor was built, which was followed by the availability of several other portable instrument, the size of a small suitcase, designed for the analysis of contaminants in soils and lead in paint. Additionally, the development of a compact LIBS rover leads the technique to space applications as chemical sensor for Mars exploration [30].

1.1.3 Detection

The choice of a detection system for LIBS is widely dependent on the final application. Most of the LIBS work published in the literature has been carried out using a conventional Czerny-Turner spectrometer coupled with a detector such as an intensified charge-coupled device (ICCD), CCD, intensified photodiode array (IPDA), or photomultipliers. Conventional Czerny-Turner spectrometer attached to linear photodiode arrays or ICCDs allows a limited spectral coverage (typically a few nm wide). A few used Echelle spectrometers, which provide a wide range of spectral wavelengths. Since the beginning of the 1990s, Echelle-based systems for simultaneous measurements of analyte lines at different wavelengths have been developed and used in inductively coupled plasma (ICP) and microwave-induced plasma (MIP) analysis, as well as astronomical spectroscopy. Recently, the arrival of a new commercial optical detector system coupling Echelle spectrometer with a time-gated ICCD detector enabled simultaneous measurements of spectral lines in a wide range with enhanced resolution. Investigations reveal that the Echelle spectrometer combined with an intensified CCD is a capable tool for LIBS analysis, particularly where it is necessary to perform a complete analysis with a single shot. In spite of its limitations, it is considered the most versatile

tool for instantaneous, multi-elemental analysis of any kind of sample, solid, liquid, or gas.

1.2 Advantages and disadvantages of LIBS

Comparing the spectroscopic techniques in terms of their analytical figure of merits, simplicity, cost, and applications, we conclude some of the distinguishing advantages of LIBS such as:

1. Minimum or no sample preparation results in a reduction of time-consuming procedures.
2. Both conducting and non-conducting materials can be tested.
3. Very small amounts of sample (0. 1 pg to 0. 1 mg) are vaporized.
4. Hard materials that can be difficult to get into solution can be analyzed (e.g. ceramics, glasses, and superconductors).
5. Multiple elements can be determined simultaneously.
6. The direct determination of aerosols or ambient air is possible.
7. The analysis is simple, rapid and produces no waste.
8. Remote sensing is possible with the use of fiber optics.
9. Samples can be analyzed in a hostile environment.
10. Underwater analysis is possible.

In addition, LIBS has some drawbacks such as:

1. Current systems are expensive and complex.
2. Obtaining suitable matrix-matched standards is difficult.
3. Interference (matrix) effects can be large.

4. Detection limits are generally 1-100 times poorer than conventional techniques such as inductively coupled plasma (ICP-atomic emission spectroscopy) for some elements.
5. Self-absorption effects significantly influence LIBS precision.

Following this introduction, a state-of-the-art of the existing optimization schemes for Laser Induced Breakdown Spectroscopy (LIBS), particularly those for in-field analyses, is given in Chapter II. The emphasis is on the research trends toward improving the figure of merit of LIBS.

Chapter III outlines the physics of the laser-surface interaction and the mechanisms for producing both the line and continuum emission of the produced plasma. The mathematical principles of the analytical laboratory plasmas are outlined. Then, characterization methods of such plasma are summarized and how they relate to the concentration of the analyte sample.

In Chapter IV, a description of the LIBS instrumentation, system calibration, and the analysis schemes for single and multi element samples, which were adopted for spectral line identification and selection, are given. The spectral characteristics of a number of considered samples are presented and discussed in the context of system optimization for analytical purposes. Results of test measurements for the consistency of our instrumentation are also presented.

The development of a Spark Discharge Laser-Induced Breakdown Spectroscopy (SD-LIBS) is presented in Chapter V, correlating the conventional configuration of LIBS to an additional cross excitation source: spark discharge. The I-V circuit characteristic has been shown and the adopted computational procedure that uses the electrical

parameters has been explained for calculating the electron density. This introduces an optimization that provides better excitation sources that consequently enhances the sensitivity of LIBS as an analytical spectroscopic technique.

The approach of self-absorption LIBS (SA-LIBS) applied to the quantitative analysis of brass samples is presented in Chapter VI. This includes the rationale for the development of such an approach, which resorts to the principles of absorption spectroscopy, the most well established, and most accurate technique compared to other analytical techniques. Time-integrated and time-resolved profiles of the selected spectral lines were used to examine the characteristics of such approach in detail. Numerous spectral profiles are explored such that the optimal analytical lines are selected and criteria of their use to perform calibration for quantitative analysis are examined.

Chapter VII outlines the prominent features of both SD-LIBS and SA-LIBS, development of their analytical method, application, and main results, which highlight the versatility of both techniques in the quantitative spectroscopy of single and binary samples, are summarized, followed by an outline of future perspectives in terms of novel instrumentation, method development and applicability to more complicated alloys, their potential compared to other techniques, and the possible future theoretical studies that can model both techniques.

References of Chapter I

- [1] N. Omenetto, In "*Analytical laser spectroscopy*," Wiley Interscience, New York, (1979).
- [2] J. A. Broekaert, In "*Analytical atomic spectrometry with flames and plasmas*," Wiley-VCH, Germany, (2002).
- [3] M. Cullin, In "*Atomic spectroscopy in elemental analysis*," Blackwell Publishing Ltd, UK, (2004).
- [4] J. Robinson, In "*Atomic spectroscopy*," Marcel Dekker Inc., New York, (1996).
- [5] R. K. Marcus, In "*Glow discharge spectroscopy*," Plenum Press, New York, (1993).
- [6] G. R. Kirchoff and R. Bunsen, "Chemical analysis by spectrum observation," *Philos. Mag.* **20**, 89-98 (1860).
- [7] S. J. Weeks, H. Haraguchi, and J. D. Winefordner, "Improvement of detection limits in laser-excited atomic fluorescence flame spectrometry," *Anal. Chem.* **50**, 360-68 (1978).
- [8] S. Sjostrom and P. Mauchien, "Laser atomic spectroscopic techniques-The analytical performance for trace element analysis of solid and liquid samples," *Spectrochim. Acta B.* **15**, 153-180 (1991).
- [9] F. Capitilli, F. Colao, M. R. Provenzano, R. Fantoni, G. Brunetti, and N. Sensi, "Detection of heavy metals in soils by Laser Induced Breakdown Spectroscopy," *Geoderma* **106**, 45-62 (2002).

- [10] O. Samek, D. C. S. Beddows, H. H. Telle, J. Kaiser, M. Liska, J. O. Caceres, and U. A. Gonzales, "Quantitative Laser-Induced Breakdown Spectroscopy analysis of calcified tissue samples," *Spectrochim. Acta B* **56**, 865-875 (2001).
- [11] R. Noll, H. Bette, A. Brysch, M. Kraushaar, I. Monch, L. Peter, and V. Sturm, "Laser-Induced Breakdown Spectroscopy: applications for production control and quality assurance in the steel industry," *Spectrochim. Acta B* **56**, 637-649 (2001).
- [12] L. J. Radziemski, D. A. Cremers, and T. R. Loree, "Detection of beryllium by Laser Induced Breakdown Spectrometry," *Spectrochim. Acta B* **38**, 349-355 (1983).
- [13] D. A. Cremers and L. J. Radziemski, "Detection of chlorine and fluorine in air by Laser Induced Breakdown Spectrometry," *Anal. Chem.* **55**, 1252 (1983).
- [14] D. A. Cremers, L. J. Radziemski, and T. R. Loree, "Spectrochemical analysis of liquids using the laser spark," *Appl. Spectrosc.* **38**, 721 (1984).
- [15] D. A. Cremers and L. J. Radziemski, "Direct detection of beryllium on filters using the laser spark," *Appl. Spectrosc.* **39**, 57 (1985).
- [16] L. J. Radziemski, D. A. Cremers, and T. M. Niemczyk, "Measurement of the properties of a CO₂ laser induced air plasma by double floating probe and spectroscopic techniques," *Spectrochim. Acta B* **40**, 517-525 (1985).
- [17] D. Anglos, S. Couris, and C. Fotakis, "Laser diagnostics of painted artworks: Laser-Induced Breakdown Spectroscopy in pigment identification," *Appl. Spectrosc.* **51**, 1025-1030 (1997).

- [18] I. B. Gornushkin, J. E. Kim, B. W. Smith, S. A. Baker, and J. D. Winefordner, "Determination of cobalt in soil, steel, and graphite using excited-state laser fluorescence induced in a laser spark," *Appl. Spectrosc.* **51**, 1055-1059 (1997).
- [19] K. Y. Yamamoto, D. A. Cremers, M. J. Ferris, and L. E. Foster, "Detection of metals in the environment using a portable Laser-Induced Breakdown Spectroscopy instrument," *Appl. Spectrosc.* **50**, 222-233 (1996).
- [20] A. V. Pakhomov, W. Nichols, and J. Borysow, "Laser Induced Breakdown Spectroscopy for detection of lead on concrete," *Appl. Spectrosc.* **50**, 880-884 (1996).
- [21] O. Samek, D. C. S. Beddows, H. H. Telle, G.W. Morris, M. Liska, and J. Kaiser, "Quantitative analysis of trace metal accumulation in teeth using Laser-Induced Breakdown Spectroscopy," *Appl. Phys. A* **69**, 179-182 (1999).
- [22] B. J. Marquardt, S. R. Goode, and S. M. Angel, "In situ determination of lead in paint by Laser-Induced Breakdown Spectroscopy using a fiber-optic probe," *Anal. Chem.* **68**, 977-981 (1996).
- [23] S. Nakamura, Y. Ito, K. Sone, H. Hiraga, and K. Kaneko, "Determination colloidal iron in water by Laser Induced Breakdown Spectroscopy with two sequential laser pulses," *Anal. Chem.* **68**, 2981-2986 (1996).
- [24] J. M. Vadillo and J. J. Laserna, "Laser-Induced Breakdown Spectroscopy of silicate, vanadate and sulfide rocks," *Talanta* **43**, 1149-1154 (1996).
- [25] L. C. Jensen, S. C Langford, J. T. Dickinson, and R. S. Addleman, "Mechanistic studies of laser-induced breakdown spectroscopy of model environmental samples" *Spectrochim. Acta B* **50**, 1501-1519 (1995).

- [26] A. S. Eppler, D. A. Cremers, D. D. Hickmott, M.J. Ferris, and A. C. Koskelo, "Matrix effects in the detection of Pb and Ba in soils using laser-induced breakdown spectroscopy," *Appl. Spectrosc.* **50**, 1175-1181 (1996).
- [27] R. Wisbrun, I. Schechter, R. Niessner, H. Schroder, and K. L. Kompa, "Detector for trace elemental analysis of solid environmental samples by laser plasma spectroscopy," *Anal. Chem.* **66**, 2964-2975 (1994).
- [28] S. Howden, C. Schneider, and Z. Grosser, "The analysis of soil, paint and house dust for lead contamination," *At. Spectrosc.* **17**, 171-175 (1996).
- [29] S. Palanco and J. J. Laserna, "Full Automation of a Laser-Induced Breakdown Spectrometer for quality assessment in the steel industry with sample handling, surface preparation and quantitative analysis capabilities," *J. Anal. At. Spectrom.* **15**, 1321-1328 (2000).
- [30] A. K. Knight, N. L. Scherbarth, D. A. Cremers and M.J. Ferris, "Characterization of Laser Induced Breakdown Spectroscopy (LIBS) for application to space exploration," *Appl. Spectrosc.* **54**, 331-340 (2000).
- [31] L. Radziemski, "Review of selected analytical applications of laser plasmas and laser ablation, 1987-1994," *Mirochem. J.* **50**, 218-234 (1994)
- [32] M. Capitelli, A. Casavola, G. Colonna, and A. DeGiacomo, "Laser-induced plasma expansion: theoretical and experimental aspects," *Spectrochim. Acta B* **59**, 271-289 (2004).
- [33] J. M. Vadillo and J. J. Laserna, " Laser-Induced Breakdown Spectrometry: Truly a surface analytical tool," *Spectrochim. Acta B* **59**, 147-161 (2004).

- [34] M. Kuzuya, M. Murakami, and N. Maruyama, "Quantitative analysis of ceramics by Laser-Induced Breakdown Spectroscopy," *Spectrochim. Acta B* **58**, 957-965 (2003).
- [35] K. J. Grant, G. L. Paul, and J. A. O'Neill, "Quantitative elemental analysis of iron ore by laser-induced breakdown spectroscopy," *Appl. Spectrosc.* **45**, 701-705 (1991).
- [36] M. Autin, A. Briand, P. Mauchien, and J. M. Mermet, "Characterization by emission spectrometry of a laser-produced plasma from a copper target in air at atmospheric pressure," *Spectrochim. Acta B* **48**, 851-862 (1993).
- [37] N. Andre, C. Geertsen, J. L. Lacour, P. Mauchien, and S. Sjostrom, "UV laser ablation optical emission spectrometry on aluminum alloys in air at atmospheric pressure" *Spectrochim. Acta B* **49**, 1363-1372 (1994).
- [38] H. Kurniawan, K. Kagawa, M. Okamoto, M. Ueda, T. Kobayashi, and S. Nakajima, "Emission spectrochemical analysis of glass containing Li and K in high concentrations using a XeCl excimer laser-induced shock wave plasma," *Appl. Spectrosc.* **50**, 299-305 (1996).
- [39] K. J. Grant, G. L. Paul, and J. A. O'Neill, "Time-resolved laser-induced breakdown spectroscopy of iron ore," *Appl. Spectrosc.* **44**, 1711-1714 (1990).
- [40] I. B. Gornushkin, J. M. Anzano, L. A. King, B. W. Smith, N. Omenetto, and J. D. Winefordner, "Curve of growth methodology applied to laser-induced plasma emission spectroscopy," *Spectrochim. Acta B* **54**, 491-503 (1999).
- [41] N. Omenetto, S. Nikdel, J. D. Bradshaw, M. S. Epstein, R. D. Reeves, and J. D. Winefordner, "Diagnostic and analytical studies of the inductively coupled

- plasma by atomic fluorescence spectrometry," *Anal. Chem.* **51**, 1521-1525 (1979).
- [42] N. Omenetto, J. D. Winefordner, and C. Th. J. Alkemade, "An expression for the atomic fluorescence and thermal-emission intensity under conditions of near saturation and arbitrary self-absorption," *Spectrochim. Acta B* **30**, 335-341 (1975).
- [43] R. Ladenburg and F. Reiche, "Über selektive absorption," *Ann. Phys.* **42**, 181-209 (1913).
- [43] A. C. G. Mitchell and M. W. Zemansky, In "*Resonance radiation and excited atoms*," Cambridge University Press, New York, (1934).
- [44] D. Bulajic, M. Corsi, G. Cristoforetti, S. Legnaioli, V. Palleschi, A. Salvetti, and E. Tognoni, "A procedure for correcting self-absorption in calibration free-laser induced breakdown spectroscopy," *Spectrochim. Acta B* **57**, 339-353 (2002).
- [45] M. Corsi, G. Cristoforetti, V. Palleschi, A. Salvetti, and E. Tognoni, "A fast and accurate method for the determination of precious alloys cartage by laser induced plasma spectroscopy," *Eur. Phys. J. D* **13** (3), 373-377 (2001).
- [46] A. Ciucci, V. Palleschi, S. Rastelli, A. Salvetti, and E. Tognoni, "New procedure for quantitative elemental analysis by laser induced plasma spectroscopy," *Appl. Spectrosc.* **53**, 960-964 (1999).
- [47] V. Lazic, R. Barbini, F. Colao, R. Fantoni, and A. Palucci, "Self-absorption model in quantitative laser induced breakdown spectroscopy measurements on soils and sediments," *Spectrochim. Acta B* **56**, 807-820 (2001).

- [48] C. Aragon, J. Bengoechea, and J. A. Aguilera, "Influence of the optical depth on spectral line emission from laser-induced plasmas," *Spectrochim. Acta Part B* **56**, 619-628 (2001).
- [49] H. Amamou, A. Bois, B. Ferhat, R. Redon, B. Rossetto, and M. Ripert, "Correction of the self-absorption for reversed spectral lines: application to two resonance lines of neutral aluminum," *J. Quant. Spectrosc. Radiat. Transfer* **77**, 365-372 (2003).
- [50] I. B. Gornushkin, C. L. Stevenson, B. W. Smith, N. Omenetto, and J. D. Winefordner, "Modeling an inhomogeneous optically thick laser induced plasma: a simplified theoretical approach," *Spectrochim. Acta B* **56**, 1769-1785 (2001).
- [51] J. A. Aguilera, J. Bengoechea, and C. Aragon, "Curves of growth of spectral lines emitted by a laser-induced plasma: influence of the temporal evolution and spatial inhomogeneity of the plasma," *Spectrochim. Acta Part B* **58**, 221-237 (2003).
- [52] C. Gautier, P. Fichet, D. Menut, J. L. Lacour, D. L'Hermite, and J. Dubessy, "Quantification of the intensity enhancements for the double-pulse Laser Induced Breakdown Spectroscopy (LIBS) in the orthogonal beam geometry," *Spectrochim. Acta B* **60**, 265-276 (2005).
- [53] C. Gautier, P. Fichet, D. Menut, J. L. Lacour, D. L'Hermite, and J. Dubessy, "Main parameters influencing the double-pulse laser induced breakdown spectroscopy (LIBS) in the collinear beam geometry," *Spectrochim. Acta B* **60**, 792-804 (2005).
- [54] F. Brech and L. Cross, "Optical microemission stimulated by a ruby maser," *Appl. Spectrosc.* **16**, 59-60 (1962).

- [55] L. Moenke-Blankenburg, In "*Laser micro-analysis*," Wiley Inter-science, New York, (1989).
- [56] L. Radziemski, "From Laser to LIBS, the path of technology development," *Spectrochim. Acta Part B* **57**, 1109-1113 (2002).
- [57] W. Sdorra, J. Brust, and K. Niemax, "Basic investigations for laser microanalysis: The dependence on the laser wavelength in laser ablation," *Mikrochim. Acta.* **108**, 1-10 (1992).
- [58] C. W. Ng, W. F. Ho, and N. H. Cheung, "Spectrochemical analysis of liquids using laser-induced plasma emissions: effects of laser wavelength on plasma properties," *Appl. Spectrosc.* **51**, 976-983 (1997).
- [59] M. Martin and M. D. Cheng, "Detection of chromium aerosol using time-resolved laser-induced plasma spectroscopy," *Appl. Spectrosc.* **54**, 1279-1285 (2000).
- [60] J. Zhou, X. Hou, K. X. Yang, S. J. Tsai, and R. G. Michel, "Lasers based on optical parametric devices: wavelength tunability empowers laser-based techniques in the UV, visible, and near-IR," *Appl. Spectrosc.* **52**, 176A-189A (1998).
- [61] P. Stchur, K. X. Yang, X. Hou, T. Sun, and R. G. Michel, "Laser excited atomic fluorescence spectrometry, " *Spectrochim. Acta B* **56**, 1565-1592 (2001).
- [62] A. Semerok, C. Chale'ard, V. Detalle, J. L. Lacour, P. Mauchien, P. Meynadier, C. Nouvellon, B. Salle, P. Palianov, M. Perdrix, and G. Petite, "Experimental investigations of laser ablation efficiency of pure metals with femto, pico and nanosecond pulses," *Appl. Surf. Sci.* **138-139**, 311-314 (1999).

- [63] S. Laville, F. Vidal, T. W. Johnston, O. Barthe'lemy, M. Chaker, B. Le Drogoff, J. Margot, and M. Sabsabi, "Fluid modeling of the laser ablation depth as a function of the pulse duration for conductors," *Phys. Rev. E* **66**, 066415 (2002).
- [64] D. Poulain and D. R. Alexander, "Influences on concentration measurements of liquid aerosols by Laser-Induced Breakdown Spectroscopy," *Appl. Spectrosc.* **49**, 569-579 (1995).
- [65] C. Aragón, J. A. Aguilera, and J. Campos, "Determination of carbon content in molten steel using Laser-Induced Breakdown Spectroscopy," *Appl. Spectrosc.* **47**, 606-608 (1993).
- [66] M. Sabsabi and P. Cielo, "Quantitative analysis of aluminum alloys by laser-induced breakdown spectroscopy and plasma characterization," *Appl. Spectrosc.* **49**, 499-507 (1995).

CHAPTER II

OPTIMIZATION OF LASER INDUCED BREAKDOWN SPECTROSCOPY (LIBS)

Laser Induced Breakdown Spectroscopy (LIBS), as a method for elemental analysis, exploits quantized transitions characteristic of each individual element, mostly in the ultraviolet, visible, and near-infrared spectral regions for qualitative identification and/or quantification. While this technique is summarized by an interaction of a focused high-energy laser beam with a specific target, it involves several complicated processes including plasma formation, ablation of matter from the sample surface, and excitation and/or ionization of the ablated material. These processes depend on the laser pulse characteristics (such as laser wavelength, pulse duration, energy) as well as the chemical and physical properties of the target. While LIBS is strongly dependent on these conditions of experimental implementation, some inherent problems such as the insufficient sensitivity (emission characteristic from the plasma), in addition to the self-absorption problem, limit the application of the technique in comparison to other atomic emission spectrometric methods such as spark discharge and inductively coupled plasma. However, the advantages of LIBS as a simple, rapid, non-contact, in-situ, real time, the absence for sample preparation requirements, and more importantly, due to the easily automated nature of the emission spectrochemical analysis; these all made an influential impact on the research and technology fields resulting in the wide applicability of LIBS in different fields, such as the online industrial quality control and environmental applications.

However, to use LIBS in a broader field of applications, significant work has been devoted to raise its analytical performance. Several papers improved the LIBS emission sensitivity while others focused their work on correcting the self-absorption effect that directly influences the LIBS detection limit. In this chapter, we firstly present various studies that investigated different parameters optimization that resulted in better coupling of laser energy to the target and/or ablated material leading to more efficient production of analyte atoms in an excited state. Secondly, we review recent studies dealing with the self-absorption problem in LIBS.

2.1 LIBS Sensitivity

2.1.1 Double Pulsation

One of the ideas to overcome the LIBS drawback of weak emission signals and, hence, low detection limit is the use a double laser pulse, one to ablate the material and the other to excite the resulting plasma. This technique is called double pulse excitation, dual pulse LIBS, or repetitive spark pair. The use of multiple laser pulses was found to produce more intense and sustained plasma emission, which accordingly improves the sensitivity of LIBS. Applying the sequential laser pulses from two Q-switched Nd:YAG lasers to quantitative analysis of colloidal and particulate of iron in water, Nakamura et al. [1] determined the FeO(OH) concentration in the tens of parts per billion (ppb). After developing a coaxial sample flow apparatus to control the atmosphere of laser-induced plasma, the detection limit of Fe was improved from 0.6 ppm to 16 ppb with the use of sequential pulse excitation. Their results show the capability of LIBS to determine suspended colloidal and particulate impurities in a simple and quick way. Furthermore, highly sensitive elemental analysis of lead carbonate colloids was demonstrated by two-

pulse laser-induced plasma spectroscopy [2]. The first laser pulse created a vapor plume with the particulates concentrated in space because of their slower propagation. The authors then used an ArF laser pulse that efficiently atomized and excited the lead analyte. They found that the lead emissions were enhanced and the background continuum interference was minimized. They have also shown that the detection limit became 14.2 ppb compared with 13 ppm achieved by conventional laser-induced breakdown spectroscopy of lead ions in water and 210 ppb for lead aerosols. Researchers extended their work to the elemental analysis of water using dual pulse LIBS [3]. While they found that the line spectra were weak in the case of a single pulse, the limit of detection was higher in the dual pulsation as a result of hotter plasma (3000 k in single pulse to 9000 k in double pulse). They explained the phenomenon that the double pulse forms a gas bubble in the surface-water interface, which allows the interaction of the second pulse with the plasma in a way similar to the gaseous environment. For solvents in water, supersensitive detection of sodium in water was developed with the use of double pulse LIBS [4]. Under optimization conditions of the timing between the laser pulses, the delay time of emission detection timing, the gate width of emission detection period, and the laser energy, the authors achieved detection limit of sodium in water in the range of 0.1 ppb. Moreover, the application of laser-induced breakdown spectroscopy to liquid samples, by use of a Nd:YAG laser in double-pulse excitation mode, has been investigated [5]. They found that the line emission from a magnesium ion or atom is more than six times greater for double-pulse excitation than for single-pulse excitation. Their study of the temporal evolution of the line emission from the plasma showed that the background, as well as the line emission, decays faster in double-pulse excitation than in

single-pulse excitation. The enhancement in the emission was attributed to an increase in the volume of the emitting gas. For a magnesium solution, they achieved a limit of detection of 69 ppb in double-pulse mode compared to 230 ppb when using the single-pulse mode.

For solid samples, Sattmann et al. [6] studied the single, double, and multiple Q-switched Nd:YAG laser pulses to vaporize the material from steel samples and induce plasma. In their work, the material ablation of different pulses, emission intensities of iron lines, and electron temperatures and densities were determined. They found that the material ablation increases with multiple pulses compared to single pulses of fixed total energy as well as electron temperatures and densities. Under their experimental conditions, the application of double pulses increased the line intensities by a factor of two. Performing quantitative microchemical analysis of low-alloy steel using single and double pulses, they concluded that the analytical performance is improved by the double-pulse technique.

Continuing the study of double pulsation on metals in air, St-Onge et al. [7] found line intensity enhancement, explaining it as a volume effect generated by the first plasma and led to a uniform absorption of the second pulse whose energy is distributed on a broader volume. They also studied the double pulsation technique with the use of different wavelengths, UV for more ablation rate and IR for higher heating efficiency [8]. They observed a significant signal increase depending on the ionization state and the energy level of the spectral line under investigation.

Colao et al. [9] compared the single and double LIBS carried out on aluminum samples in air, using 1064 nm Nd:YAG laser. They observed a lowering of the second

pulse plasma threshold, together with an overall enhancement in line emission for the investigated time delay. The laser-induced plasma originated by a single and double pulse was investigated near ignition threshold with the aim to study possible dynamical mechanisms in different regimes. Plasma relevant parameters, such as temperature and electron density, have been measured in the plasma decay on a long time scale and compared with crater shape (diameter and inferred volume). The comparison of double and single pulse laser excitation was carried out while keeping constant the energy per pulse; the influence of laser energy was investigated as well. Their results suggest that use of the double pulse technique could significantly improve the analytical capabilities of LIBS technique in routine laboratory experiments.

Stratis et al. [10] suggested a different study by firing a focused laser beam parallel to sample to form air plasma and after a few microseconds another beam is used for ablation. As a result they observed an increase in the spectral line intensity and ablation rate. They also simultaneously measured the time resolved spatially integrated emission intensity from two collection directions and concluded that the collection geometry is an important parameter in LIBS measurements. They also reported that with the use of the pre-ablation spark, there is an emission enhancement of Al, Ti, and Fe in a non-metal non-conducting matrix [11]. Scaffidi et al. also studied the orthogonal pre-ablation spark dual-pulse laser-induced breakdown spectroscopy LIBS configuration [12]. However, they combined two different lasers with different pulse duration, nanosecond and femtosecond lasers. Even without full optimization of inter-pulse alignment, ablation focus, they observed large signal, signal-to-noise ratio, and signal-to-background ratio enhancements for copper and aluminum targets. Other papers studied

the double-pulse laser-induced breakdown spectroscopy using two Nd:YAG lasers emitting at 532 nm combined in the collinear beam geometry [13]. Their experiment was performed on different types of materials: synthetic glasses, rocks, steels at atmospheric pressure in air. For all matrices, they systematically investigated the influence of the delay between the two laser pulses from temporal and spectral analyses. Furthermore, they described the correlation between the excitation energy levels of the emission lines and the increase in intensity induced by the double-pulse scheme for each material. By comparing the results, they found that the materials in the double pulse experiments displayed different behaviors due to the change in plasma temperatures for each material in the single and double-pulse configuration, determined by the Saha-Boltzmann plot method. Hence, they gave an insight into the potentialities and the limitations of the double pulse Laser Induced Breakdown Spectroscopy (LIBS) for analytical purpose so that the materials can be classified in terms of effectiveness of the double-pulse approach. The double-pulse approach ensures the preferential enhancement of the intensities of emission lines originated from high excitation energy levels for certain matrices while they are not affected very much for others. Consequently, depending on this work, the materials can be classified according to a decreasing order of effectiveness of the double-pulse approach.

2.1.2 Choice of wavelength

Different laser sources have been used in LIBS experiments, and most plasma characteristics related to various experimental conditions have been studied. However, there should be an optimization to compromise between the aim of the research and the choice of the appropriate laser wavelength. For instance, Sdorra et al. [14] compared the

characteristics of plasmas induced by infrared and UV laser wavelength (fundamental and fourth harmonic of an Nd:YAG laser). Under the same experimental conditions such as pressure and buffer gas, they found that the UV wavelength was more effective in mass ablation. They also found that using the fourth harmonic, the crater dimensions and the amount of mass ablated were almost independent on the kind of buffer gas and on the pressure value between 140 and 1000 mbar, indicating that radiation shielding is negligible at this wavelength. In their investigation of plasma temperature in the center of the plasma, the authors measured the same values either using the fundamental or the UV wavelength, observing that there was a more pronounced drop in the lateral regions in the case of the UV-induced plasma. In their conclusion, the authors evaluated the analytical results and observed that the emission signals obtained with UV radiation were not linear with analyte concentration, even after comparing the LIBS signal with reference lines. They suggested that the poor analytical results obtained with UV wavelength can be due to incomplete atomization of the material ablated and demonstrated that linearity is obtained if the vapor ablated is reheated by means of a second, independent IR pulse. However, different observations have been reported by Berman and Wolf [15], who compared the analytical results obtained in the detection of Ni in water by using alternatively the fundamental Nd:YAG wavelength and the UV third harmonic. They observed that the UV-generated spectrum has lower continuum intensity, leading to a better signal-to-noise ratio. Furthermore, after constructing the calibration curves for the same spectral lines, the one obtained with UV irradiation revealed a higher slope and allowed a better limit of detection (LOD) value. Their results also agreed with the results obtained on liquids by Ng et al. [16] who found that the main difference in the plasma

plume generated by visible or ultraviolet laser of the same fluence is in the temperature value T , which is quite lower in the second case, while the electron density n_e value is approximately the same. As an example of different laser-material coupling at different wavelengths, Mao et al. reported the reflectivity coefficient R of metallic Cu at three different typical wavelengths: R equals 0.976 at 1064 nm, 0.814 at 532 nm, and 0.336 at 266 nm [17]. The absorbed energy (a fraction $1 - R$ of the laser energy) in irradiating copper is thus much higher in the case of UV laser wavelength. The same authors, in support of this observation, experimentally demonstrated that the transition between thermal and explosive regimes in laser ablation occurs, for the different wavelengths, at power density values scaling inversely as the $(1 - R)$ factor. Cabalin and Laserna [18] found that the fluence threshold for plasma formation is higher for shorter wavelengths. They measured the emission intensity of the atomic lines characteristic of some metals depending on laser fluence, for different harmonics of a nanosecond Nd:YAG laser (fundamental, second harmonic, fourth harmonic). They found a general behavior for the three wavelengths and for the different metals: by increasing the laser fluence values above the threshold, a linear increase of the line intensity occurred, and then followed by a saturation regime. Both the thresholds for plasma formation and the saturation regime, however, were shifted towards lower fluences for IR wavelength, while the energy threshold values were higher for IR radiation. In their discussion of the results, the authors stated that reflectivity does not seem to be a relevant parameter, at high fluences (i.e. above the threshold), since the plasma formation changes substantially the properties of the target surface. However, the choice of laser wavelength is certainly dependent on the analytical task. For instance, Haisch et al. [19] preferred the second harmonic

Nd:YAG laser, instead of a higher order one, for sampling the particles deposited on a filter membrane used to select colloids from its liquid solvent.

The use of UV instead of IR laser pulses for LIBS measurements of metals, such as Al, has the advantages of increased ablation efficiency, reduction in plasma shielding effects, and stoichiometric ablation for minor constituent elements in Al alloys [17,20]. Urged by the aforementioned advantages besides the small ablation spot size dictated by their experimental aim, Cravetchi et al. used LIBS with UV laser pulses and low energies of the order of 1-10 μJ to perform multi-elemental microanalysis of commercial aluminum alloys in air [21]. They showed that LIBS technique is capable of detecting the elemental composition of particles less than 10 μm in size, such as precipitates in an aluminum alloy matrix, by using single laser shots. Moreover, they carried out chemical mapping with a lateral resolution of $\sim 10 \mu\text{m}$ of the distribution of precipitates in the surface plane of a sample. Because of the strong continuum emission that arises from the high plasma temperature of a few to tens eV in laser-induced plasma, Lo and Cheung [22] showed that lower temperatures ($< 1 \text{ eV}$) could be used for spectrochemical analysis. They also showed that using ArF (193nm) produces a low temperature plasma in aqueous samples at fluences below the breakdown threshold. Using 193-nm LIBS, the analyte emissions were found to live longer, the signal background ratios were better, and the relative limit of detection was shown to be low.

A comparison of two wavelengths, 1.06 and 2.94 μm , obtained with Nd:YAG and Er:YAG lasers, respectively, was used for LIBS analysis of aluminum alloy samples in two conditions of surrounding gas [23]. They studied the influence of the laser wavelength on the laser-produced plasma for the same irradiance by use of air or helium

as a buffer gas at atmospheric pressure. They also examined the effect of laser wavelength in two different ambient conditions in terms of spectrochemical analysis by LIBS. Their results indicated that the effect of the surrounding gas depends on the laser wavelength and the use of an Er:YAG laser could increase linearity by limiting the leveling in the calibration curve for some elements in aluminum alloys. They also showed that there is a significant difference between the plasma induced by the two lasers in terms of electron density and plasma temperature. They showed that by the use of an Er:YAG laser for LIBS analysis, different advantages could be presented. For example, it is better absorbed by organic species, it is safer for the eyes than 1.064 μm , and it is commercially available and can easily be coupled into an optical fiber.

2.1.3 Pulse duration effects

There are different characteristic time scales of the different processes involved in the formation of the plasma [24]. For example, free electron heating and thermalization takes approximately 100 fs; hot electron gas cooling and energy transfer to the lattice lasts a few ps; thermal diffusion in the bulk takes place on a time scale of 10^{-11} s; and the onset of thermal melting and ablation occurs after 10^{-10} s. An important conclusion can be drawn: a laser pulse of duration longer than a few ps does not interact the whole time with the original thermodynamic state of the material. Instead, it interacts with different transient states and with the plasma of evaporated material and buffer gas above the sample surface. The main part of the material is evaporated from molten metal, and preferential volatilization of different elements in a sample with different melting temperatures occurs. In such a case the stoichiometric composition of the gas phase does not adequately represent the composition of the bulk, and the accuracy of the analytical

procedure deteriorates. The picture changes completely if a laser pulse with duration of approximately 100 fs or shorter is used. Now the laser interacts only with the electrons of a material. Before the material undergoes any changes in thermodynamic state, the laser pulse is over and most of the energy is deposited into the sample. Material removal occurs after the laser pulse. From this brief discussion it can be concluded that an fs-laser with pulse duration of approximately 100-200 fs and shorter should be closer to an optimal laser system than other systems. However, the importance of the leading edge rise time of the laser pulse has been studied [25]. The author showed that it should be fast enough to remove material layer at a speed equal to the heat conduction moving to the bulk. Lasers with different pulse duration have been applied to LIBS, for instance, Chichkov et al. studied laser ablation of solid targets by 0.2-5000 ps Ti: Sapphire laser pulses and introduced theoretical models and qualitative explanations of their experimental results [26]. They presented the advantages of femtosecond lasers for precise material processing, well defined patterns, and its pure ablation of metal targets in vacuum, which insures its ability as a promising tool for applications in precise material processing. However, Rieger et al. investigated the emission of laser-produced silicon and aluminum plasmas in the energy range from 0.1 to 100 μJ ($0.5\text{-}500 \text{ J/cm}^2$) using 10 ns and 50 ps KrF laser pulses focused to a 5- μm diameter spot [27]. They showed that there is a little difference between 50 ps and 10 ns pulses in the plasma emission both in terms of the intensity of the emission lines and in terms of lifetime of the emission, while differences become important only at very low fluences approaching the plasma formation threshold. The effect of laser pulses of different durations has been compared mainly in terms of the amount of ablated material. Recently, studies have also compared

the spectral emission of plasmas generated by nanosecond pulses with those generated by picosecond pulses and femtosecond pulses. These studies indicate that the shorter pulse duration might be more effective for LIBS. Eland et al. have recently reported on two studies, one comparing 1.3 ps and 7 ns pulses the other comparing 140 fs and 7 ns pulses in LIBS [28]. Unfortunately, different lasers of different wavelengths and significantly different energies were used in these studies (200 mJ, 1064 nm, 7 ns vs. 1 mJ, 570 nm, 1.3 ps and 810 nm, 1 mJ, 140 fs) leading to much larger plasma in the case of nanosecond ablation and making comparison a problem. However, the authors obtained a better precision in their calibration curves when using the short laser pulses, especially in case of femtosecond ablation. Margetic et al. who investigated the spectra of brass samples using 6 ns and 170 fs pulses of 0.1-1 mJ energy from the same laser also found a better precision with short pulses under their experimental conditions. In addition, the authors referenced the higher precision in sample ablation, lower continuum background coupled with faster plasma dissipation, and the possible use of a non-gated detector as advantages due to the use of the shorter pulse duration. Le Drogoff et al. recently published a study on LIBS measurements on aluminum with 100 fs pulses (800 nm), in which the authors compare their results to a previous LIBS study with 8 ns pulses (1064 nm) by Sabsabi and Cielo. The energy density of 20 J/cm^2 and the spot size of 0.6 mm were chosen to approximately match those of Sabsabi and Cielo (21 J/cm^2 , 0.62 mm spot size). Since the temporal evolution of the plasma was found to be different for femtosecond and nanosecond pulses, Le Drogoff et al. used a shorter delay time of $1 \mu\text{s}$ and a shorter gate width of $5 \mu\text{s}$ for their detection times than Sabsabi and Cielo, who used a $10 \mu\text{s}$ delay and a $10 \mu\text{s}$ gate width. Le-Drogoff et al. presented higher detection limits that were

approximately a factor of 3-8. Hammer et al. studied the effectiveness of laser-induced plasma shielding produced when focusing visible laser pulses from 5 ns to 125 fs [29]. Their results were based on the measurements of transmission of energy through the focal volume. They found that the shielding efficiency decreases as a function of pulse duration from 5 ns to 300 fs, which they explained that the lower electron density for picosecond pulses leads to a lower probability of absorption of a photon by an electron and, hence, less efficient shielding. Moreover, they observed that the shielding time increases from 300 fs to 125 fs; they offered two hypotheses to explain this trend: the moving-breakdown model and nonlinear effects. The moving-breakdown model predicts a reversal in the direction in which the plasma moves, and this reversal may lead to increased shielding because the entire pulse is exposed to the breakdown for 125-fs pulses, whereas for longer pulses a significant amount of energy may pass the focal volume before it is shielded. Self-focusing and continuum generation change the spatial and temporal profiles of the pulse as it propagates through the focal volume. These nonlinear effects probably have an influence on the amount of energy absorbed in the plasma.

2.1.4 Background pressure and ambient gas

When a high power laser density is used, the plasma shielding effect prevents the laser from reaching the target leading to the reduction of laser-material coupling efficiency. As a result, the existence of an ambient gas plays an important role in the propagation and expansion of the produced plasma. Yasuo studied the emission characteristics of laser-induced plasma with the use of a Q-switched ruby laser of 1.5 J in argon atmosphere at reduced pressure [30]. He measured the time- and spatially-resolved

emission profiles. In argon atmosphere at reduced pressure, he showed that the emission period of plasma was elongated to over a hundred microseconds, and the emissive region expanded to more than a few tens of millimeters above the sample surface. He also demonstrated that the emission intensities of atomic lines increased several fold in an argon atmosphere, in comparison with those obtained in air at the same pressure. His experiment resulted in a moderate confinement of plasmas at 50 Torr and an increase of emission intensities. The re-excitation of emissive species by collisions with metastable argon atoms seems to be less important. These results are explained by the chemical inertness and the thermal characteristics of the argon atmosphere and the decrease in absorption of the laser pulse by the plasma plume. Lies et al. suggested that argon pressure of 140 torr yields higher intensity value for Si I 288.2-nm line in steel sample hit by Nd:YAG laser, 5 mJ pulse energy [31]. Grant and Paul studied the spatial axial emission of steel produced by excimer XeCl laser in different gas atmosphere (air, He and Ar) at pressures (5, 50 and 760 torr) [32]. They showed that the behavior of emission intensity under these variables (gas, pressure and axial distance) was too complicated, but their general conclusion was that the optimum condition which gave the higher signal-to-noise (SNR) under their experimental conditions is when argon gas at 50 torr was used and when the LIBS signal was detected 6 mm from the target.

Sdora and Niemax [13] compared the effect of different ambient gas on the spectral emission of copper target irradiated by Nd:YAG laser. They demonstrated, for constant experimental conditions, that argon showed the higher plasma temperature, electron density, the lowest ablation rate, and the higher emission intensity. Moreover, they showed that the decay time of plasma temperature during 40 μ s after the laser pulse

was slower for Ar than other gases. For Helium, it produced lower temperature, lower electron density, and emission intensity. Iida also showed higher emission intensity with Ar atmosphere at about 100 torr [33]. Thiem et al. has applied LIBS to multi-elemental analysis of transition metals found in solid and alloy samples [34]. The ablation was carried out in ultra-high vacuum, which reduced the background signal often found in atmospheric pressure analysis. Their results demonstrated the ability of this method for use of simultaneous multi-element analysis in very complex solid samples.

Choice of a buffer gas suitable for laser-induced plasma (LIP) was also studied by Joseph et al. who compared the signal enhancement in the presence of both He and Ar for solid targets: Al and Cu [35]. As a buffer gas to support LIP on Al and Cu surface, they found that helium has definite advantages over argon due to the significant population of metastable helium states which transfer energy to the metal atoms and thus enhance the emission. Increasing the pressure of He increased the enhancement effect whereas Ar showed a quenching effect on the atomic and ionic transitions. For glass analysis, Kurniwan et al. obtained a linear calibration curve with a slope of near unity at certain pressure [36]. They performed quantitative analysis on a number of glass samples using an XeCl laser under reduced pressure of 1 torr and were able to obtain lower detection limit than those usually attained. By focusing a normal-oscillation Nd:YAG laser on a brass sheet in air at reduced pressure, plasma characterized by a low ion concentration and background intensity was created [37]. The authors showed that the high temperature of the produced plasma (7000 K), in addition to the large volume of the crater (10 μg), are among other favorable conditions to make this suitable for spectrochemical analysis which permit analyses to be performed at extremely high sensitivity. The authors

suggested that with further improvements, such as the use of an Optical Multichannel Analyzer (OMA) system, this method represents a powerful tool for use in spectrochemical analysis, especially for the analysis of solid samples.

Time-integrated space-resolved laser-induced plasma spectroscopy was proved to be a useful technique in the vacuum ultraviolet (VUV) for the quantitative determination of the carbon content in steels [38]. The authors used the output of a Q-switched Nd:YAG 1064 nm laser, with a 1 J maximum output pulse energy and a 12 ns temporal pulse width, to be focused onto the surface of each sample under vacuum in order to produce the emitting plasma. They demonstrated that VUV spectroscopy allows ionic lines to be used and they obtained linear calibration curves for the five carbon spectral lines (from C^+ and C^{2+}) under investigation. They determined the limits of detection for all lines; the lowest detection limit obtained was $(87 \pm 10 \text{ ppm})$ from the C^{2+} 97.70 nm line, which compares favorably with the only available value in the literature of 100 ppm.

Kurniawan et al. performed direct spectrochemical analyses on large bulk samples, such as metal plates, by using a small vacuum chamber that they attached directly to the sample surface through an o-ring [39]. Their technique allowed the in-situ generation of laser plasma, and the presence of the o-ring near the target surface effectively shielded off the surrounding area from the undesirable continuum emission from the primary plasma and thereby enhanced the detection sensitivity of their technique. Using zinc plate and Pb glass as samples, the authors demonstrated that even the time-integrated spectra, obtained by employing an OMA system, exhibited a lower background than those obtained by ordinary time-resolved LIBS. As a result, they concluded that high sensitivity can be attained at low cost with an OMA system without

gating function. Compared with ICP-AES or ICP-MAS methods commonly employed in industries, their technique offers the obvious advantage of not requiring pretreatment of solid samples with suitable solvents. They suggested that when combining their technique with a polychromator, it is expected to be particularly suitable as a nondestructive analytical tool for antique appraisal and for rapid quality inspection of industrial materials.

Carbon content in fly ash, char, and pulverized coal under high-pressure and high-temperature conditions have been detected by Noda et al. using LIBS technique [40]. They developed an automated LIBS unit and applied it in their experiment to demonstrate its capability in actual power plant monitoring. They have examined gas composition effects to obtain the best operating parameters under actual plant conditions. Their results were compared to those obtained using the conventional method, showing satisfactory agreement. Their work confirmed the various advantages; LIBS can detect carbon content even under the high-pressure conditions typical of gasification thermal power plants, LIBS is capable of a detection time of 1 min, as compared to over 30 min of sampling and analysis time required by the conventional methods, and offers various merits as a tool for actual power-plant monitoring.

The emission characteristics of Sn and Zn in low-pressure laser-induced plasma have been examined with reference to change of the surrounding gas (Ar, Ne and He) [41]. From the pressure dependence of the intensity of Sn I 326.23-nm, Sn II 335.22-nm, Zn I 213.86-nm and Zn II 210.00-nm emission lines, Naeem et al. found that Sn and Zn atoms could be excited by the collision between surrounding gas species and ablated atoms with large kinetic energy by laser irradiation. Besides the collisional excitation,

resonance charge-transfer collision between Zn atoms and Ne ions proved to be effective in the selective excitation of Zn II 206.42-nm and 210.00-nm emission lines, because the emission intensity of these lines was strongly enhanced in Ne atmosphere, and the sum of the excitation energy of these lines and the ionization potential of Zn is very close to the ground-state energy of Ne ions.

A quantitative elemental analysis of ceramics in an argon atmosphere at reduced pressure was carried out with LIBS [42]. Kuzuya et al. analyzed the time-resolved emission spectra from laser-induced plasma and showed that in argon at ~ 200 Torr, the spectral line intensity and the line-to-background ratio were maximized by observing the laser plasma with a time delay of $0.4 \mu\text{s}$. They also showed that time-resolved measurement of a spectrum in the initial stage of plasma generation ($\sim 1 \mu\text{s}$) was effective for improving the slope of the calibration curve. Based on the results, they analyzed standard ceramic samples for magnesium, aluminum, calcium, iron, and titanium and obtained linear calibration curves with a slope of unity when using argon at 200 Torr.

2.1.5 Experimental Geometry

In laser-induced breakdown spectroscopy (LIBS), a focused laser pulse is used to ablate material from a surface and form a laser plasma that excites the vaporized material. Geometric factors, such as the distance between the sample and the focusing lens and the method of collecting the plasma light, can greatly influence the analytical results. Eppler et al. compared the precision of the results obtained using a spherical and a cylindrical lens to focus the laser pulse on the surface of a soil sample [43]. They found much more precise results using the cylindrical lens and explained the effect by considering the larger area sampled in the latter case, which allowed averaging of inhomogeneous

composition that is naturally associated with this kind of sample. Moreover, when the analytical collection system is pointed on fixed spatial regions of the plasma, changes in the plasma emission position might be interpreted as a change in concentration of the element, unless the observation region encompasses and spatially integrates the entire geometrical extent of the plasma for all power densities. This is sometimes obtained by directly facing a fiber optic to the plume, at a distance of some millimeters, in order to avoid damage by excessive heating. The control of the collection angle of the fiber end allows in fact the gathering of light from a broad plasma extension. On the other hand, the use of optical fiber bundles has been proposed for the simultaneous acquisition of spectral emission from different regions inside the plasma plume.

Due to the breakdown threshold of the optical fiber material, optical fibers were initially used in LIBS only to deliver the plasma emission to the detection system. The use of fiber-optic was then proposed also for laser beam delivery, in a configuration suitable for operating in a hostile environment, allowing for the separation of the focusing and collecting head from the most delicate parts of the instrumentation; the laser source, spectrometer, and detector. Beside flexibility, this configuration also offers an obvious advantage in terms of safety with respect to possible eye damage. On the other hand, when the laser beam is coupled into a fiber, a more restrictive limit is imposed on the maximum laser pulse energy, in order to avoid damage to the fiber itself. Various configurations have been proposed, including the use of two optical fibers (one for delivering the laser beam and one for collecting the plume emission) [44]. A comparison has been carried out between the performances of the fiber-coupled LIBS and lens-coupled LIBS: after optimization of different experimental parameters the detection

limits achieved were found to be comparable, at least for some elements [45]. The choice of on-axis plasma emission collection presents advantages in terms of simplicity and reproducibility, and this configuration is often adopted when aiming to perform on-line analysis of some evolving process. It is well known that the plasma plume expands in the direction perpendicular to the sample surface. The on-axis detection, being performed along the direction perpendicular to the surface, is less sensitive to changes in the plasma to collecting-lens distance, which occur when several shots are fired at the same place on the sample surface and a crater is formed. With on-axis collection, the plasma displacement causes minimum perturbations on the LIBS signal, because of the depth of focus of the detection optics, which is typically longer than influence of crater depth.

The geometrical shape of the plasma and the spatial emission intensity profile are strongly dependent on the laser power density and on other parameters; therefore, it is often necessary to optimize the characteristics of the experimental apparatus as a whole. To obtain the best quantitative results, Multari et al. reported the results of an investigation of the effect of sampling geometry on LIBS measurements [46]. Their diagnostics included time-resolved spectroscopy and temporally and spectrally resolved imaging using an acousto-optic tunable filter (AOTF). They investigated parameters including the type of lens (cylindrical or spherical) used to focus the laser pulse onto the sample, the focal length of the lens (75 or 150 mm), the lens-to-sample distance (LTSD), the angle-of-incidence of the laser pulse onto the sample, and the method used to collect the plasma light (lens or fiber-optic bundle). From these studies, they found that atomic emission intensities, plasma temperature, and mass of ablated material depend strongly on the LTSD for both types of lenses. For laser pulse energies above the breakdown

threshold for air, they found that these quantities exhibit symmetric behavior about an LTSD approximately equal to the back focal length for cylindrical lenses and asymmetric behavior for spherical lenses. For pulse energies below the air breakdown threshold, their results demonstrated that both lenses display symmetric behavior. In their experiment, detection limits and measurement precision for the elements Be, Cr, Cu, Mn, Pb, and Sr, determined with the use of fourteen certified reference soils and stream sediments which they found to be independent of the lens used. Their time-resolved images of the laser plasma showed that at times $>5 \mu\text{s}$ after plasma formation a cloud of emitting atoms extends significantly beyond the centrally located, visibly white, intense plasma core present at early times ($<0.3 \mu\text{s}$). They determined that, by collecting light from the edges of the emitting cloud, one can record spectra using an ungated detector (no time resolution) that resemble closely the spectra obtained from a gated detector providing time-resolved detection. Their result has implications in the development of less expensive LIBS detection systems.

The parameters for the recording of the plasma emission from steel alloy samples have been investigated and optimized [47]. The authors used focused $1.06 \mu\text{m}$ laser beam to irradiate the samples and form plasma in atmospheric air. They optimized a number of experimental parameters, for example, the distance of the focusing lens to the sample to produce stable plasma above the sample, without air breakdown. Also, they controlled the translation of the sample so that a fresh area of the sample was irradiated every few laser shots. They optimized the settings for the gate delay and width for each element to reduce the background signal, increasing the signal-to-noise ratio and stabilize the line intensity ratio. They were able to obtain calibration curves for the elements Cr and Ni

covering a wide concentration range and exhibiting a good linear fit by choosing a long delay for observation and appropriate selection of the emission lines. Similar results were obtained for Mn. However, when they investigated the wavelength dependence for the Mn calibration curve by irradiating the samples with UV 355 nm laser, the produced calibration curve showed a good linear fit as well, but with a smaller slope, indicating a reduction in sensitivity by a factor of 2, with respect to the IR irradiation. After they carried out parameter optimization, the sample analysis was an easy task, lasting less than five mins for every sample. Their results showed that this method could be appropriate for in-situ elemental analysis in their concentration range, without using very high laser intensities. They suggested that extending the measurements to the other trace elements used in steel alloys could be the basis of developing a LIBS apparatus useful for the on-line control of the steel fabrication procedure in industry.

2.1.6 Additional excitation source

For many decades, the use of laser as an ablation device such that a focused laser beam ablates a small amount of the sample (~10-50 μm spot) and produces a cloud of micro particle material. These particulates formed by the high-energy laser beam are dynamically transported via a flow of a carrier gas (an inert gas) to undergo further atomization, ionization, and excitation by an additional excitation source such as the widely applied techniques; ICP, spark, arc, or flame. The produced plasma is analyzed and detected either by emission, absorption or mass spectrometry, which have already been exploited by many applications. However, the complexity, tedious, time-consuming sample preparation, and expensive cost of such techniques make it difficult for fast, on-line, in-situ low cost applications.

Other additional excitation sources such as the application of electric or magnetic fields to the laser produced plasma have been studied and reviewed. For instance, the operation of the laser micro-spectral analysis (LMA), which was previously presented by Moeneke-Blankenburg who applied an electric field across the laser produced plasma [48]. A laser beam fired at the desired micro-region of a sample causes a small quantity of substance (about 1 μg) to be vaporized. He adjusted the synchronously produced spark discharge to be located between two electrodes, which became arc-like with increasing inductance and served as a light source for the micro-spectral emission analysis in the ultraviolet and visible and also near infrared regions. Fried et al. used a 193-nm ArF excimer laser in the photo-ablation of bulk $\text{YBa}_2\text{Cu}_3\text{O}_7$ and the oxides of barium, copper, and yttrium [49]. They studied optical emission from the plume of ablated material from 350 to 630 nm and observed the emission from ions, atoms, and diatomic molecular oxides. They also discussed the effects of applying electric and magnetic fields on the plume in vacuum and oxygen. They found that the applied electric field has enhanced the intensity of all the emitting species enabling identification of the highly congested emission lines in the spectra. They suggested that their results could help to provide a mechanism for the observed effect of an applied electric field in the production of in-situ superconducting thin films of $\text{YBa}_2\text{Cu}_3\text{O}_7$. Using a femtosecond UV laser source (248.6 nm), studies on large-gap laser-induced electrical discharges have been conducted by Rambo et al. [50]. They have presented detailed investigations of laser-induced electrical discharges using an ultrashort UV laser pulse and investigated parameters such as pressure, lens selection, focal position, and laser energy. They also presented spectroscopic analysis of the laser plasma and discharge and introduced an experimental

technique that allows the measurement of ionization cross-sections at atmospheric pressures. They showed that the high voltage (HV) breakdown threshold is linear with respect to pressure and is reduced significantly with the laser. Their investigations of lens selection and focal position revealed enhanced guidance for longer-focal-length lenses as well as reduced breakdown for focal spots near the positive electrode. They studied the saturation phenomena of the HV breakdown threshold with respect to the incident laser intensity and employed it for measuring multiphoton ionization coefficients. Their spectroscopic studies revealed distinct atomic oxygen and nitrogen in both the excited and ionized states, indicating a photo-dissociation of molecules after ionization.

An experimental study that enhanced the electron temperature of laser induced plasma was carried out by the use of radio-frequency dielectric heating [51]. The authors used a radio-frequency electric field of 140 MHz to heat the plasma produced by multi-step resonant photo-ionization. They found that when applying a radio-frequency input power of 1.0 W, the electron temperature increased from 0.3 to 1.0 eV. Also, in their experiment, applying heating induced a plasma oscillation, which they explained by the generation of ion waves in the plasma, and an enhanced electron temperature which they found to be higher than the ion temperature. They concluded that their method could improve the efficiency for extracting ions rapidly from a laser-induced plasma in atomic vapor laser isotope separation.

The effect of a pulsed magnetic field on spatially resolved emission from a laser plasma at atmospheric pressure was investigated [52]. The authors produced a pulsed magnetic field by capacitive electrical discharge through a specially designed solenoid which was oriented normal to the laser axis. They observed an enhancement in the

temporally integrated emission due to the presence of the magnetic field, and they found it to be most significant when the plasma was formed about 1 mm below the magnetic field axis. They observed that the degree of confinement of the plasma increased with the magnetic field strength. Their studies utilized the maximum magnetic field attainable with their system that did not jeopardize the structural integrity of the solenoid (~85 kG). They observed characteristic lateral resolved emission, both along and normal to the magnetic field axis, demonstrated significant radial compression and axial expansion of the laser plasma. They explained their results by the effects of $\mathbf{J} \times \mathbf{B}$ or fluid magnetic pressure interactions. They suggested the need for spatially and temporally resolved emission and absorption studies to further understand the dynamics of the magnetic field effects on plasma atomization, excitation, and ionization. In order to continue their investigation of the dynamic effects of a high-intensity pulsed magnetic field on a laser plasma, temporally resolved emission and absorbance measurements were made [53]. The authors spatially resolved the temporal-resolved emission so that the effects of the magnetic field on plasma propagation both along and normal to the magnetic field could be probed. They investigated the mechanism of interaction of the field by observing plasma emission in spatial zones, which were likely influenced by an induced secondary current in the plasma. They discriminated the emission enhancements spatially and temporally, which explained that radial compression was due to static magnetic field interactions with the laser plasma and that mild Joule-heating from the small induced current was responsible for emission enhancements later in time. They also measured the spatially integrated absorbance in the decaying plasma, which showed a decrease in absorbance as a result of the magnetic confinement. This was attributed to an increased

rate of condensation of the atoms in the vapor cloud produced by the plasma. They indicated that more efficient coupling of energy from the magnetic field to the plasma would require low-pressure operation in a controlled atmosphere and/or a pulsed magnetic field having a greater dB/dt .

Moreover, the influence of a magnetic field on the plume produced by KrF-laser ablation of magnesium in vacuum has been investigated using time-integrated photography, streak photography and spectroscopy, and charge probes [54]. The authors reported the line emission spectra in the ~ 200 -600 nm interval and effective stream velocities for the plume obtained from the spatiotemporal emission of specific neutral and ion lines. They deduced the time of flight velocities from their measurements using simple charge-collector probes. They observed an enhancement on emission and ionization and changes in the plume structure and dynamics in the presence of the field. They qualitatively explained their results in terms of a magneto-hydrodynamic model. Another investigation of the dynamics and confinement of laser-created plumes expanding across a transverse magnetic field have been presented by Harilal et al. [55]. They used $1.06 \mu\text{m}$ 8 ns pulses from a Nd:YAG laser to create an aluminum plasma that was allowed to expand across a 0.64 T magnetic field. As diagnostic tools, the authors exploited fast photography, time of flight spectroscopy, and emission spectroscopy. Their photographic studies showed that the plume is not fully stopped and diffuses across the field. Using time of flight studies, they showed that all of the species are slowed down significantly, and they observed a multiple peak temporal distribution for neutral species. In the presence of the magnetic field, they observed changes in plume structure and dynamics, enhanced emission and ionization, and velocity enhancement. They explained

that the temperature increase of the plume was due to Joule heating and adiabatic compression.

Another kind of additional excitation sources that has been combined to laser induced plasma is a hollow cathode discharge system for atomic emission spectrometry of solid samples [56]. The author vaporized a solid sample by a Q-switched Nd-YAG laser, and the vaporized material is introduced into a hollow cathode discharge by means of an argon flow. The author optimized the pressure, flow rate of argon gas, the form of electrodes, and the discharge current. In his experiment, he operated the laser in either single pulse mode or multiple-pulse mode. The latter mode offered improved precision and detection limits. He obtained analytical curves for standard samples of aluminum alloys that exhibit good linearity. Using the multiple-pulse mode, the author also reached a detection limit of a few micrograms per gram. The author suggested the use of a tighter vacuum system and a trap to avoid the molecular bands background emission stemming from gas impurities. Another way to improve LIBS analytical selectivity and sensitivity is by combining it with the technique of laser-induced fluorescence spectroscopy (LIFS) [57]. The authors conducted their measurements in air at standard atmospheric pressure and used specific set-ups for remote analysis; they used no special sample preparation and applied no laborious system alignment procedures. They pursued detection of aluminum, chromium, iron and silicon at trace level concentrations. The choice of these elements is due to their importance in numerous chemical, medical, and industrial applications, and they also exhibit suitable resonance transitions, accessible by radiation from a pulsed Ti:sapphire laser system. They concluded that fast sequential multi-element analysis is feasible only if the elements under investigation exhibit excitation transitions

within a narrow wavelength window for quick tuning. They produced calibration curves for Cr and Si using certified steel samples and estimated the detection limits to be 105 ppm and 95 ppm, respectively. The combination of LIBS and LIFS proved to be more sensitive and selective than LIBS alone, however, at the expense of higher system set-up complexity.

2.2 Self-absorption problem in LIBS

The plasma created by laser ablation is often optically thick for some particular wavelengths. The thickness of the plasma is related to a complex interaction mechanism between the atoms, ions and the radiation, which is emitted and successively reabsorbed; the result on the spectra is the occurrence of self-absorption and a pronounced non-linearity in the calibration function at increasing concentration. Plasma thickness usually occurs for the most intense lines (e.g. resonance lines) of elements present at concentrations greater than approximately 0.1%. However, the plasma can also become thick for less intense lines at higher elemental concentrations.

2.2.1 Experimental treatment

Time-resolving capability is one of the solutions for self-absorption problem. For instance, Autin et al. analyzed the laser-produced plasma formed in air at atmospheric pressure and generated by focusing a nitrogen laser on a copper target [58]. They studied the temporal characteristics of the plasma by atomic emission spectrometry. They also described the features of the spectra, such as the type of lines and the line broadening, and compared them to those obtained at reduced pressure or in other gases. As self-absorption is predominant when the plasma first forms, a time delay was used to obtain the best analytical performance. They succeeded in obtaining limits of detection in the

range of 1-10 ppm for copper. Kuzuya and Aranami also used time-resolved spectroscopy when investigating the possibility of analysis of high concentration (4.5-90%) copper in metal alloy samples (Al alloys and brass) in air at atmospheric pressure [59]. They studied the emission characteristics of plasmas produced by a Q-switched Nd:YAG laser over a laser energy range of 30-90 mJ. Another method of reducing the effect of self-absorption, showed by their experimental results, is by increasing the laser pulse energy. Moreover, their results of time-resolved spectroscopy of laser-induced plasmas indicated that self-absorption is predominant during short time-periods after the laser pulse, and a time delay is effective for the reduction of self-absorption. At high laser energy of 90 mJ, they obtained a linear calibration curve with a slope near unity for the analysis of copper in the concentration range from 4.5 to 20% with a gate width of 0.4 μ s at a delay time of 0.4 μ s after the laser pulse.

The effect of an inert gas atmosphere (e.g. argon) on the self-absorption of emission spectra of a laser-induced plasma was studied with the use of a normal laser microprobe by changing the gas pressure [60]. The authors determined the degree of self-absorption from the observed profiles of copper resonance lines using the curve-fitting method with the assumption of a Lorentzian profile. According to the results, self-absorption was reduced by decreasing the argon pressure and was eliminated at low pressures, the range of which depends on the analyte concentration. Their studies of the spatially resolved spectrum show that the confining effect of the plasma by the argon atmosphere becomes effective at higher pressures, resulting in an increase in the emission intensity. They concluded that there exists a moderate pressure at which self-absorption can be eliminated without losing too much intensity from reduction of confinement. For

the determination of copper (concentration 1-9.8%) in aluminum samples and obtaining a linear calibration graph with a slope of unity, they found that at a pressure of around 150 Torr, high emission intensity of the spectral line free from self-absorption can be obtained about 1.5 mm above the sample surface.

2.2.2 Theoretical correction

To improve the accuracy of quantitative analysis for some elements such as those of environmental interest (soils and sediments), regardless of their matrix composition plasma modeling, including the correction for line re-absorption, was investigated. For example, Lazic et al. applied LIBS in the quantitative analysis of elemental composition of soils with different origins and Antarctic marine sediments [61]. Their analytical method included the plasma modeling at local thermal equilibrium (LTE) based on average temperature and electron density values, as well as spectra normalization that they introduced in order to reduce the effects related both to the substrate optical and thermal properties and to the influence of laser parameters on quantitative data. Their computational algorithm took into account only atomic species and their first ionization states, which is sufficient at the plasma temperature measured in their experiments. They generated calibration curves for each element of interest measured on certified samples with different matrix compositions. In their paper, a model is developed that takes into account the effects responsible for non-linearity in the relationship between line intensity and elemental concentration. It considered correction of line re-absorption and contributions from space regions with different plasma densities. They successively applied it for the direct determination of a single element concentration in any sample, regardless of its unknown matrix composition. Their method was tested on a priori

unknown samples and gave uncertainties in concentration varying from 15 to 40% over a large concentration range covering several orders of magnitude. They found that the measuring error depends on element type, on the concentration value, and also on the number of certified samples used for the initial calibration. Their results are significant for field application such as on-board marine sediment analysis where a significant matrix variation with layer depth is common.

A theoretical approach is developed for optically thick inhomogeneous laser induced plasma, which can describe the time evolution of the plasma continuum, the specific atomic emission after the laser pulse, and the interaction with a target material [62]. They assumed local thermodynamic equilibrium, which allows the application of the collision-dominated plasma model and standard statistical distributions. For spectrochemical analysis, their model can be of interest as it predicts the behavior of a spectral line in terms of its usefulness for analysis; it shows if the line is self-absorbed or self-reversed and to what extent. They performed calculations for a two-component Si/N system. The number of plasma species or plasma pressure and the ratio of atomic constituents are the model input parameters while the spatial and temporal distributions of atom, ion and electron number densities, evolution of an atomic line profile and optical thickness, and the resulting absolute intensity of plasma emission in the vicinity of a strong non-resonance atomic transition are the model outputs. The practical applications of their model include prediction of temperature, electron density, and the dominating broadening mechanism. The model can also be used to choose the optimal line for quantitative analysis.

Another model of correcting the self-absorption effect in laser-induced plasma has been developed as a modification of the Calibration-Free algorithm previously presented for standard-less analysis of materials by LIBS [63]. As a test of their modified model, the algorithm for self-absorption correction is applied to three different certified steel NIST samples and to three ternary alloys (Au, Ag and Cu) of known composition. Their experimental results showed that the self-absorption corrected Calibration-Free method gives reliable results, improving the precision and the accuracy of the CF-LIBS procedure by approximately one order of magnitude.

References of Chapter II

- [1] S. Nakamura, Y. Ito, K. Sone, H. Hiraga, and K. Kaneko, "Determination of an iron suspension in water by laser-induced breakdown spectroscopy with two sequential laser pulses," *Anal. Chem.* **68**, 2981-2986 (1996).
- [2] X. Y. Pu, W. Y. Ma, and N. H. Cheung, "Sensitive elemental analysis of aqueous colloids by laser-induced plasma spectroscopy," *Appl. Phys. Lett.* **83**, 3416-3418 (2003).
- [3] A. E. Pichahchy, D. A. Cremers, and M. J. Ferris, "Elemental analysis of metals under water using laser induced breakdown spectroscopy," *Spectrochim. Acta B* **52**, 25-39 (1997).
- [4] A. Kuwako, Y. Uchida, and K. Maeda, "Supersensitive detection of sodium in water with use of dual-pulse laser-induced breakdown spectroscopy," *Appl. Opt.* **42**, 6052-6056 (2003).
- [5] V. N. Rai, F. Yu Yueh, and J. P. Singh, "Study of laser-induced breakdown emission from liquid under double-pulse excitation," *Appl. Opt.* **42**, 2094-2101 (2003).
- [6] R. Sattmann, V. Sturm, and R. Noll, "Laser-induced breakdown spectroscopy of steel samples using multiple Q-switch Nd-YAG laser pulses," *J. Phy. D.: Appl. Phys.* **28**, 2181-2187 (1995).
- [7] L. St-Onge, M. Sabsabi, and P. Cielo, "Analysis of solids using laser-induced plasma spectroscopy in double-pulse mode," *Spectrochim. Acta B* **53**, 407-415 (1998).

- [8] L. St-Onge, V. Detalle, and M. Sabsabi, "Enhanced laser-induced breakdown spectroscopy using the combination of fourth-harmonic and fundamental Nd:YAG laser pulses," *Spectrochim. Acta B* **57**, 121-135 (2002).
- [9] F. Colao, V. Lazic, R. Fantoni, and S. Pershin, "A comparison of single and double pulse laser-induced breakdown spectroscopy of aluminum samples," *Spectrochim. Acta B* **57**, 1167-1179 (2002).
- [10] D. N. Stratis, K. L. Eland, and S. M. Angel, "Dual-pulse LIBS using a pre-ablation spark for enhanced ablation and emission," *Appl. Spectrosc.* **54**, 1270-1274 (2000).
- [11] D. N. Stratis, K. L. Eland and S. M. Angel, "Enhancement of aluminum, titanium and iron in glass using pre-ablation spark dual-pulse LIBS," *Appl. Spectrosc.* **54**, 1719-1726 (2000).
- [12] J. Scaffidi, J. Pender, W. Pearman, S. R. Goode, B. W. Colston, J. C. Carter, and S. M. Angel, "Dual-pulse laser-induced breakdown spectroscopy with combinations of femtosecond and nanosecond laser pulses," *Appl. Opt.* **30**, 6099-6106 (2003).
- [13] C. Gautier, P. Fichet, D. Menut, and J. Dubessy, "Applications of the double-pulse laser-induced breakdown spectroscopy (LIBS) in the collinear beam geometry to the elemental analysis of different materials," *Spectrochim. Acta B* **61**, 210-219 (2006).
- [14] W. Sdorra and K. Niemax, "Basic investigations for laser microanalysis: III. Application of different buffer gases for laser-produced sample plumes," *Mikrochim. Acta* **107**, 319-327 (1992).

- [15] L. M. Berman and J. Wolf, "Laser-induced breakdown spectroscopy of liquids: aqueous solutions of nickel and chlorinated hydrocarbons," *Appl. Spectrosc.* **52**, 438-443 (1998).
- [16] C. W. Ng, W. F. Ho, and N. H. Cheung, "Spectrochemical analysis of liquids using laser-induced plasma emissions: Effects of laser wavelength on plasma properties," *Appl. Spectrosc.* **51**, 976-983 (1997).
- [17] X. L. Mao, A. C. Ciocan, and R. E. Russo, "Preferential vaporization during laser ablation inductively-coupled plasma atomic emission spectroscopy," *Appl. Spectrosc.* **52**, 913-918 (1998).
- [18] L. M. Cabalin and J. J. Laserna, "Experimental determination of laser induced breakdown thresholds of metals under nanosecond Q-switched laser operation," *Spectrochim. Acta Part B* **53**, 723-730 (1998).
- [19] C. Haisch, J. Liermann, U. Panne, and R. Niessner, "Characterization of colloidal particles by laser induced plasma spectroscopy (LIPS)," *Anal. Chim. Acta* **346**, 23-35 (1997).
- [20] C. Nouvellon, C. Chaleard, J. L. Lacour, and P. Mauchien, "Stoichiometry study of laser produced plasma by optical emission spectroscopy," *Appl. Surf. Sci.* **138-139**, 306-310 (1999).
- [21] I. V. Cravetchi, M. Taschuk, G. W. Rieger, Y. Y. Tsui, and R. Fedosejevs, "Spectrochemical analysis of aluminum alloys by laser-induced breakdown spectroscopy: identification of precipitates," *Appl. Opt.* **42**, 6138-6147 (2003).

- [22] K. M. Lo and N. H. Cheung, "ArF laser-induced plasma spectroscopy for part-per-billion analysis of metal ions in aqueous solutions," *Appl. Spectrosc.* **56**, 682-688 (2002).
- [23] V. Detalle, M. Sabsabi, L. St-Onge, A. Hamel, and R. Heon, "Influence of Er:YAG and Nd:YAG wavelengths on laser-induced breakdown spectroscopy measurements under air or helium atmosphere," *Appl. Opt.* **42**, 5971-5977 (2003).
- [24] V. Margetic, A. Pakulev, A. Stockhaus, M. Bolshov, K. Niemax, and R. Hergenroder, "A comparison of nanosecond and femtosecond laser-induced plasma spectroscopy of brass samples," *Spectrochim. Acta B* **55**, 1771-1785 (2000).
- [25] Y. W. Kim, In "*Fundamentals of analysis of solids by laser-produced plasmas*," in: L. J. Radziemski, D. A. Cremers (Eds.), *Laser Induced Plasmas and Applications*, Marcel Dekker, Inc, New York, (1989).
- [26] B. N. Chichkov, C. Momma, S. Nolte, F. von Alvensleben, and A. Tunnermann, "Femtosecond, picosecond and nanosecond laser ablation of solids," *Appl. Phys. A* **63**, 109-115 (1996).
- [27] G. W. Rieger, M. Taschuk, Y. Y. Tsui, and R. Fedosejevs, "Comparative study of laser-induced plasma emission from micro-joule picosecond and nanosecond KrF-laser pulses," *Spectrochim. Acta B* **58**, 497-510 (2003).
- [28] K. Eland, D. Stratis, T. Lai, M. A. Berg, S. Goode, and S. M. Angel, "Some comparison of LIBS using nanosecond and picosecond laser pulses," *Appl. Spectrosc.* **55**, 279-285 (2001).

- [29] D. X. Hammer, E. D. Jansen, M. Frenz, G. D. Noojin, R. J. Thomas, J. Noack, A. Vogel, B. A. Rockwell, and A. J. Welch, "Shielding properties of laser-induced breakdown in water for pulse durations from 5 ns to 125 fs," *Appl. Opt.* **36**, 5630-5640 (1997).
- [30] I. Yasuo, "Atomic emission characteristics of laser-induced plasmas in an argon atmosphere at reduced pressure," *Appl. Spectrosc.* **43**, 229-234 (1989).
- [31] F. Leis, W. Sdorra, J. B. Ko, and K. Niemax, "Basic investigations for laser microanalysis: I. Optical emission spectrometry of laser-produced sample plumes," *Mikrochim. Acta* **98**, 185-199 (1989).
- [32] K. J. Grant and G. L. Paul, "Electron temperature and density profiles of excimer laser-induced plasmas," *Appl. Spectrosc.* **44**, 1349-1354 (1990).
- [33] Y. Iida, "Effects of atmosphere on laser vaporization and excitation processes of solid samples," *Spectrochim. Acta B* **45**, 1353-1367 (1990).
- [34] T. Thiem, R. Salter, J. Gardner, Y. Lee, and J. Sneddon, "Quantitative simultaneous elemental determinations in alloys using laser-induced breakdown spectroscopy (LIBS) in an ultra-high vacuum," *Appl. Spectrosc.* **48**, 58-64 (1994).
- [35] M. R. Joseph, N. Xv, and V. Majidi, "Time-resolved emission characteristics and temperature profiles of laser-induced plasmas in helium," *Spectrochim. Acta B.* **49**, 89-103 (1994).
- [36] H. Kurniwan, S. Nakajima, J. Batubara, M. Marpaung, M. Okamoto, and K. Kagawa, "Laser-induced shock wave plasma in glass and its application to elemental analysis," *Appl. Spectrosc.* **49**, 1067-1072 (1995).

- [37] H. Kurniawan, W. Budi, M. Suliyanti, A. Marpaung, and K. Kagawa, "Characteristics of a laser plasma induced by irradiation of a normal-oscillation YAG laser at low pressures," *J. Phys. D: Appl. Phys.* **30**, 3335–3345 (1997).
- [38] M A Khater, P. Kampen, J. T. Costello, J-P Mosnier, and E. T. Kennedy, "Time-integrated laser-induced plasma spectroscopy in the vacuum ultraviolet for the quantitative elemental characterization of steel alloys," *J. Phys. D: Appl. Phys.* **33**, 2252-2262 (2000).
- [39] H. Kurniawan, T. Lie, K. Kagawa, and M. Tjia, "Laser-induced shock wave plasma spectrometry using a small chamber designed for in-situ analysis," *Spectrochim. Acta B* **55**, 839-848 (2000).
- [40] M. Noda, Y. Deguchi, S. Iwasaki, and N. Yoshikawa, "Detection of carbon content in a high-temperature and high pressure environment using laser-induced breakdown spectroscopy," *Spectrochim. Acta B* **57**, 701-709 (2002).
- [41] T. Naeem, H. Matsuta, and K. Wagatsuma, "Effect of plasma gas for spectrometric analysis of tin and zinc using low-pressure laser-induced plasma," *Spectrochim. Acta B* **58**, 891-899 (2003).
- [42] M. Kuzuya, M. Murakami, and N. Maruyama, "Quantitative analysis of ceramics by laser-induced breakdown spectroscopy," *Spectrochim. Acta B* **58**, 957-965 (2003).
- [43] S. Eppler, D. A. Cremers, D. D. Hickmott, M. J. Ferris, and A. C. Koskelo, "Matrix effects in the detection of Pb and Ba in soils using laser-induced breakdown spectroscopy," *Appl. Spectrosc.* **50**, 1175-1181 (1996).

- [44] R. E. Neuhauser, U. Panne, and R. Niessner, "Laser-induced plasma spectroscopy (LIPS): a versatile tool for monitoring heavy metal aerosols," *Anal. Chim. Acta* **392**, 47-54 (1999).
- [45] A. K. Rai, H. S. Zhang, F. Y. Yueh, J. P. Singh, and A. Weisburg, "Parametric study of a fiber-optic laser-induced breakdown spectroscopy probe for analysis of aluminum alloys," *Spectrochim. Acta Part B* **56**, 2371-2383 (2001).
- [46] R. Multari, L. Foster, D. Cremers, and M. J. Ferris, "Effect of sampling geometry on elemental emissions in laser-induced breakdown spectroscopy," *Appl. Spectrosc.* **50**, 1483-1499 (1996).
- [47] I. Bassiotis, A. Diamantopoulou, A. Giannoudakos, F. Roubani-Kalantzopoulou, and M. Kompitsas, "Effects of experimental parameters in quantitative analysis of steel alloy by laser-induced breakdown spectroscopy," *Spectrochim. Acta B* **56**, 671-683 (2001).
- [48] L. Moenke-Blankenburg, "New aspects of laser micro-spectral analysis LMA" *Nouv. Rev. Opt. Appl.* **5**, 243-248 (1972).
- [49] D. Fried, G. P. Reck, T. Kushida, and E. W. Rothe, "Electric field enhancement of optical emission from plasma plume generated during ArF excimer photoablation of BaO₂, Y₂O₃, CuO and YBa₂Cu₃O₇," *J. Phys. D: Appl. Phys.* **24**, 1065-1071 (1991).
- [50] P. Rambo, J. Schwarz, and J. C. Diels, "High-voltage electrical discharges induced by an ultrashort-pulse UV laser system," *J. Opt. A: Pure Appl. Opt.* **3**, 146-158 (2001).

- [51] A. Ohzu, Y. Suzuki, Y. Maruyama, and T. Arisawa, "Enhancement of electron temperature in a laser-induced plasma using a radio-frequency electric field," *Phys. Plasmas* **7**, 770-772 (2000).
- [52] K. Mason and J. M. Goldberg, "Characterization of laser plasma in a pulsed magnetic field. Part I: Spatially resolved emission studies," *Appl. Spectrosc.* **45**, 370-379 (1991).
- [53] K. Mason and J. M. Goldberg, "Characterization of laser plasma in a pulsed magnetic field. Part II: Time-resolved emission and absorption Studies," *Appl. Spectrosc.* **45**, 1444-1455 (1991).
- [54] L. Dirnberger, P. E. Dyer, S. R. Farrar, and P. H. Key, "Observation of magnetic-field-enhanced excitation and ionization in the plume of KrF-laser-ablated magnesium," *Appl. Phys. A: Materials Science and Processing* **59**, 311-316 (1994).
- [55] S. S. Harilal, M. S. Tillack, B. O'Shay, C. V. Bindhu, and F. Najmabadi, "Confinement and dynamics of laser-produced plasma expanding across a transverse magnetic field," *Phys. Rev. E* **69**, 026413: (1-10) (2004).
- [56] Y. Iida, "Laser vaporization of solid samples into a hollow-cathode discharge for atomic emission spectrometry," *Spectrochim. Acta B* **45**, 427-438 (1990).
- [57] H. H. Telle, D. C. Beddows, G. W. Morris, and O. Samek, "Sensitive and selective spectrochemical analysis of metallic samples: the combination of laser-induced breakdown spectroscopy and laser-induced fluorescence spectroscopy," *Spectrochim. Acta B* **56**, 947-960 (2001).

- [58] M. Autin, A. Briand, and P. Mauchien, "Characterization by emission spectrometry of a laser-produced plasma from a copper target in air at atmospheric pressure," *Spectrochim. Acta B* **48**, 851-862 (1993).
- [59] M. Kuzuya and H. Aranami, "Analysis of a high-concentration copper in metal alloys by emission spectroscopy of a laser-produced plasma in air at atmospheric pressure," *Spectrochim. Acta B* **55**, 1423-1430 (2000).
- [60] M. Kuzuya and O. Mikami, "Effect of argon pressure on spectral emission of a plasma produced by a laser microprobe," *J. Anal. At. Spectrom.* **7**, 493-497 (1992).
- [61] V. Lazic, R. Barbini, F. Colao, R. Fantoni, and A. Palucci, "Self-absorption model in quantitative laser induced breakdown spectroscopy measurements on soils and sediments *Spectrochim. Acta B* **56**, 807-820 (2001).
- [62] I. B. Gornushkin, C. L. Stevenson, B. W. Smitha, N. Omenetto, and J. D. Winefordner, "Modeling an inhomogeneous optically thick laser induced plasma: a simplified theoretical approach," *Spectrochim. Acta B* **56**, 1769-1785 (2001).
- [63] D. Bulajic, M. Corsi, G. Cristoforetti, S. Legnaioli, V. Palleschi, A. Salvetti, and E. Tognoni, "A procedure for correcting self-absorption in calibration free-laser induced breakdown spectroscopy," *Spectrochim. Acta B* **57**, 339-353 (2002).

CHAPTER III

PRINCIPLES OF LASER INDUCED BREAKDOWN SPECTROSCOPY (LIBS)

Spectroscopic standard techniques such as Laser Induced Breakdown Spectroscopy (LIBS) are normally used to determine the qualitative and quantitative composition from the emitted spectrum of the produced plasmas. LIBS involves focusing a pulsed laser onto a target, causing formation of optically induced plasma from the target species and finally analyzing the emitted spectrum to determine the type and/or concentration of the elements composing the target. Evaporation, atomization, excitation and ionization of the target material are also among the processes experienced during the interaction of the intense focused laser beam and the sample under investigation. The excitation is accompanied by prompt atomic, molecular and ionic spectral emission over a broad range of spectra. Most of the radiation results from the early stages of the plasma, electron-ion, and electron-atom interaction and from recombination. As the plasma cools, broadband emission decays and atomic and ionic lines are emitted as a result of the subsequent relaxation of the excited species in the matrix which is the characteristic radiation from the matrix elements that is detected and measured.

To ablate the target and produce the plasma, the laser must generate pulses of sufficient energy above a certain threshold whose values depend on the target and the laser characteristics. Optimization of such parameters to improve the performance of the technique has been reviewed in the previous chapter. Moreover, the understanding of the basic principles of LIBS is of great importance which has resulted in the growing interest

on laser-induced plasma to generate numerous theoretical models in order to improve the basic knowledge and determine the best experimental conditions of LIBS processes. This chapter will be dedicated to giving some physical fundamentals of the technique which includes laser target interaction, plasma formation and characterization, plasma propagation and spectrum analysis. Finally, the methods of measuring the analyte concentration will be presented.

3.1 Laser-target interaction

The various complex mechanisms involved in a laser ablation process includes laser absorption by the target material, evaporation, transient gas dynamics, ionization, and recombination [1]. There are several diagnostic techniques for characterizing a laser-produced plasma including optical emission spectroscopy, [2-4] mass spectroscopy, [5] laser induced fluorescence, [6] Langmuir probe [7], photothermal beam deflection, [8] microwave and laser interferometry [9,10], and Thomson scattering [11]. Fast photography adds another dimension to ablation diagnostics by providing two-dimensional snap shots of the three-dimensional plume propagation [12-14]. These capabilities become essential for understanding of the plume hydrodynamics, propagation and reactive scattering. The interaction of high-intensity laser pulses with a solid target can be divided into two regimes:

(a) At low laser fluence: the vapor produced by the leading edge of the laser pulse behaves like a thin medium and the laser beam passes nearly unattenuated through the vapor.

(b) At high laser fluence the vapor temperature is high enough to cause appreciable atomic excitation and ionization. Then the vapor begins to absorb the incident laser radiation leading to vapor breakdown and plasma formation.

In the first regime, the main physical process involves heat conduction, melting and vaporization of the target. In the second regime, the density and temperature of the laser-produced plasma can be so high that an efficient shielding of the target occurs during the laser pulse. The properties of the laser-ablation process in this last case are strongly influenced by both laser-plasma coupling and plasma kinetics. In nanosecond laser heating of metals, the absorbed laser energy heats up the target to the melting point and then to the vaporization temperature. In this case, evaporation occurs from the liquid metal, and heat conduction into the solid target is the main source of energy loss. Some works have used a one-dimensional or a two-temperature diffusion model, assuming that the laser energy is absorbed by free electrons, due to the inverse Bremsstrahlung. [15,16] Then the evolution of the absorbed laser energy involves thermalization within the electron subsystem, energy transfer to the lattice, and energy losses due to the electron heat transport into the target. They assumed that the thermalization within the electron subsystem is very fast and that the electron and the lattice subsystems can be characterized by their temperatures (T_e and T_i), thus, energy transport into the metal can be described by:

$$C_e \frac{\partial T_e}{\partial t} = -\frac{\partial Q(z)}{\partial z} - \gamma(T_e - T_i) + S \quad (1)$$

$$C_i \frac{\partial T_i}{\partial t} = \gamma(T_e - T_i), \quad (2)$$

$$Q(z) = -k_e \frac{\partial T_e}{\partial z}, S = I(t)A\alpha \exp(-\alpha z) \quad (3)$$

Here z is the direction perpendicular to the target surface, $Q(z)$ is the heat flux, S is the laser heating source term, $I(t)$ is the laser intensity, $A = I - R$ and α are the surface transmissivity and the material absorption coefficient, C_e and C_i are the heat capacities (per unit volume) of the electron and lattice subsystems, γ is the parameter characterizing the electron-lattice coupling, k_e is the electron thermal conductivity. In the above equations a thermal conductivity in the lattice subsystem (phonon component) is neglected. The electronic heat capacity is much less than the lattice heat capacity; therefore electrons can be heated to very high transient temperatures. Equations (1-3) have three characteristic time scales τ_e , τ_i and τ_L , where $\tau_e = C_e/\gamma$ is the electron cooling time, $\tau_i = C_i/\gamma$ is the lattice heating time ($\tau_e \ll \tau_i$) and τ_L is the duration of the laser pulse. These parameters define three different regimes of the laser-metal interaction which are femtosecond, picosecond and nanosecond regimes. In the nanosecond regime the absorbed laser energy first heats the target surface to the melting point and then to the vaporization temperature, noting that metals need much more energy to vaporize than to melt. During the interaction the main source of energy losses is the heat conduction into the solid target. The heat penetration depth is given by $l \sim (Dt)^{1/2}$, where D is the heat diffusion coefficient, $D = k_i/C_i$. The heating process is described by using the heat flow equation in the following form [17]:

$$\rho c \frac{\partial T}{\partial t} = \frac{\partial T}{\partial z} \left(k \frac{\partial T}{\partial t} \right) + \alpha A I_0 \exp(-\alpha z) \quad (4)$$

where T , ρ , c , k and α are temperature, mass density, specific heat, thermal conduction and surface absorbance of the target, respectively, while I_0 is the intensity of the incident laser pulse, and z the coordinate normal to the target surface.

3.2 Plasma formation

There are two dominant photon absorption processes in matter, which lead to breakdown and consequently formation of plasma [18]. One is inverse Bremsstrahlung (IB) absorption, by which free electrons gain kinetic energy from the laser beam, thus producing a cascade of ionization and excitation through collision with excited and ground state neutrals.

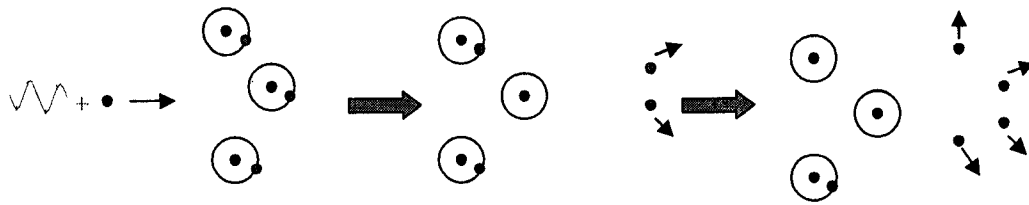


Fig. 3.1 Schematic illustration of Inverse Bremsstrahlung absorption, IB.

The large density of neutrals in the initial vapor significantly enhances the IB process which is usually described by the inverse absorption length α_{IB} (cm^{-1}) given by:

$$\alpha_{IB} \approx \left[\text{const.} \lambda^3 T_e^{-0.5} \left(\frac{N_0}{200} + n_e \right) \right] n_e \quad (5)$$

where λ is the laser wavelength in nm, T_e is the electron temperature in eV, and N_0 and n_e are the neutral atom and electron densities in cm^{-3} , respectively. The IB process is less efficient in the UV than in the visible part of the spectrum, because of the λ dependence

of IB on the laser wavelength. The efficiency of the laser heating of the plasma by IB decreases with the square of the laser wavelength when the degree of ionization is low and as the cube of the wavelength when the ionization is extensive [19]. The efficiency of the IB photon absorption is such that the plasma acts as a shield for the laser radiation, completely preventing the last part of the beam pulse to reach the target surface.

The second mechanism of photon absorption by matter is photoionization (PI) of excited species and, at sufficiently high laser intensity, multiphoton ionization (MPI) of excited or ground-state atoms. By considering some matter, with high ionization potential E_i , is ionized by the intense photon flux of Q-switched lasers by simultaneously absorbing $E_i/h\nu$ quanta. This is not possible since atoms and molecules exist only in discrete energy states and photon absorption cannot take place unless there is resonance between an allowed state and the quantum energy $h\nu$. However, it is possible for a virtual excited state of the atom to exist on absorbing a photon for a time dictated by the Uncertainty principle. If photons are absorbed with sufficient frequency in a succession of higher energy states, ionization can result. An atom will acquire $E_i/h\nu = k$ quanta to be ionized.

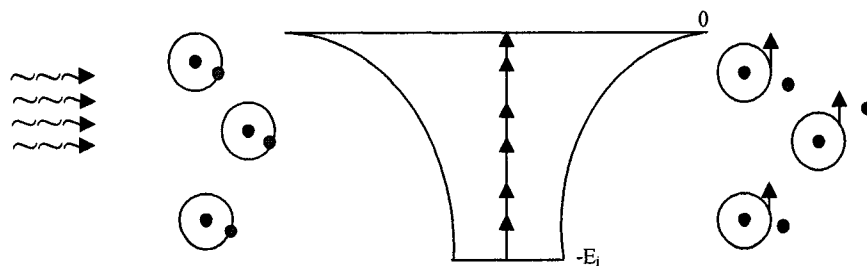


Fig. 3.2 Schematic illustration of multiphoton ionization.

This process of successive absorption into a sequence of virtual states is known as multiphoton absorption. Consider N atoms in a unit volume, which is illuminated by a spatially uniform and temporally constant laser beam comprising photons of energy $h\nu$, which create a flux density of F photons $\text{cm}^{-2} \text{sec}^{-1}$. At $t = 0$, we imagine that the laser flux F is instantly established in the focal volume which contains only unexcited atoms, i.e. no free electrons are present. Under the influence of the constant flux, F , atoms will absorb photons from the beam. The ionization rate per atom in a uniform and temporally constant flux density F is:

$$W = BF^k \quad (6)$$

where B is the ionization probability per atom per unit time per unit flux.

During nanosecond laser ablation, the produced high-density plasma (10^{17} – 10^{19}cm^{-3}) is heated to high temperatures (6000–20,000 K) and is ionized by both IB and the PI processes, expanding rapidly ($\sim 10^6 \text{cm/s}$) perpendicularly to the surface [20]. During the expansion, the main mechanism of transition of bound electrons from the lower level to the upper level and vice versa is driven by inelastic collisions of electrons with heavy particles, while the concentration of charged particles is controlled by the electron impact ionization and the three-body recombination of electrons with ions. Radiative processes as re-absorption, spontaneous and stimulated emission are also important in determining the concentration of emitting levels. The basic processes occurring during the expansion makes the analysis of the plume complex and theoretical studies are still in progress for the interpretation of the experimental data.

3.3 Plasma characterization

The characterization of laser-induced plasmas through the determination of their main parameters, such as the temperature, the electron density and the number densities of the different species present in the plasma, has produced interest in recent years because it allows improvement of their applications and provides a better understanding of these complex and versatile spectroscopic sources [21]. For example, the temperature is a crucial parameter that, if local thermodynamic equilibrium (LTE) is satisfied, determines the distribution of level excitation through the Boltzmann equation and the ionization equilibrium through the Saha equation. For LTE to exist in the plasma, the electron density has to be high enough so that the collisional rates exceed the radiative rates. In this case, the so-called excitation (Boltzmann) and ionization (Saha) temperatures coincide with the electronic temperature, that is, with the temperature of the Maxwellian distribution of electron velocities $F(v)$ which is defined by:

$$\frac{3}{2} k T_e = N \int \frac{1}{2} m v^2 F(v) dv \quad (7)$$

If some volume of the plasma is in LTE, the following distributions should be satisfied,

i) Maxwell distribution of energies of free electrons:

$$dn_e = n_e F(\epsilon) d\epsilon \quad (8)$$

$$F(\epsilon) = 2\pi^{-1/2} T^{-3/2} \epsilon^{1/2} \exp(-\epsilon/T)$$

where T is the electron temperature in energy units ($1\text{eV} = 11605 \text{ k} = 8066 \text{ cm}^{-1}$).

ii) The population distribution of each species over energy levels E_k is described by the Boltzmann equation:

$$\frac{N_k}{N_0} = \frac{U_k}{U_0} \exp(-\beta_k), \quad \beta_k = \frac{E_k - E_0}{T} \quad (9)$$

where U_k and U_0 are statistical weights of the levels k and 0 .

iii) The population distribution among two successive ionization stages is described by the Saha-Boltzmann distribution of atoms over degrees of ionization:

$$\frac{N^{(z+1)}}{N^{(z)}} = \frac{U_{z+1}}{U_z} S \exp(-\beta_z), \quad \beta_z = \frac{E_z}{T} \quad (10)$$

$$S = 2 \left(\frac{mT}{2\pi\hbar^2} \right)^{3/2} n_e^{-1} \quad (11)$$

where E_z is the ionization energy of the atom X_z , and U_z is its partition function defined as:

$$U_z = \sum_k U_k^{(z)} \exp(-\beta_k) \quad (12)$$

A necessary (but not sufficient) criterion, which defines the required minimum electron density for LTE [22]:

$$n_e \geq 1.4 \times 10^{14} T_e^{1/2} (eV) [\Delta E (eV)]^3 \text{ cm}^{-3} \quad (13)$$

where ΔE is the energy difference between the states which are expected to be in LTE.

3.3.1 Temperature determination using spectral line ratios.

As previously discussed, the assumption of the LTE should be fulfilled and correspondingly, the plasma should be optically thin. If the two spectral lines whose intensity I (spectral energy per unit of time per unit of projected source area per unit of observational spatial angle and integrated over the line profile) (indexed i and j) are measured such that the two wavelengths arise from different upper excitation energy levels, E whose upper level energies difference is large enough. It is necessary to

determine the relative response of the system separately at the two wavelengths by means of a standard emission source. Also, the values of A (the Einstein coefficient; transition probability) reported in the literature have large uncertainties, being better known and reliable for the longer, than the shorter wavelengths, and for the lighter elements than the heavier ones, they can be a source of random errors in the intensity measurements. The temperature can be given by [23]:

$$T = \frac{E_j - E_i}{k} \ln\left(\frac{I_j g_i A_i \lambda_j}{I_i g_j A_j \lambda_i}\right) \quad (14)$$

with the degeneracy of the upper levels denoted by g , the transition probability by A , and the wavelength by λ . The advantage of the two-line method is avoiding the need for knowing the value for the effective path length through the source, the total particle number density, the partition function, the absolute intensity calibration of the detection system and absolute transition probabilities. Considerations, when selecting a line pair, are to have the wavelengths nearly identical and the difference in upper energies of the two transitions as large as possible. The first criterion is useful as the relative intensity calibration is easier and more accurate and the second assures that the calculated temperature is more reproducible and not over-sensitive to small fluctuations in the radiance ratio measurement.

3.3.2 Temperature determination using Boltzmann plots

The most widely used method to determine the temperature of laser-induced plasmas is the Boltzmann plot method, which provides the excitation temperature from the measurement of the line emissions from a single species. In some works, the Boltzmann plots have been obtained from a high number of emission lines [24-30]; in this case, a

good correlation of the experimental data to a linear fit is an indication of the validity of the Boltzmann equation. In some cases, the measured line intensities corresponded to the emission from the whole plasma, so the Boltzmann plot method provided a single value of the excitation temperature of the plasma. Generally, time resolution is also used in light detection, as the plasma temperature is known to experience a rapid decrease due to the plasma expansion. In other cases, the emission from the plasma is spatially resolved in order to obtain the temperature at a given distance from the sample [27-29], the axial profile [30,31], lateral profiles [32,33] or two-dimensional distributions [33] of the temperature. In some work, the Boltzmann equation was applied to a pair of neutral atom (Cu I) emission lines and also to a pair of ion (Ba II) lines, in order to obtain the temperature of the plasma plume formed in laser ablation of YBCO in an oxygen atmosphere [34]. The results for the temperature obtained with the ion lines were considerably higher than those obtained with the neutral atom lines, a behavior that the authors attribute in part to the collection of the emission that integrated different spatial regions of the expanding plume. By extending the two-line ratio technique to a larger number of lines from the same element and ionization stage and rearranging the spectral line radiance equation for multiple lines, indexed i from the same element and ionization stage, it gives:

$$\ln\left(\frac{I_i \lambda_i}{g_i A_i}\right) = -\frac{1}{T} \left(\frac{E_i}{k}\right) + \ln\left(\frac{\ell h c n_i}{4\pi U}\right) \quad (15)$$

where ℓ is the effective path length through the radiation source, n_i is the particle number density, U is the partition function and the other symbols have been defined above. If we now treat the quantity $\ln\left(\frac{I_i \lambda_i}{g_i A_i}\right)$ as the dependent variable and E_i/k as the independent

variable for a set of lines from the same species and otherwise identical conditions, a linear relationship with a slope of $(-1/T)$ and an intercept of $\ln(\frac{hc \ln I_l}{4\pi U})$ results. The Boltzmann plot also needs calibration of the intensities at each of the analytical wavelengths, just as with the two-line ratio technique. In the Boltzmann plot method, the main source of inaccuracy is the small difference in energy of the upper levels of spectral lines from the same ionization stage. However, the accuracy of the computations is based on selecting lines carefully from a large database; the lines chosen should have a large range of upper energy levels as possible, and the chosen lines must be well-resolved for accurately in determining the intensities.

3.3.3 Temperature determination using Saha-Boltzmann plots

The determination of the plasma temperature is also possible using relative intensities of spectral lines from the same element but from successive ionization stages. This would suffice to overcome the sources of error due to the small differences in the upper energy levels of the spectral lines in the Boltzmann plot method. This method, used in some works [35-37] to obtain the plasma temperature, is based on the Saha equation that relates the number densities of consecutive ionization stages of an element, in combination with the Boltzmann equation that gives the population distribution for each species level. In this method, the ionization temperature is obtained from the emission lines of the neutral atom and the ion of an element. For optically thin plasma the ratios of line intensities of successive ionization of the same element can be used to determine the ionization temperature and is given by:

$$\frac{I'}{I} = \left(\frac{f'g'\lambda^3}{fg\lambda'^3} \right) (4\pi^{3/2}a_0^3n_e)^{-1} \left(\frac{kT}{E_H} \right)^{3/2} \exp\left(-\frac{E' + E_\infty - E}{kT} \right) \quad (16)$$

where the prime symbol represents the line of the atom with higher excitation stage, f is the oscillator strength, g the statistical weight, a_0 the Bohr radius, E_n the ionization energy of the hydrogen atom, E the excitation energy, T the ionic temperature and E_∞ is the ionization energy, n_e is electron density.

The advantage of this method, with respect to the Boltzmann plot method, is that a wider range of the upper level energies may be obtained by including lines from neutral atoms and ions, which results in a higher accuracy of the resulting temperature value. The ionization temperature was obtained in some cases from the emission intensity of the whole plasma [36-38] and in some other cases, with spatial resolution in the axial direction [38,39]. In most works, the Saha-Boltzmann method was applied using two lines, one from the neutral atom and another from the ion [36-40]. Yalcin et al. have applied the Saha-Boltzmann analysis including several neutral atom and ion lines, to determine the ionization temperature of laser-induced plasma generated in air containing various metals in the form of aerosols. Using the Saha-Boltzmann plot, they obtained a significant difference between the ionization temperature and the Boltzmann excitation temperature depicted by the slope of the neutral atom data. The authors attributed the discrepancy of the temperatures to the lower reliability of the Boltzmann analysis, due to the smaller energy spread of the data. Few works have been published in which both the Boltzmann and Saha-Boltzmann methods have been applied to determine the temperature of laser-induced plasma [41]. In these works, the values obtained for the ionization Saha-Boltzmann temperature were often higher than those of the excitation

Boltzmann temperature, especially at initial times of the plasma evolution. Their explanation of these temperature differences is the absence of LTE in the plasma. Other possible causes that may lead to the difference found usually between the temperature values obtained from the neutral atom and ion emission lines, even if LTE is satisfied, is the use of integrated measurements in an inhomogeneous laser induced plasma, in which the populations of neutral atoms and ions may have separated spatial distributions, so the integrated measurements can result in different averaging of these populations [42].

3.3.4 Temperature determination using line to continuum ratio

Under the assumption of local thermal equilibrium (LTE), the electron temperature T_e can be assumed equal to the excitation temperature T_{exc} , namely $T_e = T_{exc} = T$. Therefore, the plasma temperature T can be determined by the relative line to continuum intensity ratio using the following equation [43]:

$$\frac{\varepsilon_l(\lambda)}{\varepsilon_c} = C_r \frac{A_{21} g_2 \lambda_c^2}{Z_1 \lambda_1 T_e} \times \frac{\exp\left[\frac{E_i - E_2 - \Delta E_i}{kT_e}\right]}{\left\{ \xi \left(1 - \exp\left[\frac{-hc}{\lambda k T_e}\right] \right) + G \left(\exp\left[\frac{-hc}{\lambda k T_e}\right] \right) \right\}} \quad (17)$$

where ε_c is the continuum emission coefficient, and ε_l is the integrated emission coefficient over the line spectral profile. The ratio $\frac{\varepsilon_l}{\varepsilon_c}$ can be calculated from the

integrated line intensity and continuum intensity at certain adjacent wavelength positions.

λ_c , λ_l are the continuum and center wavelength of the spectral line, respectively. By using a Lorentzian fit, the position was obtained, so $\lambda_c = \lambda_l$. Z_1 is the partition function for ions and must be calculated as a function of temperature. A_{21} is the Einstein transition probability of spontaneous emission and E_i is the ionization potential. E_2 and g_2 are upper

level energy and degeneracy, respectively. ΔE_i is the lowering of the ionization potential of atoms in the presence of a field of ions and is small enough to be neglected. G is the free-free Gaunt factor, and ξ is the free-bound continuum correction factor.

3.3.5 Electron density measurements

Populations of the various species existing in the plasma and of their respective energy levels, as well as many other plasma properties, are often described in terms of the electron number density n_e which also defines the strength of the spectral lines. The rate of change of electron density can be described as follows [44]:

$$\frac{dn_e}{dt} = \nu_i n_e + W_m I^m N - \nu_a n_e - \nu_r n_e + \nabla \cdot (D_a \nabla n_e) \quad (18)$$

where:

n_e is the number of electrons per unit of volume

ν_i is the impact ionization frequency

W_m is the multiphoton rate coefficient (MPI)

I is the intensity, W/cm^2

m is the number of photons of a specified wavelength needed to ionize one atom

N is the number of atoms per unit volume

ν_a is the attachment frequency

ν_r is the recombination frequency

D_a is the ambipolar electron diffusion coefficient

The left term is the time rate of change of the number of electrons. The first additive term on the right represents electron generation due to impact ionization. The second additive

term represents the multiphoton ionization MPI rate. The exponent on the intensity is the number of photons of a specified wavelength needed to ionize one electron of the material illuminated. The third and fourth terms are negative and represent electron attachment and recombination. The fifth term represents the electron ambipolar diffusion. One of the most powerful spectroscopic techniques to determine the electron density with reasonable accuracy is obtained by measuring the Stark broadening profile of an isolated atom. For electron density measurements, the Stark broadening profile of an isolated atom or singly charged ion is the most commonly used technique. The FWHM of the stark broadening lines $\Delta\lambda_{1/2}$ is related to the electron density by the expression [45]:

$$\Delta\lambda_{1/2} = 2w \left(\frac{n_e}{10^{16}}\right) + 3.5A \left(\frac{n_e}{10^{16}}\right)^{1/4} (1 - 1.2N_D^{-1/3})w \left(\frac{n_e}{10^{16}}\right)A \quad (19)$$

where the first term on the right side of Eq. (19) gives the contribution of electron broadening, and the second is the ion broadening correction. The parameter w represents electron impact, and A is the ion broadening parameter. Both w and A are weak functions of temperature, n_e is the electron density (cm^{-3}) and N_D the number of particles in the Debye sphere given by:

$$N_D = 1.27 \times 10^9 \frac{T_e^{3/2} eV}{n_e^{1/2} (\text{cm}^{-3})} \quad (20)$$

In order to determine the electron density, some authors such as Gomba et al. [46] used the Saha-Boltzmann equation (Eq. (16)).

3.4 Plasma propagation

Thermal and fluid dynamic processes can influence the correlation between time-integrated emission intensity measurements and calculated temperature spatial profiles of

an expanding ablation plume. Geohegan published time-resolved photographs of visible plasma emission from laser ablation of YBCO target at 1 J/cm^2 under 100 mTorr oxygen [12]. Two components of the expanding plasma were identified [47]. The first component with gas velocities of 10^6 cm/s lasted about $1 \text{ }\mu\text{s}$. The second component appeared after $2 \text{ }\mu\text{s}$, and existed for $500 \text{ }\mu\text{s}$ in a vacuum. At atmospheric pressure, the laser-induced plasma propagates into an ambient gas as a shock wave. The expansion boundary of this luminous plume was described by a shock wave model or a drag model [48,49]. The plume expansion has been also investigated using Monte Carlo (MC) simulations [50], hydrodynamic models [51], or by using a hybrid model (combination of both) [52,53]. Among the hydrodynamic models, the pressure is mostly limited until maximum, which is about 100 Pa. [54]. The plume expansion into 1-atm background gas was investigated only in several references such as reference 51. It should be mentioned that it would take a much longer calculation time to study the plume expansion into a high-pressure background gas with the MC simulations or hybrid models. Therefore, generally one makes use of hydrodynamic models to study the plume expansion into 1-atm background gas. The general effect of the background gas is reported to be the spatial confinement and slowing down of the expanding plume. Moreover, the material can even move backward [55]. Detalle et al. experimentally studied the influence of long wavelengths on LIBS measurements under air or helium atmosphere [56]. Gnedovets et al. [57] reported a hydrodynamic model with two distinct species (material plume and background gas) and interactions between them. This model is applied to expansion in a background gas at 1 atm, but for a long laser pulse (millisecond-range) at very low laser irradiance ($10^4\text{--}10^5 \text{ W/cm}^2$), so that no plasma is formed.

When a large amount of energy is deposited in a small volume, a shock wave is formed by the piston-like action of the quickly expanding ablated material pushing outward on the backing gas. As the shock expands, more background gas is swept up by the shock front, and since the laser pulse delivers a finite amount of energy, the expansion velocity decreases with increasing distance from the target. The wave moves symmetrically outward at very high velocity such that the rate of deceleration increases for increasing pressure, since the wave must push more gas at the higher pressure.

A perfect gas was considered with constant specific heats and density ρ_0 , in which a large amount of energy E is focused in a small volume during a short time interval. The gas motion is determined by two-dimensional parameters, the deposited energy E , and the initial density ρ_0 . These parameters cannot be combined to yield scales with dimensions of either length or time. Hence, the motion will be a function of a particular combination of the coordinate R (distance from the center of the irradiation) and the time t . The dimensional combination, which contains only length and time, is the ratio E to ρ_0 , with the dimensions $[E/\rho_0] = [\text{cm}^5 \cdot \text{sec}^{-2}]$.

The shock wave front is defined by a given value of the independent variable. The distance of the wave front $R(t)$ from the sample surface is governed by the relationship [49]:

$$R(t) = \xi_0 \left(\frac{E}{\rho_0} \right)^{1/5} t^{2/5} \quad (21)$$

ξ_0 is a dimensionless parameter determined from the condition of energy conservation.

The propagation velocity of the shock wave (V) is:

$$V = \frac{dr}{dt} = \frac{2R}{5t} = \xi_0 \frac{2}{5} \left(\frac{E}{\rho_0}\right)^{1/5} t^{-3/5} \quad (22)$$

An adiabatic model is often used to describe laser-induced plasma expansion. For an adiabatic expansion, the expressions for plasma temperature and electron number density as a function of time are [58]:

$$T(t) \propto t^{-2\alpha(\gamma-1)/[\alpha(\gamma-1)+2]}, n_e \propto t^{-2\alpha/[\alpha(\gamma-1)+2]} \quad (23)$$

where γ is the ratio of specific heat capacities at constant pressure to constant volume, and α is the flow dimensionality: $1 < \alpha < 3$

3.5 Spectrum analysis

At the early time of breakdown, the plasma becomes an electron-rich high temperature environment due to the ionization process produced by multiphoton absorption and inverse Bremsstrahlung, which leads to cascade breakdown. This results in the formation of a time-dependant continuum radiation that may last for hundreds of nanoseconds. As the boundary of the plasma propagates in the direction of the laser beam, the particle number density begins to decrease. After the end of the laser pulse, when the plasma power source is terminated, it begins to cool down and recombination and de-excitation events dominate. Thus, during the plasma relaxation, the neutral and singly charged characteristic spectral line emission prevails.

3.5.1 Line emission

The basic concept of line emission is explained by the Bohr model. The model consists of an atom that has two electronic energy states, the ground state (m) and the excited state (n), with energies E_n and E_m , respectively. If the atom is in the excited state, it may spontaneously decay into the ground state, releasing the difference in energies

between the two states as a photon with a frequency ν and energy $h\nu$. The well-known unperturbed centre-line emission wavelength can be given by:

$$E_n - E_m = h\nu = hc/\lambda_{nm}, \quad (24)$$

where h is Planck's constant.

An atom or ion immersed in plasma will emit radiation when radiative transitions between various quantum states occur. In plasma spectroscopy, the interaction of ions and electrons with the radiating species is important; the quantum states do not necessarily correspond exactly to those of the isolated atom or ion. Between the upper energy level E_n and a lower level E_m of an excited atom in a system, there are three types of possible radiative transitions: spontaneous, stimulated emission and absorption. Spontaneous emission is characterized by a transition probability per unit time A_{nm} . The other two (stimulated emission and absorption) are dependent on the presence of a radiation field so they are more important in the interaction of a laser field with atoms. Dipole transitions have the largest values and are called allowed; the lifetime of the excited state E_n , its transition probability into lower states m , and the absorption oscillator strength are related. In a group of such atoms, if the number of atoms in the excited state is given by N_n , the rate at which spontaneous emission occurs is given by:

$$\partial N_{nm}/\partial t = A_{nm} N_n \quad (25)$$

where A_{nm} is a proportionality constant for this particular transition in this particular atom and is referred to as the Einstein A coefficient. The rate of emission is thus proportional to the number of atoms in the excited state, N_n .

The above equation can be solved to give:

$$N(t) = N_n \exp(-t/\tau_{21}) \quad (26)$$

where N_n is the initial number of atoms in the excited state n , and τ_{21} is the radiative lifetime of the transition, $\tau_{21} = (A_{nm})^{-1}$.

The intensity I_{nm} of a spectral line emitted at the frequency ν may be calculated from the number of atoms (molecules) undergoing the transition n to m is then given by:

$$I_{nm} = A_{nm} N_n h \nu_{nm} \quad (27)$$

The calculation of the energy of an excited electron in a one-electron system is the solution of the Schrödinger equation in the central field approximation of a nucleus of charge Z . It ends up with the eigenvalues E_n expressed as a function of only the principal quantum number, n , thus:

$$E_n = \frac{R_y Z^2}{n^2} \quad n = 1, 2, 3, \dots \quad (28)$$

where R_y is the Rydberg constant.

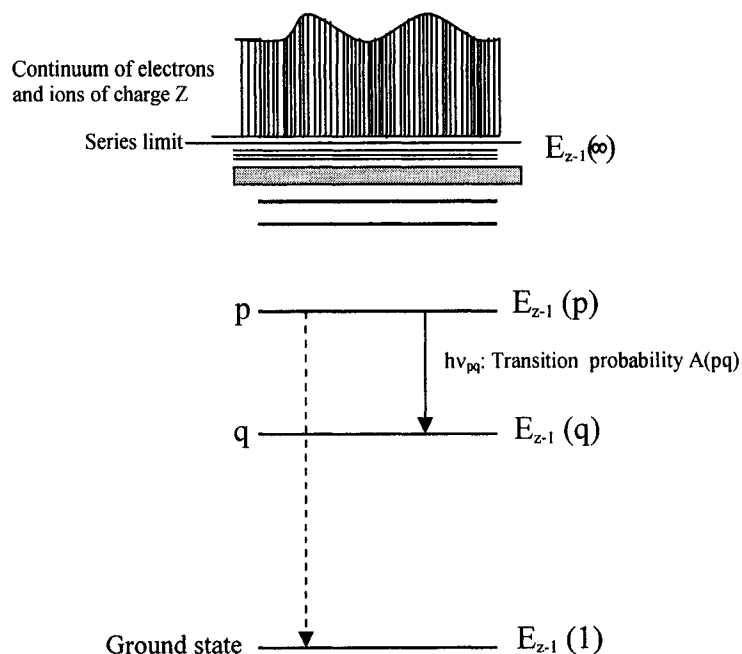


Figure 3.3 Schematic energy level diagram for a hydrogenic species of charge $Z-1$.

A schematic energy level diagram (Fig. 3.3) illustrates a hydrogenic species (this being an atom or ion having a single bound electron). Bound, discrete, energy levels occur below the ionization limit $E(\infty)$ and a continuum of levels above. In Fig. 3 line radiation occurs for electron transitions between bound levels leading to line spectra. Thus, if ν_{pq} is the frequency of radiation when a transition from a level of principal quantum number p and energy $E(p)$ to a level of energy $E(q)$ occurs, then the energy $h\nu_{pq}$ will be the difference between $E(p)$ and $E(q)$. In optically thin plasmas, the intensity of line radiation is determined by the wavelength's emission coefficients. The wavelength integrated emission coefficient ε is given by:

$$\varepsilon = \int_0^{\infty} \varepsilon_{\lambda} d\lambda \quad (29)$$

This gives an expression for the total radiant power emitted by a plasma per unit volume per unit solid angle in the absence of absorption. The net emission coefficient is defined as the derivative of the intensity, I , evaluated at the end of a line-of-sight path length ℓ into an isothermal, homogeneous plasma. It can be expressed in the form:

$$I = \int_0^{\infty} b_{\lambda} \{1 - \exp(-k'(\lambda)\ell)\} d\lambda \quad (30)$$

where b_{λ} is the Planck's blackbody function which is an ideal source function; usually surface discharges do not radiate as ideal blackbodies. $k'(\lambda)$ is the spectral absorption coefficient including induced emission.

3.5.2 Background continuum radiation

Continuous radiation observed experimentally does not originate from just one elementary process. There are free-bound and free-free electron transitions and

corresponding continua [59]. Additionally, continua may be superposed belonging to different ionic states of the same atomic species. Also, different atomic species present in the plasma may contribute to the continuous radiation.

3.5.2.a The free-bound radiation (f-b)

Recombination (free-bound) radiation occurs when an electron in the continuum recombines with the ion. Since the upper level is continuous, the radiation is continuous; however, there is some structure due to the discrete nature of the lower energy levels. For an electron of mass m and velocity v , recombination into state p gives:

$$h\nu_{pq} = E(\infty) + 0.5mv^2 - E(p) \quad (31)$$

When a free electron collides with an ion, the electron can be captured and forms a new excited ion (with one unit of charge less) or a neutral particle. In plasmas, a number of different continua connected to transitions into all discrete energy levels are superposed. This superposition can be substituted by integration for sufficiently dense lying discrete states. In the case of hydrogen, the integration is sufficiently correct for all levels higher than the principle quantum number $n = 4$, i.e. in the infrared spectral region $\lambda > 13,000 \text{ \AA}$. For this spectral region the f-b continuous radiation is described by the expression:

$${}^H \epsilon_{\nu}^{\text{fb}} = \text{const.} \frac{n_+ n_e}{T^{1/2}} (1 - \exp\{h\nu/kT\}) \quad (32)$$

with $\text{const.} = 16\pi e^6/c^3(6\pi m^3 k)^{1/2}$.

Passing from hydrogen to other elements, the electron considered penetrates partly into the cloud of charges surrounding the nucleus. This effect is described by a factor $\xi(\nu, T)$ into which, in addition, all other deviations from hydrogen are included

(different dependence of e , on frequency, and the Gaunt factors). Besides a factor γ is added which takes account of the different statistical weights of the ground term of the parent ion as compared to hydrogen. For other elements rather than Hydrogen, Eq. (32) can be written as:

$$\epsilon_{\nu}^{fb} = {}^H \epsilon_{\nu}^{fb} Z^2 \gamma_{\zeta}(\nu, T) \quad (33)$$

with Z the nuclear charge.

3.5.2.b The free-free transitions

Free-free radiation occurs owing to transitions between two free energy levels because of the classical concept, a moving charge radiates whenever it is accelerated or retarded. It also arises when Bremsstrahlung radiation is caused by the acceleration of charged particles in the Coulomb field of other charged particles. The major part of the Bremsstrahlung is due to electron-ion collisions, and, since the initial and final states are continuous, the Bremsstrahlung spectrum is also continuous. For precise quantitative work, the spectral free-free contributions from each species need to be added together to obtain the total free-free contribution.

Radiation emitted or absorbed when a free electron is accelerated in the field of an atomic nucleus but remains in a hyperbolic orbit without being captured. Since it happens in the continuum (no quantization), photons of any wavelength can be emitted or absorbed. The emissivity in case of hydrogen plasma is:

$$\epsilon_{\nu}^{ff} = \text{const.} Z^2 \frac{n_+ n_e}{T^{1/2}} \exp\{-h\nu / kT\} \quad (34)$$

The f-f transition is important in the UV spectral region while the f-b transition is important at longer wavelength. The spectral intensity distribution for the continuum radiation is given by [60]:

$$\begin{aligned}
 I(\nu)d\nu = & Kx n_e x n_r x r^2 / (T_e)^{1/2} x \exp[(-h\nu)/(kT_e)] x d\nu (free - free) \\
 & + K' x 1/(j^3) x n_e x n_z x (Z^4)/(T_e^{3/2}) \\
 & x \exp[-(U_j - h\nu)/kT_e] (free - bound)
 \end{aligned} \tag{35}$$

K and K' are constants, n_e is the electron number density, n_r is the number density of ions with a charge of r times the elementary charge, T_e is the electron temperature and is a measure the kinetic energy of electrons in the plasma. ν is the frequency, h and K are the Planck and Boltzmann constants, respectively, U_j is the ionization energy and n_z is the number density of the atoms with atomic number Z .

The spectral wavelength (λ)-dependent emission coefficient ϵ_λ is thus the sum of the emission coefficients for each mechanism:

$$\epsilon_\lambda = \epsilon_{l,\lambda} + \epsilon_{f-f,\lambda} + \epsilon_{f-b,\lambda} \tag{36}$$

$\epsilon_{l,\lambda}$ can be obtained by adding together the spectral emission coefficients of individual measured lines that affect the wavelength of interest. For spectroscopic as well as engineering work, wavelength quantities (integrated emission coefficients and the net emission coefficients) are more desirable than spectral values.

3.6 Sample concentration measurements

Because the interaction of laser-beams with surfaces is nonlinear, it cannot be accurately predicted. Furthermore, the mechanical, physical, and chemical properties of the sample influence the interaction, which results in a strong matrix effect [61]. As a

result of this limitation, the analytical performance of LIBS for direct quantitative analysis is unsatisfactory in terms of accuracy, precision, and detection limit. Fortunately, these limitations can be overcome or at least minimized using:

3.6.1 Calibrated standard

Consider the laser-sample interaction, which has the effect of vaporizing and atomizing a small region of the sample surface, to result in the production of a hot plume consisting of both the ejected material and the atmospheric plasma [62]. During this interaction, the laser beam energy is absorbed by the sample and by the atmospheric plasma. Several phenomena also occur that are responsible for back reflection of the radiation, electron emission, sample heating, and phase changes. Such processes affect the physical properties of the plume in a way different from the sample composition. [63] Assuming that the plasma has reached the condition of local thermodynamical equilibrium (LTE), the spectrally integrated line intensity, corresponding to the transition between levels E_k and E_i of the atomic species with concentration C_α can be expressed as:

$$I_\alpha = FC_\alpha \frac{g_k A_{ki} e^{-E_{ki}/k_B T}}{U_\alpha(T)} \quad (37)$$

where T is the plasma temperature, $U_\alpha(T)$ is the partition function, k_B is the Boltzmann constant, and F is a constant depending on experimental conditions. A first-order approximation of LIBS-measured concentrations can be obtained by the comparison of a given line intensity from an unknown sample to that from a certified sample.

Under the hypothesis of constant and easily reproducible plasma temperature and plasma density, all factors in Eq. (37) can be obtained for a specific transition from tables

in literature except for the concentration and line intensity for each element. This allows one to establish a simple linear relationship between the specific line intensity and the relevant elemental concentration. In practical situations, the use of calibration curves built in this way has proven to be valid for determining the concentration of a single species and in a well-defined matrix.

By rationing the line intensities originated by the sample and by a reference material (with known elemental concentration), at temperatures T_α and T_r , respectively, we obtain from (36):

$$\frac{I_\alpha(T_\alpha)}{I_r(T_r)} = \frac{C_\alpha}{C_r} \frac{\exp(-E_{ki}/(1/T_\alpha - 1/T_r))}{U_\alpha(T_\alpha)/U_r(T_r)} \quad (38)$$

Equation (38) allows us to evaluate C_α from the measured LIBS line intensity, while the other parameters are derived from atomic databases at known plasma temperatures.

3.6.2 Calibration-free laser induced breakdown spectroscopy (CF-LIBS)

Assuming that the plasma composition is mainly the composition of the sample under consideration, one can consider the natural logarithm of Eq. (37) [64]:

$$\ln\left(\frac{I_\alpha}{g_k A_{ki}}\right) = -\frac{E_{ki}}{k_B T_\alpha} + \ln\left(\frac{C_\alpha F}{U_\alpha(T_\alpha)}\right) \quad (39)$$

In the two-dimensional Boltzmann plane identified by the left-hand term of (39) and by E_{ki} , different emission line intensities belonging to the same element in the same spectrum lie along a straight line with a slope of $1/k_B T_\alpha$.

If experimental and theoretical data are available for each element in the sample, it is possible to evaluate the element concentration. The partition function is given by:

$$U_{\alpha}(T) = \sum_i g_i \exp\left(-\frac{E_i}{kT}\right) \quad (40)$$

where g_i is the degeneracy or statistical weight of the i^{th} energy level E_i .

$$g_i = 2J_i + 1 \quad (41)$$

J_i is the angular momentum quantum number of the level. E_i and J_i values are obtained from the NIST database.

In order to apply the CF-LIPS procedure, it is assumed that the plasma composition is representative of the actual material composition prior to the ablation (this is the basic assumption for application of LIBS technique, which is well realized in the range of the laser energies used in LIBS experiments) [65]. Moreover, we assume that in the actual temporal and spatial observation window the plasma is in local thermal equilibrium (LTE) condition and the radiation source is optically thin (this hypothesis is in general fulfilled in LIBS experiments where the main ionization process is produced through impact excitation by thermal electrons). In LTE approximation, the line integral intensity corresponding to the transition between two levels E_k and E_i of an atomic species s can be expressed as:

$$I_{\lambda}^{ki} = N_s A_{ki} \frac{g_k e^{-\frac{E_k}{K_B T}}}{U_s(T)} \quad (42)$$

where λ is the wavelength of the transition, N_s is the number density (particle/cm³) of the emitting atoms for each species, A_{ki} is the transition probability for the given line, g_k is the k level degeneracy, K_B the Boltzmann constant, T the plasma temperature and $U_s(T)$ is the partition function for the emitting species at the plasma temperature. The emitted intensity is expressed in photons/(scm³). In actual measurements, the efficiency of the

collecting system significantly affects the measured intensity of the line, so that it can be written as:

$$\overline{I}_{\lambda}^{ki} = FC_s A_{ki} \frac{g_k e^{-\frac{E_k}{K_B T}}}{U_s(T)} \quad (43)$$

where $\overline{I}_{\lambda}^{ki}$ represents the measured integral line intensity, C_s is the concentration of the emitting atomic species and F is an experimental parameter that takes into account the optical efficiency of the collection system as well as the plasma density and volume. Now, we can define the following quantities:

$$y = \ln \frac{\overline{I}_{\lambda}^{ki}}{g_k A_{ki}}, x = E_k, m = -\frac{1}{K_B T}, q_s = \ln \frac{C_s F}{U_s(T)} \quad (44)$$

Taking the logarithm of Eq. (43) and substituting the above definitions, we obtain the following relationship between the x and y parameters:

$$y = mx + q_s \quad (45)$$

The two-dimensional space identified by the above-defined x and y co-ordinates is called Boltzmann plane. A similar relation for each species in the plasma can be written. According to Eq. (45), the slope m is related to the plasma temperature, while the intercept q_s is proportional to the logarithm of the species concentration, by the factor F .

The F factor can be determined by normalizing to unit the element concentration C_s :

$$\sum_s C_s = \frac{1}{F} \sum_s U_s(T) e^{q_s} = 1 \quad (46)$$

Finally, the concentration of all the atomic elements of the sample can be obtained as:

$$C_s = \frac{1}{F} \sum_s U_s(T) e^{q_s} \quad (47)$$

where all the factors are known. The concentration value determined by Eq. (47) refers to one species; in order to obtain the elemental composition, it is sufficient to add the values corresponding to the neutral and single ionized species of the same element.

References of Chapter III

- [1] S. S. Harilal, C. V. Bindhu, and M. S. Tillack, F. Najmabadi, and A. C. Gaeris, "Internal structure and expansion dynamics of laser ablation plumes into ambient gases," *J. App. Phys.* **93**, 2380-2388 (2003).
- [2] A. A. Voevodin, J. G. Jones, and J. S. Zabinski, "Characterization of ZrO_2/Y_2O_3 laser ablation plasma in vacuum, oxygen, and argon environments," *J. Appl. Phy.* **88**, 1088-1096 (2000).
- [3] S. Amoruso, R. Bruzzese, N. Spinelli, and R. Velotta, "Characterization of laser-ablation plasmas," *J. Phys. B* **32**, R131-172 (1999).
- [4] S. S. Harilal, "Expansion dynamics of laser ablated carbon plasma plume in helium ambient," *Appl. Surface Sci.* **172**, 103-109 (2001).
- [5] S. M. Park and J. Y. Moon, "Laser ablation of graphite in an oxygen jet," *J. of Chem. Phys.* **109**, 8124-8129 (1998).
- [6] S. J. P. Laube and A. A. Voevodin, "In situ time of flight laser induced florescence spectroscopy of carbon by pulsed laser deposition," *Surf. Coat. Technol.* **105**, 125-129 (1998).
- [7] R. M. Mayo, J. W. Newman, A. Sharma, Y. Yamagata, and J. Narayan, "Electrostatic measurement of plasma plume characteristics in pulsed laser evaporated carbon," *J. Appl. Phys.* **86**, 2865-2871 (1999).
- [8] S. H. Jeong, R. Greif, and R. E. Russo, "Shock wave and material vapor plume propagation during excimer laser ablation of aluminum samples," *J. Phys. D* **32**, 2578-2585 (1999).

- [9] D. Kim, H. K. Park, and C. P. Grigoropoulos, "Interferometric probing of rapid vaporization at a solid-liquid interface induced by pulsed-laser irradiation," *Int. J. Heat Mass Transfer* **44**, 3843-3853 (2001).
- [10] T. Masubuchi, T. Tada, E. Nomura, K. Hatanaka, H. Fukumura, and H. Masuhara, "Laser-induced decomposition and ablation dynamics studied by nanosecond interferometry. 4. A polyimide film," *J. Phys. Chem. A* **106**, 2180-2186 (2002).
- [11] S. H. Glenzer, K. B. Fournier, C. Decker, B. A. Hammel, R. W. Lee, L. Lours, B. J. MacGowan, and A. L. Osterheld, "Accuracy of K-shell spectra modeling in high-density plasmas," *Phys. Rev. E* **62**, 2728-2738 (2000).
- [12] D. B. Geohegan, "Fast intensified-CCD photography of $\text{YBa}_2\text{Cu}_3\text{O}_{7-x}$ laser ablation in vacuum and ambient oxygen," *Appl. Phys. Lett.* **60**, 2732-2734 (1992).
- [13] S. S. Harilal, C. V. Bindhu, and H. J. Kunze, "Time evolution of colliding laser produced magnesium plasmas investigated using a pinhole camera," *J. Appl. Phys.* **89**, 4737-4740 (2001).
- [14] S. S. Harilal, C. V. Bindhu, V. P. Shevelko, and H. J. Kunze, "XUV diagnostics of colliding laser-produced magnesium plasmas," *J. Phys. B* **34**, 3717-3726 (2001).
- [15] B. N. Chichkov, C. Momma, S. Nolte, F. von Alvensleben, and A. Tunnermann, "Femtosecond, picosecond and nanosecond laser ablation of solids," *Appl. Phys. A* **63**, 109-115 (1996).
- [16] V. Margetic, K. Niemax, and R. Hergenroder, "A study of non-linear calibration graphs for brass with femtosecond laser-induced breakdown spectroscopy," *Spectrochim. Acta B* **56**, 1003-1010 (2001).

- [17] S. Amoruso, R. Bruzzese, N. Spinelli, and R. Velotta, "Characterization of laser-ablation plasmas," *J. Phys. B: At. Mol. Opt. Phys.* **32**, 131-172 (1999).
- [18] E. Tognoni, V. Palleschi, M. Corsi, and G. Cristoforetti, "Quantitative micro-analysis by Laser Induced Breakdown Spectroscopy: a review of the experimental approaches," *Spectrochim. Acta B* **57**, 1115-1130 (2002).
- [19] S. Amoruso, M. Armenante, V. Berardi, R. Bruzzese, and N. Spinelli, "Absorption and saturation mechanisms in aluminum laser ablated plasmas," *Appl. Phys. A* **65**, 265-271 (1997).
- [20] M. Capitelli, A. Casavola, G. Colonn, and A. De Giacomo, "Laser-induced plasma expansion: theoretical and experimental aspects," *Spectrochim. Acta B* **59**, 271-289 (2004).
- [21] J. A. Aguilera and C. Aragon, "Characterization of a laser-induced plasma by spatially resolved spectroscopy of neutral atom and ion emissions: Comparison of local and spatially integrated measurements," *Spectrochim. Acta B* **59**, 1861-1876 (2004).
- [22] H. R. Griem, In "*Plasma Spectroscopy*," McGraw-Hill, Inc., New York, (1964).
- [23] B. C. Castle, K. Visser, B. W. Smith, and J. D. Winefordner, "Level populations in a Laser-Induced Plasma on a lead target," *Spectrochim. Acta B* **52**, 1995-2009 (1997).
- [24] Y. Iida, "Effects of atmosphere on laser vaporization and excitation processes of solid samples," *Spectrochim. Acta B* **45**, 1353-1367 (1990).

- [25] M. Sabsabi and P. Cielo, "Quantitative analysis of aluminum alloys by Laser-Induced Breakdown Spectroscopy and plasma characterization," *Appl. Spectrosc.* **49**, 499-507 (1995).
- [26] R. Sattmann, V. Sturm, and R. Noll, "Laser-induced breakdown spectroscopy of steel samples using multiple Q-switch Nd:YAG laser pulses," *J. Phys. D. Appl. Phys.* **28**, 2181-2187 (1995).
- [27] J. Hermann, C. Boulmer-Leborgne, B. Dubreuil, and I. N. Mihailescu, "Influence of irradiation conditions on plasma evolution in laser-surface interaction," *J. Appl. Phys.* **74**, 3071-3079 (1993).
- [28] J. Hermann, A. L. Thomann, C. Boulmer-Leborgne, B. Dubreuil, M. De Giorgi, A. Perrone, A. Luches, and I. N. Mihailescu, "Plasma diagnostics in pulsed laser TiN layer deposition," *J. Appl. Phys.* **77**, 2928-2936 (1995).
- [29] K. J. Grant and G. L. Paul, "Electron temperatures and density profiles of excimer laser-induced plasmas," *Appl. Spectrosc.* **44**, 1349-1354 (1990).
- [30] Y. I. Lee and J. Sneddon, "Spatial and temporal characteristics of an excimer laser-induced lead plasma emission," *Spectrosc. Lett.* **29**, 1157-1171 (1996).
- [31] M. Essien, L. J. Radziemsky, and J. Sneddon, "Detection of cadmium, lead and zinc in aerosols by laser-induced breakdown spectrometry," *J. Anal. At. Spectrom.* **3**, 985-988 (1988).
- [32] M. R. Joseph, N. Xu, and V. Majidi, "Time-resolved emission characteristics and temperature profiles of laser-induced plasmas in helium," *Spectrochim. Acta B* **49**, 89-103 (1994).

- [33] J. A. Aguilera and C. Aragon, "Temperature and electron density distributions of Laser-Induced Plasmas generated with an iron sample at different ambient gas pressures," *Appl. Surf. Sci.* **197-198**, 273-280 (2002).
- [34] A. H. El-Astal, S. Ikram, T. Morrow, W.G. Graham, and D. G. Walmsley, "A quantitative investigation of emission from low temperature laser-induced $\text{YBa}_2\text{Cu}_3\text{O}_x$ plasma plumes," *J. Appl. Phys.* **77**, 6572-6580 (1995).
- [35] L. J. Radziemski, T. R. Loree, D. A. Cremers and N. M. Hoffman, "Time-resolved Laser-Induced Breakdown Spectrometry of aerosols," *Anal. Chem.* **55**, 1246-1252 (1983).
- [36] J. B. Simeonsson and A. W. Miziolek, "Time-resolved emission studies of ArF-laser-produced microplasmas," *Appl. Opt.* **32**, 939-947 (1993).
- [37] M. Milan and J. J. Laserna, Diagnostics of silicon plasmas produced by visible nanosecond laser ablation, *Spectrochim. Acta Part B* **56**, 275-288 (2001).
- [38] S. S. Harilal, C.V. Bindhu, R. C. Isaac, V. P. N. Nampoore, and C. P. G. Vallabhan, "Electron density and temperature measurements in a laser produced carbon plasma," *J. Appl. Phys.* **82**, 2140-2146 (1997).
- [39] S. S. Harilal, C. V. Bindhu, V. P. N. Nampoore, and C. P. G. Vallabhan, "Temporal and spatial behavior of electron density and temperature in a laser-produced plasma from $\text{YBa}_2\text{Cu}_3\text{O}_7$," *Appl. Spectrosc.* **52**, 449-455 (1998).
- [40] X. Yalcin, D. R. Crosley, G. P. Smith, and G.W. Faris, "Influence of ambient conditions on the laser air spark," *Appl. Phys. B* **68**, 121-130 (1999).
- [41] B. Le Drogoff, J. Margot, M. Chaker, M. Sabsabi, O. Barthelemy, T. W. Johnston, S. Laville, F. Vidal, and Y. von Kaenel, "Temporal characterization of

- femtosecond laser pulses induced plasma for spectrochemical analysis of aluminum alloys," *Spectrochim. Acta B* **56**, 987-1002 (2001).
- [42] B. C. Castle, K. Visser, B. W. Smith, and J. D. Winefordner, "Level populations in a laser-induced plasma on a lead target," *Spectrochim. Acta B* **52**, 1995-2009 (1997).
- [43] X. Zeng, S. S. Mao, C. Liu, X. Mao, R. Greif, and R. E. Russo, "Plasma diagnostics during laser ablation in a cavity," *Spectrochim. Acta B* **58**, 867-877 (2003).
- [44] J. Cortes, E. R. Cepedes, and B. H. Miles, "Development of Laser Induced Breakdown Spectroscopy for Detection of Metal Contaminants in Soils," Technical report IRRP-96-4, U.S. Army Engineer Waterways Experiment Station, Vicksburg, MS, (1996).
- [45] G. Bekefi, In "*Principles of Laser Plasma*," Wiley, New York, (1976).
- [46] J. M. Gomba, C. D'Angelo, D. Bertuccelli, and G. Bertuccelli, "Spectroscopic characterization of laser induced breakdown in aluminium-lithium alloy samples for quantitative determination of traces," *Spectrochim. Acta B* **56**, 695-705 (2001).
- [47] D. B. Geohegan, "Imaging and blackbody emission spectra of particulates generated in the KrF-laser ablation of BN and $\text{YBa}_2\text{Cu}_3\text{O}_7$," *Appl. Phys. Lett.* **62**, 1463-1465 (1993).
- [48] M. A. Liberman and A. L. Velikovich, In "*Physics of Shock Waves in Gases and Plasmas*," Springer, Berlin, (1986).

- [49] Ya. B. Zel'dovich, and Yu. P. Raizer, In "*Physics of Shock Waves and High-Temperature Hydrodynamics Phenomena*," Academic, New York (1966).
- [50] F. Garrelie, J. Aubreton, and A. Catherinot, "Monte Carlo simulation of the laser-induced plasma plume expansion under vacuum: Comparison with experiments," *J. Appl. Phys.* **83**, 5075-5085 (1998).
- [51] A. V. Gusarov and I. Smurov, "Near-surface laser-vapor coupling in nanosecond pulsed laser ablation," *J. Phys. D* **36**, 2962-2971 (2003).
- [52] T. E. Itina, J. Hermann, Ph. Delaporte, and M. Sentis, "Combined continuous-microscopic modeling of laser plume expansion," *Appl. Surf. Sci.* **208-209**, 27-32 (2003).
- [53] Z. Chen and A. Bogaerts, "Laser ablation of Cu and plume expansion into 1 atm ambient gas," *J. Appl. Phys.* **97**, 063305:1-12 (2005).
- [54] A. V. Gusarov, A. G. Gnedovets, and I. Smurov, "Gas dynamics of laser ablation: Influence of ambient atmosphere, " *J. Appl. Phys.* **88**, 4352-4364 (2000).
- [55] K. R. Chen, J. N. Leboeuf, R. F. Wood, D. B. Geohegan, J. M. Donato, C. L. Liu, and A. A. Puretzky, "Modeling of dynamical processes in laser ablation," *Appl. Surf. Sci.* **96-98**, 14-23 (1996).
- [56] V. Detalle, M. Sabsabi, L. St-Onge, A. Hamel, and R. Héon, "Influence of Er:YAG and Nd:YAG wavelengths on laser-induced breakdown spectroscopy measurements under air or helium atmosphere" *Appl. Opt.* **42**, 5971-5977 (2003).
- [57] A. G. Gnedovets, A. V. Gusarov, and I. Smurov, "A model for nanoparticles synthesis by pulsed laser evaporation, " *J. Phys. D* **32**, 2162-2168 (1999).

- [58] C. R. Phipps, R. W. Dreyfus, In: A. Vertes, R. Gijbels, and F. Adams (Eds.), *"Laser Ionization Mass Analysis,"* John Wiley & Son, New York, (1993).
- [59] W. Lochte-Holtgraven, In *"Plasma Diagnostics,"* AIP, New York, (1995).
- [60] J. Broekaert, In *"Analytical Atomic Spectrometry with Flames and Plasmas,"* Wiley-Vch, Weinheim, Germany, (2002).
- [61] R. Barbini, F. Colao, R. Fantoni, A. Palucci, and F. Capitelli, "Application of Laser Induced Breakdown Spectroscopy to the analysis of metals in soil," *Appl. Phys. A* **69**, 175-178 (1999).
- [62] E. H. Piepmier, In *"Laser Ablation for Atomic Spectroscopy,"* Analytical Application of Laser, ed. By E. H. Piepmier, Wiley, New York (1986).
- [63] J. L. Todoli and J. M. Mermet, "Study of polymer ablation products obtained by ultraviolet laser ablation-inductively coupled plasma atomic emission spectrometry," *Spectrochim. Acta B* **53**, 1645-1656 (1998).
- [64] A. Ciucci, M. Corsi, V. Palleschi, S. Rastelli, A. Salvetti, and E. Tognoni, "New procedure for quantitative elemental analysis by laser-induced plasma spectroscopy," *Appl. Spectrosc.* **53**, 960-964 (1999).
- [65] I. Borgia, L. Burgio, M. Corsi, R. Fantoni, V. Palleschi, A. Salvetti, M. C. Squarzialupi, and E. Tognoni, "Self-calibrated quantitative elemental analysis by laser-induced plasma spectroscopy: application to pigment analysis," *J. Cult. Heritage* **1**, 281-286 (2000).

CHAPTER IV

INSTRUMENTATION AND EXPERIMENTAL PARAMETERS

Laser Induced Breakdown Spectroscopy (LIBS) has received increasing attention as an analytical technique due its versatility, rapidity, minimal sample preparation and simplicity. Recently, there have been many studies using LIBS for quantitative analysis [1-3]. However, LIBS has some disadvantages, such as the relatively large interference effects and the moderately poor detection limits and precision. Many works have studied the variables affecting LIBS analytical figures of merit (accuracy, precision and detection limit) such as laser parameters, pulse duration, laser energy and repetition rate [4,5]. Other variables affecting the LIBS analytical performance is the sample characteristics: homogeneity, roughness, matrix composition and moisture content. The sampling and detection geometry also play an important role in LIBS measurements and results. Many works have been devoted to optimizing such variables and overcoming LIBS drawbacks, which prevented a multipurpose implementation of the technique. Developments in laser sources have contributed to more reproducible plasma generation and the introduction of intensified solid-state detectors, which are launching some solutions to enhance LIBS applicability.

In this chapter, we introduce the basic steps followed in our primary LIBS experiments, including instrumentation, data acquisition, sample selection, optimized setup and detection geometry, and data analysis. Better understanding of the variables that can be controlled, for example, choice of the analytical line, laser-shot-to-shot

variance, method of data analysis and atmospheric conditions, have been carried out. The sampling geometry, which includes the lens-to-sample distance, the orientation of the sample, with respect to the incident laser pulses, the method of focusing the laser pulse to generate the spark and the method of collecting the spark emitted light have been optimized to produce the best results. The plasma properties, such as plasma temperature and its determination method, have been introduced in detail.

4.1 Nanosecond LIBS

The experimental setup consists of a Nd:YAG laser; the excitation source operated at the fundamental wavelength of 1064 nm at 50 Hz repetition rate. The laser pulse energy of 34 mJ and pulse duration of 35 ns FWHM is delivered by a set of IR mirrors to be focused by a 10 cm-lens on the target under investigation. Two spectrographs and a photomultiplier tube (PMT) are used for detection and are connected to a PC for control, data acquisition and data processing. An x-y translational stage is used for the sample under investigation to create reproducible positioning and to allow for a fresh spot in each run. Two fiber bundles are used to collect the light emitted from the produced plasma to the entrance slits of the two spectrographs. The resultant dispersed emission for each spectrograph is detected by a CCD detector and processed by data acquisition software. The following table summarizes the components of our experimental setup.

Table 1: List of LIBS components.

Component	Description
Laser	Lumonics YM-200
Wavelength (nm)	1064
Pulse energy (mJ)	15-34
Pulse repetition (Hz)	50
Focusing lens (cm)	10
Signal detection	<ul style="list-style-type: none"> • CVI Spectrometer SM 240 Spectral range (200-978 nm) • Ocean optics Spectrometer HR 1200 Spectral range (805- 955 nm) • Monochromator (1440 nm/mm) • Photomultiplier tube (PMT) • Oscilloscope (Tektronix, 300 MHz)
Signal collection	Fiber optic

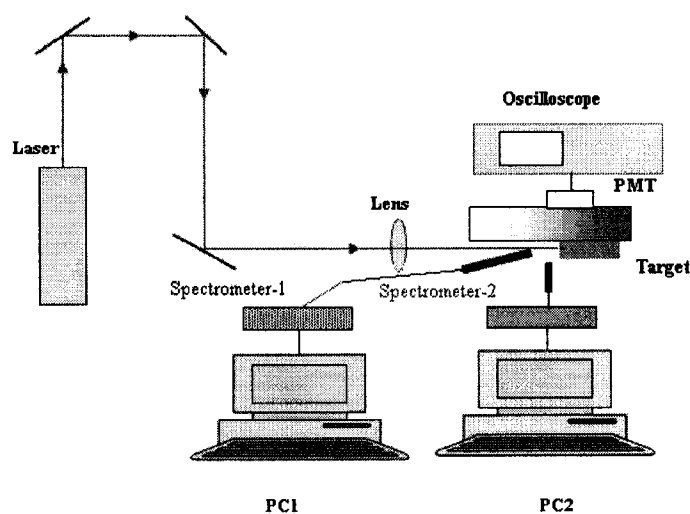


Fig. 4.1 Schematic diagram of the experimental setup. The laser has been directed to be focused on the target under investigation and the emitted light is detected using two spectrometers with different spectral range. A monochromator and a PMT provided time-resolved data.

4.1.1 Laser characterization and pulse width.

The Q-switched Nd:YAG laser operating at 1064 nm is used in this experiment as the excitation source. The output laser pulse shape, shown in Fig. 4.2, is detected using a fast detector and is displayed in an oscilloscope to be transferred and plotted using a computer. It can be seen that the pulse width (FWHM) is about ~ 35 ns.

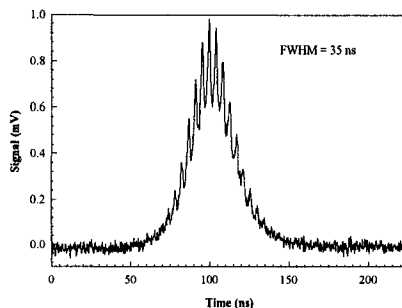


Fig. 4.2 Laser pulse shape as detected with a diode detector. The FWHM was measured to be 35 ns.

By changing the focusing lens position with respect to the target position using a translational stage and running the knife edge measurement, the focal spot at each position was measured. Then, the pulse profile is deduced as a function of the position between the focusing lens and target surface and plotted in Fig. 4.3. The FWHM of the laser spot on the focus is around 0.01 cm.

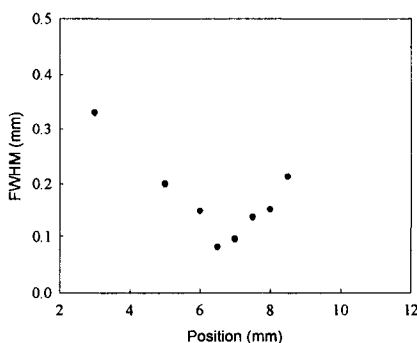


Fig. 4.3 FWHM of the laser beam as a function of position of the focusing lens to the target surface.

Calibration for the detector wavelength was conducted by using the emission from a mercury lamp. The spectrum of Hg lamp is shown in Fig. 4.4. These emission lines are compared with those listed in the NIST database and a calibration of wavelength shift error is plotted in Fig. 4.5.

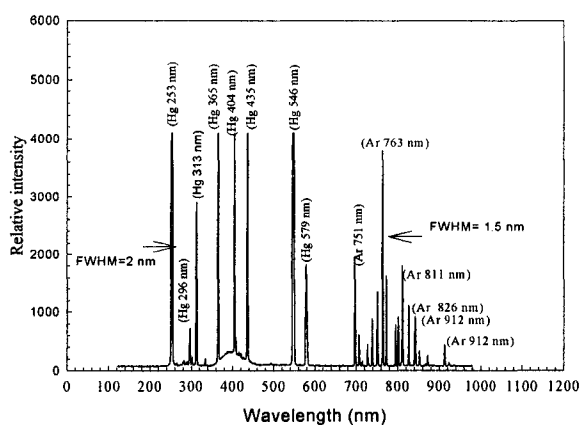


Fig. 4.4 Hg lamp spectrum detected by CVI spectrometer. This was done to calibrate the spectrometer and define the wavelength shift.

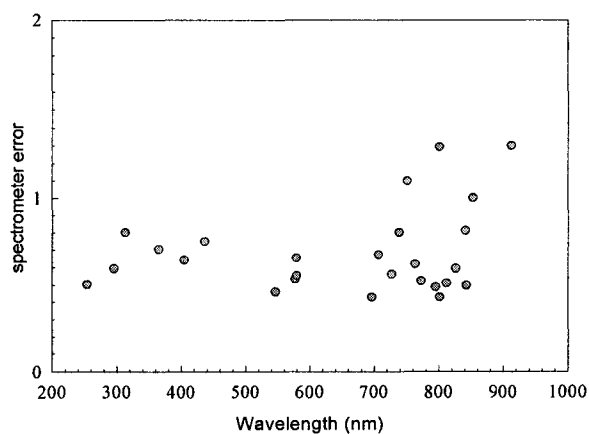


Fig. 4.5 Measured detector wavelength shift error. The maximum wavelength shift error is less than 1 nm for wavelengths (λ) < 700 nm and less than 1.5 nm for λ > 700 nm.

4.1.2 Integrated spectra

Using the setup shown in Fig. 4.6, we obtained the integrated spectra of the samples of interest, which are copper, aluminum, carbon and Ni alloys (Figs. 4.7-4.9). As

it is apparent, the atomic emission lines are imposed on the continuum background radiation, which is representative to the high temperature occurring at the onset of the laser pulse. This intense continuum is attributed to the Bremsstrahlung process (collision of electrons with ions and atoms, free-free emission) and recombination of electrons with ions (free-bound emission) [6]. The separation of the emission lines is limited by the (~ 1 -nm) resolution of the spectrometer used in this experiment. In Cu, Al, C spectra, it can be noticed that the neutral lines, along with ionic lines, emerge as a result of the high laser fluence in the range of $49\text{-}87\text{ J/cm}^2$ after being focused by the 10 cm quartz lens.

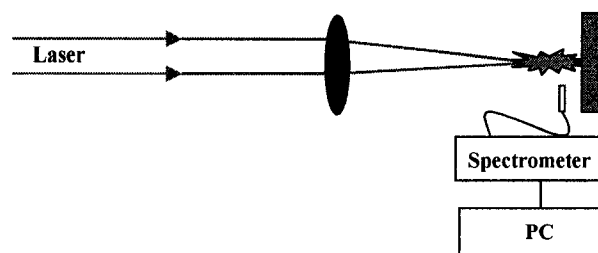


Fig. 4.6 Schematic diagram of time-integrated LIBS experiment. The laser beam is focused on the target to produce a plasma which is detected by a CVI spectrometer.

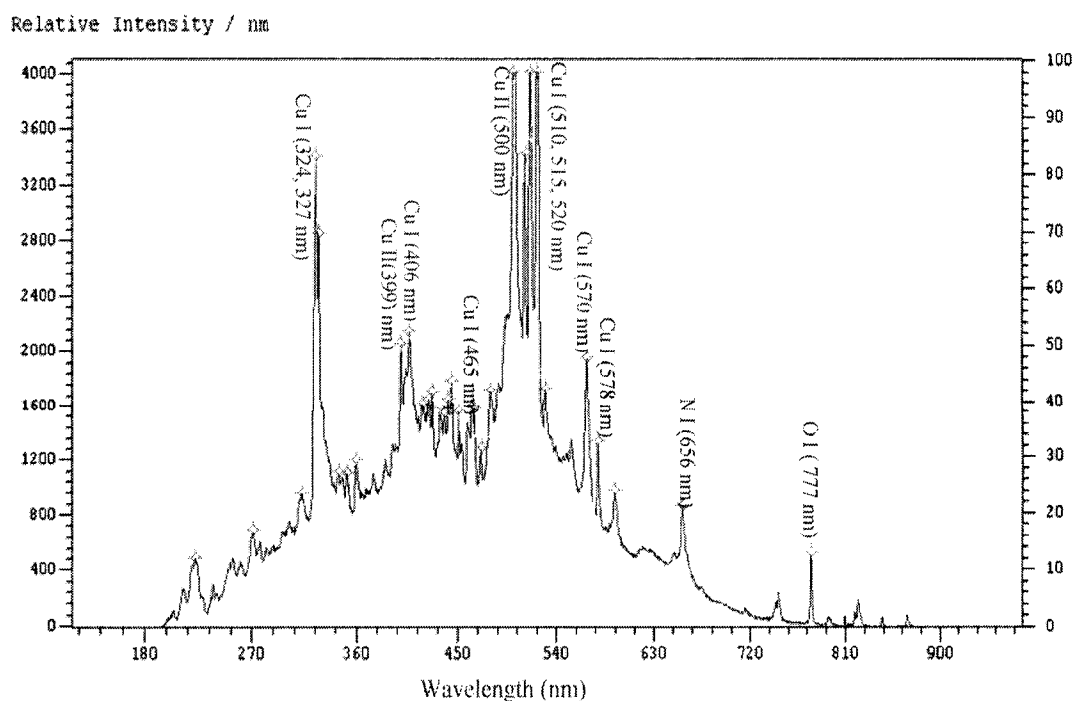


Fig. 4.7 Time-integrated LIBS spectrum of Cu in air.

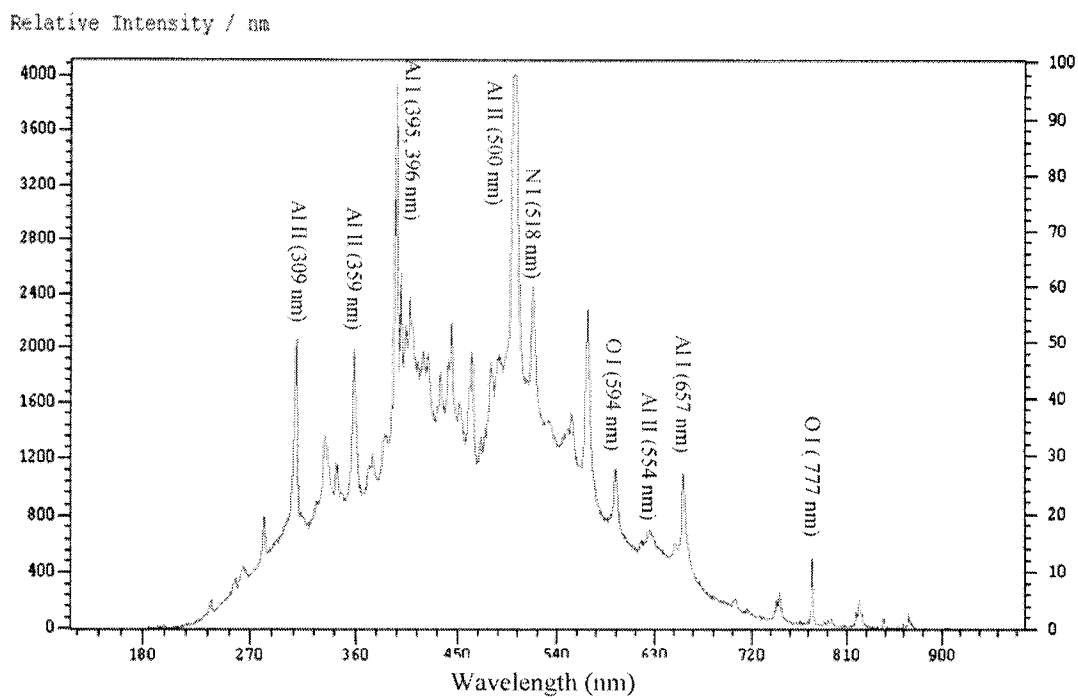


Fig. 4.8 Time-integrated LIBS spectrum of Al in air.

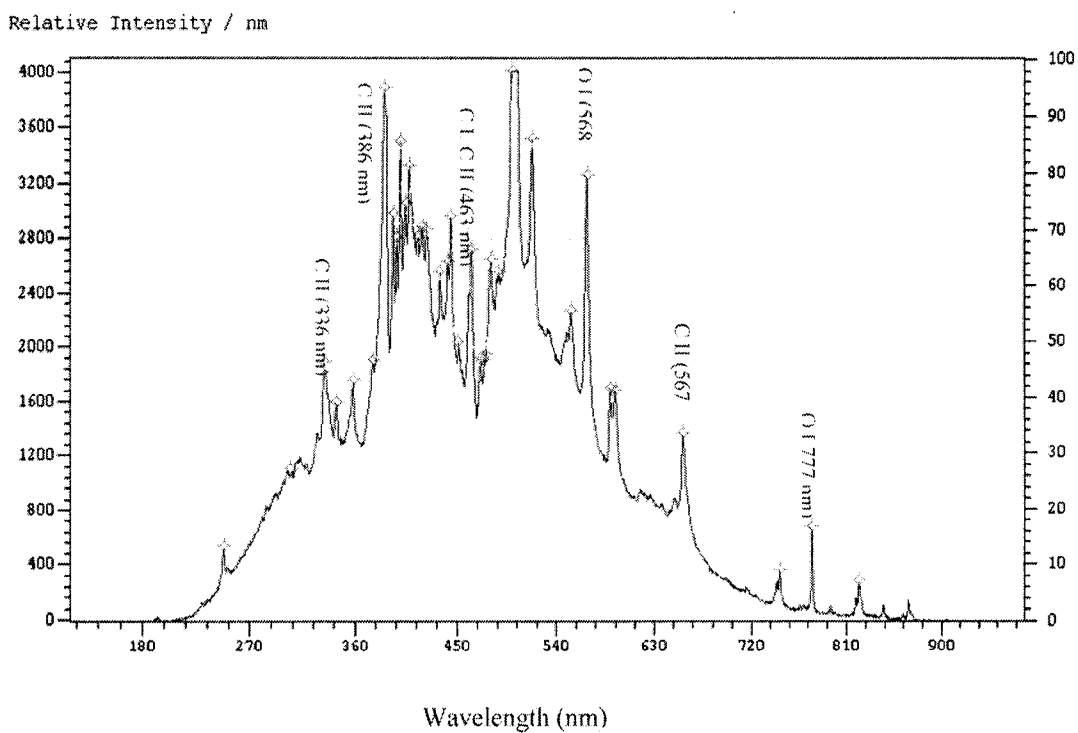


Fig. 4.9 Time-integrated LIBS spectrum of C in air.

It is also apparent that, besides the Cu spectral lines, there are O I and N I lines as a result of air breakdown. The ratio of line emission intensity can be used to determine the excitation temperature of the plasma.

4.1.3 Time-resolved line emission

In a time-resolved experiment, the emission spectrum passes through the 100- μm -entrance slit of a monochromator. The dispersed light is collected by a collimating mirror to the exit slit at which a photomultiplier tube (PMT) is located. The exit slit only allows a narrow part of the spectrum to pass through, which corresponds to a certain line belonging to an element in the studied sample. The signal is displayed on an oscilloscope screen and could be transferred to a computer for plotting, manipulation and analysis.

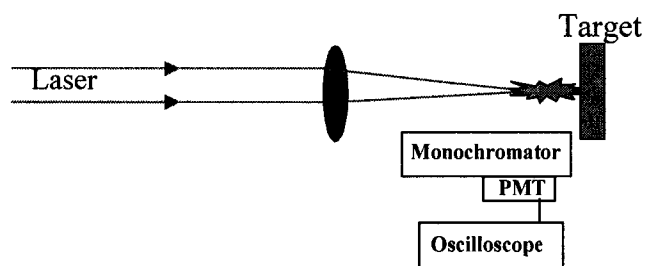


Fig. 4.10 Schematic diagram of the time-resolved LIBS experiment. The temporal behavior of the emitted spectral lines is detected by a monochromator, PMT, an oscilloscope and a computer.

The choice of emission lines for the time resolved experiments is based on the non-interference of the chosen line with other emission lines. The fast decay of the continuum compared to emission line signal is noticeable. In the case of Al, the decay time of the superposition of Al 358.6 nm and the continuum emission (Fig. 4.11 (a)) is about 1.2 μs while the decay time of the continuum (Fig. 4.11 (b)) is about 0.4 μs . The Al

358 nm decay time can be obtained by subtracting the graph in Fig. 4.11 (b) from that in Fig. 4.11 (a). The decay time of the line intensity of the Al 358 nm is about $0.8 \mu\text{s}$ (Fig. 4.11 (c)). Another line was chosen; Al 309, whose superposition with the continuum background (Fig. 4.12 (a)) gives a decay time of $2 \mu\text{s}$. While the continuum (Fig. 4.12 (b)) is evaluated to be about $0.2 \mu\text{s}$, the decay time of Al 309 nm spectral line (Fig. 4.12 (c)) is about $1.8 \mu\text{s}$. A result is deduced that the strong continuum emission occurs in time scales of less than a microsecond, while the line emission lasts for a few microseconds [7].

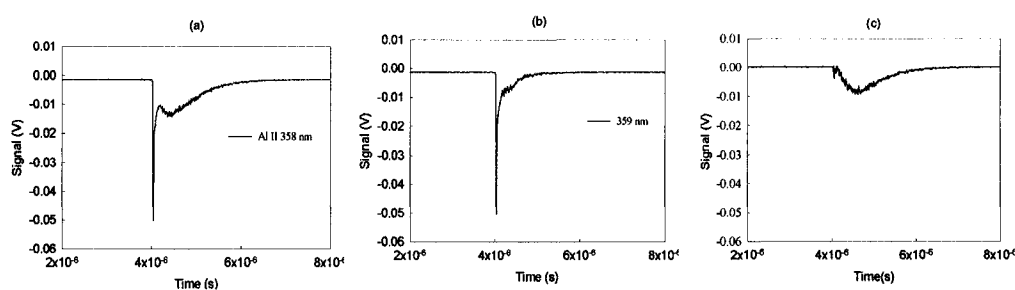


Fig. 4.11 Time-resolved line Al II 358.6 nm intensity.

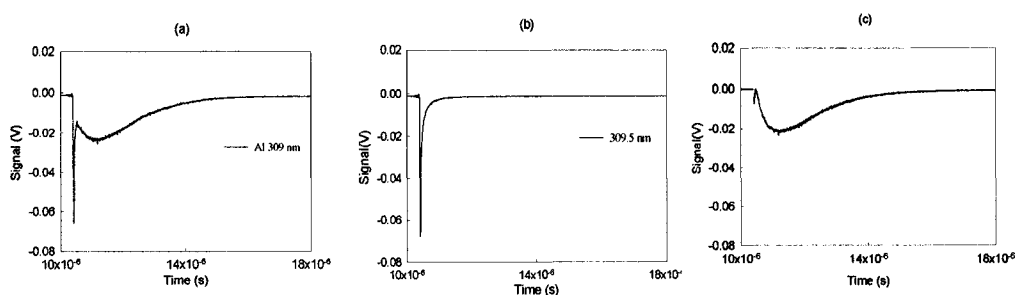


Fig. 4.12 Time-resolved of Al I line 309.2 nm intensity.

4.2 Single-element experiments (Cu, Al and C)

4.2.1 Experiment

A Cu sample, placed at the focal length of a 10-cm lens, is irradiated with Nd-YAG laser with different laser energies ranging from 15.6 to 27.4 mJ and spot size ≈ 0.08

mm. The energy is varied using microscope glass slides. Fresh spots of the sample were subject to the laser beam at each run. Data acquisition consists of 856 frames, and each frame shows the spectrum resulting from one pulse out of three successive laser pulses. The spectrum is obtained using our setup shown previously. Figure 4.13 shows the Cu spectrum with its characteristic line emission identified.

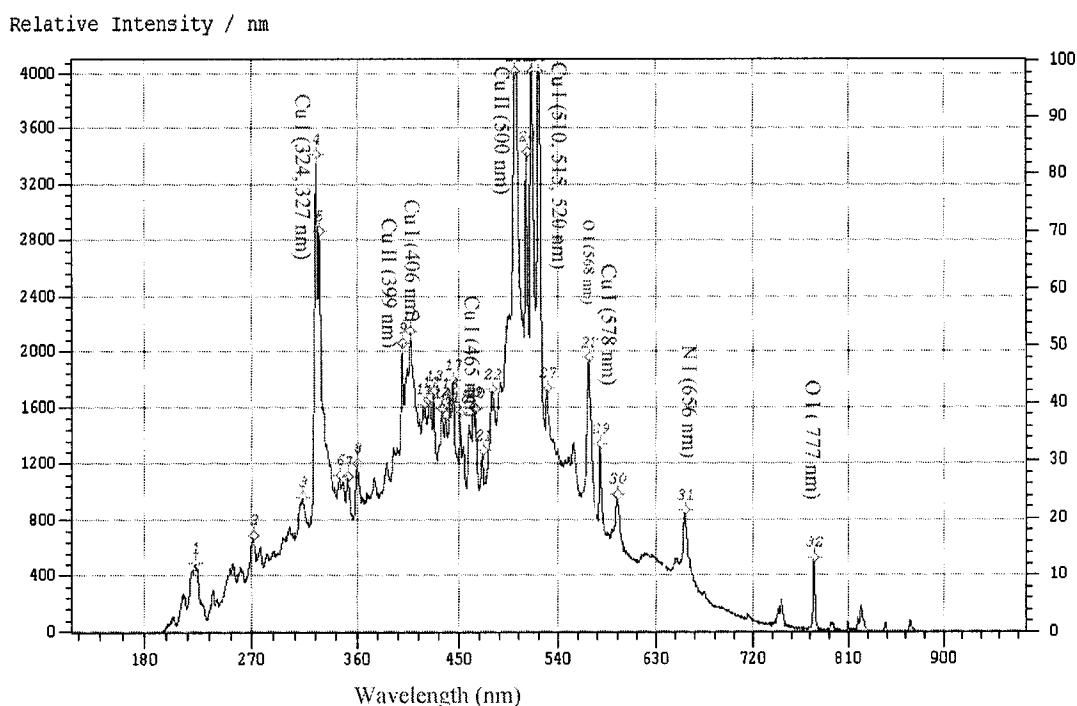


Fig. 4.13 Time-integrated spectrum of Cu in air.

Information about the origin of each line emission for Cu can be explained using the following diagram (Fig. 4.14).

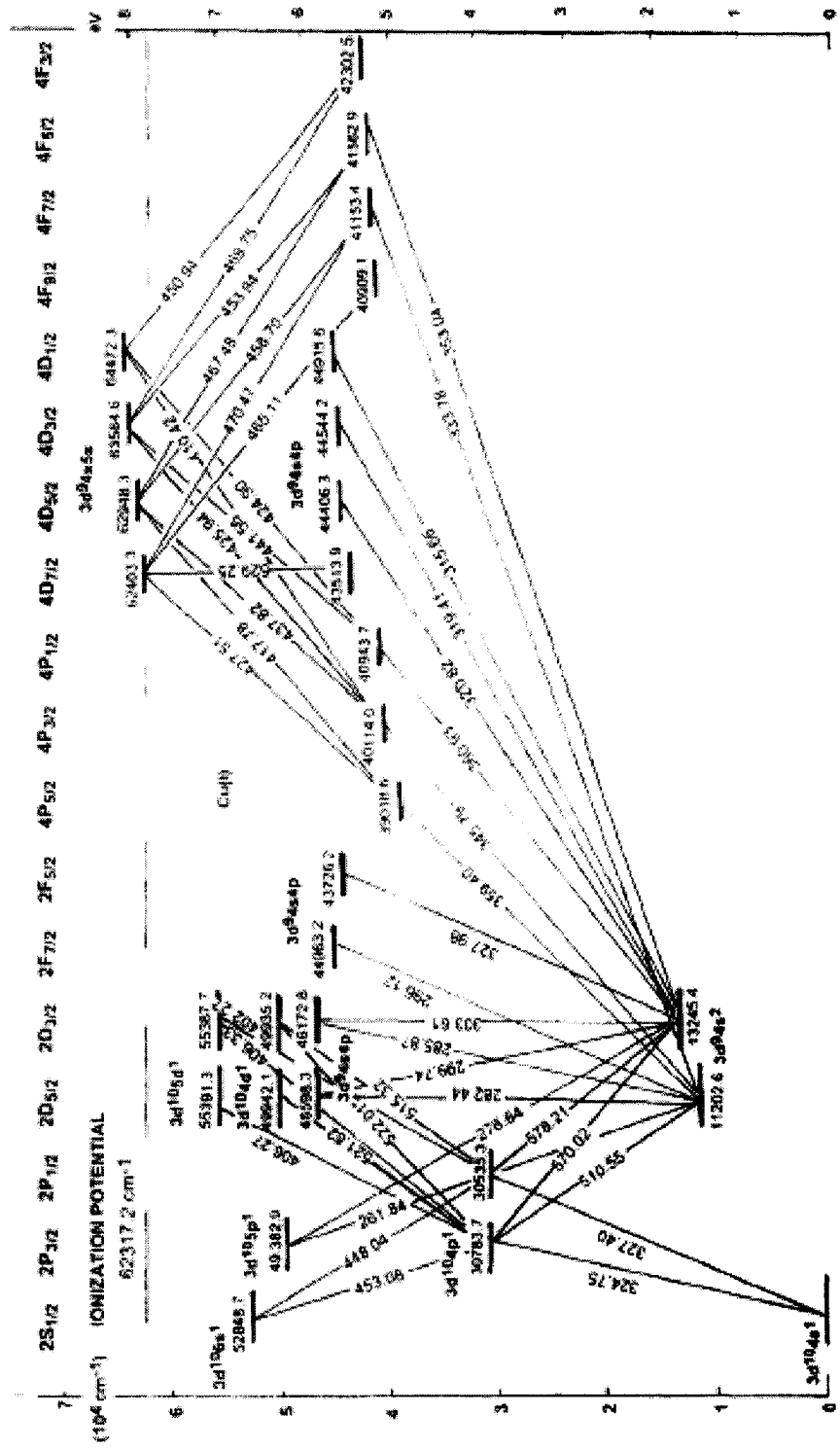


Fig. 4.14 Grotrian energy level diagram of Copper; Cu given by B. Nemet and L. Kozma [8].

4.2.2 Blackbody calibration method

The methodology we followed in order to extract the peak line intensity is to calibrate our data to the blackbody emission taking into consideration the detector response. To correct for detector response, a calibration method has been applied using a calibrated continuum source, which emits a continuum spectrum depending on its temperature. A blackbody source can be understood as an idealized object that emits and absorbs thermal radiation perfectly. The Planck's equation for blackbody radiation is:

$$I = \frac{2hc^2}{\lambda^5} \frac{1}{\exp\left(\frac{hc}{\lambda KT}\right) - 1} \quad (1)$$

I : Radiation emitted per wavelength, λ : Wavelength (m), h : Planck' constant (6.6238 x 10⁻³⁴ J.s), c : speed of light (3x10⁸ m/s), K : Boltzmann constant (1.3807x10⁻²³ J/k).

Our method is summarized in the following steps:

1. Acquiring the spectrum of the continuum source at different temperatures.
2. Calculating the theoretical continuum spectrum at the same temperatures using the above equation.
3. Plotting our calibration curve by comparing both values from steps 1 and 2 after normalization.

Figures 4.15-17 show the experimental and theoretical intensity plots at different temperatures 3000, 2800 and 2600 k, respectively, and the corresponding calibration curves at the each temperature value.

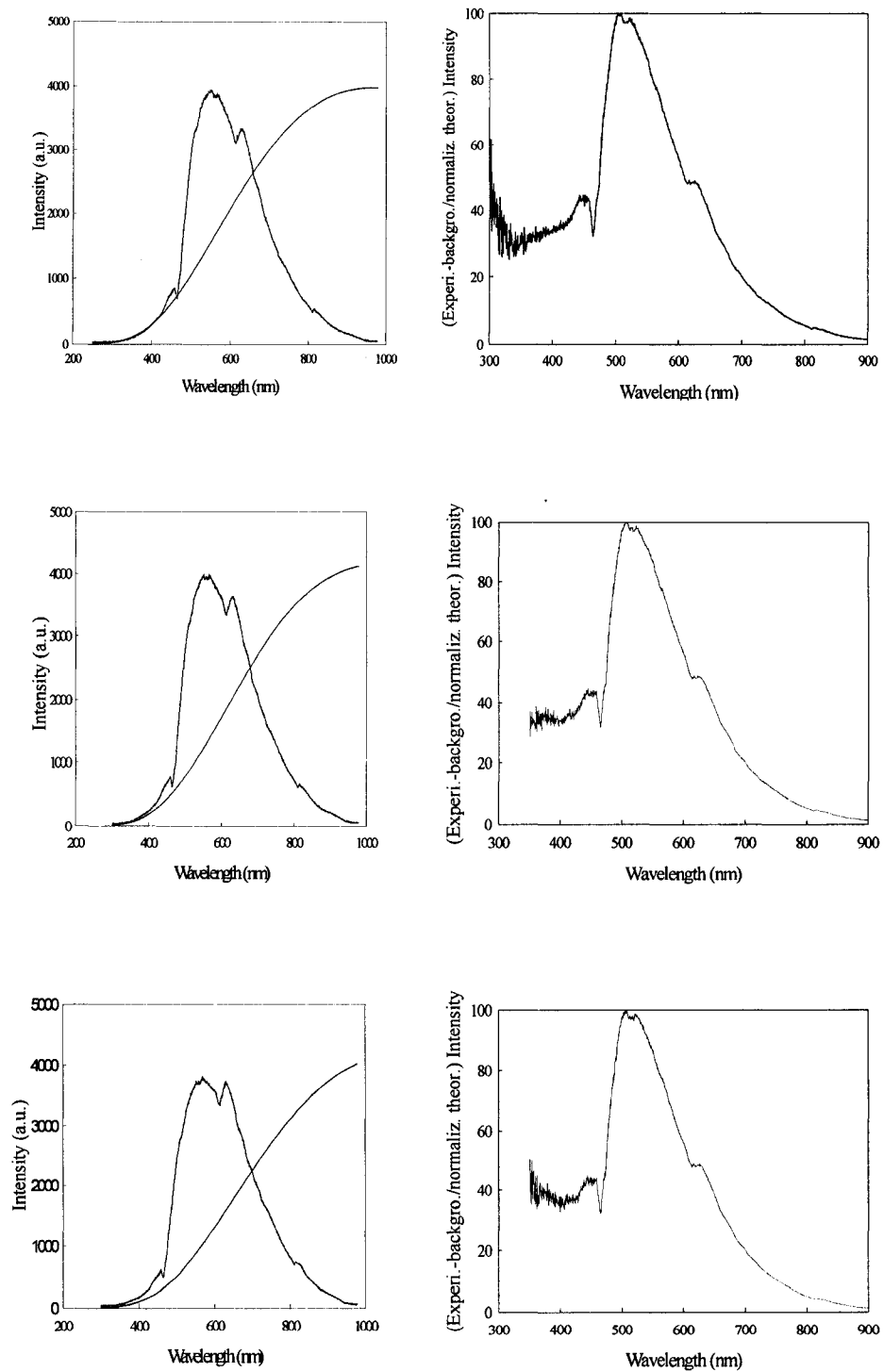


Fig. 4.15 Blackbody calibration method used to correct for the detector intensity response. Steps 1 through 3 are plotted systematically at temperatures 3000, 2800 and 2600 k, respectively.

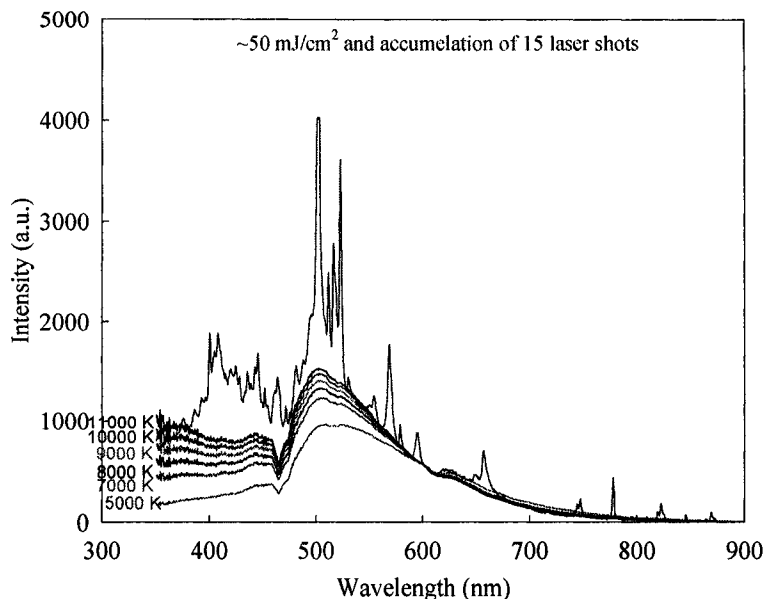


Fig. 4.16 Cu spectrum with calibrated blackbody emission at different temperatures.

In a collision dominated, optically thick LTE plasma, the emission intensity of homogeneous plasma along a line of sight can be represented by Planck's function (Eq. 1) [9,10]. The blackbody plots shown in the above graph are normalized to a chosen wavelength (600 nm) for different laser fluences ranging from ~ 50 to 87 mJ/cm^2 . In order to find the most appropriate plot that fits this spectrum, the minimum percentage error, with respect to experimental data at a certain temperature, was considered. Table 2 summarizes the experimental data compared to the corresponding value after calibration at different temperatures.

Table 2. Comparison of calibrated intensity values at different temperatures and the obtained experimental values.

Wavelength nm	Experimental Intensity	5000 k	7000 k	8000 k	9000 k	10,000 k	11,000 k
543	1105	896	1027	1069	1102	1129	1151
560	921	797	874	898	917	932	944
577	765	702	741	752	761	768	774
583	652	657	683	690	696	701	705
588	624	630	647	652	656	659	661
617	492	487	470	465	462	459	451
645	404	402	368	358	351	346	342
653	426	358	322	313	305	300	296
672	250	278	242	233	226	220	216
700	132	187	155	147	141	137	134
714	87	152	124	117	111	108	105
739	53	109	86	80	76	72	70

The error percentages corresponding to 5000, 7000, 9000, 10000, 11000 k are 0.2442, 0.1558, 0.1373, 0.1234, 0.1194, 0.1200, respectively. According to the blackbody calibration procedure we followed, the average plasma temperature is estimated to be \approx 10,000 k. We assumed that the temperature is constant in the range of experimental laser fluence 49.6-87.26 J/cm², which is also supported by St-onge et al. and Yalcin et al.

[11,12], who showed that the temperature increases only slightly with a two-fold increase in laser energy.

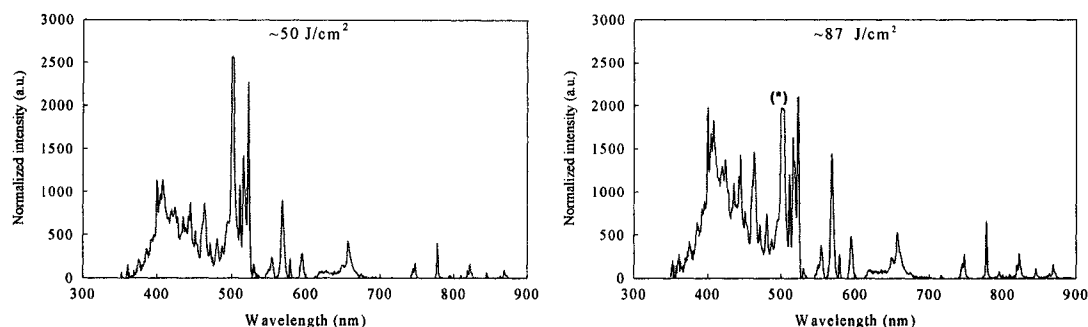


Fig. 4.17 Calibrated Cu spectrum at the two extreme values of laser fluence used in this experiment using the blackbody emission calibration method [(*) : Saturated lines have not been analyzed].

4.2.3 Laser fluence effect

The behavior of line emission intensity versus incident fluence has been extensively investigated by several authors. They found an initial linear correlation, probably due to the increase of ablated material; subsequently, for higher fluence values, the emission signal reaches a saturation regime attributed to the absorption of the laser beam by the plasma formed in front of the sample [13-15]. The starting point of the saturation regime is element-dependent and correlated with the value of the threshold. The same behavior of coupling efficiency was found in dependence of the power density for nanosecond and picosecond lasers: the mass ablation rate increases linearly with power density, then undergoes a regime change, followed by saturation. In order to obtain the maximum efficiency in mass removal, a study by Chan and Russo suggested the use of power densities of the order of 1 GW/cm^2 for a copper target [15]. Higher power densities produced constant mass ablation rate, due to the shielding of the laser energy

acted by the plasma itself. Stratis et al., studied the line intensity over some laser fluence range 0.6 and 1.2 GW/cm² and found that it is linearly correlated to the laser fluence, which they also attributed to the increased ablation rate of the material [16]. In our experiment, we studied the influence of laser fluence on the line intensity of some spectral lines of Cu. All data analysis was applied to the fifth frame in our data acquisition method. We noticed that there is a linear relationship between the line intensity of some spectral lines of Cu in the laser fluence range ~ 50 - 87mJ/cm² (Fig. 4.18).

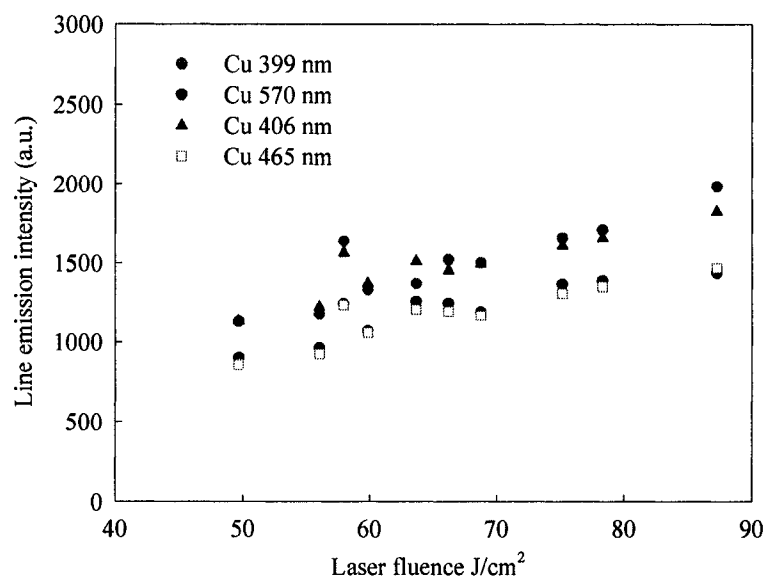


Fig. 4.18 Cu line emission as a function of laser fluence for different Cu lines.

4.2.4 Boltzmann Plot

Temperature is an important property of an analytical excitation, and it needs to be known to understand the excitation processes. It can be determined by the Boltzmann method from relative line intensities. The spectral line radiance equation for multiple

lines, indexed i from the same element and ionization stage with the assumption of LTE, is:

$$\ln\left(\frac{I_i \lambda_i}{g_i A_i}\right) = -\frac{1}{T} \left(\frac{E_i}{k}\right) + \ln\left(\frac{hc n_t}{4\pi Z}\right) \quad (2)$$

where l is the effective path length through the radiation source, n_t is the particle number density, Z is the partition function.

The quantity $\ln\left(\frac{I_i \lambda_i}{g_i A_i}\right)$ is assumed the dependent variable and E_i/k the independent variable for a set of lines from the same species and otherwise identical conditions, a linear relationship with a slope of $(-1/T)$ and an intercept of $\ln\left(\frac{hc n_t}{4\pi Z}\right)$ results. The spectroscopic parameters are given below in Table 3 as given in Ref. 17.

Table 3. Spectroscopic parameters for Cu lines.

Wavelength (nm)	E (eV)	g_m	$A_{mn} (10^{-8} \text{ sec}^{-1})$
Cu 406	6.8790	6	2.1×10^{-1}
Cu 465	7.7500	8	3.8×10^{-1}
Cu 510	3.8230	4	2×10^{-2}
Cu 515	6.2019	4	6×10^{-1}
Cu 570	3.8230	4	2.4000×10^{-3}
Cu 578	3.7900	2	1.6500×10^{-3}

(Spectroscopic data are obtained from NIST database) [17].

Using the following graphs, the plasma temperature was calculated to be in the range from 9750 k to 11,500 k. Line intensities from the fifth frame at laser fluences 60, 75, and 87 J/cm², respectively, were used to obtain the Boltzmann plots (Fig. 4.19).

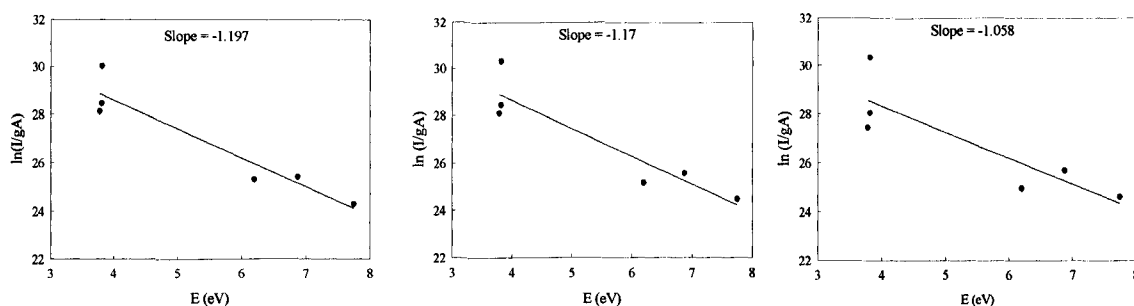


Fig. 4.19 Boltzmann plots used for plasma temperature determination. By applying eq. (2) such that $\ln\left(\frac{I_i \lambda_i}{g_i A_i}\right)$ is assumed as the dependent variable and E_i/k is the independent variable, the slope is equal to $(-1/T \text{ (in Kelvin)})$.

4.2.5 Pulse accumulation effect

As a result of the number of laser shots, it is observed that the Cu lines' intensity is always following the same behavior. It is highly fluctuating during the first two hundred laser shots, and then it is almost stable during the following laser pulses. This can be attributed to the high mass ablation rate, which happens as a result of the laser energy deposition over the sample during the early laser shots. This produces a plasma that shields the laser energy to reach the target resulting in the almost stable behavior observed in Fig. 4.20. This result implies that, for quantitative analysis, it will be necessary to apply about two hundred laser shots to be able to get stable measurements. This result is similar to that presented by Hemmerlin et al. [18], who observed that the Fe 281.3 nm emission line becomes stable after 400 laser shots.

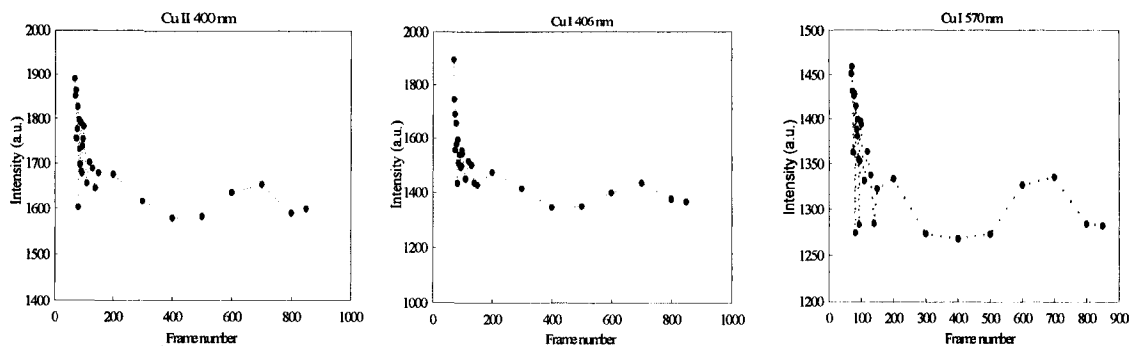


Fig. 4.20. Cu line emission as a function of number of laser shots (one frame is equivalent to 3 pulses).

4.2.6 Spatially resolved spectra-expansion mechanism

Line broadening and self-absorption have been reported for laser-induced plasmas for short time decay with the use of time resolved experiments [19]. If self-absorption occurs, it should be noticeable at the high power density and the full width at half maximum (FWHM) of the emission line will change at the different axial positions, due to electron density change. The lines selected in our work show the same line width (within the ~ 1 nm spectral resolution of the spectrometer) at the different axial positions and the various power densities studied. Therefore, broadening is assumed to be negligible in the time-integrated emission lines studied here [7]. Fig. 4.21 shows the spatial evolution of plasma temperature above the target. It can be seen that the plasma temperature changes as a function of axial position from the surface of the target. For each position, the Cu time-integrated spectrum was obtained and was calibrated as previously explained in Sec. 4.2.2. Then, the normalized line intensity for Cu spectral lines have been plotted versus axial position as shown in Fig 4.22. The zero point corresponds to the closest position between the sample and the tip of the fiber optic (~ 500 μm).

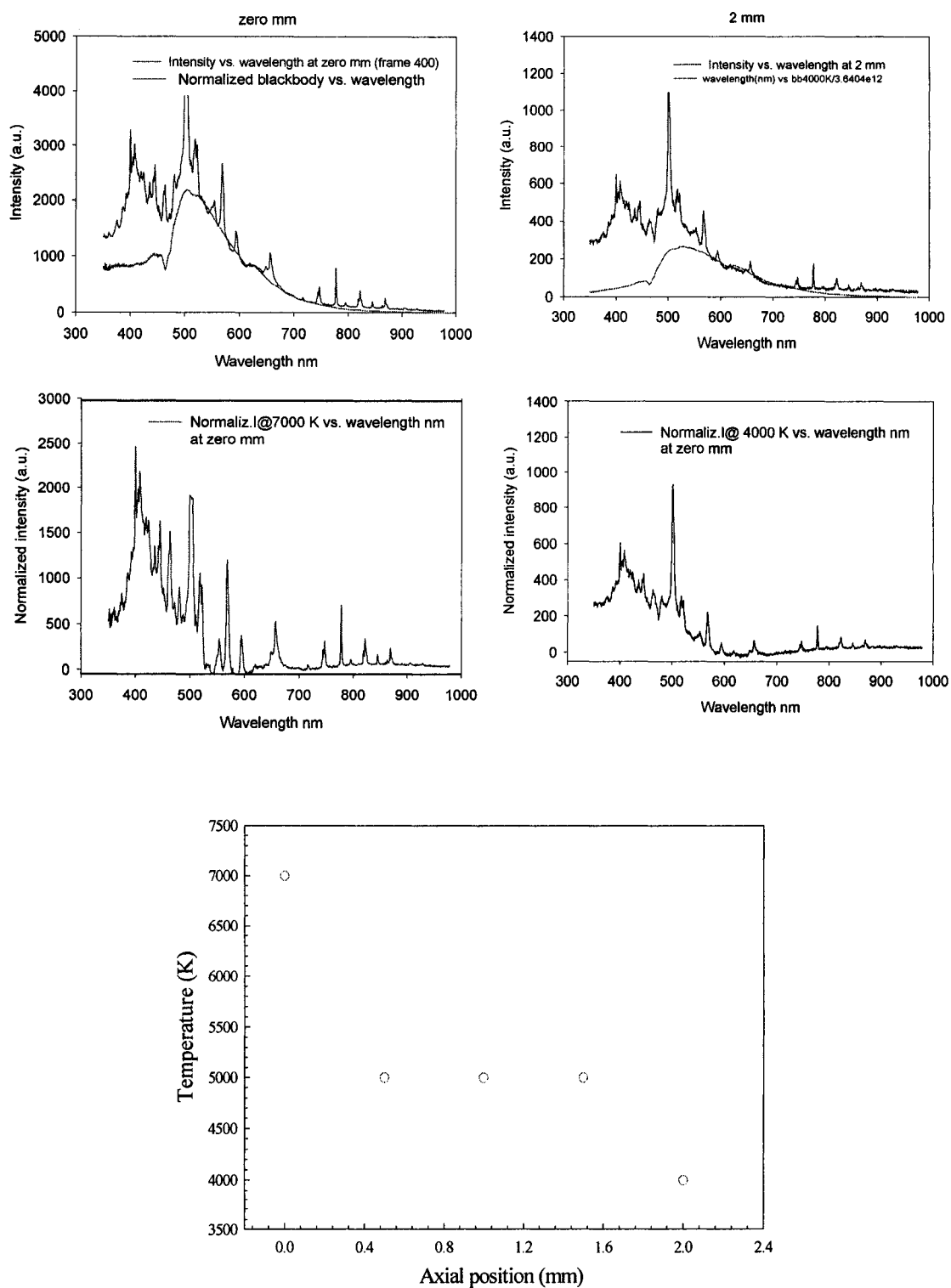


Fig. 4.21 Cu plasma temperature as a function of axial position measured from the sample surface. The error is estimated as 10% due to the uncertainty of the tabulated transition probabilities and the degeneracy and also due to the experimental errors.

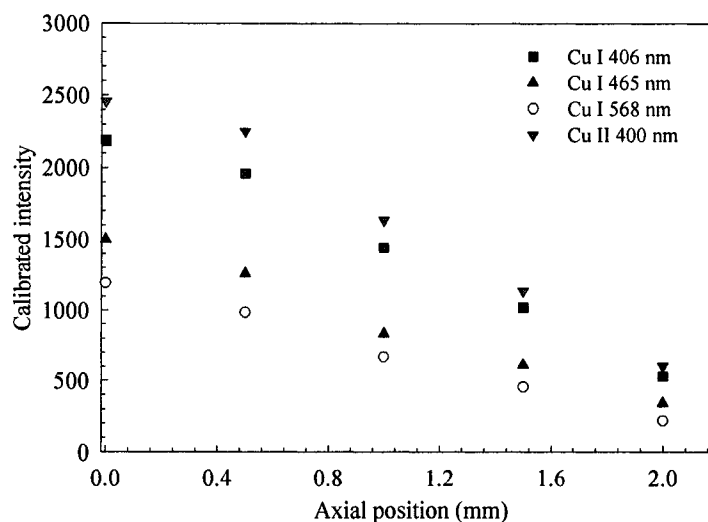


Fig. 4.22 Cu line emission as a function of axial position measured from the sample surface. The line intensity is linearly decreasing as increasing the axial distance away from the target in the direction of the laser beam.

As a continuation of the previous work, we studied the effects of several parameters, which affect LIBS measurements, such as ambient atmosphere and single pulse spectrum.

4.2.7 Pressure effect

Generally, the analysis at atmospheric pressure is characterized by the presence of a broadband background emission spectrum generated by atmospheric elements; therefore, many authors [20-22] preferred the use of a vacuum chamber and different ambient gases in order to obtain better signal-to-noise ratios. At low ambient pressure (<1 mbar), the ablated vapor can expand almost freely, and the outer part of the plasma becomes colder than the core because of the higher energy loss. When increasing the pressure to approximately 1 mbar, the confining effect of the vapor by the ambient causes a reduction in energy loss and a more uniform distribution. The decay rates at late times of the plasma lifetime were reduced, as a consequence of the confinement of the vapor plasma by the ambient gas, which prevents electrons or ion from rapidly escaping from

the observation point and facilitate the atomization of droplets and particles. With respect to the free expansion in vacuum, elastic and inelastic collisions occur between target vapor and ambient gas species. Thus, the plasma density decreases monotonically and, as an effect of inelastic collision, the kinetic energy is partially transformed in excitation energy.

The experimental setup used to obtain the effect of the pressure on the element spectrum is demonstrated in Fig. 4.23. It is noticed that when comparing the spectra at atmospheric pressure with that at reduced pressure the spectrum main feature is the low continuum background. As the pressure is reduced, the collision frequency is decreased leading to the decrease of the signal. On the other hand, as the material vapor is produced above the target surface, it produces a shock wave propagating towards the laser source; consequently, the plasma density is decreased resulting in the penetration of the laser beam to the target surface without any beam absorption loss. This produces the maximum mass ablation and hence, increases the signal (Fig. 4.24).

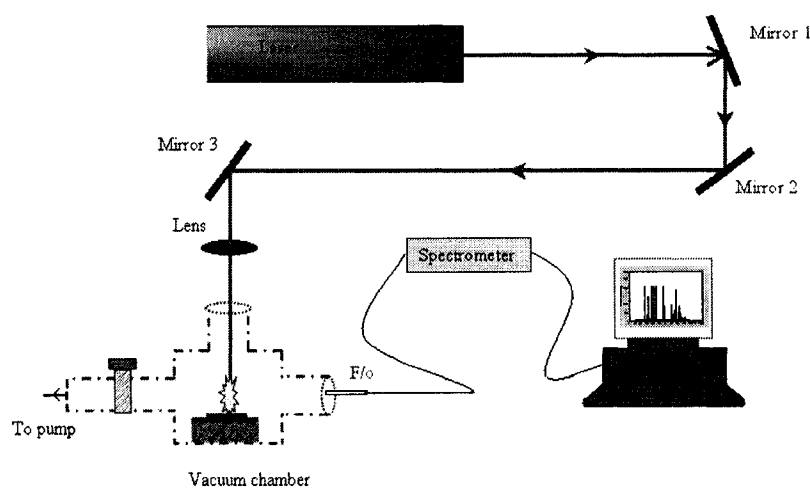


Fig. 4.23. Schematic diagram for the experimental setup for LIBS using a vacuum chamber.

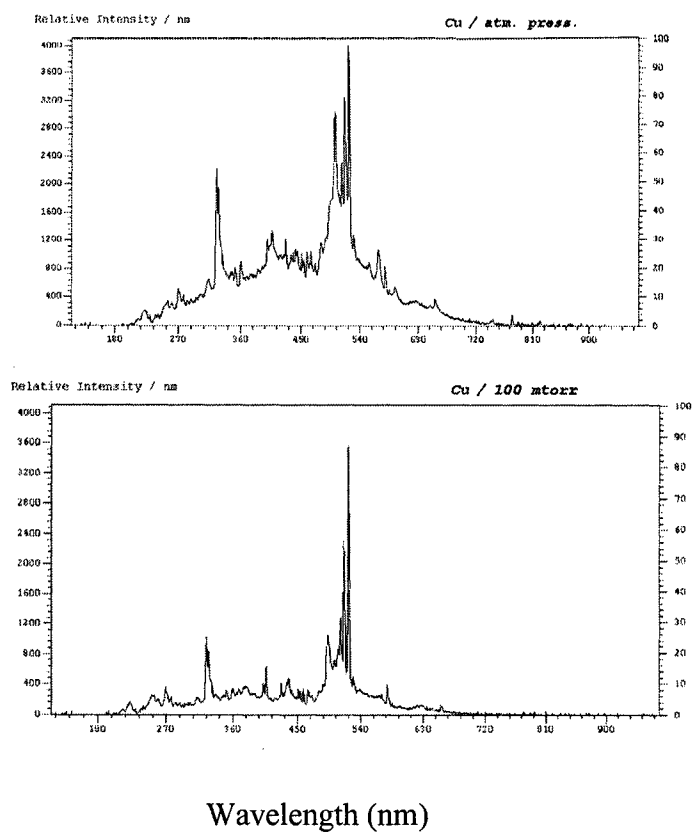


Fig. 4.24. Spectra of Cu, both at atmospheric pressure and ~ 100 mtorr.

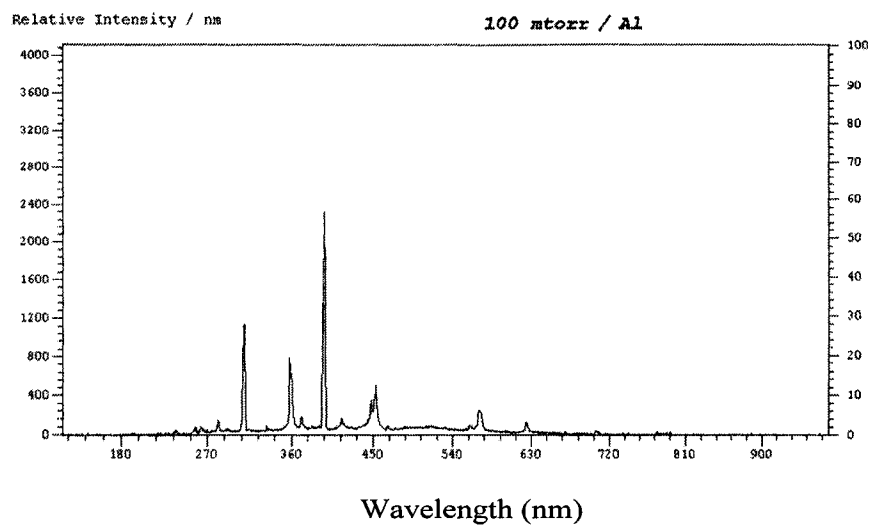


Fig. 4.25 Time-integrated spectrum of Al, at ~ 100 mtorr.

4.2.8 Single pulse spectrum

In order to increase the signal-to-background ratio, it is suggested that data acquisition is done for an accumulated number of laser shots [4]. In order to monitor the signal and the plasma in a more stable method, an average of the spectra resulting from an accumulated number of laser shots is applied to give a more reliable data. Multiple laser shot spectra could be stored by the SM32-Pro software, either as single frame or accumulation. When multiple LIBS spectra were stored as single frames, each individual spectrum, from a single shot, was stored within a file. When accumulation was selected, the multiple LIBS spectra were summed and stored as one spectrum. Using this mode, all the one-to-one shot fluctuations were lost. The single laser shot spectrum; Fig. 4.26 gives the same spectrum presented before for Cu but it is only a single laser shot spectrum. It is obvious that the signal to background (S/B) is relatively low.

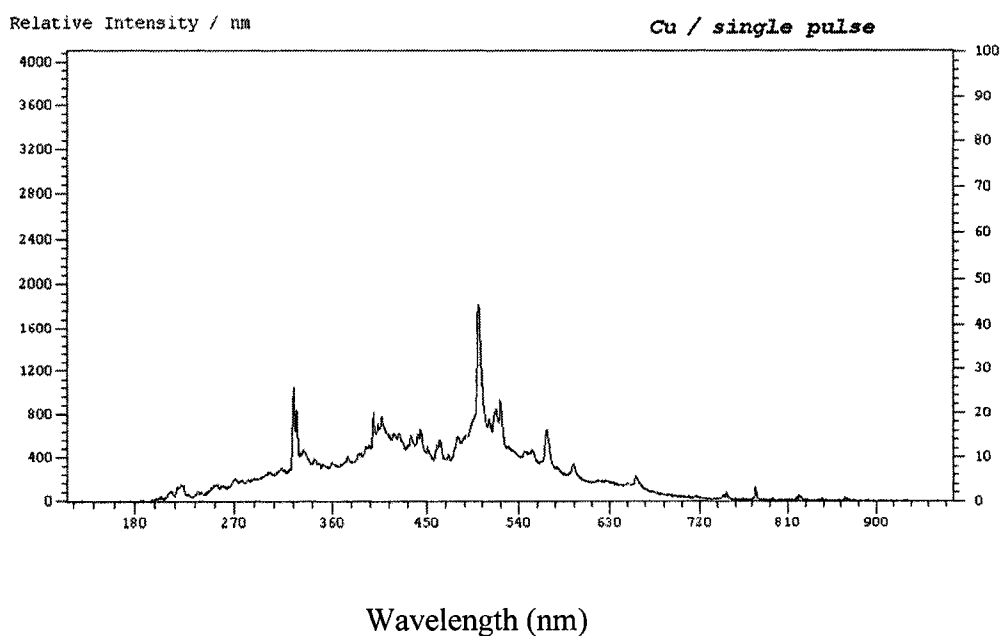


Fig. 4.26 Single pulse integrated spectrum of Cu in air.

4.3 Multi-element experiments

Using our setup, we were able to identify the different elements of the steel alloy with some constraints due to the limitation of the spectrometer used in our measurements. Thus, according to our available instrumentations, we were able to analyze steel alloy only qualitatively and consequently we had to direct our attention to focus our study on single and/or binary alloy samples.

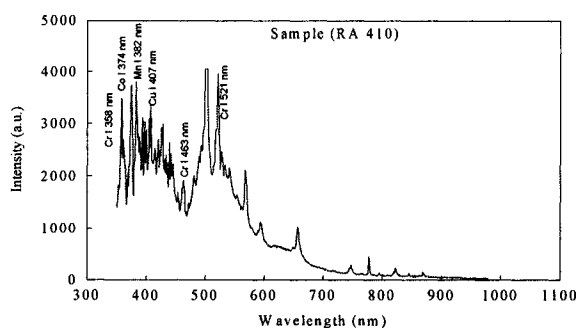


Fig. 4.27 Spectral line identification of Ni alloy.

4.4 Picosecond LIBS

The use of short laser pulses (on the order of picoseconds or shorter) has been recently applied to LIBS. They were reported to produce higher mass ablation rates, probably because they are not affected by the plasma shielding and also because the fraction of the pulse energy loss by thermal diffusion in the sample is much lower than in the case of nanosecond pulses [23]. For example, Rieger et al. [24] investigated the emission of laser-produced silicon and aluminum plasmas in the energy range from 0.1 to 100 mJ using 10 ns and 50 ps KrF laser pulses focused to a 5- μ m diameter spot. They showed that there is a little difference between 50 ps and 10 ns pulses in the plasma emission both in terms of the intensity of the emission lines and in terms of lifetime of the emission for energies higher than 3 mJ. Differences become important only at very

low fluences approaching the plasma formation threshold; this threshold is significantly lower for ps pulses. On the other hand, Eland et al. compared spectra of glass, steel, and copper using 570 nm, 1.3 ps and 1064 nm, 7 ns laser pulses. The background was low enough that excellent LIBS spectra were obtained using the 1.3 ps laser pulse and a non-gated detector. They presented the temperature dependence on the time after the laser pulse and showed that the electronic temperature is higher in the ps regime and consider this result is rather insignificant, since it is not likely that either plasma is at thermodynamic equilibrium.

We obtained the integrated spectra for the same elements used previously, using picosecond laser with high frequency (800 Hz), shown in Fig 4.28. A comparison between the ps laser and those of the ns laser results has been previously reported. It is obvious that the continuum background is less due to the shorter pulse duration and the high frequency of the picosecond laser used in this experiment. In both cases, nanosecond and picosecond lasers, the same setup shown in Fig. 4.6, was used.

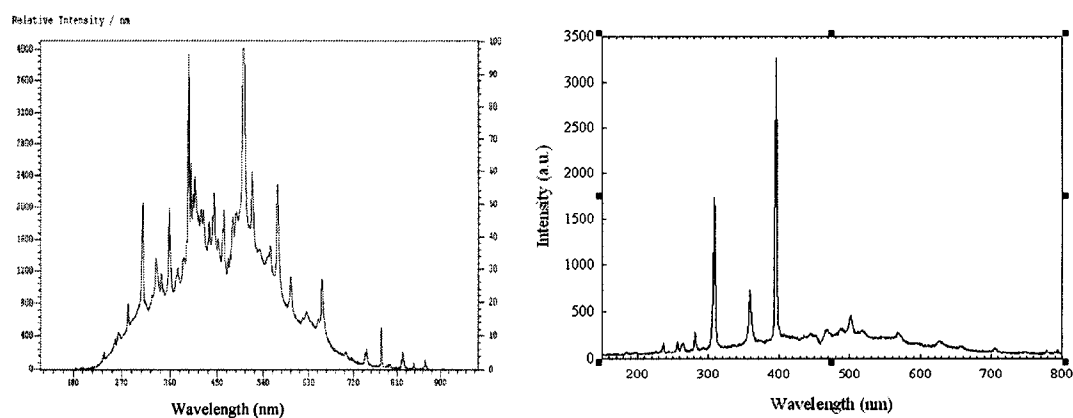


Fig. 4.28 Nanosecond (left) and picosecond (right) spectra resulting from a focused laser beam on Al sample. It is clear that using the picosecond laser with laser pulse power \sim 530 mW and 800 Hz. The high repetition rate and shorter pulse duration result in low background and high S/B ratio.

References of Chapter IV

- [1] Y. Lee, Y. J. Yoo, and J. Sneddon, "Recent advances in Laser-Induced Breakdown Spectrometry" *Spectroscopy* **13**, 14-21 (1998).
- [2] K. Song, H. Cha, J. Lee, L. S. Choi, and Y.I. Lee, "Determination of trace elements using Laser Induced Breakdown Spectroscopy (LIBS)," *J. Kor. Phys. Soc.* **30**, 463-468 (1997).
- [3] L. St-Onge, M. Sabsabi, and P. Cielo, "Quantitative analysis of additives in solid zinc alloys by laser-induced plasma spectrometry," *J. Anal. At. Spectrom.* **12**, 997-1004 (1997).
- [4] B. C. castle, K. Talabardon, B. W. Smith, and J. D. Winefordner, "Variables influencing the precision of Laser-Induced Breakdown Spectroscopy measurements," *Appl. Spectrosc.* **52**, 649-657 (1998).
- [5] R. Wisbrun, I. Schechter, R. Niessner, H. Schroeder, and K. L. Kompa, "Detector for trace elemental analysis of solid environmental samples by Laser Plasma Spectroscopy," *Anal. Chem.* **66**, 2964-2975 (1994).
- [6] G. Bekefi, C. Deutsch, and B. Yaakobi, In "*Spectroscopic diagnostics of laser plasmas*," in: G. Bekefi Ed., *Principles of Laser Plasmas*, Wiley Interscience, New York, (1994).
- [7] K. J. Grant and G. L. Paul, "Electron temperature and density profiles of excimer laser-induced plasmas," *Appl. Spectrosc.* **44**, 1349-1354 (1990).
- [8] B. Nemet and L. Kozma, "Time-resolved optical emission spectrometry of Q-switched Nd-YAG laser-induced plasmas from copper targets in air at atmospheric pressure," *Spectrochim. Acta B* **50**, 1869-1888 (1995).

- [9] A. Borghese and S. S. Merola, "Time-resolved spectral and spatial description of laser-induced breakdown in air as a pulsed, bright, and broadband ultraviolet-visible light source," *Appl. Opt.* **37**, 3977-398(1998).
- [10] J. Grees, P. A. Hilton, C. Y. Barlow, and W. M. Steen, "Spectroscopic studies of plume/plasma in different gas environments," *Proceedings of ICALEO*, (2001).
- [11] L. St-Onge, M. Sabsabi, and P. Cielo, "Quantitative analysis of additives in solid zinc alloys by laser-induced plasma spectrometry," *J. Anal. Atom. Spectr.* **12**, 997-1004 (1997).
- [12] S. Yalcin, D. R. Croley, G. P. Smith, and G. W. Faris, "Influence of ambient condition on the laser air spark," *Appl. Phys. B* **68**, 121-130 (1999).
- [13] M. Milan and J. J. Laserna, "Diagnostics of silicon plasmas produced by visible nanosecond laser ablation," *Spectrochim. Acta B* **56**, 275-288 (2001).
- [14] R. E. Russo, "Laser ablation," *Appl. Spectrosc.* **49**, 14A-28A (1995).
- [15] W. T. Chan and R. E. Russo, "Study of laser-material interactions using inductively coupled plasma-atomic emission spectrometry," *Spectrochim. Acta B* **46**, 1471-1486 (1991).
- [16] D. N. Stratis, K. L. Eland, and S. M. Angel, "Dual-pulse LIBS using a pre-ablation spark for enhanced ablation and emission," *Appl. Spectrosc.* **54**, 1270-1274 (2000).
- [17] NIST Electronic Database:http://physics.nist.gov/cgi-bin/AtData/lines_form.
- [18] M. Hemmerlin, R. Meilland, H. Falk, P. Wintjens, and L. Paulard, "Application of vacuum ultraviolet laser-induced breakdown spectrometry for steel analysis

- comparison with spark optical emission spectrometry figures of merit," *Spectrochim. Acta B* **56**, 661-669 (2001).
- [19] X. Mao, M. Shannon, A. Fernandez, and R. Russo, "Temperature and emission spatial profiles of laser-induced plasmas during ablation using time-integrated emission spectroscopy," *Appl. Spectrosc.* **49**, 1054-1062 (1995).
- [20] R. Wisbrun, I. Schechter, R. Niessner, H. Schroder, and K. Kompa, "Detector for trace elemental analysis of solid environmental samples by laser plasma spectroscopy," *Anal. Chem.* **66**, 2964-2975 (1994).
- [21] J. Hermann, C. B. Leborgne, and D. Hong, "Diagnostics of the early phase of an ultraviolet laser induced plasma by spectral line analysis considering self-absorption," *J. Appl. Phys.* **83**, 691-696 (1998).
- [22] T. L. Thiem, R. H. Salter, J. A. Gardner, Y. I. Lee, and J. Sneddon, "Quantitative simultaneous elemental determinations in alloys using Laser-Induced Breakdown Spectroscopy (LIBS) in an ultra-high vacuum," *Appl. Spectrosc.* **48**, 58-64 (1994)
- [23] X. L. Mao, A. C. Ciocan, O. V. Borisov, and R. E. Russo, "Laser ablation processes investigated using inductively coupled plasma-atomic emission spectroscopy (ICP-AES)," *Appl. Surf. Sci.* **127-129**, 262-268 (1998).
- [24] V. Margetic, A. Pakulev, A. Stockhaus, M. Bolshov, K. Niemax, and R. Hergenroder, "A comparison of nanosecond and femtosecond laser-induced plasma spectroscopy of brass samples," *Spectrochim. Acta B* **55**, 1771-1785 (2000).

CHAPTER V

SPARK DISCHARGE LASER INDUCED BREAKDOWN SPECTROSCOPY (SD-LIBS)

Laser Induced Breakdown Spectroscopy (LIBS) is combined with a spark discharge to operate in a laser triggered spark discharge mode. This spark discharge laser induced breakdown spectroscopy (SD-LIBS) is evaluated for Al and Cu targets in air under atmospheric pressure. Significant enhancement in the measured line intensities and the signal-to-background ratios, which depends on the spark discharge voltage and the laser fluence, is observed in SD-LIBS when compared to LIBS alone for similar laser conditions. The measured line intensities increase with the applied voltage for both targets, and the ratio of the measured line intensity using SD-LIBS to that using LIBS is found to increase as the laser fluence is decreased. For Al II 358.56, such intensity enhancement ratio increases from ~50 to ~400 as the laser fluence is decreased from 48 to 4 J/cm² at an applied voltage of 3.5 kV. Thus, SD-LIBS allows for using laser pulses with relatively low energy to ablate the studied material, causing less ablation, and, hence, less damage to its surface. Moreover, applying SD-LIBS gives up to 6-fold enhancement in the S/B ratio compared to those obtained with LIBS for the investigated spectral emission lines.

5.1 Introduction

Many conventional techniques of elemental analysis rely on the use of plasma discharges to excite the analyte. Then its composition can be identified and determined by atomic emission spectroscopy (AES) or by atomic absorption spectroscopy (AAS).

One of the AES-based techniques is Laser Induced Breakdown Spectroscopy (LIBS) in which a laser pulse ablates a sample while the spectral emission from the laser-induced plasma is recorded and analyzed. The main advantage of this technique is the large number of samples that can be processed in a short time with minimal sample preparation [1,2]. With an automated LIBS system, it could take only a few seconds to obtain the elemental composition of a sample. While other plasma-based techniques tend to have better accuracy, precision, limit of detection, and dynamic range than LIBS, most require extensive sample preparation, and some of them are limited to certain sample types [3]. On the other hand, LIBS has the ability to study any sample type including non-conducting samples, liquids, droplets, and aerosols [4]. Also, its ability to map the surface and depth composition, in addition to the fast output and relative ease of operation, are important features that make it suitable for industrial settings and environmental and quality control operations [5]. Comparisons of different elemental analytical techniques were previously given by several authors [6-10].

The main shortcomings of LIBS are the limitation on the quantitative measurement due to insufficient sensitivity, matrix effects, and self-absorption [11-13]. The limited sensitivity arises from the characteristic continuum emission, which is non-element specific and acts to reduce the signal-to-background ratio (S/B). Several approaches were implemented to overcome the LIBS insufficient sensitivity by enhancing the S/B ratio, which can advance the use of simple, compact, and inexpensive spectrometers in field applications. Moreover, a reduction of the needed laser pulse energy, while maintaining an acceptable signal and S/B ratio, would allow for the use of compact lasers for LIBS leading to the development of a system that can be readily

deployed in industrial and environmental applications. Since the continuum emission decays at a faster rate than the line emission, the use of sophisticated gated optical spectrometers was suggested to obtain satisfactory S/B ratios after some delay from the laser pulse [14]. Other approaches to increase S/B ratio based on combining different analytical techniques were investigated by different groups [6,15]. For example, laser ablation has been coupled with additional excitation sources, such as inductively coupled plasma, microwave induced plasma, and hollow cathode discharge [16-18]. Improved precision and dynamic range have been obtained compared to simply using LIBS. However, a carrier gas, e.g. argon, is needed to transport the ablated sample to an additional excitation chamber, which adds to the size and complexity of these techniques.

In this work, we re-configure an approach, previously introduced by several authors [6,15], in which a spark discharge is combined with LIBS, with no requirement of a gas transport or a vacuum system. This approach is based on a laser-triggered spark gap in which a Q-switched laser beam is focused onto the sample placed either behind or in a mid-plane point between two spark discharge electrodes. The SD-LIBS is triggered by the plasma formed from the laser-ablated target. The spark discharge provides a low-cost analytical approach that enhances the emission line signal with better S/B ratio and allows for significant reduction of the required laser pulse energy and consequently less sample surface damage. The results for Al and Cu targets obtained using SD-LIBS are discussed and compared to those obtained using LIBS.

5.2 Experiment

The SD-LIBS experiment is performed in an atmospheric pressure environment without any special gas transport or vacuum preparations. A Q-switched Nd:YAG pulsed

laser (Lumonics YM-200), ~20 ns FWHM, operating at its fundamental wavelength, 1064 nm, is used to ablate the surface of the sample and to produce plasma between the two electrodes of a spark gap. A lens with 15-cm focal length is used to focus the laser beam on the surface of the sample to a spot size ~300 μm , as measured with the sharp edge method. The laser-induced plasma of the ablated target then triggers the spark gap. When the SD-LIBS is used, the laser is operated in a single pulse mode. For signal accumulation in LIBS operated without the discharge, we sometimes operated the laser at a repetition rate of 50 Hz for 200 ms to accumulate 10 pulses.

The spark gap consists of two 99.95% tungsten cylindrical rods of 3.175 mm diameter placed 2.2 mm apart with their axis parallel to the surface of the sample and located ~3.6 mm away from it as shown in Fig. 5.1 One of the tungsten electrodes is connected to a 0.25 μF capacitor through a 500 k Ω current-limiting resistor. The other electrode is grounded through a 2.5 m wire that provides some additional inductance in the circuit. The voltage difference between the two electrodes is maintained by using a high voltage dc power supply, which provides up to 10 kV. Upon the application of the laser pulse, a time-damped spark, synchronized with the pre-existing laser ablated plasma, produces an oscillating discharge voltage, which is measured using a high voltage probe. The spark discharge can occur without laser triggering when the gap breakdown voltage is applied, which depends on the gap distance [19]. Irradiating the sample surface with the laser beam reduces the voltage needed for breakdown, and the breakdown voltage can be as low as 0.5 kV. A grounded metal shield around the discharge is used to limit both the electric noise and the airflow near the gap.

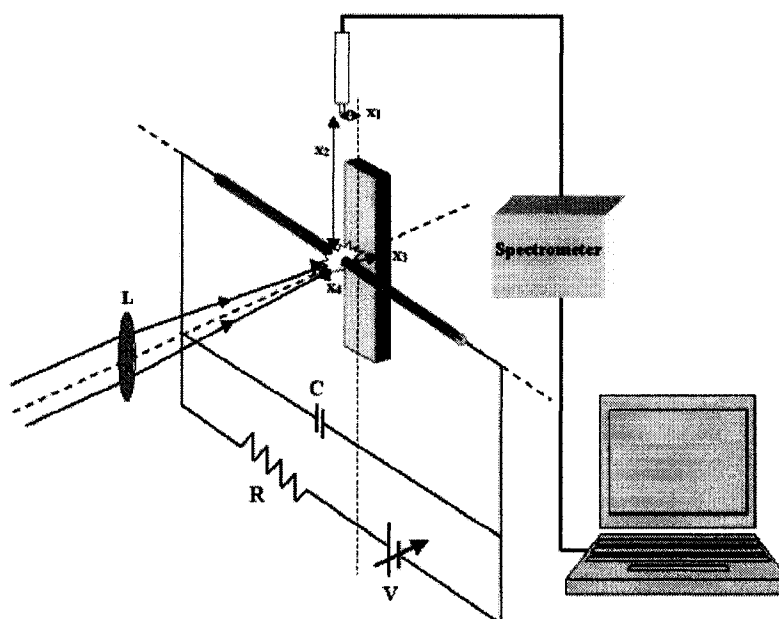


Fig. 5.1 The experimental setup used for LIBS and spark discharge assisted LIBS (SD-LIBS). A Q-switched Nd:YAG laser beam is focused on the target surface by a 15-cm focal length lens to form LIBS plasma between the two tungsten electrodes. Two modes of operations are compared; conventional LIBS (when no voltage is applied between the two electrodes; $V = 0$) and SD-LIBS (with applied voltage V). ($x_1 = 2.5$ mm, $x_2 = 37$ mm, $x_3 = 3.6$ mm, $x_4 = 2.2$ mm)

The sample is placed such that the laser-generated plume expands in the gap between the two electrodes. The voltage across the spark gap is raised below the spark gap self-breakdown voltage. The focused laser beam ablates the surface of the target generating plasma that expands between the spark gap electrodes. Thus, the laser-induced plasma triggers the spark gap causing significant energy (up to several joules) to be deposited in the plasma containing the analyte, and subsequently produces a spark discharge. Two operation modes are compared: conventional LIBS, with no applied voltage, and SD-LIBS with different applied voltages, obtained using the same experimental setup shown in Fig. 5.1. The integrated emission of the formed plasma is directly transferred, without an imaging lens, to a spectrometer (CVI model SM240, 600 grooves mm^{-1} grating, spectral range 200-978 nm with a reciprocal linear dispersion of $\sim 1 \text{ nm mm}^{-1}$) using a 2-

m long, 0.6 mm in diameter fiber optic bundle. Since the expansion of the plasma is strongly confined by the surrounding air, the emitting region is localized to approximately 3 mm above the sample surface [20]. Thus, the fiber bundle is vertically positioned normal to the laser beam with its axis displaced ~ 2.5 mm from the surface of the sample and its input surface placed ~ 37 mm away from the produced plasma. Such a position is chosen far enough from the LIBS plasma to obtain spatially integrated spectra from the plasma. Also, for SD-LIBS, this distance reduces the signal enough to avoid the saturation of the detector. All measurements are taken at this fixed position of the fiber optic. The data is then collected, saved, and analyzed using a personal computer. To obtain the temporal development of emission lines for both LIBS and SD-LIBS, a monochromator ($1440 \text{ grooves mm}^{-1}$ grating, slit width $100 \text{ }\mu\text{m}$) is used. The signal is collected by a built-in lens inside the monochromator placed ~ 150 mm away from the plasma and then detected using a photomultiplier (PMT) connected to a 300 MHz digital sampling oscilloscope for data acquisition. The studied samples are placed on a manual vertical translational stage in order to expose a fresh spot for each measurement. Results for a 99.99% pure Al and oxygen-free high conductivity (OFHC) 99.95% Cu samples are discussed.

5.3 Results and discussion

In the SD-LIBS, the plasma containing the analyte under test is formed in the laser ablation process. The initial formed plasma expands within the space between the spark electrodes through electron avalanche driven by the high electric field. The plasma produced by LIBS supplies the spark gap with sufficient electrons; therefore, the breakdown occurs at voltages less than the self-breakdown voltage of the gap. The spark

discharge expands by further avalanching and convection from an inner radial point to an outer radial point [21]. The plasma is confined within a high-density shell of neutral gas that traps ionizing radiation in a region of low E/N (electric field divided by gas density), thereby inhibiting further expansion by non-hydrodynamic means (electron avalanche). The electric circuit behavior in SD-LIBS, plasma emission, and plasma characterization for both LIBS and SD-LIBS are discussed in the following sections. Finally, we show that because SD-LIBS increases the signal and S/B ratio of atomic and ionic lines, allows for the use of low laser energies, and requires less ablation rate and hence less surface damage occurs.

5.3.1 Electric circuit characteristics

The analytical performance of the SD-LIBS is strongly dependent on the electric circuit parameters. Previously, the spark discharge was modeled as a combination of time-dependent resistance and inductance in series [22-24]. Experimentally, the properties of the spark discharge depend on the circuit inductance, gas type, gas pressure, and the gap distance [19,22]. In our experiment, the observed fluctuating temporal behavior of the discharge voltage and current, as shown in Fig. 5.2(a), suggests that the circuit is characterized by a high induction throughout the discharge. The 3.5-kV applied voltage across the two electrodes exhibits a sudden decay, in a fraction of a microsecond, due to the spark discharge. It is then sustained for $\sim 60 \mu\text{s}$, oscillating around zero voltage with maximum amplitude of $\sim 500 \text{ V}$ due to the presence of plasma. Furthermore, the measured current shows a damped oscillating behavior with an absolute maximum of $\sim 300 \text{ A}$. Fig. 5.2(b) shows that the integrated light emission intensity is directly affected by the change in the deposited electric power [25]. The emission signal is dependent on

the energy stored in the capacitor, the electric circuit parameters, and the electrode geometry. This behavior was also observed by Bredice *et al.*, who studied the breakdown characteristics of a solid target placed between two plates of a planar charged capacitor [26]. The peak power that resulted from our setup was ~ 170 W, which decays to 50 W in 4 μs , then oscillates while diminishing with time (Fig. 5.2(b)). In a previous study, a discharge peak power of 2-3 kW, lasting for a time period of 10 μs , was used during the detection of Cu emission lines [27].

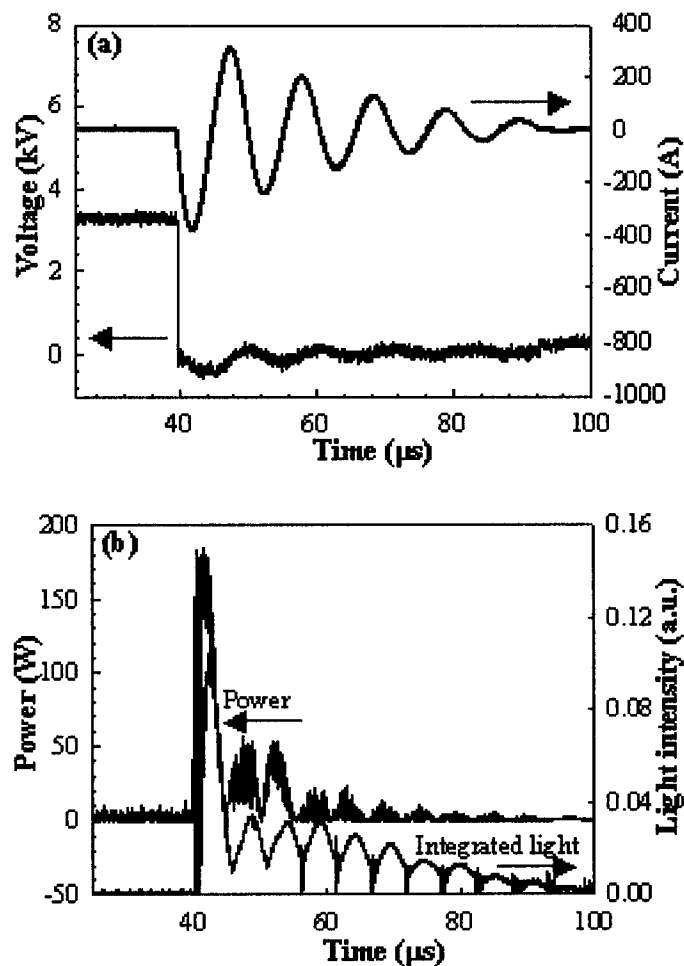


Fig. 5.2 (a) The temporal shape of the discharge voltage and current; (b) the time evolution of the deposited electric power in the plasma and the emitted integrated light intensity for a laser fluence of 48 J/cm^2 and an applied voltage of 3.25 kV.

5.3.2 Plasma emission

When LIBS is operated in air at atmospheric pressure, there are spectral ranges where the plasma emission lines are closely overlapped by spectral lines of air components. Because of the limited resolution of our spectrometer (~ 1 nm), it becomes important to avoid including in the analysis lines due to air constituents or tungsten lines arising from any possible erosion of the electrodes that might overlap with lines from the sample. To assure that no lines due to air constituents are interfering with those of the analyte, a small vacuum system operating at ~ 50 mTorr is initially used to obtain the LIBS spectra of the studied samples and of the tungsten electrode material. The obtained spectra (Fig. 5.3 a, c and e) are then compared to those obtained at atmospheric pressure (Fig. 5.3 b, d and f). For the Al and Cu samples, only the intense and well-isolated strong plasma emission lines are included in our analysis. Based on this, we identified that the Al 281.61, 309.27 and 358.65 nm lines and Cu 324.75, 327.39, 510.55, 515.32, and 521.82 nm lines are not overlapping with lines due to air constituents or W lines that could come from potential erosion of the electrodes during the spark.

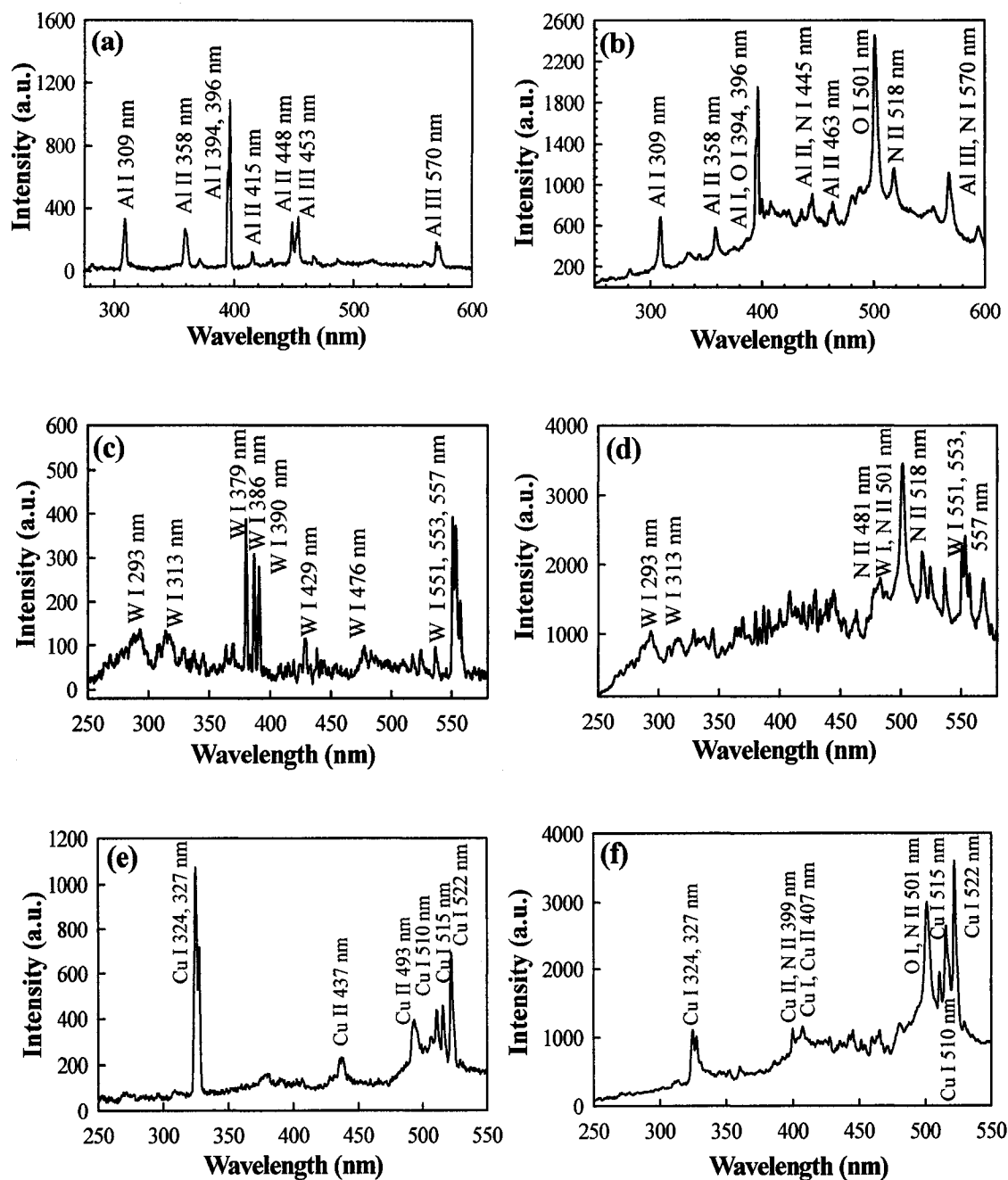


Fig. 5.3 The integrated spectra for Al, W and Cu under a background of partial vacuum of 50 mTorr (a, c, e) and at atmospheric pressure (b, d, f). These spectra are used to determine the spectral lines of Al and Cu that do not overlap with possible lines from either air constituents or the W electrode.

Time integrated spectra of Al, without introducing any delay from the laser pulse, are recorded. Single laser pulses of pulse energy in the range of 3-34 mJ were used in both LIBS and SD-LIBS. The applied voltage of 3.5 kV used in SD-LIBS is below the self-breakdown voltage of air at atmospheric pressure, which is ~ 7 kV in our case ($\sim 3 \times 10^6$ V/m [14]). A comparison of the Al spectra obtained using these two modes of operation at laser fluences of 4 and 48 J/cm² are shown in Fig. 5.4(a) and 5.4(b). Using only conventional LIBS gives weak line signals, especially at low laser fluences, compared to those obtained with the SD-LIBS. When operating in the SD-LIBS mode, using a laser fluence of 48 J/cm², acts to enhance the aluminum line intensities, with respect to those obtained by LIBS, by factors of ~ 35 , 15, 50 for Al 281.61 nm, Al I 309.27 nm, and Al II 358.65 nm, respectively. While for a lower laser fluence of 4 J/cm², operation in SD-LIBS mode causes an increase in line intensities by ~ 150 times for the Al II 281.61 nm and Al I 309.27 nm lines and ~ 400 times for the Al II 358.65 nm line. Thus, applying SD-LIBS with lower laser fluences introduces higher enhancements since the energy deposited in the spark discharge is basically independent of that laser fluence and is dependent on the energy stored in the capacitor (C in Fig. 5.1) Thus, using SD-LIBS becomes more attractive when small laser pulse energies are available, such as would be the case in a compact mobile system. However, since the amount of ablated material depends on the laser pulse energy, sufficient energy needs to be available to ablate enough analyte into the spark discharge. Applying SD-LIBS to Cu samples, the emitted spectrum, obtained using a single laser pulse with a fluence of 20 J/cm² and an applied voltage of 3 kV, is shown in Fig. 5.4(c). This SD-LIBS spectrum is compared to a LIBS spectrum obtained with fifty accumulated laser pulses of the same laser fluence.

Improvements of ~80, 65, 800, 600 and 500 times are observed for the spectral emission lines of Cu at 324.75, 327.39, 510.55, 515.32 and 521.82 nm, respectively. It is clear that in the case of SD-LIBS, the additional source of electrical energy stored in the capacitor, which is in the range of several joules, increases the rate of collisional processes leading to improvement in the spectral emission intensity of the analyte signal when compared to the use of laser alone.

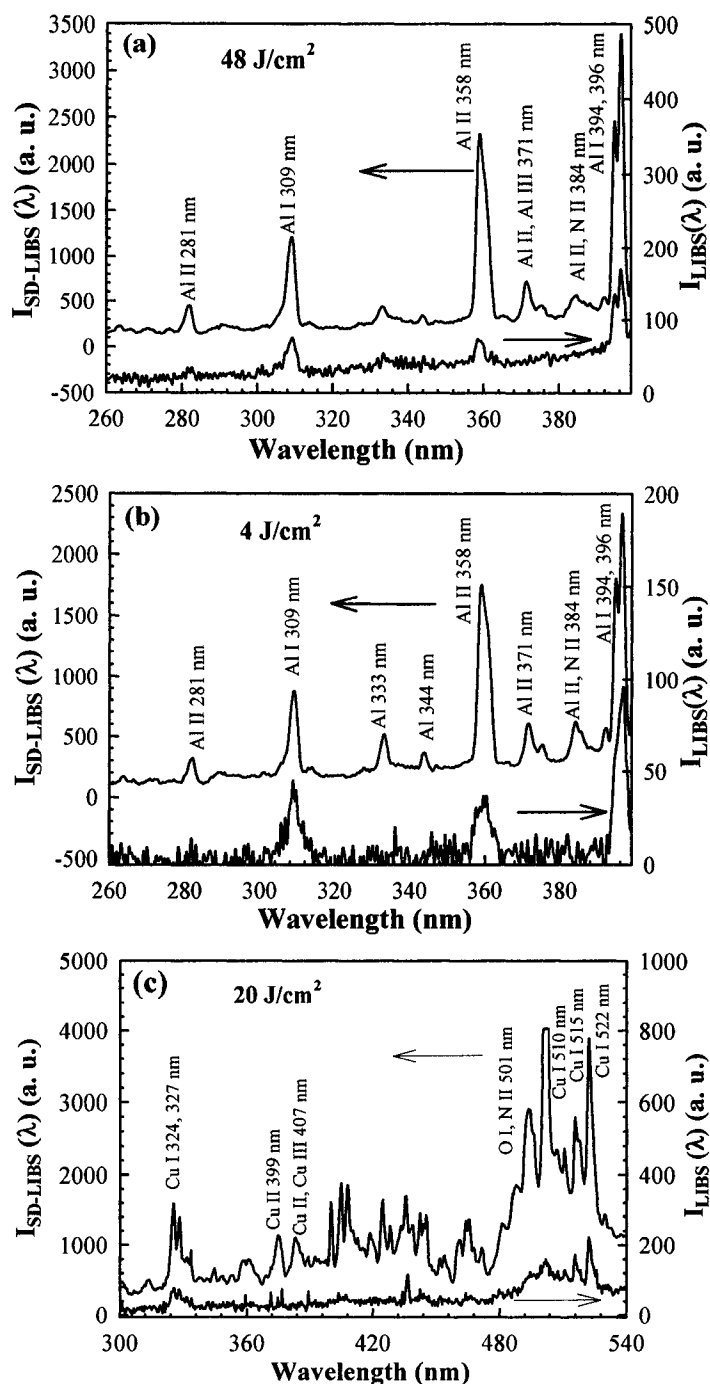


Fig. 5.4 Al spectral lines Al II 281, Al I 309, Al II 358, Al I 394, and Al I 396 nm observed in conventional LIBS (I_{LIBS}) and spark discharge assisted LIBS with an applied voltage of 3.25 kV ($I_{SD-LIBS}$); (a) laser fluence of 48 J/cm², with each spectrum obtained with a single laser pulse; (b) laser fluence of 4 J/cm², with $I_{SD-LIBS}$ is taken with one pulse while I_{LIBS} spectrum is a result of accumulation of 10 pulses (c) Cu spectral lines Cu I 324, 327, 510, 515 and 521 nm obtained by accumulating 50 spectra each with a laser fluence of 20 J/cm² laser pulses in case of LIBS and a single 20 J/cm² laser pulse with 3 kV applied voltage in case of the SD-LIBS.

Figure 5.5 shows the Al line intensity as a function of the applied voltage for the laser fluences of 4 and 48 J/cm², respectively. With the increase in the electrode potential, an increase in the line intensity is observed due to the increase in the energy deposited in the spark discharge. Increased energy deposition in the spark discharge affects both the plasma density and the plasma effective electron temperature, which depends on the reduced electric field E/N [28,29]. Although, the ablated material is increased at the high laser fluence, their transient time in the spark discharge is reduced because of the expected increase of the plume speed with the increased laser fluence [30]. The reduction of the plume transient time in the discharge limits the increase in the line intensity at high laser fluences. Thus, the observed signal is not linear with the amount of ablated plume. The effect of plume transient time in the auxiliary discharge was noted previously [6,31]. The signal dependence on the laser fluence and applied voltage is complicated by the dependence of plume speed on laser fluence, distance of sample from the spark discharge electrodes, and ambient conditions. Moreover, the complex interaction of the spark discharge filaments with the laser ablated plume could also repel part of that plume causing a reduction of the signal that is dependent on many parameters, such as the laser fluence and spark discharge conditions [6]. Optimization of plume coupling to the spark discharge can be accomplished by external timing of the laser pulse and the discharge triggering time and by varying the electrode configuration and distance from sample [6]. This signal dependence on plume coupling to the spark discharge does not prevent SD-LIBS from being used for quantitative studies, as long as the laser and spark conditions remain unchanged for the studied sample and the calibration reference [6].

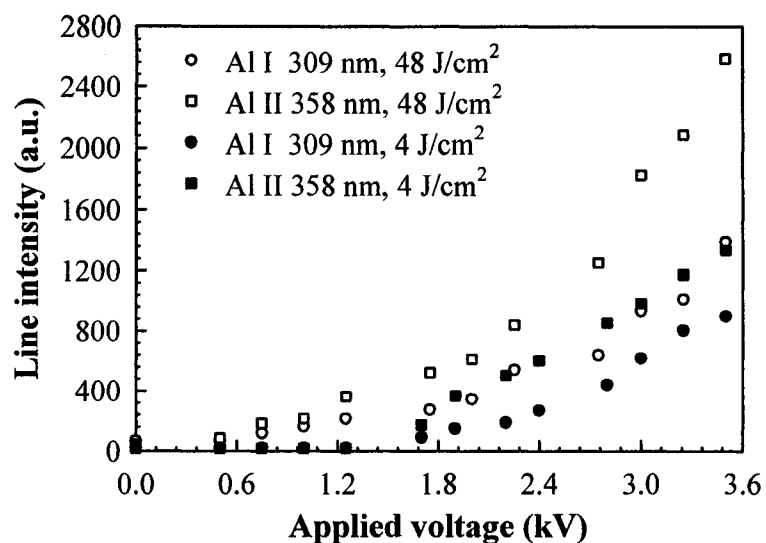


Fig. 5.5 Intensity of the Al spectral emission lines Al I 309 and Al II 358 nm as a function of the applied voltage (Laser fluence $\sim 4 \text{ J/cm}^2$ and $\sim 48 \text{ J/cm}^2$). All lines follow the same trend of increase in their intensity as a result of the applied voltage.

The S/B ratio affects the performance of an analytical technique, particularly when measuring near the limits of detection [32]. Due to the high characteristic continuum background of LIBS, significant efforts have been made to increase the ratio of line emission, which is element specific, to that of the broad background, which contains no elemental information and constitutes noise. The enhancement of such ratio can be obtained by several approaches. The most widely used approach is based on the observation that the background emission decays faster than the line emission [33-34]. Using a gated spectrometer to observe the plume a few microseconds after ablation, the S/B ratio is typically maximized. This approach, however, requires the use of expensive spectrometers and adds significantly to the size of the experimental setup. Another approach is based on the confinement and the thermal insulation of the plasma plume by containing the sample in an environmentally controlled chamber, either in vacuum or in a background of a noble gas [35,36]. This approach again adds to the size and complexity

of the technique. It was recently demonstrated that a satisfactory S/B ratio is achieved for relatively low laser pulse energies, without the need of the gated detection, for nanosecond, picosecond, and femtosecond laser ablation [37]. The continuum radiation intensity is mainly controlled by the laser energy [28], not the pulse duration as previously reported [38].

In the current work, we demonstrate that employing SD-LIBS improves the S/B ratio compared to LIBS operated at the same laser and background conditions. Figure 6 shows the variation of the S/B ratio of both Al I 309.27 and Al II 358.65 as a function of the capacitor voltage in SD-LIBS. The threshold voltage after which enhancement of the signal and the S/B ratio takes place, apparent in Fig. 5.5 and Fig. 5.6, is due to the applied voltage threshold for breakdown to initiate the spark discharge. This breakdown voltage depends on the laser fluence used to ablate the target. Thus, the spark discharge occurred at 1.5 kV for 4 J/cm² and 0.5 kV for 48 J/cm². In obtaining the S/B ratio, the background value is determined by taking the minimum background along 40 pixels (~16 nm) in interference free region near the peak of the spectral line of interest. For Al, the atomic emission lines of interest are in the ultraviolet (UV) part of the spectra in which the background from either the Bremsstrahlung or the recombination processes is low compared to the visible and near-infrared parts of the spectra [39]. Tungsten electrodes were chosen due to its low sputter rate, which ensures low probability of tungsten spectral line emission. Figure 5.6 shows that in conventional LIBS (applied voltage = 0 V) lower S/B ratios for the Al 309.27 and 358.65 nm lines are obtained for the lower laser fluence (4 J/cm²). This is consistent with previous observations of the dependence of S/B ratio on the laser pulse energy [37]. Operation in the SD-LIBS mode yields S/B

values that increase with the applied voltage for both laser fluences. Using SD-LIBS gives up to 6-fold enhancement in the S/B ratio compared to those obtained with LIBS for the atomic line, Al I 309.27, and the ionic line, Al II 358.65 nm. The more energy provided to the plasma by the spark discharge compared to the laser pulse, the better enhancement in the S/B ratio for the experimental conditions studied. This is due to the reduced continuum emission in the spark discharge compared to laser-produced plasma. A related observation was made by Rai et al., who combined LIBS with a magnetic field [29] and noted that the increase in the optical line emission was absent when the plasma was dominated by continuum emission as a result of high laser energy. Also, application of a uniform electric field enhanced line intensities enabling identification of the highly congested emission lines in the spectra, in addition to enhancing S/B ratio [26,28,40].

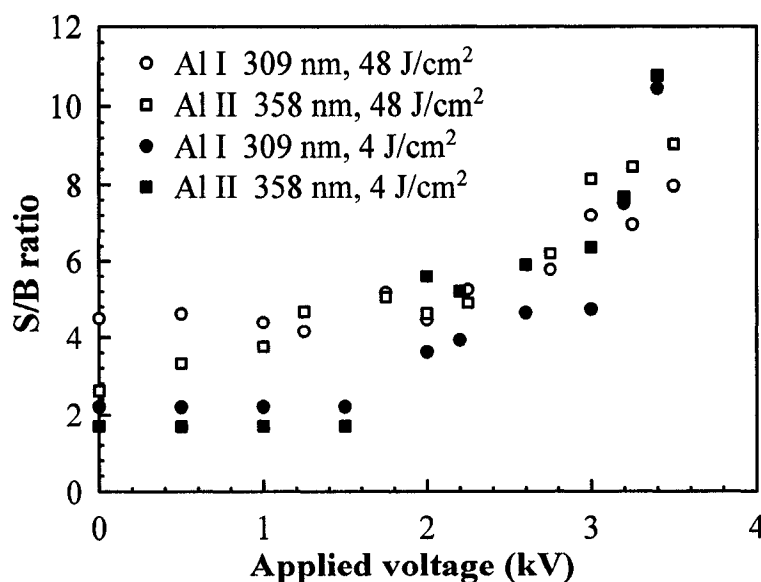


Fig. 5.6 Signal-to-background ratio S/B of Al spectral emission lines Al I 309 and Al II 358 nm as a function of the applied voltage (Laser fluence ~ 4 and ~ 48 J/cm²). Up to 6-fold enhancement in the S/B ratio is obtained for both laser fluences compared to those obtained with conventional LIBS.

The temporal evolution of spectral emission lines is element and atomic energy level specific. Fig. 5.6 shows the intensity of the Al I 309.27 and Al II 358.65 nm for LIBS and SD-LIBS in which each measurement corresponds to the sum of plasma emission of 10 laser pulses for both cases. The temporal shift between the two Al lines in LIBS and SD-LIBS is made to better show the temporal development of each line. Using LIBS, the ionic emission line, Al 358.65 nm, showed a faster decay profile compared to the neutral line, Al 309.27 nm, Fig. 5.6(a), which is affected by the temperature decay of LIBS plasmas. In SD-LIBS, the Al spectral lines decay time is considerably longer, with about the same peak intensity, as shown in Fig. 5.6(b). Generally, the temporal profile of line emission depends on the dynamics of atomic and ionic emission, which could be described by the post-atomization and ionization of the ablated species in the hot plume, followed by the recombination and emission of the excited neutral atoms at later stages of the plasma evolution. The fluctuating behavior of SD-LIBS temporal line profiles, particularly the ionic line Al 358.65 nm, is strongly dependent on the circuit parameters and the inductance of the spark, which is time-dependent [22]. Thus, the increase in the intensity of line emission in SD-LIBS detected by the spectrometer is due to the increased emission time rather than peak intensity.

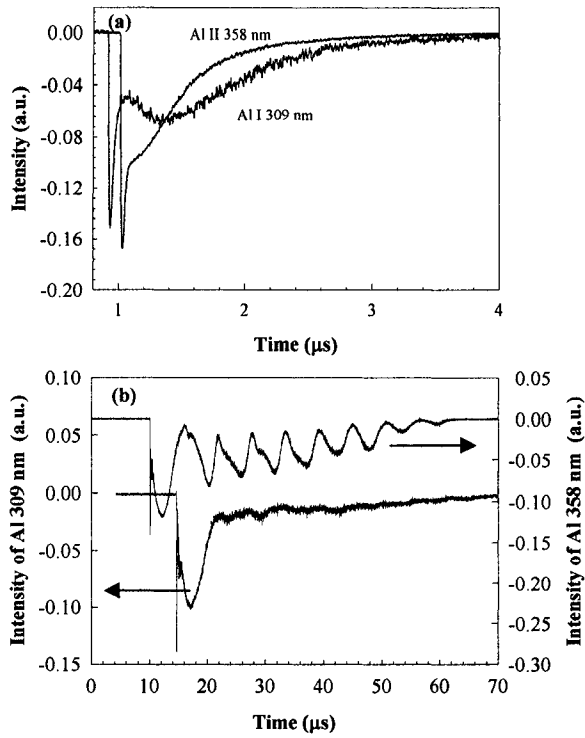


Fig. 5.7 Comparison of the Al time profile spectral lines Al II 358 nm and Al I 309 nm using both LIBS (a) and SD-LIBS (b) with 48 J/cm^2 laser fluence and 2 kV-applied voltage.

5.3.3 Plasma characterization

One of the spectroscopic techniques used for determining the plasma temperature is the line emission intensity analysis, provided that the plasma is in local thermodynamic equilibrium (LTE) and is applicable in cases of plasmas in LIBS and spark discharge [41,42]. The excitation temperature T can be determined using:

$$T = \frac{E_2 - E_1}{k} \left[\ln \left(\frac{I_1 \lambda_1 g_2 A_2}{I_2 \lambda_2 g_1 A_1} \right) \right]^{-1} \quad (1)$$

where E_1 and E_2 are energies of upper transition levels of two lines belonging to the same atomic species, I_1 and I_2 are the line intensity of the two lines, A_1 , g_1 and λ_1 are transition probability, degeneracy, and wavelength, respectively, of one spectral line, whereas A_2 ,

g_2 and λ_2 correspond to the same quantities for the other emission line of the same species, and K is Boltzmann's constant. The excitation temperature is calculated using Cu atomic lines Cu I 510.55, Cu I 515.32, and Cu I 521.82 nm at a delay of 1 μs and 4 μs after the laser pulse for LIBS and SD-LIBS, respectively. Table 1 includes the spectroscopic parameters for Cu atomic emission lines, obtained from Refs. [43] and [44]. Figure 5.7 shows that the excitation temperature exhibits a fast decay from ~ 9500 k to ~ 6000 k in both modes of operation at 10 μs and 60 μs after the laser pulse for both LIBS and SD-LIBS, respectively. The decay in plasma temperature is due to the expanding and cooling of the produced plasma with time. The deposition of energy stored in the capacitor, in the case of SD-LIBS, gives rise to the creation of plasma that lasts for a longer time and has a larger volume compared to the LIBS plasma. The temperature calculation method is accompanied by large systematic errors due to uncertainty in the transition probabilities A_1 and A_2 , which are sometimes known only within 50% accuracy [38].

Table 1. Cu spectroscopic parameters used for the determination of plasma temperature.

Wavelength (nm)	E (cm^{-1})	g_i-g_k	A (10^8 s^{-1})
510	30783.7	6-4	0.02
515	49935.2	2-4	0.6
521	49942.1	4-6	0.75

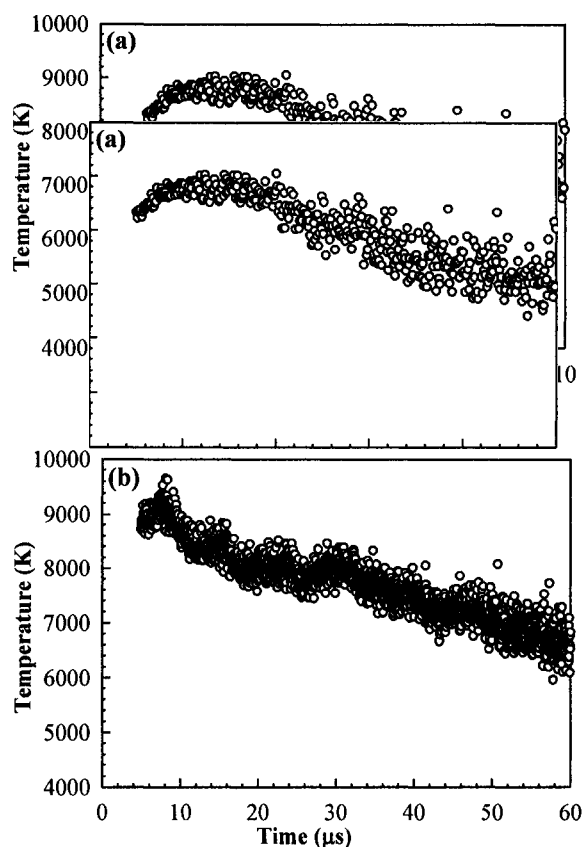


Fig. 5.8 The time resolved temperature of (a) conventional LIBS; and (b) spark discharge assisted LIBS (SD-LIBS) using 8-averaged scans of Cu I 510, Cu I 515 and Cu I 521 nm (Applied voltage = 3 kV and laser fluence of 48 J/cm^2).

For electron density measurements, the Stark broadening profile of an isolated atom or singly charged ion is the most commonly used technique [41]. However, due to the limited spectral resolution of the spectrometer used, it was not possible to apply this technique in the present work. In SD-LIBS, the primary radiation emerging from the initial laser plume could be neglected in comparison with the one produced by the additional excitation from the spark discharge. Thus, the spectral characteristics are mainly determined by the parameters of the spark [6]. Therefore, the electric circuit parameters were used to estimate the average value of the electron density, n_e , within the

plasma [45]. Using the measured values of the applied electric field, E , and the current density, j , one can use Ohm's law to calculate n_e , such that:

$$n_e = j / E \mu_e e \quad (2)$$

where μ_e is the electron mobility which is a function of pressure, field strength, and plasma temperature. At constant gas density and applied field, the electron mobility can be related to the plasma temperature by [46]:

$$\mu_e p = CT^\beta, \quad (3)$$

where C is a constant that depends on the electric field and pressure of the plasma, and β is a constant exponent that has a value close to unity for N_2 or air plasma [46,47]. By knowing the value of the product $\mu_e p$ at a known temperature, its value at any other temperature can be found using Eq. (3). For atmospheric pressure air plasma, $\mu_e p$ is approximately calculated to be $0.45 \times 10^6 (cm^2 Torr / Vs)$ at room temperature [48]. Since the measurements were made at times $> 1 \mu s$, the hot gas is assumed to reach a pressure comparable to the unperturbed atmospheric pressure [14,49,50]. The estimated temporal development of the plasma electron density is obtained, based on Eq. (2) and (3), and the result is shown in Fig. 5.8. The electron density exhibits a decaying oscillating behavior due to the fluctuating electric power deposited in the spark discharge shown in Fig. 5.2.

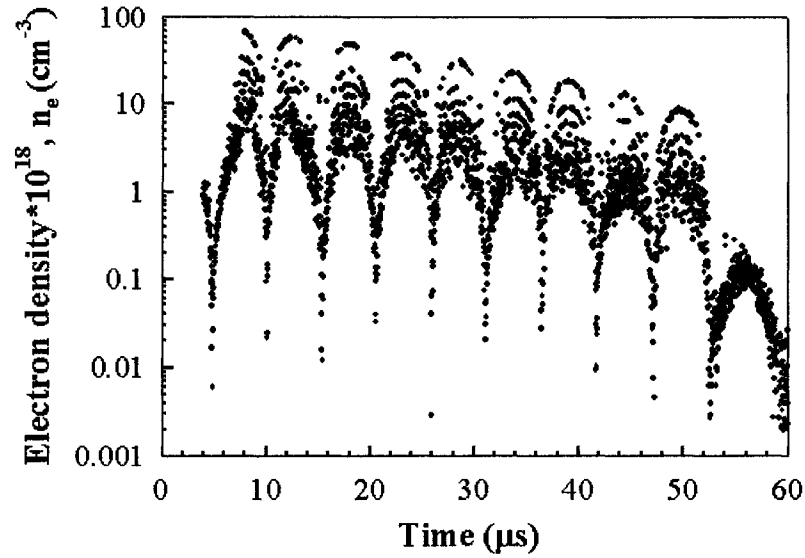


Fig. 5.9 Temporal behavior of electron density n_e (cm^{-3}) of Cu plasma induced by spark discharge assisted LIBS (SD-LIBS), 4 μs after the laser pulse. The oscillations observed in the electron density correspond to the development and dissipation of electric power in the spark discharge, which are time and circuit parameters dependent.

To insure that the plasma is in LTE; a condition which must be satisfied for the determination of plasma temperature, the necessary LTE criterion that defines the lower limit of electron density is given by [29]:

$$n_e \geq 1.4 \times 10^{14} T^{1/2} (eV) [\Delta E (eV)]^3 \quad (5)$$

where ΔE is the energy difference between the states, which are expected to be in LTE. For the observed lines, the largest energy difference is about 2.4 eV and the highest electron temperature observed was approximately 0.8 eV. When substituting in Eq. 5, LTE is accomplished for an electron density greater than 10^{15} cm^{-3} over the time scale investigated and for the range of obtained temperature in Fig. 5.8(b). Observing that the lowest value of electron density is $\sim 2 \times 10^{15} \text{ cm}^{-3}$ (Fig. 5.9), we can safely predict that the assumption of LTE is valid for the time considered.

The calculated peak electron densities for SD-LIBS are in the same order of magnitude as those previously reported for some LIBS studies [33,38]. In addition, we have observed that the peak electron temperature was about the same for both LIBS and SD-LIBS. Thus, the noticeable increase in line intensity is due to the extended time scale of the spectral emission lines in SD-LIBS and the increased plasma volume.

The following figure (Fig. 5.10) shows the SD-LIBS produced plasma size compared to that produced by LIBS, using different filters. It is obvious that the SD-LIBS plasma is of larger size compared to that produced by LIBS.

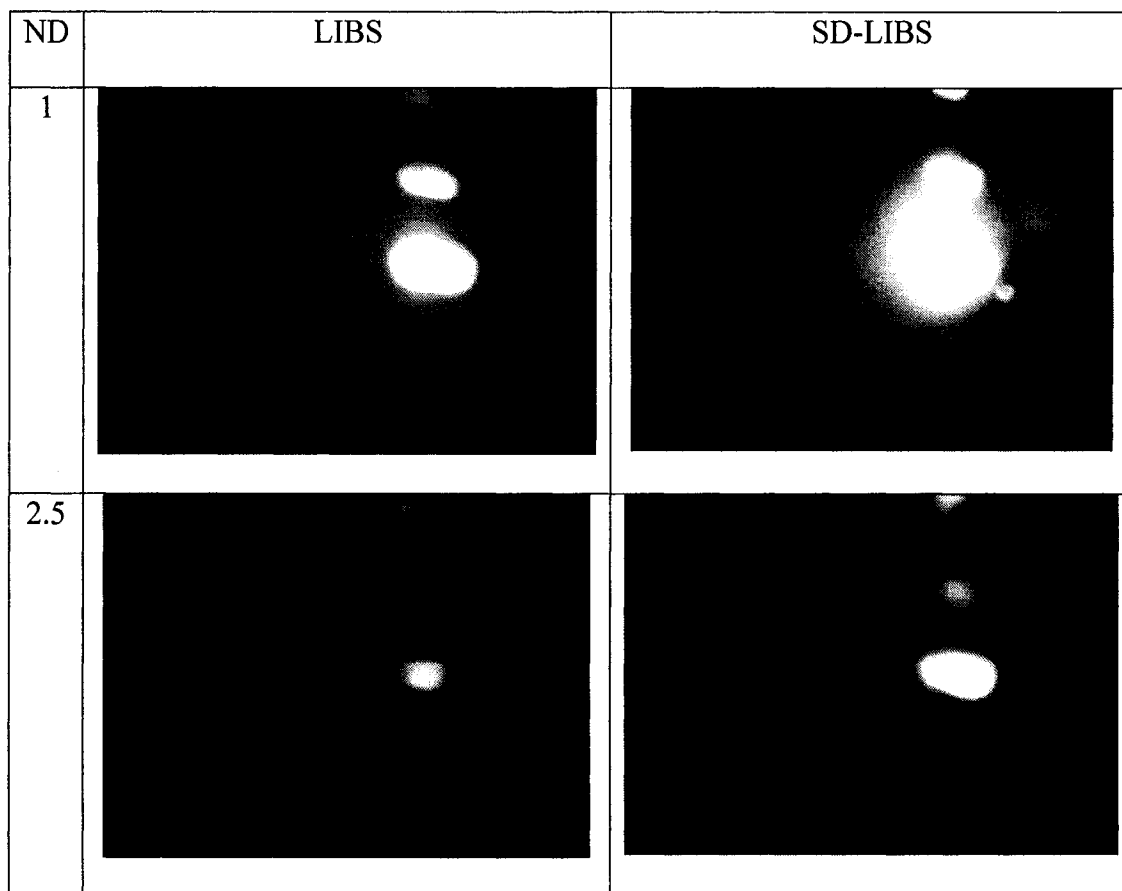


Fig. 5.10 Comparison of the size of the plasma produced by SD-LIBS compared to that produced by conventional LIBS. A clear increase of the plasma size using SD-LIBS is shown. In the case of the ND = 1, 10% of the originally produced plasma light is shown while for ND = 2.5 less than 1% of the plasma light is transmitted and photographed.

For accurate measurements, a line profile was applied to the SD-LIBS and LIBS produced plasma images in Fig. 5.10 with the use of the 2.5 ND, which produces images with intensity under the saturation levels. This was shown in Fig. 5.11 and demonstrated that the plasma size was doubled using SD-LIBS. The plasma length in both x and y axes was measured as 90% of the whole bright length taking into account any errors due to stray or background light.

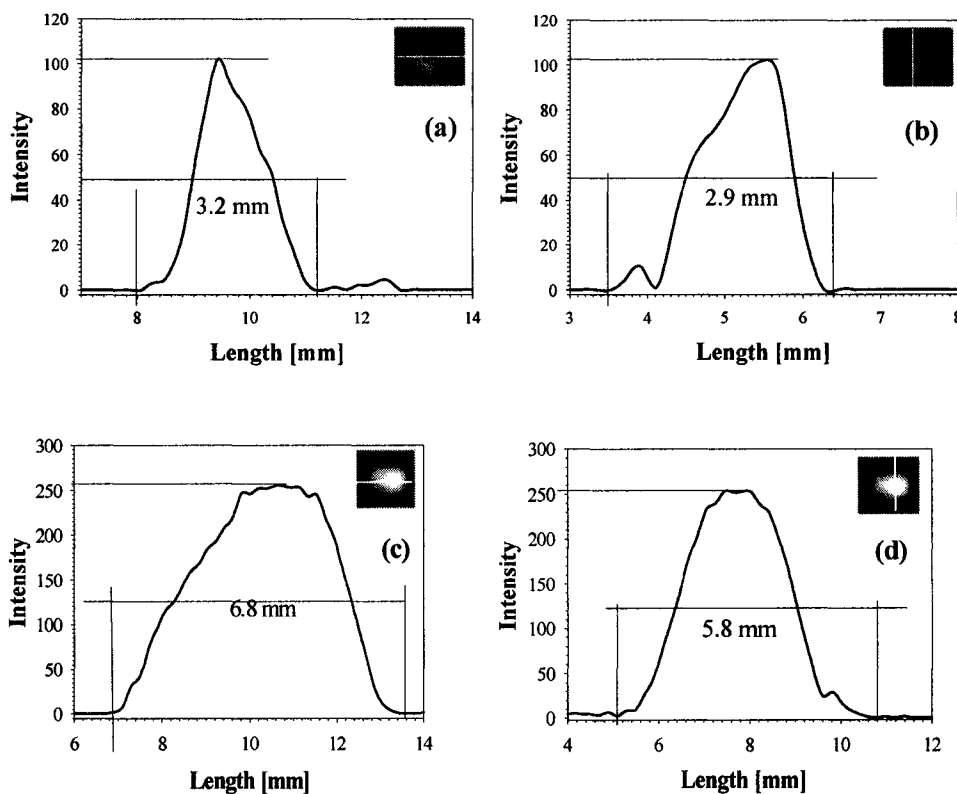


Fig. 5.11 Line profile of LIBS produced plasma compared to that produced by SD-LIBS. This shows that the SD-LIBS produced plasma increase by a factor of ~ 2 . ((a) and (b) represent the line scan for LIBS plasma both in x and y axes when using a 48 J/cm^2 laser fluence, $V = 0$ and an ND filter while (c) and (d) indicate those for SD-LIBS plasma under the same conditions with $V = 3.5 \text{ kV}$).

5.3.4 Sample ablation

The surfaces of the Al samples were examined using an optical microscope and a profileometer after performing LIBS and SD-LIBS. Figure 5.12 gives the depth profiles of Al samples as a result of accumulated five laser shots when using SD-LIBS with 4 J/cm² laser fluence and 3.5 kV-applied voltage. The sample was divided into 14 equal divisions where depth profile was performed at each line to check the maximum produced depth using the SD-LIBS technique.

Figure 5.12(a) shows the effect of five laser pulses of a fluence of 48 J/cm² on a surface placed in the focal position, while Fig. 5.12(b) shows the effect of the same number of pulses of 4 J/cm² under an applied voltage of 3.5 kV. The laser-produced ablation, shown in Fig. 5.12(a), exhibits typical features of laser-surface interactions: a central crater surrounded by splashed, resolidified, and re-deposited molten material, while the heat-affected zone exhibits irregularities at the edges of the crater. The crater depth in this case is ~36 μm, as shown in the corresponding line profile. Laser surface ablation in SD-LIBS, shown in Fig. 5.12(b), produced a crater of smaller area and a depth of only ~8 μm. About seventeen laser pulses with a fluence of 48 J/cm² in the LIBS configuration yield comparable line intensities to those using a single 4 J/cm² laser pulse with an applied voltage of 3.5 kV in the SD-LIBS configuration. The ablation rate can be roughly estimated from the optical microscope images and profileometer scans obtained in several sections across the damage area. The ablation rate is dependent on many factors that include the laser parameters, surface conditions, and laser absorption in the plasma [51].

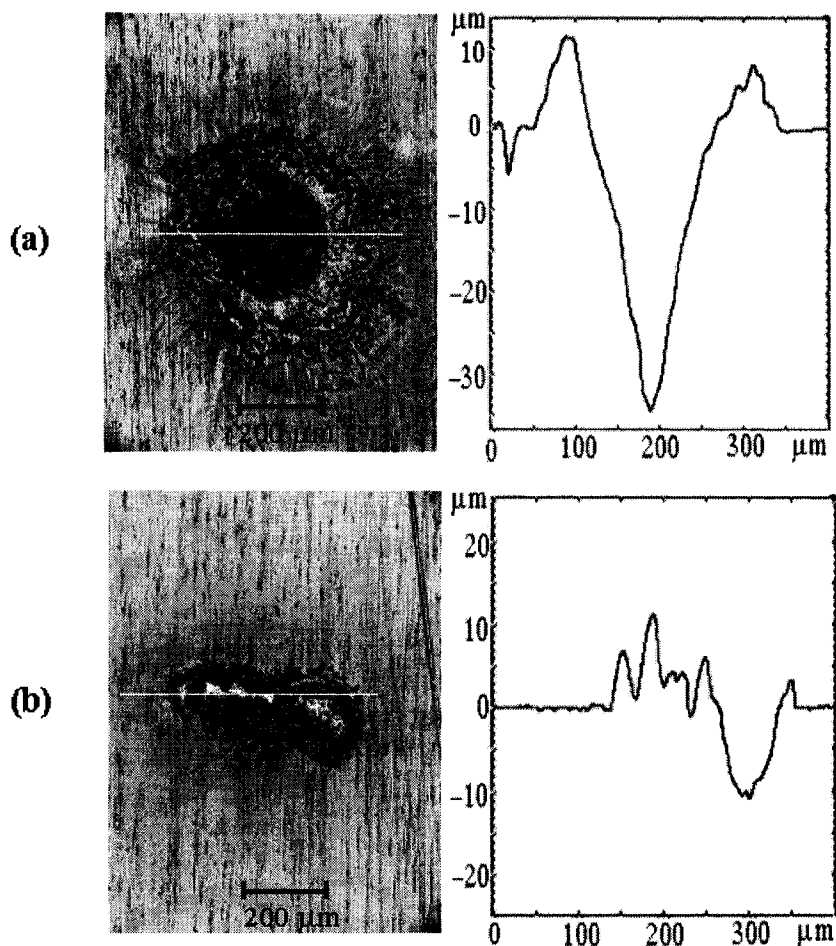


Fig. 5.12 Optical microscopy images and depth profiles of Al samples as a result of accumulated 5 laser shots for both modes of operation; (a) conventional LIBS with 48 J/cm^2 laser fluence; (b) SD-LIBS with 4 J/cm^2 laser fluence and 3.5 kV applied voltage. SD-LIBS produces less damage in the sample.

For a laser fluence of 48 J/cm^2 , a rough estimate on the ablation rate is $\sim 0.5 \text{ } \mu\text{g/pulse}$, while it was ~ 5 times less for a fluence of 4 J/cm^2 . This rough estimation for ablation rates did not include the resolidified volumes resulting from the re-deposition of the splashed target material. In order to examine the possibility that the plasma-surface interaction in SD-LIBS could be contributing to surface damage, surface images and depth profiles formed by 4 J/cm^2 laser pulses along with a spark discharge of 3.5 kV applied voltage were compared to those obtained using the same number of pulses with

the 4 J/cm^2 laser alone. It was found that the areas and depths of the craters are about the same in both cases. Thus, the produced plasma due to the spark discharge has a negligible effect on the sample surface, for the used configuration. Similar results were also obtained for the Cu samples. Therefore, SD-LIBS allows for the use of significantly less laser pulse energy resulting in less surface ablation area and a shallower crater than those obtained by LIBS.

5.4 Summary

SD-LIBS of Al and Cu samples was compared to conventional laser induced breakdown spectroscopy (LIBS). Enhanced spectral line intensity and S/B ratio were observed. Also, significant reduction in laser energy requirement can be achieved in SD-LIBS compared to standard LIBS. The peak plasma temperature was about the same for both SD-LIBS and LIBS. The estimated peak plasma electron density in SD-LIBS is comparable to those reported for conventional LIBS. The noticeable increase in line emission signal is explained by the extended temporal evolution of the line emission in SD-LIBS and the increase in the size of the plasma. Since SD-LIBS also allows for the significant reduction in the laser pulse energy, it causes less surface area damage and shallower craters. Although the initiation of the spark discharge with the laser plume simplifies the operation of SD-LIBS, it introduces signal dependence on plume transient time and spark discharge interaction with the plume. Optimization of SD-LIBS can include external triggering of the spark discharge and electrode shape modification to achieve better energy coupling to the plume.

References of Chapter V

- [1] E. Tognoni, V. Palleshi, M. Corsi, and G. Cristoforetti, "Quantitative micro-analysis by laser-induced breakdown spectroscopy: a review of the experimental approaches," *Spectrochim. Acta Part B* **57**, 1115-1130 (2002).
- [2] R. Russo, X. Mao, H. Liu, J. Gonzalez, and S. Mao, "Laser ablation in analytical chemistry- a review", *Talanta* **57**, 425-451 (2002).
- [3] A. Bogaerts, E. Neyts, R. Gijbels, and J. Mullen, "Gas discharge plasmas and their applications," *Spectrochim. Acta Part B* **57**, 609-658 (2002).
- [4] J. Vadiillo and J. Laserna, "Laser-induced plasma spectrometry: truly a surface analytical tool," *Spectrochim. Acta Part B* **59**, 147-161 (2004).
- [5] I. V. Cravetchi, M. Taschuk, Y. Y. Tsui, and R. Fedosejevs, "Scanning microanalysis of Al alloys by laser-induced breakdown spectroscopy," *Spectrochim. Acta Part B* **59**, 1439-1450 (2004).
- [6] N. Omenetto, In "*Analytical Laser Spectroscopy*," Wiley Interscience, New York, (1979).
- [7] J. A. Broekaert, In "*Analytical Atomic Spectrometry with Flames and Plasmas*," Wiley-VCH, Germany, (2002).
- [8] M. Cullin, In "*Atomic Spectroscopy in Elemental Analysis*," Blackwell Publishing Ltd, UK, (2004).
- [9] J. Robinson, In "*Atomic Spectroscopy*," Marcel Dekker Inc., New York, (1996).
- [10] R. K. Marcus, *Glow Discharge Spectroscopy*, Plenum Press, New York, (1993).
- [11] H. Telle, D. C. S. Beddows, G. W. Morris, and O. Samek, "Sensitive and selective spectrochemical analysis of metallic samples: the combination of laser-induced

- breakdown spectroscopy and laser-induced fluorescence spectroscopy," *Spectrochim. Acta Part B* **56**, 947-960 (2001).
- [12] R. Wisburn, I. Schechter, R. Niessner, H. Schroder, and K. Kompa, "Detector for trace elemental analysis of solid environmental samples by laser plasma spectroscopy," *Anal. Chem.* **66**, 2964-2975 (1994).
- [13] M. Kuzuya and H. Aranami, "Analysis of a high-concentration copper in metal alloys by emission spectroscopy of a laser-produced plasma in air at atmospheric pressure," *Spectrochim. Acta B* **55**, 1423-1430 (2000).
- [14] L. J. Radziemski, T. R. Loree, D. A. Cremers, and N. M. Hoffman, "Time-resolved laser-induced breakdown spectrometry of aerosols," *Anal. Chem.* **55**, 1246-1252 (1983).
- [15] K. Dittrich and R. Wennrich, "Laser vaporization in atomic spectroscopy," *Prog. Analyt. Atom. Spectrosc.* **7**, 139-198 (1984).
- [16] Y. Iida, "Laser vaporization of solid samples into a hollow-cathode discharge for atomic emission spectrometry," *Spectrochim. Acta Part B* **45**, 427-438 (1990).
- [17] R. L. Dahlquist and J. W. Knoll, "Inductively coupled plasma-atomic emission spectrometry: Analysis of biological materials and soils for major, trace, and ultra-trace elements," *Appl. Spectrosc.* **32**, 1-30 (1987).
- [18] A. Aziz, J. A. Brekaert, K. Laqua, and F. Leis, "A study of direct analysis of solid samples using spark ablation combined with excitation in an inductively coupled plasma," *Spectrochimica Acta Part B* **39**, 1091-1103 (1984).
- [19] K. Slickers, *Automatic Atomic Emission Spectroscopy*, Bruhlsche Universitätsdruckerei, Germany, (1993).

- [20] Y. Iida, "Atomic emission characteristics of laser-induced plasmas in an argon atmosphere at reduced pressure," *Appl. Spectrosc.* **43**, 229-2344 (1989).
- [21] M. J. Kushner, R. D. Milroy, and W. D. Kimura, "A laser-triggered spark gap model," *J. Appl. Phys.* **58**, 2988-3000 (1985).
- [22] P. Persephonis, K. Vlachos, C. Georgiades, and J. Parthenios, "The inductance of the discharge in a spark gap," *J. Appl. Phys.* **71**, 4755-4762 (1992).
- [23] H. Hess, "On the theory of the spark plasma in nanosecond light sources and fast spark-gap switches," *J. Phys. D: Appl. Phys.* **8**, 685-689 (1975).
- [24] H. Hess and R. Radtke, "On the calculation of low-inductance spark discharges," *J. Phys. D: Appl. Phys.* **11**, 681-684 (1975).
- [25] A. Descoeur, Ch. Hollenstein, R. Demellayer, and G. Walder, "Optical emission of electrical discharge machining plasma," *J. Phys. D: Appl. Phys.* **37**, 875-882 (2004).
- [26] F. Bredice, D. Orzi, D. Schinca, H. Sobral, and M. Villagran-Muniz, "Characterization of pulsed laser generated plasma through its perturbation in an electric field," *IEEE Trans. Plasma Sci.* **30**, 2139-2143 (2002).
- [27] C. Yang, K. Ingeneri, and W. Harrison, "A pulsed Grimm glow discharges as an atomic emission source," *J. Anal. Atom. Spectrom.* **14**, 693-698 (1999).
- [28] D. Fried, G. Rech, T. Kushida, and E. Rothe, "Electric field enhancement of optical emission from plasma plume generated during ArF excimer photoablation of BaO₂, Y₂O₃, CuO and YBa₂Cu₃O₇," *J. Phys. D: Appl. Phys.* **24**, 1065-1071 (1991).

- [29] V. Rai, H. Zhang, F. Yueh, J. Singh, and A. Kumar, "Effect of steady magnetic field on laser-induced breakdown spectroscopy," *Appl. Opt.* **18**, 3662-3669 (2003).
- [30] M. Qaisar and G. Pert, "Laser ablation of Mg, Cu, and Pb using infrared and ultraviolet low-fluence lasers," *J. Appl. Phys.* **94**, 1468-1477 (2003).
- [31] L. Moenke-Blankenburg, "New aspect of laser micro-spectral analysis with the LMA," *Nouv. Rev. Optique appliquee* **3**, 243-248 (1972).
- [32] T. R. Harville and R. K. Marcus, "Line selection and evaluation of radio frequency glow discharge atomic emission spectrometry for the analysis of copper and aluminum alloys," *Anal. Chem.* **65**, 3636-3643 (1993).
- [33] X. Zeng, S. S. Mao, C. Liu, X. Mao, R. Greif, and R. E. Russo, "Plasma diagnostics during laser ablation in a cavity," *Spectrochim. Acta Part B* **58**, 867-877 (2003).
- [34] A. De Giacomo and O. De Pascale, "Laser induced plasma spectroscopy by air spark ablation," *Thin Solid Films* **453**, 328-333 (2004).
- [35] S. L. Lui and N. H. Cheung, "Resonance-enhanced laser-induced plasma spectroscopy: ambient gas effects," *Spectrochim. Acta Part B* **58**, 1613-1623 (2003).
- [36] T. M. Naeem, H. Matsuta, and K. Wagatsuma, "Effect of plasma gas for spectrometric analysis of tin and zinc using low-pressure laser-induced plasma," *Spectrochim. Acta Part B* **58**, 891-899 (2003).

- [37] J. Siven, B. Bousquet, L. Canioni, and L. Sarger, "Time-resolved and time-integrated single-shot laser-induced plasma experiments using nanosecond and femtosecond laser pulses," *Spectrochim. Acta Part B* **59**, 1033-1039 (2004).
- [38] B. Le Drogoff, J. Margot, M. Chaker, M. Sabsabi, O. Barthelemy, T. W. Johnston, S. Laville, F. Vidal, and Y. von Kaenel, "Temporal characterization of femtosecond laser pulses induced plasma for spectrochemical analysis of aluminum alloys," *Spectrochim. Acta Part B* **56**, 987-1002 (2001).
- [39] T. Kim, C. T. Lin, and Y. Yoon, "Compositional mapping by laser induced breakdown spectroscopy," *J. Phys. Chem. B* **102**, 4284-4287 (1998).
- [40] J. Lash, R. Gilgenbach, and C. Ching, "Laser-ablation-assisted-plasma discharge of aluminum in a transverse-magnetic field. *Appl. Phys. Lett.* **65**, 531-533 (1994).
- [41] H. Griem, In "*Principles of Plasma Spectroscopy*," Cambridge University Press, Cambridge, (1997).
- [42] C. A. Bye and A. Schheeline, "Saha-Boltzmann statistics for determination of electron temperature and density in spark discharges using an Echelle/CCD system," *Appl. Spectrosc.* **47**, 2022-2030 (1993).
- [43] NIST Atomic Spectra Database, <http://physics.nist.gov>.
- [44] B. Nemet and L. Kozma, "Time-resolved optical emission spectrometry of Q-switched Nd:YAG laser-induced plasmas from copper targets in air at atmospheric pressure," *Spectrochim. Acta B* **50**, 1869-1888 (1995).
- [45] R. H. Stark and K. H. Schoenbach, "Direct current glow discharges in atmospheric air," *Appl. Phys. Lett.* **74**, 3770-3772 (1999).

- [46] A. A. Kulikovsky, "Positive streamer between parallel plate electrodes in atmospheric pressure air," *J. Phys. D: Appl. Phys.* **30**, 441–450 (1997).
- [47] R. S. Sigmond, "The residual streamer channel: Return strokes and secondary streamers," *J. Appl. Phys.* **56**, 1355-1370 (1984).
- [48] Y. P. Raizer, In "*Gas Discharge Physics*," Springer, Berlin, (1992).
- [49] H. Sobral, M. Villagran-Muniz, R. Navarro-Gonzalez, and A. Raga, "Temporal evolution of the shock wave and hot core air in laser induced plasma," *Appl. Phys. Lett.* **77**, 3158-3160 (2000).
- [50] S. Yalcin, D. Crosley, G. Smith, and G. Faris, "Influence of ambient conditions on the laser air spark," *Appl. Phys. B: Lasers Opt.* **68**, 121-130 (1999).
- [51] T. Efthimiopoulos, E. Kritsotakis, H. Kiagias, C. Savvakis, and Y. Bertachas, "Laser ablation rate of materials using the generated acoustic waves," *J. Phys. D: Appl. Phys.* **31**, 2648-2652 (1998).

CHAPTER VI

SELF-ABSORPTION LASER INDUCED BREAKDOWN SPECTROSCOPY (SA-LIBS)

Although mainly used for solutions, Atomic Absorption Spectroscopy (AAS) is, however, the most sensitive and practically reliable technique. AAS can be used for elemental analysis of powders, solutions, foils, and wires. With atomic line sources, AAS is generally a single element detection method. Recent advances have been made to overcome this limitation. In AAS, continuum sources that extend well into the ultraviolet range are limited and not widely available. Another problem encountered in AAS is the generation of a broadband spectral background. The background arises from absorption caused by residual molecules or molecular fragments in the atom source and by scattering from smoke and other airborne particulates. It is, thus, considered necessary to employ some form of background correction schemes and different temperature programs for each element investigated. On the other hand, the considerations of line shapes and of spatial distributions make absorption measurements just as complex to interpret quantitatively as are optical emission (OE) measurements of self-absorbed emission lines. Furthermore, quantitative interpretation of absorption measurements requires the use of a light source with known and controlled spectral properties. Figure 6.1 summarizes the typical configuration applied in the AAS experiment.

Therefore, the problem of self-absorption which is defined as the re-absorption of some spectral lines within the plasma emission causes the non-linear effect in the calibration curves that can be very critical in quantitative analysis using atomic

spectroscopy (AS). Because of the complex interaction mechanisms between the atoms/ions and the emitted radiation, the measured concentration, estimated based on the intensity of some emission lines, would be significantly in error. For dense plasmas such those created by laser ablation, self-absorption may be crucial for some specific wavelengths. As the number of emitting atoms increases, the probability of self-absorption increases and there is no longer a linear relationship between the number of emitting atoms and the measured intensity. Therefore, one must avoid self-absorbed lines in determining the elemental concentrations and/or using any correction procedures that might compensate for it.

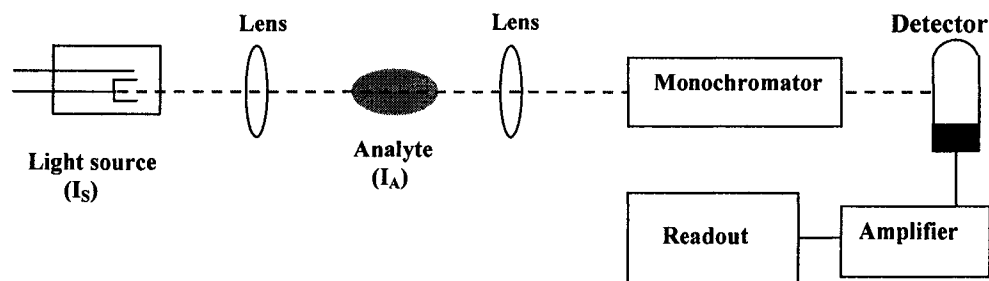


Fig. 6.1 Schematic diagram of a typical atomic Absorption Spectroscopy (AAS) experiment. Hollow cathode lamps are usually used as the light source (I_s). The atomized sample represents the analyte (I_A) under investigation.

Several papers discussed different theoretical models that consider the self-absorption problem and correct its effect in order to obtain linear calibration curves. For instance, Lazic et al. studied the application of LIBS in the quantitative analysis of elemental composition of soils with different origins [1]. In their paper, they developed a model which takes into account the effects responsible for non-linearities in the

relationship between line intensity and elemental concentration. Their model properly included line re-absorption and contributions from space regions with different plasma densities. The application of their model permits obtaining correlation coefficients between the LIBS measured and certified concentration of each element analyzed. Their analytical method included the plasma modeling at local thermal equilibrium (LTE) based on average temperature and electron density values, as well as spectra normalization, introduced in order to reduce the effects related both to the substrate optical and thermal properties and to the influence of laser parameters on quantitative data. Their computational algorithm took into account only atomic species and their first ionization states, which is sufficient at the plasma temperature measured in their experiments. They generated calibration curves for each element of interest measured on certified samples with different matrix composition. Their model was successively applied in analytical LIBS measurements allowing for the direct determination of a single element concentration in any sample, regardless of its unknown matrix composition. Their LIBS method was tested on unknown samples and gave uncertainties in concentration varying from 15 to 40% over a large concentration range covering several orders of magnitude. Their results are significant for some field application, such as on-board marine sediment analysis where a significant matrix variation with layer depth is common.

Gornushkin et al. developed a simplified theoretical approach for an optically thick inhomogeneous laser induced plasma [2]. Their model described the time evolution of the plasma continuum and specific atomic emission after the laser pulse has terminated and interaction with a target material has ended. They assumed local thermodynamic

equilibrium and applied the collision-dominated plasma model and standard statistical distributions. Their calculations were performed for a two-component SiN system. They introduced functions that describe the evolution of the temperature and the size of the plasma. Their model included input parameters, such as the number of plasma species or plasma pressure and the ratio of atomic constituents, which were experimentally measurable. While its outputs were the spatial and temporal distributions of atom, ion and electron number densities, evolution of an atomic line profile and optical thickness and the resulting absolute intensity of plasma emission in the vicinity of a strong non-resonance atomic transition. Their model can be used to choose the optimal line for quantitative analysis and other applications, including prediction of temperature, electron density and the dominating broadening mechanism.

The effect of self-absorption on the shape of spectral lines of silicate plasmas created by laser pulses was studied by Amamou et al. who considered such plasmas to be homogeneous and at local thermodynamic equilibrium [3]. They derived expressions of correcting factors of height and width of spectral lines. They theoretically described the effects of self-absorption on both Lorentzian and Gaussian profiles. They also presented a method of determining the ratios of transition probabilities and ratios of optical thicknesses for the case of Lorentzian profile of lines emitted by plasma in presence of self-absorption. They applied their method to multiple lines of Si II emitted by a plasma created by laser in a silicate solid.

Another model of the self-absorption effect in laser-induced plasma has been developed by Bulajic et al. [4]. Their goal was to provide a tool for automatic correction in the Calibration-free algorithm which they developed for standard-less analysis of

materials by LIBS. As a test of their model, the algorithm for self-absorption correction is applied to three different certified steel NIST samples and to three ternary alloys (Au, Ag and Cu) of known composition. Their experimental results show that the self-absorption corrected Calibration-free method gave reliable results, improving the precision and the accuracy of the CF-LIBS procedure by approximately one order of magnitude.

Sherbini et al. [5] proposed a simple method for quantifying the effect of self-absorption on atomic and ionic emission lines in LIBS measurements. Their method relied on the quantification of the line width and on the evaluation of the electron density, which are easily measurable from an experimental emission spectrum. The validity of their method is restricted to the cases where the spatial (and temporal along the acquisition window) plasma inhomogeneities can be neglected (i.e. self reversal effect is not present). Considering the error associated to the self absorption evaluation, they found that it is mainly caused by the line width and the electron density measurement and is affected by the accuracy of the Stark parameter ω_s ; this implies an optimization of the experimental apparatus and by using lines whose Stark parameters are known with good precision. In their test measurements, performed in air on pure aluminum samples in single and in double pulse configurations, they measured the electron density from the Stark broadening of the optically thin Ha line at 656.3 nm. Under these conditions, they evaluated the self-absorption coefficient with a 30% uncertainty, which turns out to be a definite improvement compared to previous approaches. They have also shown that the calculated self-absorption coefficients can be used for improving the precision in plasma temperature determination, which is highly desirable in quantitative analysis using standard-less techniques.

One way to make use of the self-absorption is to use it as a tool for elemental analysis and let the plasma probe itself. In that content, the plasma is considered as a broadband light source that fulfills the requirement for resonance or near-resonance transitions for the element under study. In this study, in order to measure the self-absorption within the plasma, two approaches were investigated. One approach uses a metallic mirror behind the plasma such that the emitted radiation is reflected back into the plasma, leading to more pronounced absorption of the emitted lines. The emitted radiation will be measured with and without the mirror. After appropriate adjustment, the intensity line decrease due to self-absorption which could be measured and related to the element concentration. The second approach depends on producing a system of plasmas analogous to AAS such that one spot is assigned as the light source and the second plasma as the analyte. Therefore, the plasma is allowed to probe itself.

6.1 Theory of emission and absorption

Laser-induced plasmas are emission sources that generally present a high density of atoms and ions. As a consequence, the self-absorption increases the line width and decreases the line height. The optical thickness and the corresponding saturation of the line height are functions of two factors. First, the optical thickness depends on the density of the emitting particles. Second, the optical thickness depends on the emission line considered. Generally, the intense lines are more affected by the self-absorption than the weak lines. The optical thickness and its influence on line emission are determined taking in account the plasma temperature, the electron density and the transition probabilities. One method used for the determination of the ratios of transition probabilities for

multiple lines emitted by homogeneous and LTE plasma, taking into account self-absorption, is applied to plasma created by laser in a silicate solid [3].

For the case of optically thin line emission for LTE and homogeneous plasma, the total line radiance is given by $I_{\lambda}^{Thin} = \epsilon_{\lambda} R$ where R is the path length in cm and ϵ_{λ} is the emission coefficient in $\text{J s}^{-1} \text{m}^{-2} \text{cm}^{-1} \text{rad}$. The emission coefficient for spectral line is defined in term of the normalized profile of emission P_{λ} of the line [3]:

$$\epsilon_{\lambda} = \epsilon_{\nu} \frac{d\nu}{d\lambda} = \frac{hc}{2\lambda_0} A_{ul} g_u \frac{N_z}{\Phi_z} \exp\left(\frac{-E_u}{KT}\right) P_{\lambda} \quad (1)$$

with h the Planck's constant, c velocity of light, ν frequency, λ wavelength, λ_0 line-center wavelength, A_{ul} transition probability from the line superior level u to the line lower level l , g_u statistical weight of level u , N_z density of ionization state z , Φ_z partition function of ionization state z , E_u energy of state u , K Boltzmann's constant and T temperature of plasma.

The optical thickness at wavelength λ is defined by $\tau_{\lambda} = k_{\lambda} R$, where k_{λ} is the absorption coefficient in cm^{-1} . Therefore optical thickness is dimensionless. The absorption coefficient for a spectral line is defined by [3]:

$$k_{\lambda} = k_{\nu} = \frac{\lambda_0^4}{8\pi c} A_{ul} g_u \frac{N_z}{\Phi_z} \left(\exp\left(-\frac{E_l}{KT}\right) - \exp\left(-\frac{E_u}{KT}\right) \right) P_{\lambda} \quad (2)$$

where E_l is the energy of state l .

The line profile is due to the two main broadening mechanisms of the spectral lines. The first factor responsible for this broadening is the interaction of the emitted species with surrounding ones. This pressure effect includes broadening by collision with

foreign species, resonance broadening and Stark broadening. In this case, the spectral line shape is described by a Lorentz function:

$$P_{\lambda} = \frac{1}{\pi} \frac{\Delta\lambda_L / 2}{(\lambda - \lambda_0)^2 + (\Delta\lambda_L / 2)^2} \quad (3)$$

where $\Delta\lambda_L$ is the Lorentzian width.

The second important factor causing the broadening is the Doppler effect indirectly related to the temperature of radiating species. When velocity distribution of these particles is Maxwellian, the spectral line shape has a Gaussian profile:

$$G_{\lambda} = \frac{2\sqrt{\log(2)}}{\Delta\lambda_D \sqrt{\pi}} \exp\left(-4\log(2)\left(\frac{\lambda - \lambda_0}{\Delta\lambda_D}\right)^2\right) \quad (4)$$

$$\Delta\lambda_D = 7.16 \times 10^{-7} \frac{1}{\lambda_0} \sqrt{\frac{T}{\mu}} \quad (5)$$

$\Delta\lambda_D$ is the Doppler width, T is the temperature of the radiating atoms and μ is the mass number.

To calculate the actual emission of a plasma source, the self-absorption inside the plasma in a homogeneous plasma, the spectral emission and absorption coefficients are independent of x so the spectral radiance is given by:

$$I_{\lambda} = \frac{\epsilon_{\lambda} R}{k_{\lambda} R} (1 - \exp(-k_{\lambda} R)) \quad (6)$$

and it can then be expressed as follows:

$$I_{\lambda} = \frac{I_{\lambda}^{thin}}{\tau_{\lambda}} (1 - \exp(-\tau_{\lambda})) \quad (7)$$

6.2 Optical Absorption Technique

The strength of the optical emission source depends on the oscillator strength of the transition being observed and the population of the upper state of the transition, which depends on electron density and temperature, collision rates, radiative transfer, and populations of other states. If the population in the lower level of the optical transition, being observed by OES, is highly populated, as often is the case for intense emission lines, then a significant fraction of the emitted photons can be reabsorbed in the trapping plasma radiation before they reach the detector. The absorption depends on the oscillator strength and wavelength of the transition. In these cases, radiation-transport calculations that take into account the line shapes of both the emitters and absorbers in the plasma, along with their spatial distributions, are required to gain a quantitative understanding of the net optical emission. The self-absorption phenomenon causes the optical emission intensity to depend nonlinearly on the population in the excited state being measured, which is the upper level of the observed optical transition. In the case of Doppler-broadened emission lines, dependence on translational temperature arises.

Optical absorption measurements were previously performed using the plasma's own optical emission as the light source [6], which is an alternative to OES for measuring excited-state populations. In this case, a light source tuned to an optical transition is passed through the plasma. Absorption is caused by the difference in populations of the lower and upper levels of the optical transition to which the light source is tuned. In many cases, it may be easier to calibrate quantitative fractional absorption measurements than to calibrate absolute emission measurements. However, the considerations of line shapes and of spatial distributions make absorption measurements just as complex to interpret

quantitatively as are OE measurements of self-absorbed emission lines. Furthermore, quantitative interpretation of absorption measurements requires the use of a light source with known and controlled spectral properties. Optical absorption measurements are complimentary to OE measurements; however, the main advantage of optical absorption measurements is that they can probe the densities of the most highly populated excited states, such as metastable and quasi-metastable states. Figure 6.2 shows the essence of the technique for measuring optical absorption using the plasma's own emission light as the optical source. The technique requires two windows at opposite ends of a chord through the plasma. Light emitted in one direction by the plasma is modulated by a chopping wheel and reflected by a mirror back through the plasma. A detector measures the sum of the light emitted directly by the plasma and that reflected back through the plasma by the mirror. A filter or monochromator selects a particular line or band of interest. The level of modulation on the detected light is indicative of the degree of absorption of the chopped light beam. The modulation fraction f was defined as the ratio of the peak-to-peak amplitude of the modulated ac signal to the maximum signal at the detector.

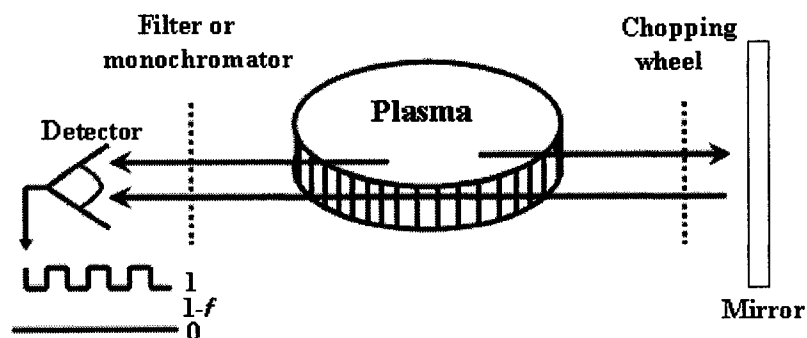


Fig. 6.2 Schematic diagram of a technique for measuring optical absorption using the plasma's own emission light as the optical source.

For dense plasmas such those created by laser ablation, self-absorption is crucial for some specific wavelengths. As the number of emitting atoms increases, the probability of self-absorption increases, and there is no longer a linear relationship between the number of emitting atoms and the measured intensity. Therefore, one must avoid self-absorbed lines in determining the elemental concentrations and/or using any correction procedures that might compensate for it. One way to keep away from such complexity is to use the self-absorption as a tool for elemental analysis and let the plasma probe itself. In that content, the plasma is considered as a broadband light source that fulfills the requirement for resonance or near-resonance transitions for the element under study. Self-absorption is used as an analytical tool in this study. In order to measure the self-absorbed within the plasma, a metallic mirror behind the plasma is used, such that the emitted radiation is reflected back into the plasma, leading to more absorption of the emitted lines. The emitted radiation will be measured with and without the mirror. After appropriate adjustment, the intensity line decrease due to self-absorption could be measured and related to the element concentration.

6.3 Experiment

A schematic diagram of the experimental setup is shown in figure 6.3. The laser beam from a 1064 nm Q-switched Nd :YAG laser delivering ~35 mJ, pulse duration of 20 ns and 50 Hz repetition rate was used to ablate the Cu target. The laser beam was focused through a 50 mm lens on the target in air. The target was adjusted to avoid surface damage and to make the laser pulse hit a fresh target surface using an x-y translational stage. A square aluminum mirror of 1cm length, positioned ~2 cm from the plasma boundary, was used. It was controlled by a flip holder which allows the data

acquisition with and without reflection from the mirror. The plasma emitted light passing in the direction of the mirror will be reflected back into the plasma where self-absorption acts more significantly upon the double path length traveled by the light.

The emission from the plume was registered by a CVI spectrometer in conjunction with an optical fiber (core diameter 600 μm) placed at right angle to the direction of the plasma expansion. The detection system is covering the range between 200 and 900 nm and an optical resolution of ≈ 1 nm. For a time resolved experiment, a monochromator along with a PMT and an oscilloscope, previously specified, are used. The detection system is triggered by the Q-switched Nd:YAG laser to record the emission spectrum from the plume and the output data were averaged for eight and ten laser shots. The data acquired simultaneously by both systems are stored in a PC through SMPRO software or xls-format files for subsequent analysis.

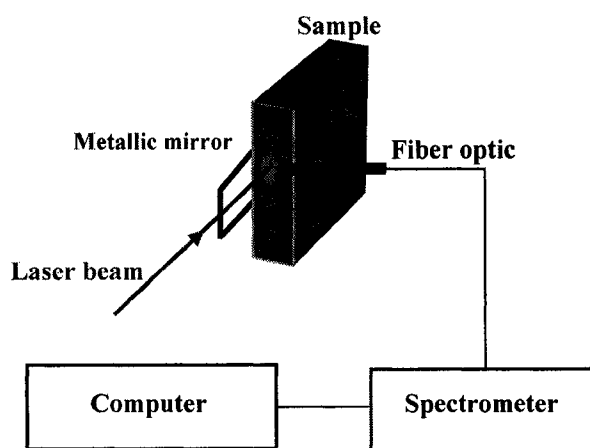


Fig. 6.3 Schematic diagram of the configuration applied in our experiment using the plasma's own emission light as a broadband light source which probes itself to measure the optical absorption.

For integrated spectra intensities (Table 1) and the temporal development of the selected spectral lines (Fig. 6.4) both show that by comparing the line-intensity for the two spectral lines, some definite differences are clear. About double the intensity of Cu 330 nm was detected with and without the mirror, while ~50% of the intensity of CuI 327 nm has been reabsorbed when using a laser pulse fluence of 3.5 mJ/cm². This can be traced back to differences in the final transitions of the chosen spectral lines that are referred to as resonance or non-resonance lines. During the first hundreds of microseconds, the temporal evolution shows strong continuous background radiation dominates and measurement of atomic and ionic lines with a good signal-to-noise ratio is poor. Thus, under these experimental conditions at laser fluence of 8 and 3.5 mJ/cm², resonant spectral lines which are more susceptible to self-absorption can be distinguished and detected. The amount of self-absorption could also be measured.

Table 1: Comparison of the integrated line and background intensities of CuI 324 and CuI 327 nm with and without the metallic mirror at laser fluence 3.5 mJ/cm².

	No mirror	No mirror	With mirror	With mirror	Net Line intensity	Net line intensity	Line ratio	Background ratio
nm	I (line)	I (backgr.)	I (line)	I (backgr.)	No mirror	With mirror		
324	1930	425	2190	606	1505	1584	1.052	1.425
327	1567	499	1852	729	1068	1096	1.026	1.4609

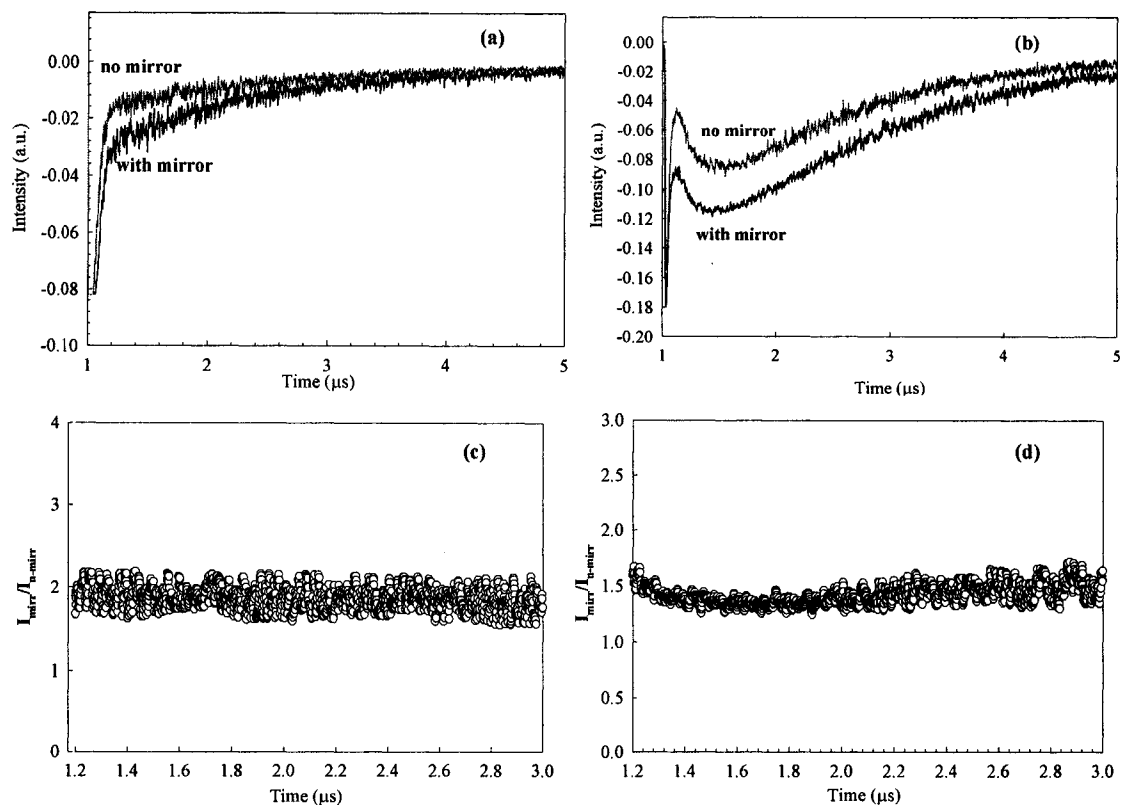


Fig. 6.4 Temporal development of Cu 330 and 327 nm with no mirror (red line) and when reflected by applying the mirror (black line) [a and b]. The intensity ratio of each line with the mirror to that without it is represented in c and d. It is clear that when using a laser fluence of 8 mJ/cm^2 the intensity ratio of Cu 330 nm is approximately doubled while that of Cu 327 nm is asymptotically reaching ~ 1.5 . This shows that Cu330 nm is not susceptible to self-absorption on contrary to Cu 327 nm

Therefore, we found that carrying out the experiment in air at atmospheric pressure, at different laser pulse energies, results in fluctuating values of the line absorption with the accumulation of either eight or sixteen successive scans. This introduced complexity to obtain reproducible results that leads to the conclusion that working under controlled pressure conditions, which was previously applied to the known Optical Absorption technique by Miller et al. [6], upon which our work was

based, has been of great assistance in order to increase the S/B ratio and obtain more reliable results.

6.4 Modification of previous experiment

The previous experiment inspired us to apply the next approach for the self-absorption-LIBS (SA-LIBS) in which we used the experimental setup shown in Fig. 6.5. The output of 1064 nm Q-switched Nd-YAG laser beam (Lumonics YM-200), ~20 ns FWHM, was directed by a set of mirrors and was directly transmitted through a half wave plate and a thin film polarizer (TFP) to be focused on the target using a 50-mm focal length convex lens and to form a 400 μ m-FWHM spot size as measured with the sharp edge method. Thus, the formed plasma produced from one spot acts as the light source I_S (light bulb, analogous to AAS). The reflected portion of the laser beam from the TFP was re-directed through an IR mirror focused on the same sample, to act as the analyte; I_A . In this way, we followed the general idea of AAS but with the modification that our technique can be used for multi-element analysis and the requirement of exchanging the light bulb for different elements has been avoided. In other words, the plasma is probing itself.

The pulse profile and duration of the pulses was measured with a fast detector and it was checked that the optical components of the experimental arrangement (beam splitters, filters) did not significantly affect the duration of the pulses or its Gaussian shape. The laser energy, measured with a joule-meter, was varied using glass filters that introduced an easy method of changing energy and has been tested to show no effect on laser pulse profile.

The analytical signal was detected when the geometrical focus was located on the sample surface. The focusing geometry could be changed and optimized by precise translation of the lens and the sample holder with micrometer screws. The integrated emission of the formed plasma was directly transferred, without an imaging lens, to a spectrometer (CVI model SM240, 600 grooves mm^{-1} grating, spectral range 200-978 nm with a reciprocal linear dispersion of $\sim 1 \text{ nm mm}^{-1}$) using a 2-m long, 600 μm in diameter fiber optic bundle. To obtain the temporal development of emission lines for both SA-LIBS, a monochromator (1440 grooves mm^{-1} grating, slit width 100 μm) was used. The signal was collected by a built-in lens inside the monochromator, placed $\sim 150 \text{ mm}$ away from the plasma, and then detected using a photomultiplier (PMT) connected to a 300 MHz digital sampling oscilloscope for data acquisition.

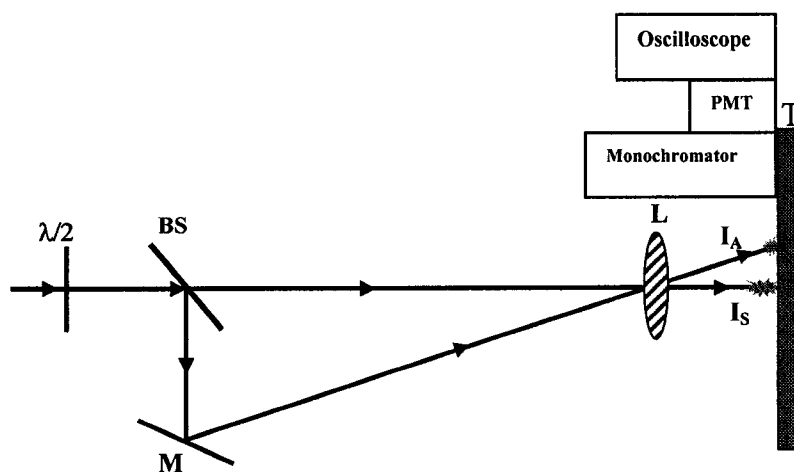


Fig. 6.5 Schematic diagram of Self-Absorption LIBS (SA-LIBS) experimental setup.

The incoming laser beam is passing through a half-wave plate ($\lambda/2$) and a beam splitter (BS) to be focused by a lens (L) on a target (T). The light intensity coming from the two produced plasma will be detected and analyzed using a monochromator, PMT and an oscilloscope. Analogous to AAS, one spot is denoted by I_s (represents the light source) and the other spot I_A (represents the analyte spot).

The experiments were performed with brass Zn/Cu compacted powder disks prepared in our laboratories. Our choice of such simple bi-elemental samples was because they are the next complicated matrices relative to matrices with only one major component. However, it was shown that due to the significant differences in vapor pressure of the main components, Zn and Cu, and also due to structural differences, they are known to be difficult. The concentrations of both elements in the alloys are listed in Table 2. Both weight and weight error % were calculated as the average value of EDS output for three randomly chosen spots on each sample. In addition to the brass samples, pure zinc and copper samples were also used in this study.

Table 2: Composition of brass samples used in this study.

	<i>Element</i>	<i>Weight %</i>	<i>Wt.% Err</i>
<i>SAMPLE 1</i>	<i>Cu</i>	0.66	+/- 0.27
	<i>Zn</i>	99.34	+/- 0.57
<i>SAMPLE 2</i>	<i>Cu</i>	1.47	+/- 0.29
	<i>Zn</i>	98.53	+/- 0.58
<i>SAMPLE 3</i>	<i>Cu</i>	3.35	+/- 0.48
	<i>Zn</i>	96.65	+/- 0.80
<i>SAMPLE 4</i>	<i>Cu</i>	5.36	+/- 0.56
	<i>Zn</i>	94.64	+/- 1.11
<i>SAMPLE 5</i>	<i>Cu</i>	8.31	+/- 0.57
	<i>Zn</i>	91.69	+/- 1.44
<i>SAMPLE 6</i>	<i>Cu</i>	13.47	+/- 0.65
	<i>Zn</i>	86.53	+/- 1.62
<i>SAMPLE 7</i>	<i>Cu</i>	47.95	+/- 0.60
	<i>Zn</i>	52.05	+/- 1.87

6.5 Theory

The Beer-Lambert law, which assumes a linear relationship between the absorbance and concentration of an absorbing species, generally applies to the atomic absorption spectroscopy (AAS); however, in our configuration some parameters are not constants, such as the number of excited species present along the produced plasma or the plasma width traveled by the photons. We considered the molecules present in the analyte plasma as an opaque disk with a cross-sectional area, σ , which represents the effective area seen by a photon of frequency ω . If the frequency of the light is far from resonance, the area is approximately zero. If ω is close to resonance, the area is a maximum.

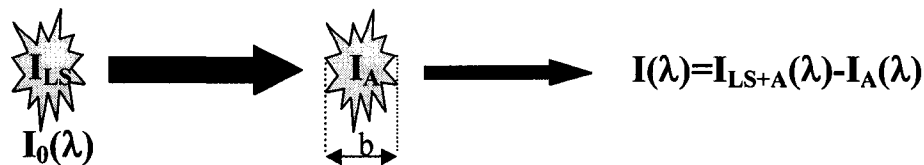


Fig. 6.6 Schematic diagram of the idea of SA-LIBS configuration. The source plasma emitted light (I_{LS}) is absorbed by the excited atoms while passing through the analyte plasma whose emission is I_A resulting in a detected emission intensity $= I_{LS+A}(\lambda) - I_A(\lambda)$.

Assuming that $I_0(\lambda)$ emitted from the source plasma is the intensity entering the sample (the second plasma representing the analyte) at $x = 0$, and I_z is the intensity entering an infinitesimal slab dz at position z along the width of the analyte plasma, dI is the intensity absorbed in the slab, and $I(\lambda)$ is the intensity of light leaving the analyte sample. Thus:

$$dI / I_z = -\sigma * N(z) * dz \quad (8)$$

For simplicity, we assumed that the excited species follow a Gaussian distribution and considered the plasma to have a constant width, b . By integrating Eq. (1), it gives [7]:

$$\int_{I_0}^I \frac{dI}{I} = -n_0 c_{\text{exp}} \sigma \int_0^b e^{-z^2} dz \quad (9)$$

$$\ln \frac{I}{I_0} = -n_0 c_{\text{exp}} \sigma \int_0^b e^{-z^2} dz = -n_0 c_{\text{exp}} \sigma \frac{\sqrt{\pi}}{2} \text{erf}(b) \approx -\sigma c_{\text{exp}} n_0 \left(\frac{\sqrt{\pi}}{2} - \frac{e^{-b^2}}{2b} \right) \quad (10)$$

$$\frac{I}{I_0} \sim \exp \left\{ -n_0 c_{\text{exp}} \left(\frac{\sigma \sqrt{\pi}}{2} - \frac{\sigma e^{-b^2}}{2b} \right) \right\} \quad (11)$$

where c_{exp} is a constant, n_0 is the maximum density of the excited species and σ is the absorption coefficient (cm^2) which can be derived from [8]:

$$\sigma = 0.33\lambda_0^3 \sqrt{\frac{M}{T}} \frac{g_j}{g_i} A_{ji} \quad (12)$$

where M is the atomic weight, T the absolute temperature of the plasma (K), λ_0 the wavelength (in m) at the centre of the line, A_{ji} is in s^{-1} , g is the statistical weight of the level which is equal to $2J+1$ where J is the total angular momentum quantum number of the level.

6.6 Results and discussion

Using the setup shown in Fig. 6.5, Cu and Zn targets were irradiated by a focused 1064 nm laser beam such that the laser fluence deposited on the spot, which acts as the light source is $\sim 14 \text{ J/cm}^2$, while that of the analyte spot is $\sim 5.7 \text{ J/cm}^2$, the emission lines of the produced plasma are dispersed and detected while passing through a spectrometer transferred and saved by SM-Pro software for further analysis. The spectra were acquired during an integration time = 20 ms with 50 Hz laser repetition rate, which results in a single laser pulse produced spectrum. The integrated spectra (Fig. 6.7(a)) were acquired using the brass compacted discs from which we have plotted the calibration graphs (Fig. 6.7(b)) for the well-defined spectral lines with no overlapping with adjacent lines which was limited by our instrumental resolution. It is shown that these selected spectral lines show linear calibration graphs. On the contrary, different authors reported that brass alloys represent the worst case scenario in the sense of non-linear calibrations, which they attributed to the changes in mass ablation and fractionation [9-12]. Recently, Gaegan and Mermet and Russo et al. [9] have also investigated the non-linearity of the calibration graphs for brass samples ablated with lasers of different wavelengths, energies and pulse durations. Their measurements showed clearly that the non-linearities could be addressed

to differences in the mass ablation rate. Several factors are likely to play a role: different energy loss mechanisms like changes in reflectivity, thermal conductivity and electron-phonon coupling, structural changes due to different sample compositions and treatments.

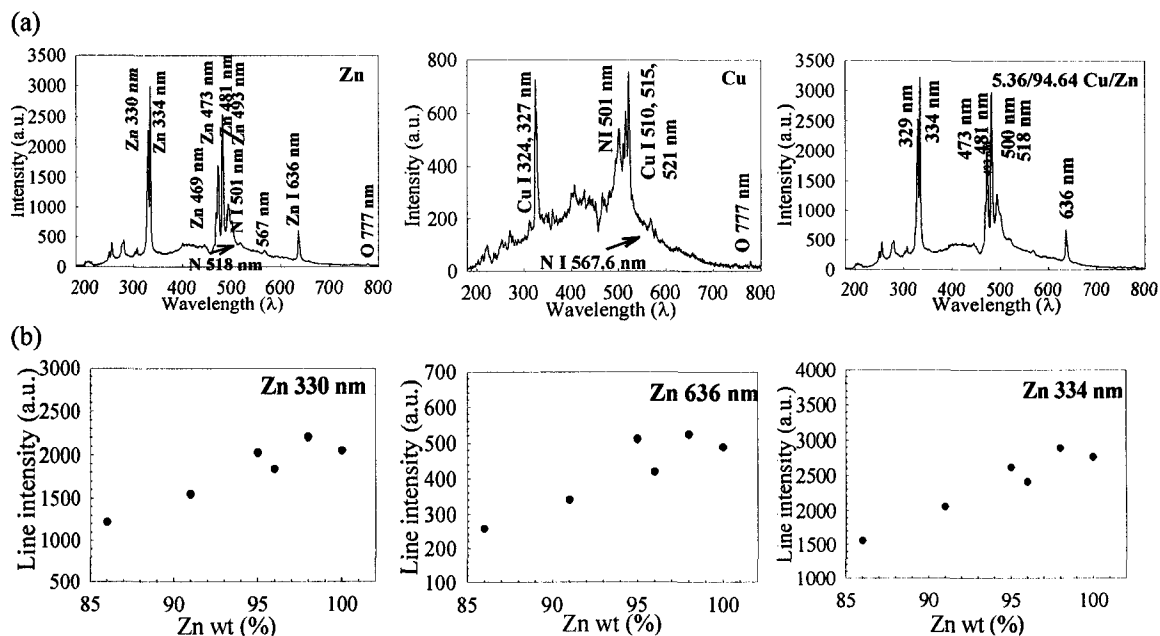


Fig. 6.7 (a) Integrated spectra of pure Zn, Cu and 5.36/94.64 Cu/Zn samples. (b) Calibration curves resulted from Self-absorption-LIBS technique using the integrated intensities of different spectral lines of Zn.

The integrated spectral emission of Cu I 522 nm and Zn 481 nm has been plotted for the brass sample with 47.95/52.05 Cu/Zn concentration ratio as a function of the laser pulse energy (Fig. 6.8). The emission lines of Cu I 521.8 nm and Zn I 481.0 nm were selected because both lines have comparable transition probabilities; the energy difference between the upper levels of both lines is relatively small ($\sim 3700 \text{ cm}^{-1}$) and neither of the lines interfered with emission lines of other elements in the sample. This assures that our experimental parameters, especially the laser pulse energy, have not produced a saturation regime and plasma shielding has no effect on suppressing the increase of the

emission intensities. It is shown that the emission intensity for the selected spectral lines increases proportionally with the increase of the laser pulse energy in the range from ~ 5.9 to 18 J/cm^2 .

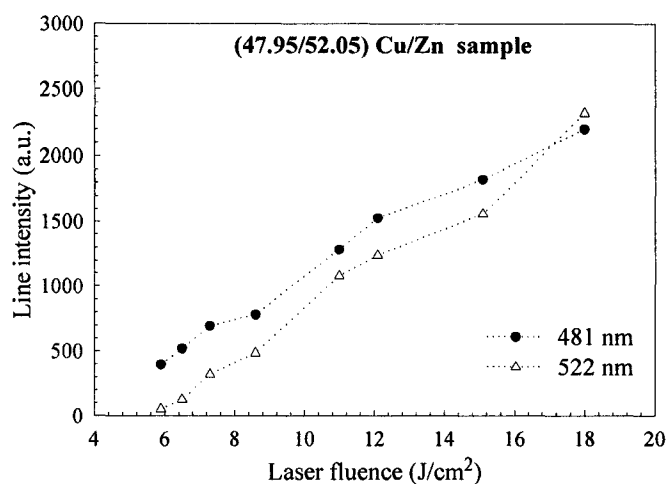


Fig. 6.8 The emission intensity for the spectral lines; CuI 522 and ZnI 481 nm as a function of the laser fluence for the 47.95/52.05 Cu/Zn sample.

However, the experiment instrument capabilities are limited by the spectrometer low resolution that hindered the analysis of other spectral lines, an issue which directed us to perform the experiment with the temporal-resolved setup. The temporal profile of Cu I 324, 327 and 330 nm resulting from thirty two laser pulses are averaged and recorded using an oscilloscope triggered by the 20-ns-laser pulse and shown in Fig. 6.9(a). The condition of the deposited laser energy ratio of the analyte to the light source spots was optimized to provide more pronounced self-absorption effects. The laser fluence deposited on the spot, which acts as the light source, was $\sim 12.7 \text{ J/cm}^2$, while that of the analyte spot was $\sim 5.7 \text{ J/cm}^2$. Moreover, the background and continuum emission

were recorded. The subtraction of the continuum and background signal was checked and found to have no influential effect on the development and the line decay time of the investigated emission lines under the experimental condition. Thus, for the Cu 324, 327 and 330 nm, there is no necessary consideration that should be taken to account for the background subtraction. Also the transmission of those mentioned emission lines as a function of time and laser fluence incident on the spot acting as the light source are shown in Fig 6.9(b) and (c). It is shown that by the change of the light source the absorption is approximately 70% for Cu 324 and 327 nm while its value is ranging between 25% for Cu 330 nm. This difference is due to the fact that Cu 324 and 327 nm are resonant lines, more subject to self-absorption resulting in a significant absorption and a decrease in their intensity under atmospheric pressure. The standard deviation of repeatability of measurements, defined as the root mean square of the deviation of the values from their arithmetic mean, was calculated as:

$$s^2 = \sum_{i=1}^k (\bar{x} - x_i)^2 / k \quad (13)$$

where k (= 4, in our case) is the number of measurements, x_i and \bar{x} are the measurement and its mean value for each i th sample. For laser fluence 12.7 J/cm^2 the standard deviation of emission of 324, 327 and 330 nm are $4\text{e-}3$, $1\text{e-}2$ and $2\text{e-}3$ respectively while for laser fluence 7.8 J/cm^2 they are calculated for the same spectral lines to be $3\text{e-}3$, $3\text{e-}3$ and $1.7\text{e-}4$, respectively. These are too unnoticeable errors to be seen in Fig. 6.9(c).

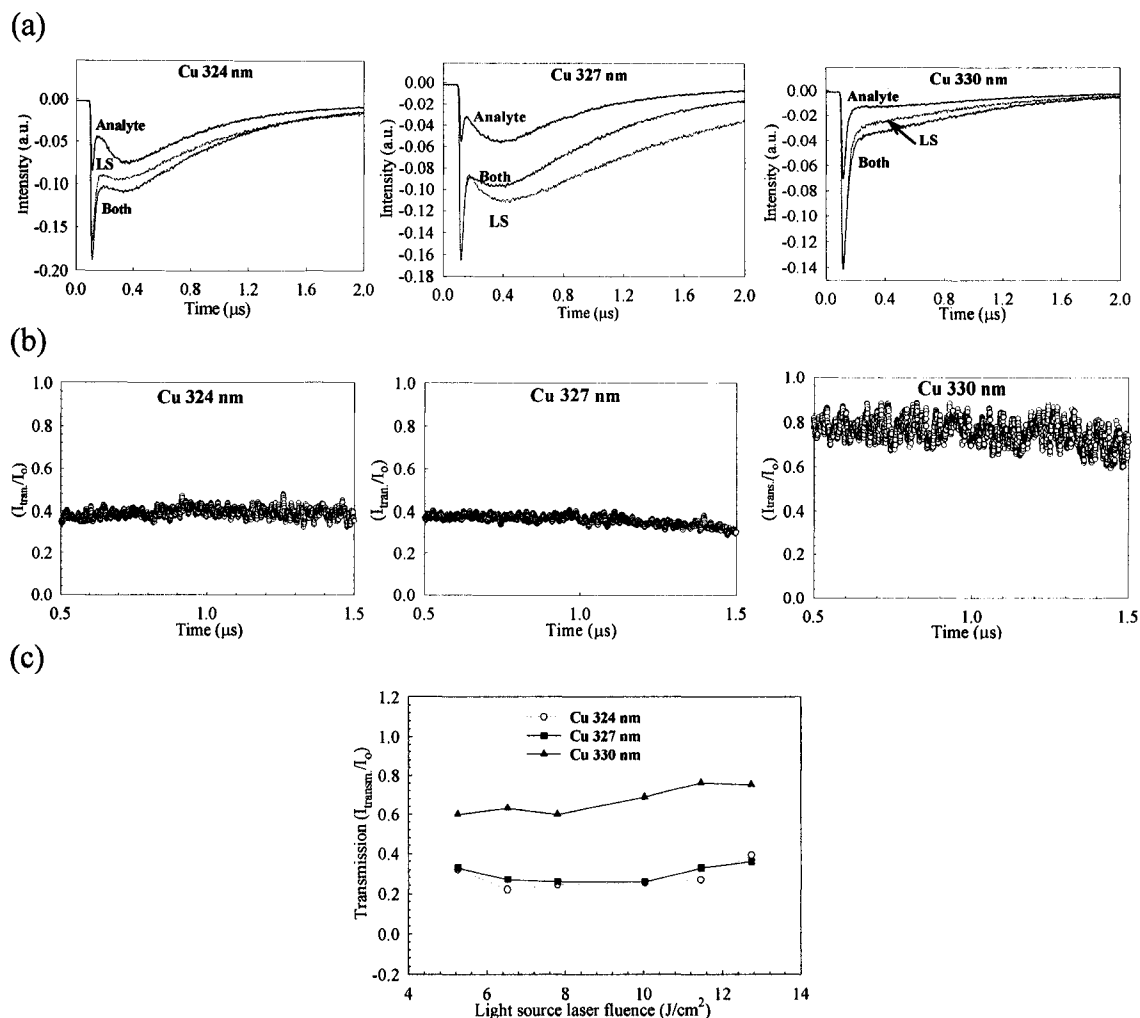


Fig. 6.9 Temporal development of some spectral lines Cu 324, 327 and 330 nm (a) at laser fluence = 5.7 and 12.7 J/cm^2 for the light source spot and the analyte spot, respectively. (b) Temporal development of their corresponding transmission. (c) The average transmission of such lines over 1 μs (from 0.5 to 1.5 μs) as a function of incident laser energy of the light source spot.

The temporal development of some atomic emission lines of Cu is obtained for the two focused laser beams on the target individually (denoted as analyte intensity; I_A) and light source intensity; I_{LS}) along with the emission of both spots together (I_{Both}). Then, the latter emission (I_{Both}) is compared to the sum of intensities emitted from each plasma separately ($I_A + I_{LS}$) for the atomic emission lines of interest. The current

technique was able to distinguish between resonant emission lines, which are highly suffering self-absorption, and the non-resonant emission lines. While in case of significant self absorption, $I_{\text{Both}} < I_{\text{A}} + I_{\text{LS}}$, whereas for lines which are not suffering self-absorption $I_{\text{Both}} \cong I_{\text{A}} + I_{\text{LS}}$. The emission of the spectral lines 324.4 nm, 327 nm, 328 nm, 330 nm, 334 nm, 468 nm, 471 nm, 481 nm and 522 nm were obtained. The data acquisition and data analysis procedures are summarized as follows:

1. The light emitted from each spot; the light source, the analyte and the light collected from both spots all together were acquired at a specific wavelength using the monochromator, PMT and an oscilloscope.
2. Each measurement was an accumulation of 265 scans triggered by the laser pulse whose repetition rate is 50 Hz. The laser fluence deposited on the spot, which acts as the light source, is $\sim 14.8 \text{ J/cm}^2$, while that of the analyte spot is $\sim 5.9 \text{ J/cm}^2$.
3. Each measurement was repeated for three times, saved and transferred to a computer for data analysis. The laser pulse energy was measured in the beginning and at the end of each run.
4. The output data acquired by the oscilloscope was plotted for the emission of each spot (LS and Analyte) and the emission from both spots together (Both).
5. The calculation of the transmission defined as the ratio of the transmitted to the initial emission ($I_{\text{trans.}}/I_0$) was obtained and plotted for each wavelength.
6. The values of the transmission were integrated over a period of time $1 \mu\text{s}$, which leads to reasonable results (except for the emission calibration curve in which we presented the data over $2 \mu\text{s}$, to allow us to compare our results to those obtained

by some previous work). This was repeated for the three measurements and averaged to get the average transmission of certain spectral line over 1 μ s.

7. The previous steps were repeated for all samples in order to construct the calibration curves based on the absorption ($1 - (I_{\text{trans.}} / I_0)$) or just the transmission ($I_{\text{trans.}} / I_0$) as followed in our analysis.

Some raw data including the emission of Cu I 324, 327 and Zn I 481 nm for the three repeated acquisitions as a function of time for the 0.66/99.34, 1.47/98.34, 8.31/91.69 and 13.47/86.53 Cu/Zn samples are shown in Fig. 6.10 to Fig.6.14, respectively. The laser fluence of the light source spot is $\sim 14.8 \text{ J/cm}^2$, while that is incident on the analyte spot is $\sim 5.9 \text{ J/cm}^2$. This enabled us to deduce the calibration curves based on the transmission of some of the previously mentioned emission lines.

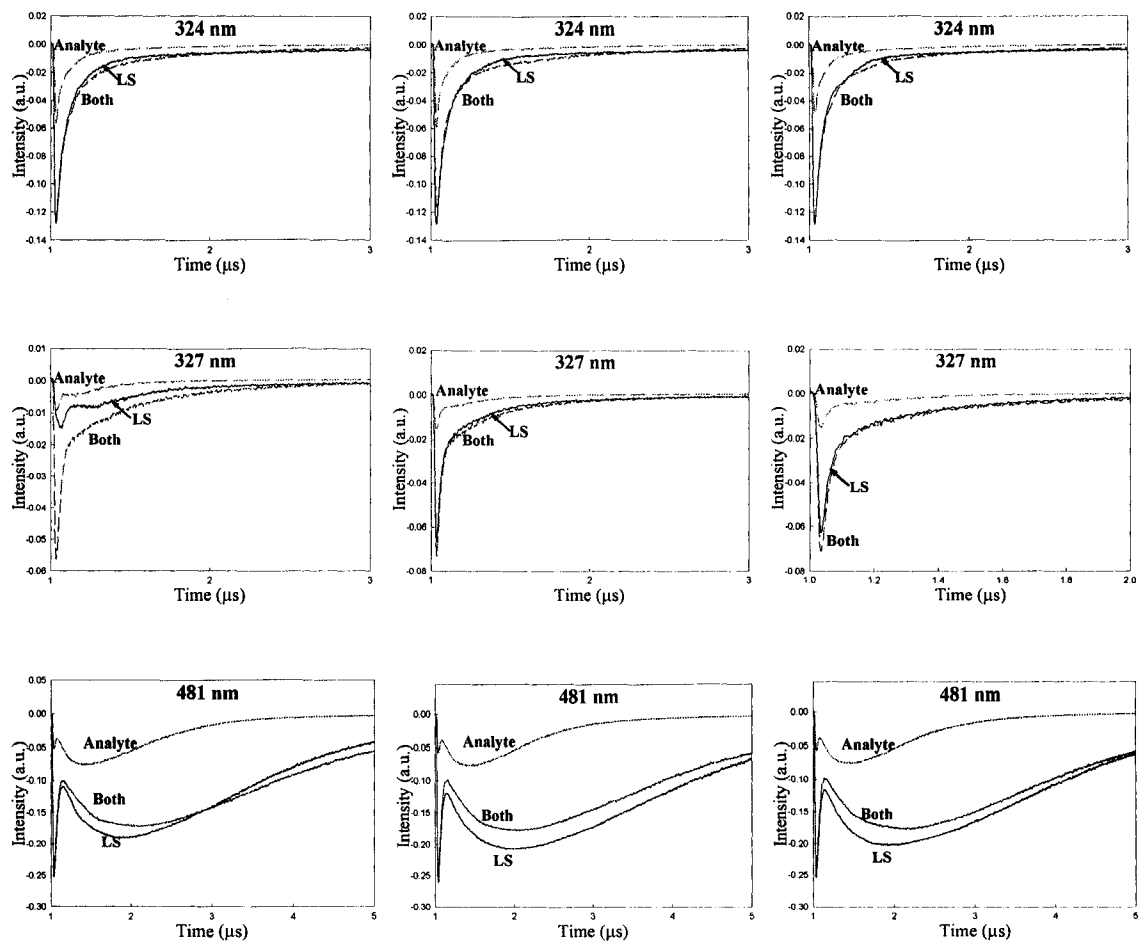


Fig. 6.10 The emission intensity resulting from the three acquired measurements for the spectral lines; Cu I 324 and 327 and Zn I 481 nm as a function of the time for the 0.66/99.34 Cu/Zn sample.

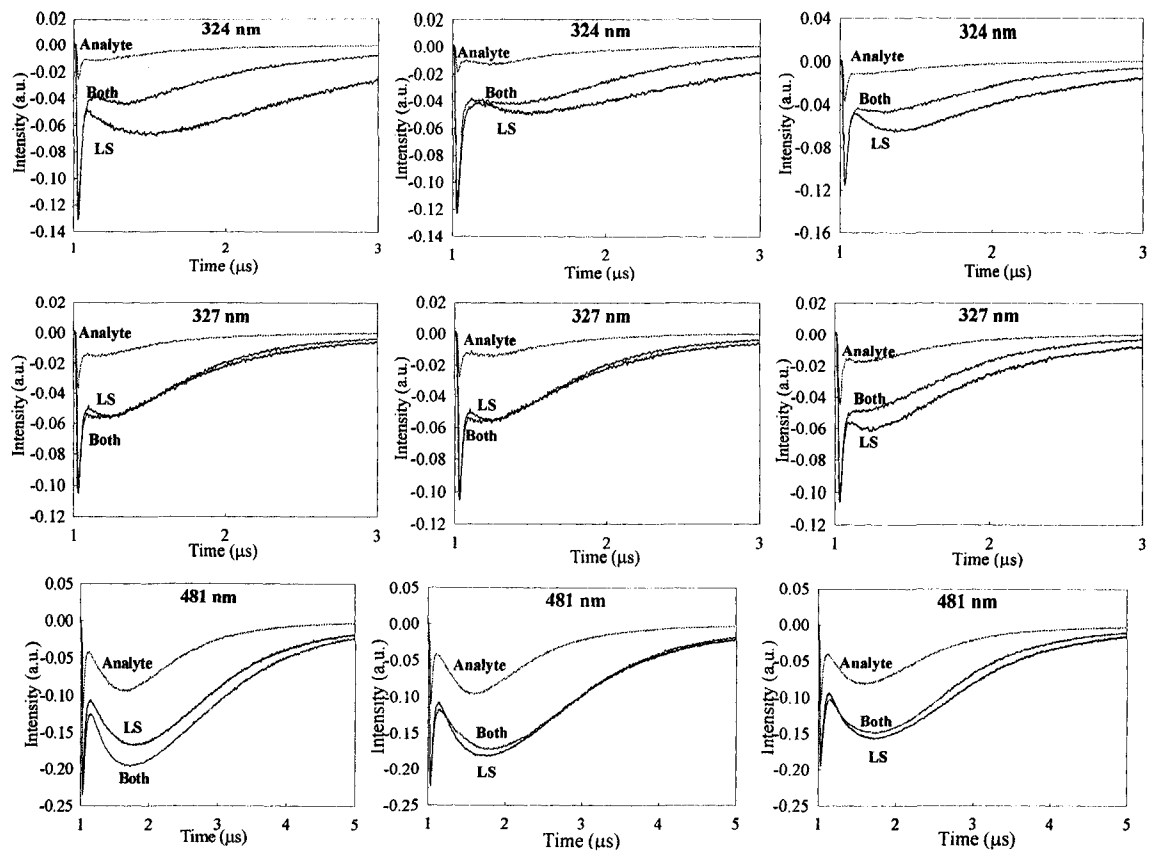


Fig. 6.11 The emission intensity resulting from the three acquired measurements for the spectral lines; Cu I 324 and 327 and Zn I 481 nm as a function of the time for the 1.47/98.34 Cu/Zn sample.

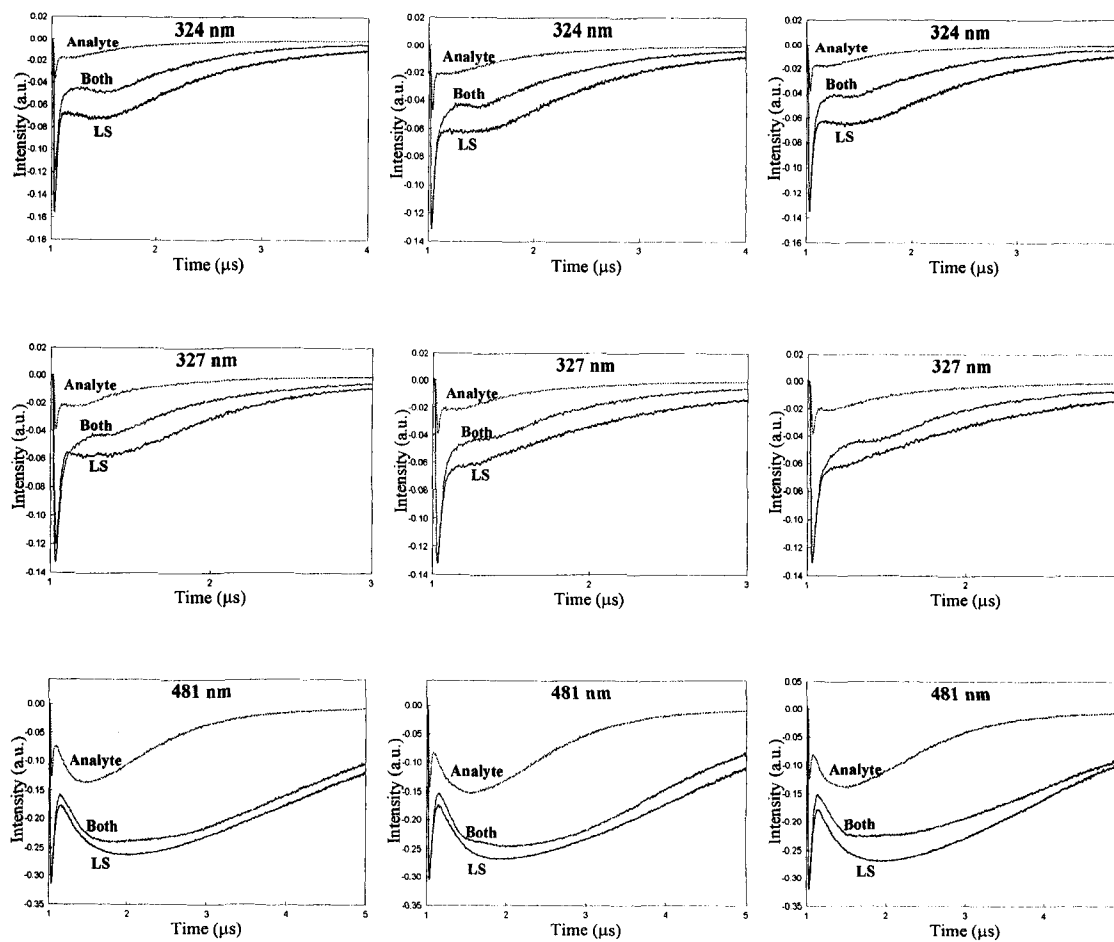


Fig. 6.12 The emission intensity resulting from the three acquired measurements for the spectral lines; Cu I 324 and 327 and Zn I 481 nm as a function of the time for the 8.31/91.69 Cu/Zn sample.

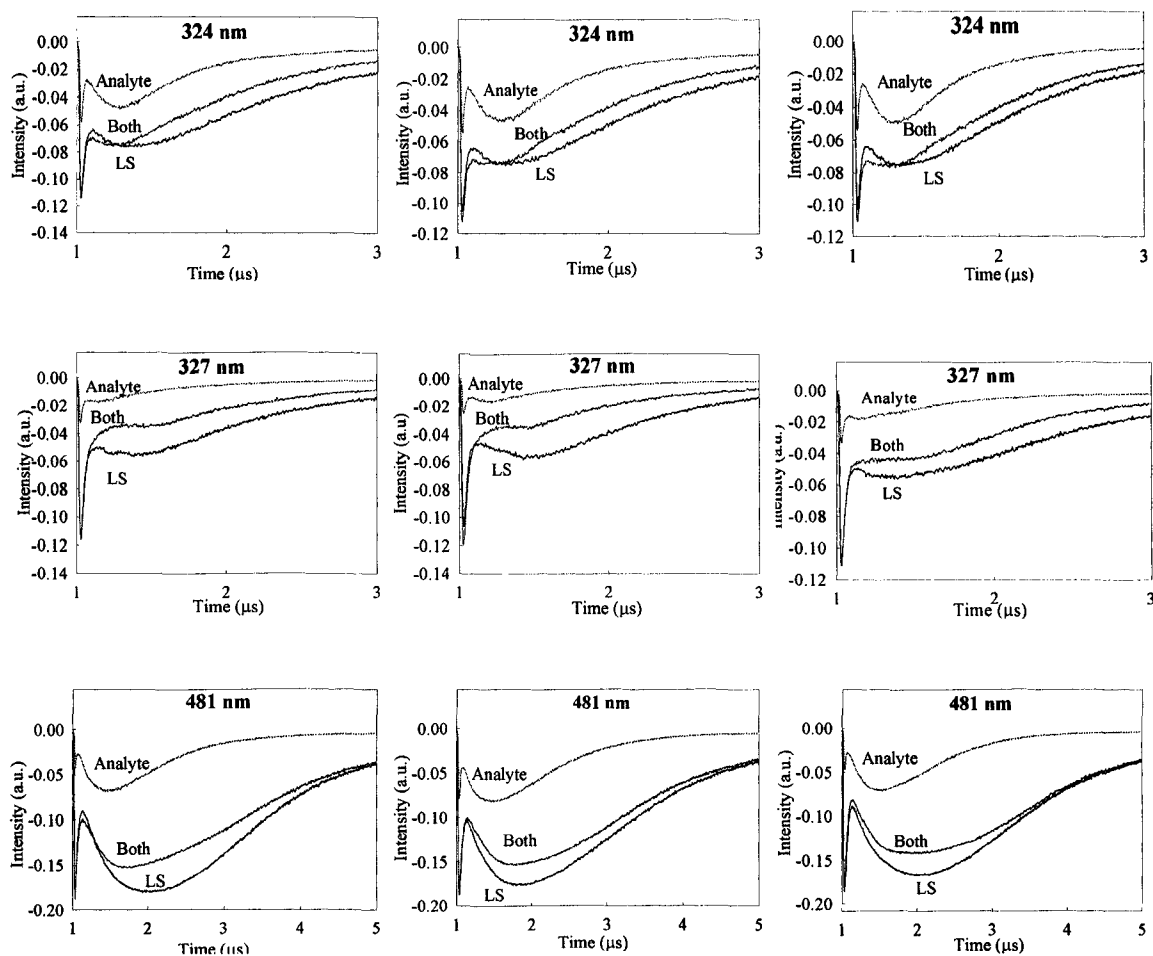


Fig. 6.13 The emission intensity resulting from the three acquired measurements for the spectral lines; Cu I 324 and 327 and Zn I 481 nm as a function of the time for the 13.47/86.53 Cu/Zn sample.

Figure 6.14 displays the calibration graphs for Cu and Zn obtained from a SA-LIBS experiment measured at atmospheric pressure and laser fluence of $\sim 14.8 \text{ J/cm}^2$ for the laser incident on the spot representing the light source and $\sim 5.9 \text{ J/cm}^2$ for the analyte spot. For each measurement, emission light was accumulated from 256 consecutive scans for the light source I_{LS} , analyte I_A and both spots together I_{Both} , which was initially triggered by the laser pulse. The curves are highly non-linear and show decreasing Cu line intensities with increasing Cu content, which is similar to the trend reported by Gagean

and Mermet [9], who studied the influence of different laser wavelengths on the ablation process in detail. Their detector was an inductively coupled plasma atomic-emission spectrometer. This non-linearity can be attributed to the structural changes in the alloys that result in different ablation rates for the samples with different Zn/Cu compositions under atmospheric pressure. The error bars representing the standard deviation are clearly shown and demonstrated in Fig. 6.14 for 324, 481 and 522; however, it is hardly noticed for Cu522 nm, since they are so small ($\sim 1.3e-3$ and $1.5e-3$).

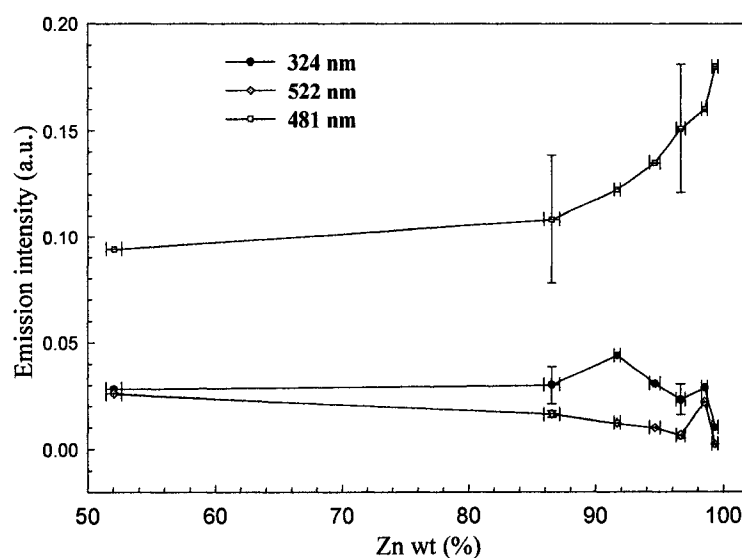


Fig. 6.14 Calibration curves for different Cu and Zn emission lines resulted from Self-absorption-LIBS technique (SA-LIBS) using the integrated intensities of those spectral lines over a time period of $2 \mu\text{s}$ (from 1.2 to $3.2 \mu\text{s}$).

Another possible explanation to account for the non-linearity of the calibration graphs is that the plasma conditions are influenced by differences of the ablated mass and by changes in the bulk stoichiometry. A study of the efficiency of laser ablation was investigated by Borisov et al. [10], who used three different laser systems with 35 ps and

6 and 30 ns at 532, 266 and 252 nm, respectively. In their work, the ablated material was transported to and detected in an inductively coupled plasma mass-spectrometer. Their measurements showed that non-linearity in calibration graphs during laser ablation of brass samples are independent of the laser pulse length or wavelength and are most probably connected with changes in the mass ablation rate. They explained this behavior by structural changes that influence the melting temperature and the reflectivity of the sample surface. Therefore, the mass ablation rate is a function of the Zn/Cu ratio. Another important observation is that there is a relation between the non-linearity of the Cu calibration and the thermal pre-treatments of samples during their production. The same behavior was found in experiments with fs-pulses and direct detection of the emission spectra of a laser plasma. Therefore, the observed non-linearity of the calibration plots for the two elements is not attributed to changes in the plasma conditions, but it is due to changes in the ablated mass.

Changes in mass ablation rate from sample to sample due to differences in the structure of the material can be overcome by analytical approaches like internal standardization [9]. Therefore, using internal standardization of the Zn to the Cu line intensity, linear calibration curves can be obtained (Fig 6.15).

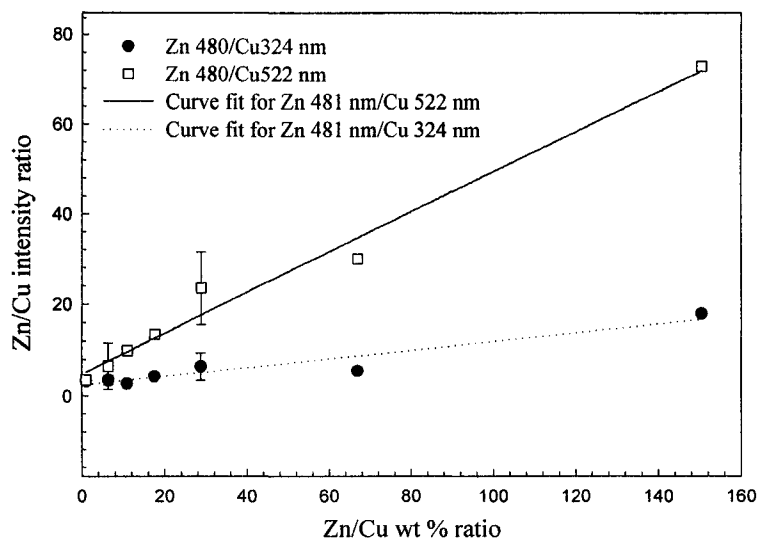


Fig. 6.15 Calibration curves for Zn signal normalized to the Cu line intensity resulted from SA-LIBS technique.

The transmission calibration curves for the samples listed in Table 1 are plotted in Fig. 6.16 and 6.17. The standard deviation for laser pulse energy is 0.1159 and 0.0371 for both LS and analyte spots. It can be seen that the exponential fit applied to the calibration curves using the chosen wavelengths ($\lambda = 324, 327$ nm) are obtained as a result of SA-LIBS approach and was assumed by equation 11. For $\lambda = 481, 472, 522$ and 468 nm, an approximately unchanged absorption value was demonstrated that can be attributed to the origin of such wavelengths from the some atomic levels insusceptible to self-absorption (Fig. 6.18 and 19).

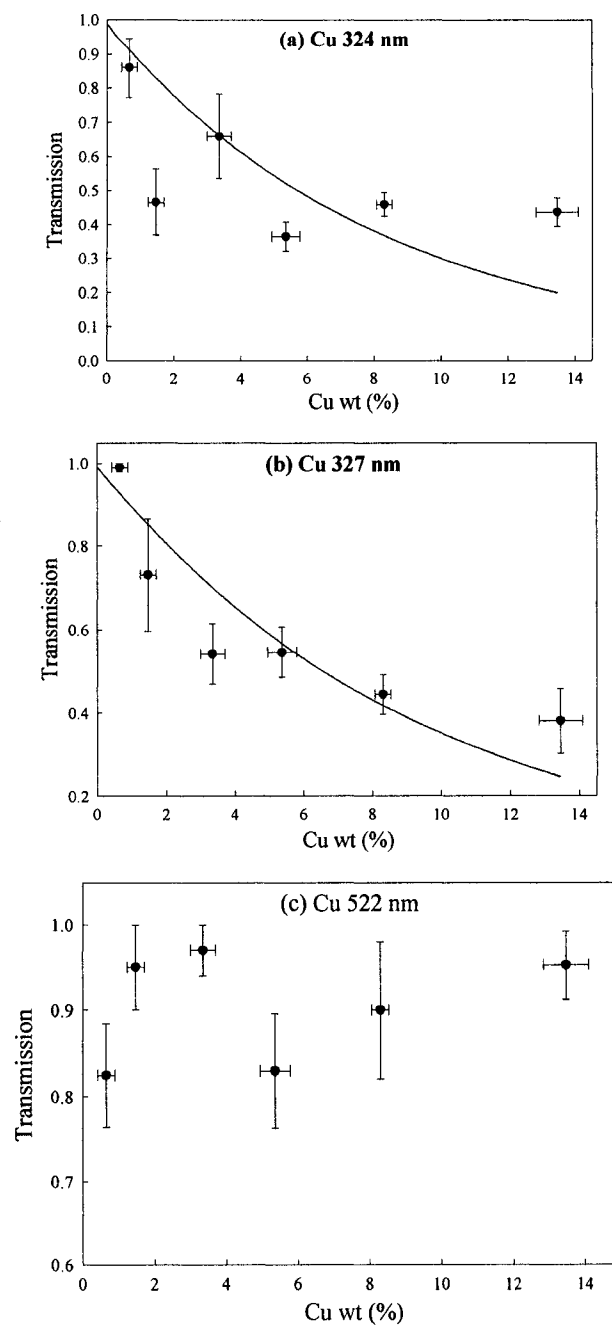


Fig. 6.16 The average transmission for the spectral lines of Cu (a) 324 nm, (b) 327 nm and (c) 522 nm as a function of the Cu wt %. For 324 and 327 nm, the fitting equation is $F = a \cdot \exp(-m \cdot x)$ with $a = 0.9859$, $m = 0.1189$ for $\lambda = 324$ nm while $a = 0.9907$, $m = 0.1038$, for $\lambda = 327$ nm.

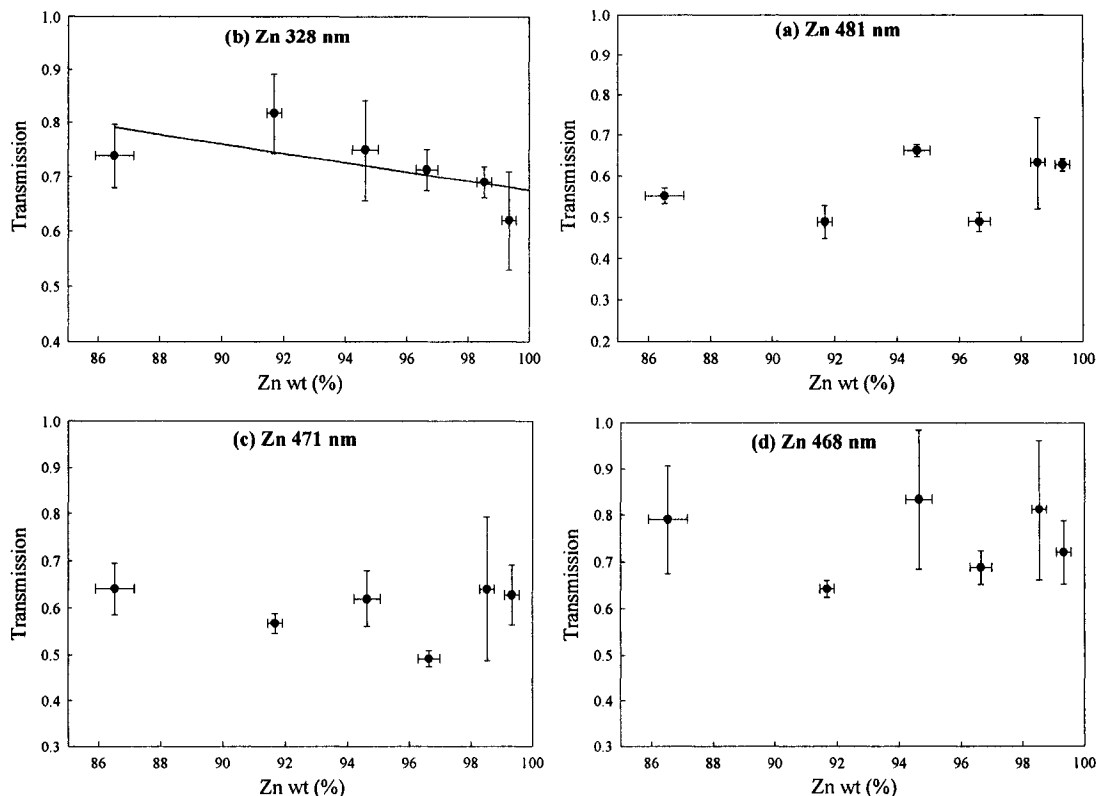


Fig. 6.17 The average transmission for the spectral lines of Zn (a) 481 nm, (b) 471 nm and (c) 468 nm as a function of the Zn wt %. For 328 nm, the fitting equation is $f = a \cdot \exp(-b \cdot x)$ with $a = 2.1525$ and $m = 0.0116$.

The plasma temperature has been evaluated using the ratio of the relative intensities of spectral lines [13,14]:

$$\frac{I_1}{I_2} = \frac{g_1 A_1 \lambda_2}{g_2 A_2 \lambda_1} \exp \left[- \left(\frac{E_1 - E_2}{k T_e} \right) \right] \quad (14)$$

In this equation, subscripts 1 and 2 refer to the two spectral lines of the same element, respectively. The spectroscopic constants I_i , λ_i , g_i , A_i and E_i ($i = 1, 2$) represent the line intensity, wavelength, statistical weight, transition probability and the energy of the excited state, respectively. These relevant spectroscopic constants are tabulated in Table 2. T_e and k are the electron temperature and the Boltzmann constant, respectively. The Grotrian diagram showing the possible spectral lines of both Cu and Zn, which we used

in our analysis, is shown in Fig. 6.13 and 14. Two of the emission lines of Zn(I), $4s4d\ ^3D_3 \rightarrow 4s4p\ ^3P_2$ at 334.5 nm and $4s5s\ ^3S_1 \rightarrow 4s4p\ ^3P_2$ at 481.0 nm have been used to determine the electron temperature under the condition of local thermodynamic equilibrium (LTE) [15]. While for Cu sample, CuI 510, 515 and 522 nm have been used for temperature determination [16-17]. When evaluating the electron temperature by this method, it is important to verify that the plasma is not optically thick for the lines used. Systematic errors could also be present, and, thus, the temperatures are assumed to be extracted with $\sim \pm 10\%$ uncertainty, coming mainly from the uncertainties in the transition probabilities and the measurement of the integrated intensity ratios of the spectral lines used in equation (4). The plasma temperature (Fig. 6.20) is concluded to be the same for both Cu and Zn species present in the plasma under the assumption of local thermodynamic equilibrium (LTE), which was also reported by different authors [18].

Table 3: Copper and Zn spectral line parameters used for the determination of plasma temperature [15-17].

Wavelength (nm)	E (cm ⁻¹)	g _i -g _k	A _{ki} (10 ⁸ s ⁻¹)
510	30783.700	6-4	0.02
515	49935.200	2-4	0.60
522	49942.100	4-6	0.75
334	62776.981	7-5	1.50
481	53672.240	3-5	0.70
472	53672.240	3-3	0.458
468	53672.240	3-1	0.155

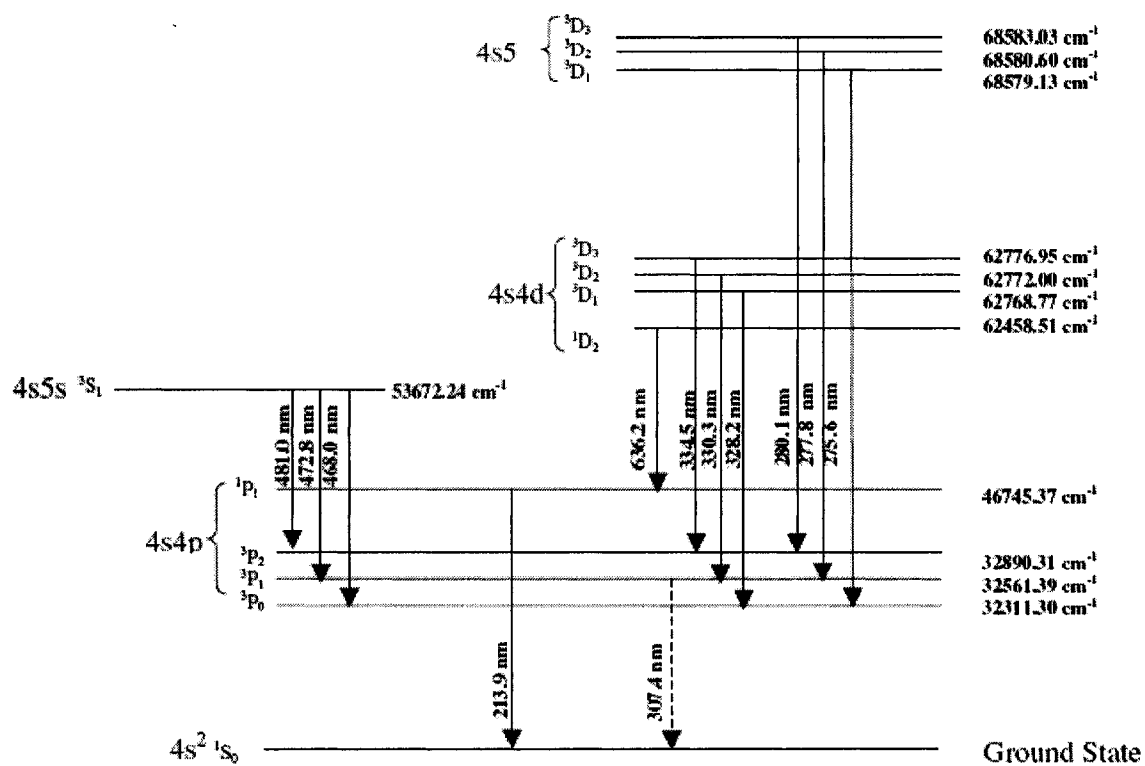


Fig. 6.18 Grotrian diagram of Zn showing the different prominent spectral lines of Zn [15].

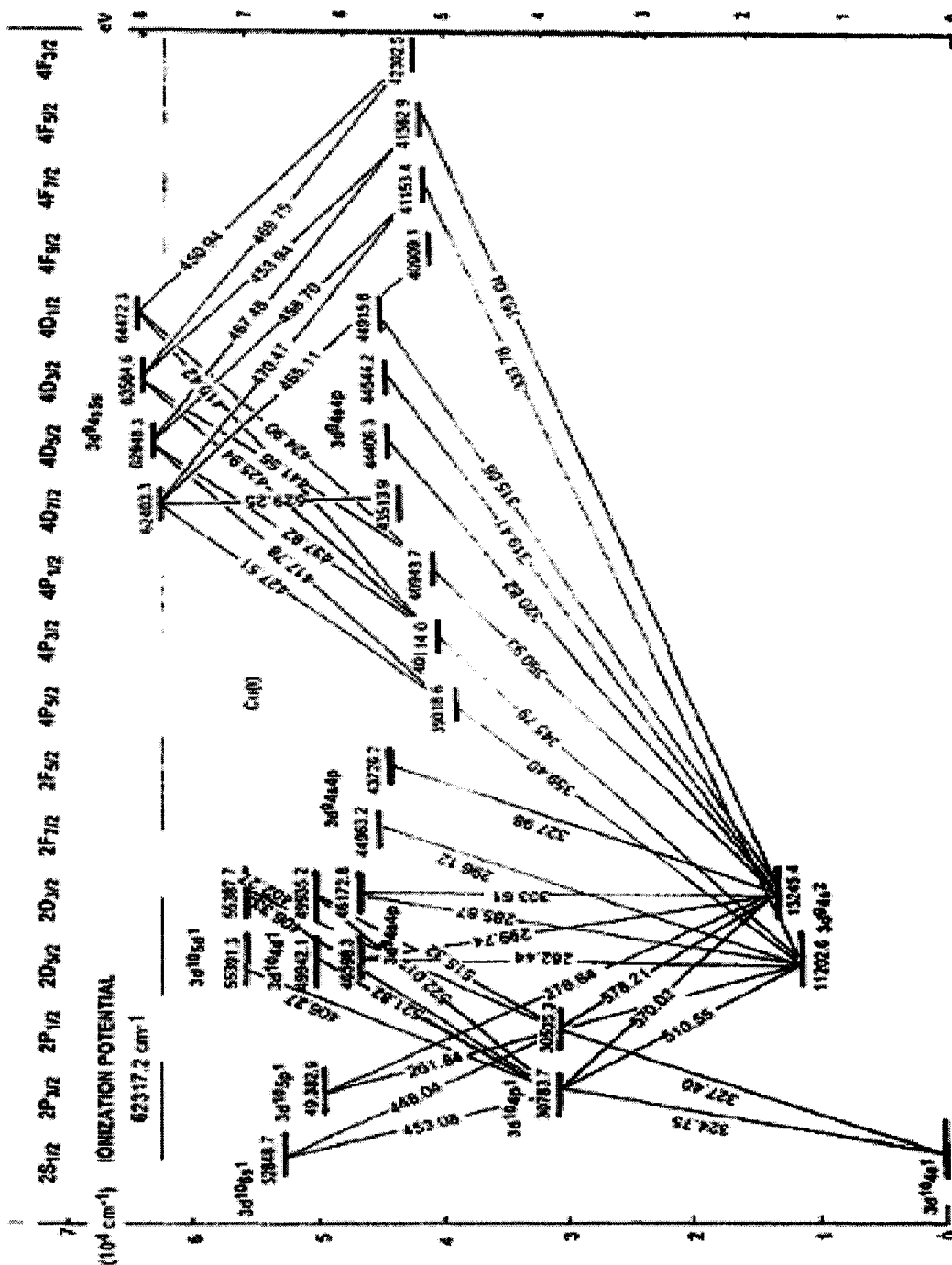


Fig. 6.19 Grotrian diagram of Cu that shows the possible atomic transition of its spectral lines [17].

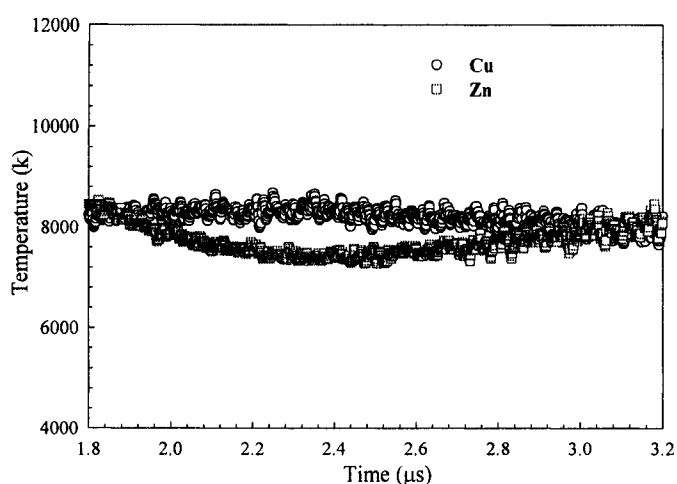


Fig. 6.20 Temporal development of plasma temperature for Cu which was calculated using the spectral lines Cu I 510, 515 and 522 nm while the plasma temperature for Zn the Zn I 334 and 481 nm were used at laser fluence of $\sim 14.5 \text{ J/cm}^2$ for the light source spot and $\sim 5.9 \text{ J/cm}^2$ for the analyte spot.

6.7 Summary

SA-LIBS of compacted brass samples was introduced as a new approach whose principle stems from the well-known Atomic absorption Spectroscopy (AAS) technique. Two closely produced plasmas were generated; one acts as the light source analogous to AAS; the other acts as the analyte. Thus, we let the plasma probe itself. Temporal development of Cu spectral lines was initially obtained so that we could examine which lines are more susceptible to self-absorption. SA-LIBS showed that Cu 324 and 327 nm are considerably subject to self-absorption while Cu 330 nm is not, a result that agrees with those reported in literature. Non-linear calibration curves were also obtained, a problem which was previously demonstrated in several reports for brass samples and was attributed to the difference in ablation rate. Internal standardization of emission lines is a method that results in linear calibration curves. Assuming that the concentration of the

absorbing species follows a Gaussian distribution, we tried to solve the familiar Beer-Lambert's law for our specific experimental condition. Linear calibration curves of the logarithm of the absorption and absorbing species concentration or equivalently exponential relationship between them have been obtained. The plasma temperature was about the same for both Zn and Cu species, which is reasonably accepted under the assumption of LTE.

References for Chapter VI

- [1] V. Lazic, R. Barbini, F. Colao, R. Fantoni, and A. Palucci, "Self-absorption model in quantitative laser induced breakdown spectroscopy measurements on soils and sediments," *Spectrochim. Acta B* **56**, 807-820 (2001).
- [2] I. B. Gornushkin, C. L. Stevenson, B. W. Smith, N. Omenetto, and J. D. Winefordner, "Modeling an inhomogeneous optically thick laser induced plasma: a simplified theoretical approach," *Spectrochim. Acta B* **56**, 1769-1785 (2001).
- [3] H. Amamou, A. Bois, B. Ferhat, R. Redon, B. Rossetto, and P. Matheron, "Correction of self-absorption spectral line and ratios of transition probabilities for homogeneous and LTE plasma," *J. Quantit. Spectrosc & Radiat. Transfer* **75**, 747-763 (2002).
- [4] D. Bulajic, M. Corsi, G. Cristoforetti, S. Legnaioli, V. Palleschi, A. Salvetti, and E. Tognoni, "A procedure for correcting self-absorption in calibration free-laser induced breakdown spectroscopy," *Spectrochim. Acta B* **57**, 339-353 (2002).
- [5] A. M. El Sherbini, Th. M. El Sherbini, H. Hegazy, G. Cristoforetti, S. Legnaioli, V. Palleschi, L. Pardini, A. Salvetti, and E. Tognoni, "Evaluation of self-absorption coefficients of aluminum emission lines in laser-induced breakdown spectroscopy measurements," *Spectrochim. Acta B* **60**, 1573-1579 (2005).
- [6] P. A. Miller, G. A. Hebner, and R. L. Jarecki, "Optical self-absorption technique for qualitative measurement of excited-state densities in plasma reactors," *J. Vac. Sci. Technol. A* **16**(6), (1998).
- [7] G. N. Watson, "Theorems Stated by Ramanujan (IV): Theorems on Approximate Integration and Summation of Series," *J. London Math. Soc.* **3**, 282-289 (1928).

- [8] P. S. Doidge, "A compendium and critical review of neutral atom resonance line oscillator strengths for atomic absorption analysis," *Spectrochim. Acta B* **50**, 209-263 (1995).
- [9] J. Baldwin, "Q-Switched laser sampling of copper-zinc alloys," *Appl. Spectrosc.* **24**, 429-435 (1970).
- [10] E. Cromwell and P. Arrowsmith, "Fractionation effects in laser ablation inductively coupled plasma mass spectrometry," *Appl. Spectrosc.* **49**, 1652-1660 (1995).
- [11] M. Gagean and J. M. Mermet, "Study of laser ablation of brass materials using inductively coupled plasma atomic emission spectrometric detection," *Spectrochim. Acta B* **53**, 581-591 (1998).
- [12] O. V. Borisov, X. L. Mao, A. Fernandez, M. Caetano, and R. E. Russo, "Inductively coupled plasma mass spectrometric study of non-linear calibration behavior during laser ablation of binary Cu-Zn alloys," *Spectrochim. Acta B* **54**, 1351-1365. (1999).
- [13] V. Margetic, A. Pakulev, A. Stockhaus, M. Bolshov, K. Niemax, and R. Hergenroder, "A comparison of nanosecond and femtosecond laser-induced plasma spectroscopy of brass samples," *Spectrochim. Acta B* **55**, 1771-1785 (2000).
- [14] H. Griem, In "*Principles of Plasma Spectroscopy*," Cambridge University Press, Cambridge, (1997).

- [15] N. M. Shaikh, B. Rashid, S. Hafeez, Y. Jamil, and M. A. Baig, "Measurement of electron density and temperature of a laser-induced zinc plasma," *J. Phys. D: Appl. Phys.* **39**, 1384-391 (2006).
- [16] NIST Atomic Spectra Database, <http://physics.nist.gov>.
- [17] B. Nemet and L. Kozma, "Time-resolved optical emission spectrometry of Q-switched Nd:YAG laser-induced plasmas from copper targets in air at atmospheric pressure," *Spectrochim. Acta B* **50**, 1869-1888 (1995).
- [18] W. Mohamed and A. Askar, "Study of the matrix effects on the plasma characterization of heavy elements in soil sediments using LIBS with a portable Echelle spectrometer," *Prog. Phys.* **1**, 46-52 (2007).

CHAPTER VII

CONCLUSIONS AND FUTURE WORK

As a consequence of the drawbacks of the current quantitative methods commonly used for routine analysis of difficult solid materials or non-conducting solids, the development of the existing techniques or searching for new methods was a logical demand. Some attention was focused on Laser Induced Breakdown Spectroscopy (LIBS) which is considered one of the most successful spectrometric methods based on emission spectroscopy due to its simplicity, quickness and its in-situ, real time characteristics. Various approaches for the optimization of LIBS sensitivity were investigated in this dissertation, with first focusing on increasing its sensitivity, which included the enhancement of the signal-to-background (S/B) ratio. Second, we reconfigured the LIBS experimental setup in such a way to replicate that of the Atomic Absorption Spectroscopy (AAS) since it represents the most sensitive technique compared to other spectroscopic methods. The first approach could be developed to introduce a low cost probe and a measuring tool to develop real-time, non-contact, distant measurement technique for the determination of concentration of any type of samples with the aid of the commercially available portable low power laser sources. For the second approach, theoretical modeling work could be more extensively performed to investigate its application in the determination of the trace elements.

7.1 Conclusions of the present work

Chapters II and III emphasize the research trends toward improving the figure of merit of LIBS. This was followed by the physics outlines of the laser-surface interaction

and the mechanisms for producing both the line and continuum emission of the produced plasma. The mathematical principles of the analytical laboratory plasmas are outlined. Then characterization methods of such plasma are summarized and how they relate to the concentration of the analyte sample.

Chapter IV, V, and VI include a description of the LIBS instrumentation, system calibration and the analysis schemes for single and multi element samples, which were adopted for spectral line identification and selection. The spectral characteristics of a number of considered samples were also presented and discussed in the context of system optimization for analytical purposes. Results of test measurements for the consistency of our instrumentation were also presented. This was followed by investigating two main experimental approaches whose aim was to present new optimization method for LIBS to enhance its sensitivity and to benefit from the self-absorption method and use it as an advantage of the technique. In Chapter V, the Spark Discharge assisted Laser Induced Breakdown Spectroscopy (SD-LIBS) of single-element samples in which a transient plasma propagating along the surface of a solid matrix is enforced between a pair of electrodes in air at atmospheric pressure was compared to conventional LIBS. Enhanced spectral line intensity and signal-to-background (S/B) ratio were observed. Also, significant reduction in laser energy requirement can be achieved in SD-LIBS compared to standard LIBS. The peak plasma temperature was about the same for both SD-LIBS and LIBS. The estimated peak plasma electron density in SD-LIBS is comparable to those reported for conventional LIBS. The noticeable increase in line emission signal is explained by the extended temporal evolution of the line emission in SD-LIBS and the increase in the size of the plasma. Since SD-LIBS also allows for the significant

reduction in the laser pulse energy, it causes less surface area damage and shallower craters. Although the initiation of the spark discharge with the laser plume simplifies the operation of SD-LIBS, it introduces signal dependence on plume transient time and spark discharge interaction with the plume. Optimization of SD-LIBS can include external triggering of the spark discharge and electrode shape modification to achieve better energy coupling to the plume.

Chapter VI embodied the results of a systematic study on the self absorption LIBS technique that aimed to use the plasma to probe itself. Time-integrated and time-resolved profiles of the selected spectral lines were used to examine the characteristics of such approach in detail. Numerous spectral profiles were explored so that the optimal analytical lines were selected and criteria of their use to perform calibration for quantitative analysis were examined. Non linear calibration curves are obtained that are attributed to the structural changes in the samples, which result in different ablation rates for the samples with different Zn/Cu compositions under atmospheric pressure. Using internal standardization of the Zn to the Cu line intensity, linear calibration curves have been obtained. The transmission curves were found to be exponentially proportional to the concentration, which is equivalent to the linear relationship between the logarithm of the transmission and the concentrations.

7.2 Future Work

The SD-LIBS is a simple technique and could be a robust method for environmental applications such as the analysis of heavy elements in soil and could be used as a direct simultaneous trace quantitative analysis of non-conductive solids. In SD-LIBS, better signal-background ratios may be achieved by optimizing the instrument to

observe emission either away from or in the discharge axis. Time-resolved spark spectroscopy should give a clearer picture of the discharge development with high temporal resolution. For the production of time-resolved spectra, an electronically controlled source operating with a high precision in time is needed. Recently developed CCDs allow measurements of spectral intervals with time resolutions of ns. The differences in decay time between ionic and atomic lines can provide a good mechanistic insight into, and suggest additional practical applications of, the spark discharge-LIBS plasma. All these parameters will allow a more exact knowledge of its dynamics and density, which leads to fully exploit the spark discharge-LIBS plasma for accurate quantitative analysis.

A more comprehensive optimization of spark spectrometry asks for detailed knowledge on the fundamental processes of sample vaporization and signal generation. The spark source should be optimized in the physical ablation so that the maximum amount of sample is vaporized with minimum ejection of molten material. Although the thermal interaction of plasma with sample may be reduced with state-of-the-art source, only separation of the vaporization and excitation can lead to lower matrix effects and detection of less complex emission spectra. The future of spark spectroscopy lies with the development of a fully automated portable system, with data processing facilities, for on-line and in-situ analysis. Automated quantitative and semi-quantitative analysis routines using spectral databases, coupled with multivariate statistical analysis and spectral libraries, should lead to a broader range of the technique's applicability. A software expert can, for instance, integrate the optimal, appropriate number of ablation shots for each element, spectral line, and sample matrix. The use of neural networks then becomes

important. When considering future improvements, however, it should be borne in mind that any developments ought to be weighed against the risk of reducing the technique's simplicity.

While the experiments presented here are primarily ablation of solids by focusing a laser beam normal to the assisted spark, it would be of considerable interest to study ablation with the electric field in the direction of the laser beam. Such an extension would show potentials for a variety of applications requiring real-time, non-contact, remote monitoring of elemental analysis. The study of SD-LIBS, when combined with laser ablation using picosecond or femtosecond laser, would also be of interest.

A direct extension of the second experiment SA-LIBS would be a parametric study of the formation and dynamics of the SA-LIBS plasmas. It would be of great interest to investigate these types of plasmas under different ambient gas environments with different target materials (e.g., semiconductors and insulators). A slightly different direction would be a study of laser pulse duration and wavelength influence on the initiation and expansion of the laser ablation plasma. No such information, both experimental and theoretical, is available at the present time.

APPENDIX

Cu/Zn Samples used in this work

Preparation procedure for Cu/Zn samples

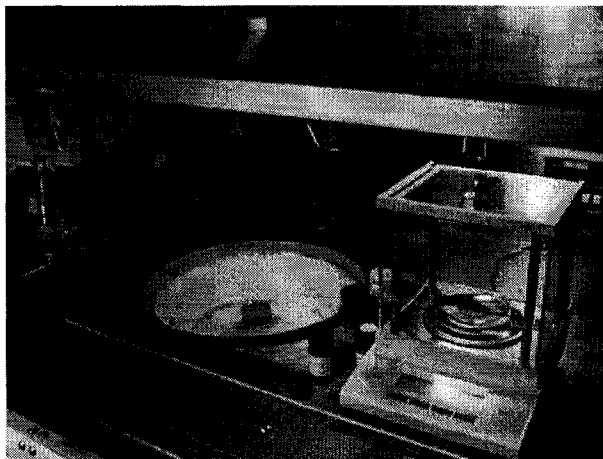
Equipment and materials needed:

1. Corning stirring /hotplate.
2. Glass vial with plastic lid.
3. Magnetic stirring beads.
4. Satorious GC 503 scale.
5. Buehler Specimen Mount Press with heater.
6. Syringe to inject argon gas.
7. Zn powder (Alfa Aesar stock # 10835, 6-9 micron).
8. Cu powder (Alfa Aesar stock # 43978, 0.2-0.3 micron).

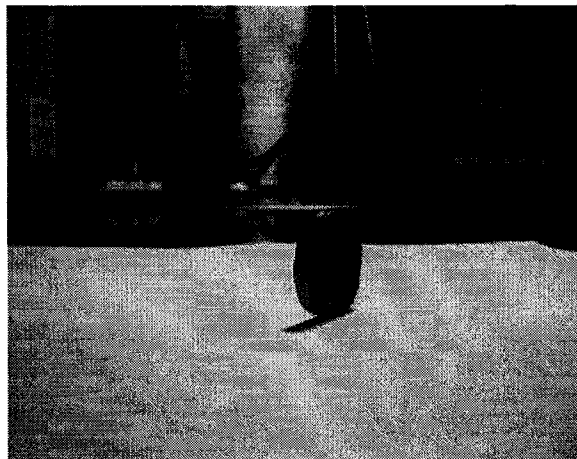
Procedure:

- Using the scale, weigh the desired amount of Cu (e.g. 0409 g) and Zn (e.g. 9.9036 g) separately. Total weight needed for a disc is ~ 10.0 g.
- Pore the Cu and Zn into glass vial with magnetic stirring bead cover with thin plastic lid and punch two holes in the lid with syringe. Fill the syringe with argon and inject into the lid of the glass vial.
- Place the Cu/Zn sample on the corning stirring plate and clamp in place with rod and holder. Set stirring rate at 10. Stirring the sample at least one hour.
- Place the Cu/Zn sample in Buehler specimen mount. Tap the side of the mount to uniform Cu/Zn evenly. While placing specimen mounts cover

on, carefully use the argon syringe to displace the air. Place holder and heater unit in press and apply 9000 lbs of pressure. Desired time for heater is 6 hrs and 12 hrs of continuous pressure.

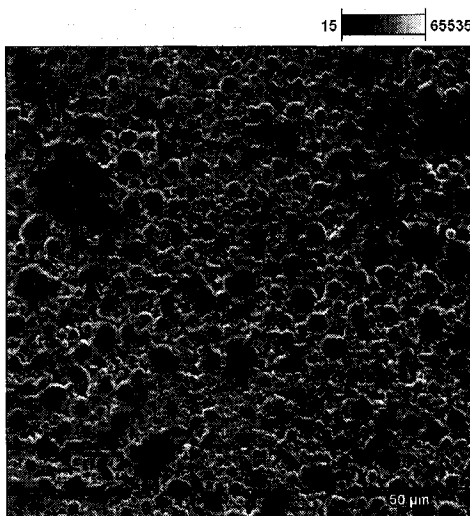


SPINCOATER FOR MIXING



Cu/Zn PRESSED SAMPLE

- **Sample (1)**



Accelerating Voltage: 20.0 kV Magnification: 500

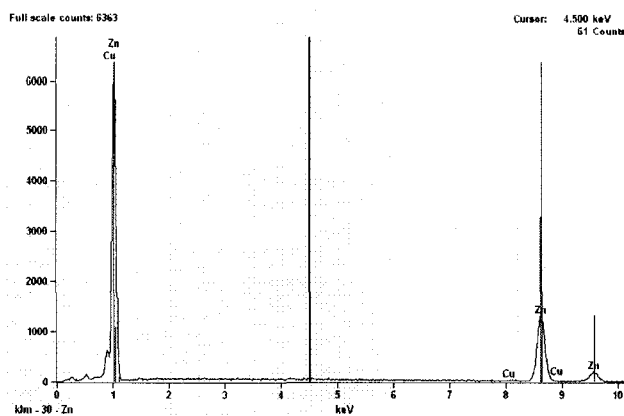


Table 1. Quantitative results of sample (1) – spot 1

<i>Element</i>	<i>Net Counts</i>	<i>Weight %</i>	<i>Norm. Wt. %</i>	<i>Norm. Wt. % Err</i>	<i>Atom %</i>	<i>Atom % Error</i>
<i>Cu</i>	94	0.40	0.40	+/- 0.27	0.42	+/- 0.27
<i>Cu</i>	537	---	---	---	---	---
<i>Zn</i>	23541	---	---	---	---	---
<i>Zn</i>	55777	99.60	99.60	+/- 0.57	99.58	+/- 0.57
<i>Total</i>		100.00	100.00		100.00	

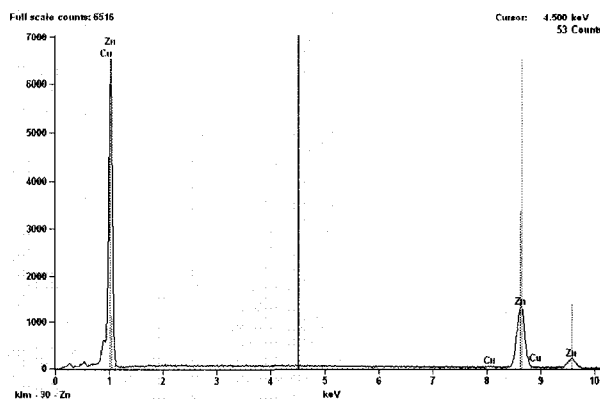


Table 2. Quantitative results of sample (1) – spot 2

<i>Element</i>	<i>Net Counts</i>	<i>Weight %</i>	<i>Norm. Wt. %</i>	<i>Norm. Wt. % Err</i>	<i>Atom %</i>	<i>Atom % Error</i>
<i>Cu</i>	233	0.97	0.97	+/- 0.26	0.99	+/- 0.27
<i>Cu</i>	551	---	---	---	---	---
<i>Zn</i>	24622	---	---	---	---	---
<i>Zn</i>	56211	99.03	99.03	+/- 0.57	99.01	+/- 0.57
<i>Total</i>		100.00	100.00		100.00	

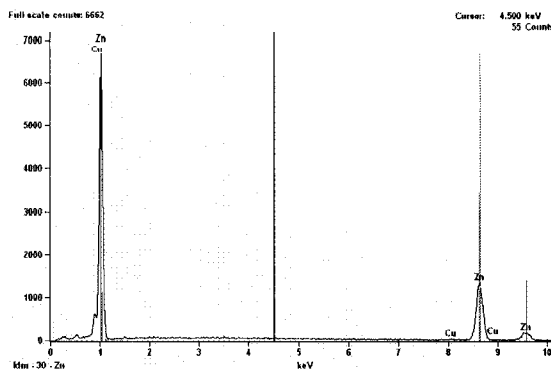
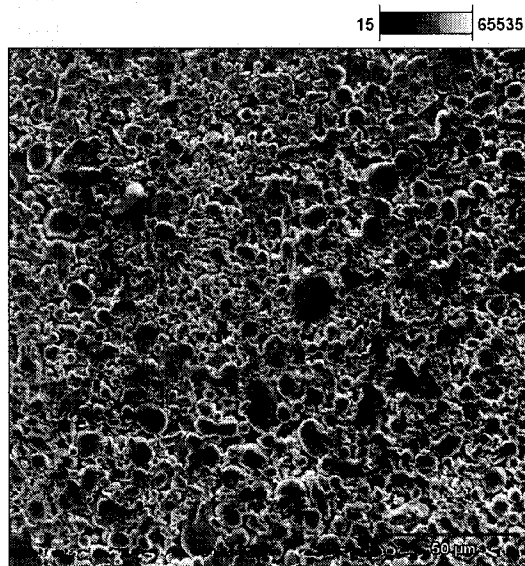


Table 3. Quantitative results of sample (1) – spot 3

<i>Element</i>	<i>Net Counts</i>	<i>Weight %</i>	<i>Norm. Wt. %</i>	<i>Norm. Wt. % Err</i>	<i>Atom %</i>	<i>Atom % Error</i>
<i>Cu</i>	144	0.60	0.60	+/- 0.26	0.62	+/- 0.27
<i>Cu</i>	647	---	---	---	---	---
<i>Zn</i>	24826	---	---	---	---	---
<i>Zn</i>	56498	99.40	99.40	+/- 0.57	99.38	+/- 0.57
<i>Total</i>		100.00	100.00		100.00	

- **Sample (2)**



Accelerating Voltage: 20.0 kV Magnification: 500

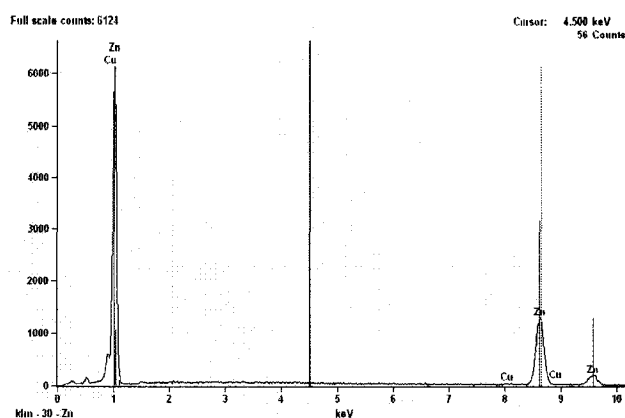


Table 4. Quantitative results of sample (2) – spot 1

<i>Element</i>	<i>Net Counts</i>	<i>Weight %</i>	<i>Norm. Wt. %</i>	<i>Norm. Wt. % Err</i>	<i>Atom %</i>	<i>Atom % Error</i>
<i>Cu</i>	327	1.42	1.42	+/- 0.27	1.46	+/- 0.28
<i>Cu</i>	959	---	---	---	---	---
<i>Zn</i>	23693	---	---	---	---	---
<i>Zn</i>	52367	98.58	98.58	+/- 0.58	98.54	+/- 0.58
<i>Total</i>		100.00	100.00		100.00	

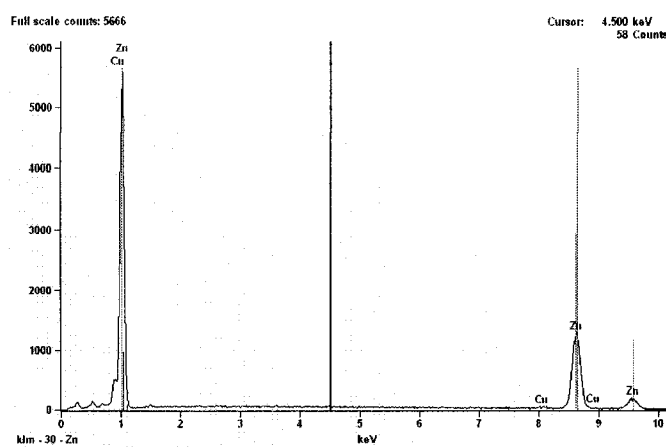


Table 5. Quantitative results of sample (2) – spot 2

<i>Element</i>	<i>Net Counts</i>	<i>Weight %</i>	<i>Norm. Wt. %</i>	<i>Norm. Wt. % Err</i>	<i>Atom %</i>	<i>Atom % Error</i>
<i>Cu</i>	379	1.73	1.73	+/- 0.31	1.78	+/- 0.31
<i>Cu</i>	522	---	---	---	---	---
<i>Zn</i>	23288	---	---	---	---	---
<i>Zn</i>	49327	98.27	98.27	+/- 0.59	98.22	+/- 0.59
<i>Total</i>		100.00	100.00		100.00	

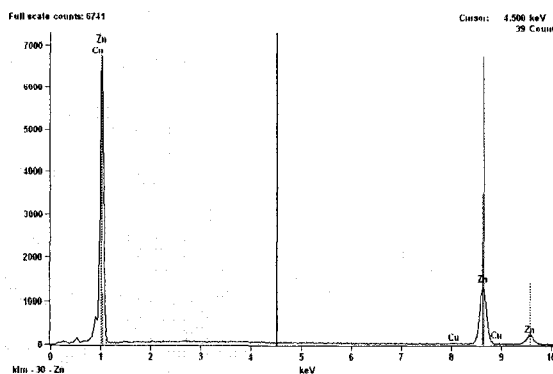
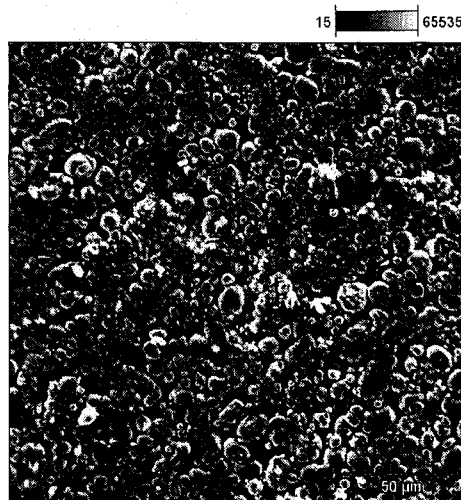


Table 6. Quantitative results of sample (2) – spot 3

<i>Element</i>	<i>Net Counts</i>	<i>Weight %</i>	<i>Norm. Wt. %</i>	<i>Norm. Wt. % Err</i>	<i>Atom %</i>	<i>Atom % Error</i>
<i>Cu</i>	324	1.27	1.27	+/- 0.26	1.30	+/- 0.27
<i>Cu</i>	522	---	---	---	---	---
<i>Zn</i>	24943	---	---	---	---	---
<i>Zn</i>	58693	98.73	98.73	+/- 0.56	98.70	+/- 0.56
<i>Total</i>		100.00	100.00		100.00	

- **Sample (3)**



Accelerating Voltage: 20.0 kV Magnification: 500

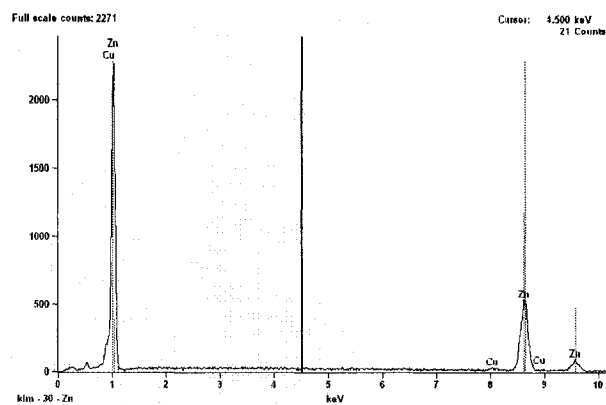


Table 7. Quantitative results of sample (3) - spot 1

<i>Element</i>	<i>Net Counts</i>	<i>Weight %</i>	<i>Norm. Wt. %</i>	<i>Norm. Wt. % Err</i>	<i>Atom %</i>	<i>Atom % Error</i>
<i>Cu</i>	292	3.10	3.10	+/- 0.49	3.19	+/- 0.50
<i>Cu</i>	374	---	---	---	---	---
<i>Zn</i>	9655	---	---	---	---	---
<i>Zn</i>	19998	96.90	96.90	+/- 0.81	96.81	+/- 0.81
Total		100.00	100.00		100.00	

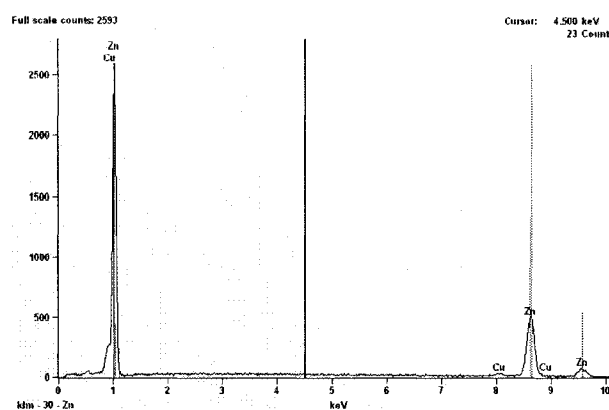


Table 8. Quantitative results of sample (3) - spot 2

<i>Element</i>	<i>Net Counts</i>	<i>Weight %</i>	<i>Norm. Wt. %</i>	<i>Norm. Wt. % Err</i>	<i>Atom %</i>	<i>Atom % Error</i>
<i>Cu</i>	374	3.60	3.60	+/- 0.47	3.70	+/- 0.48
<i>Cu</i>	742	---	---	---	---	---
<i>Zn</i>	9100	---	---	---	---	---
<i>Zn</i>	21617	96.40	96.40	+/- 0.79	96.30	+/- 0.79
Total		100.00	100.00		100.00	

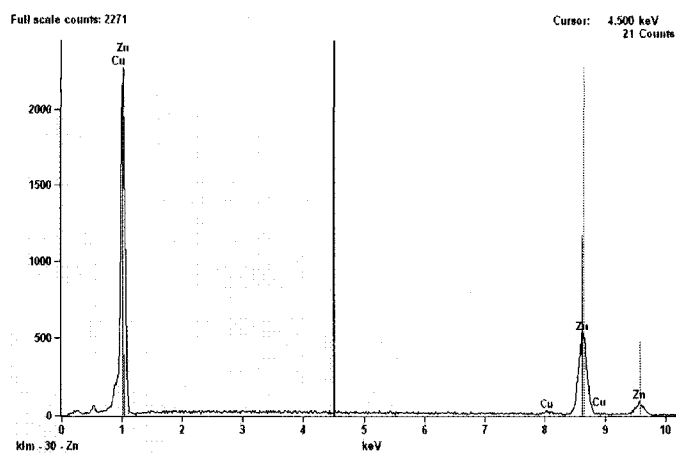
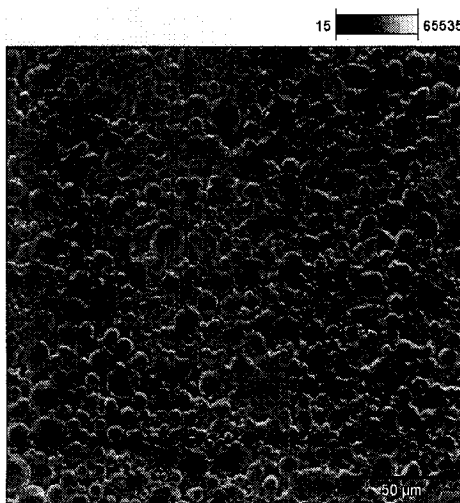


Table 9. Quantitative results of sample (3) - spot 3

<i>Element</i>	<i>Net Counts</i>	<i>Int. Cps/nA</i>	<i>ZAF</i>	<i>Weight %</i>	<i>Norm. Wt. %</i>	<i>Norm. Wt. % Err</i>	<i>Atom %</i>	<i>Atom % Error</i>
<i>Cu</i>	292	---	1.003	3.10	3.10	+/- 0.49	3.19	+/- 0.50
<i>Cu</i>	374	---	0.000	---	---	---	---	---
<i>Zn</i>	9655	---	0.000	---	---	---	---	---
<i>Zn</i>	19998	---	1.109	96.90	96.90	+/- 0.81	96.81	+/- 0.81
<i>Total</i>				100.00	100.00		100.00	

- **Sample (4)**



Accelerating Voltage: 20.0 kV Magnification: 500

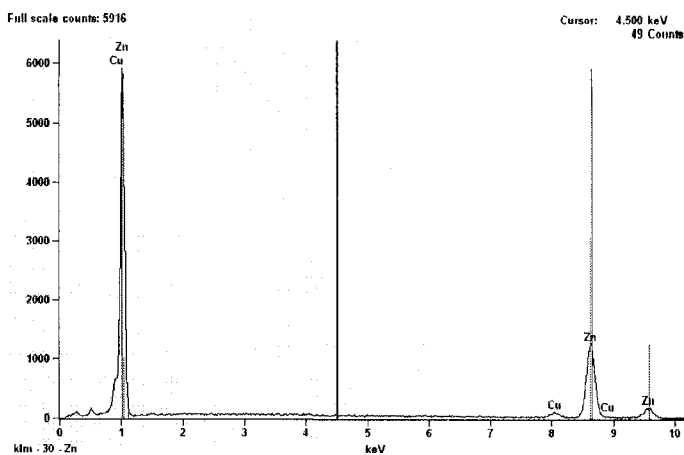


Table 10. Quantitative results of sample (4) – spot 1

<i>Element</i>	<i>Net Counts</i>	<i>Weight %</i>	<i>Norm. Wt. %</i>	<i>Norm. Wt. % Err</i>	<i>Atom %</i>	<i>Atom % Error</i>
<i>Cu</i>	1381	5.27	5.27	+/- 0.57	5.41	+/- 0.58
<i>Cu</i>	2187	---	---	---	---	---
<i>Zn</i>	22927	---	---	---	---	---
<i>Zn</i>	50769	94.73	94.73	+/- 0.57	94.59	+/- 0.57
<i>Total</i>		100.00	100.00		100.00	

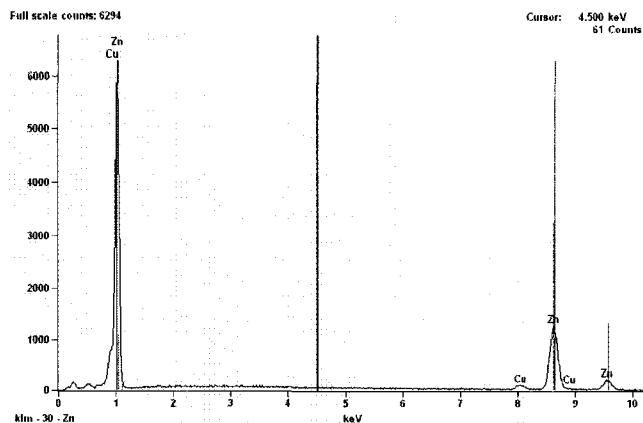


Table 11. Quantitative results of sample (4) – spot 2

<i>Element</i>	<i>Net Counts</i>	<i>Weight %</i>	<i>Norm. Wt. %</i>	<i>Norm. Wt. % Err</i>	<i>Atom %</i>	<i>Atom % Error</i>
<i>Cu</i>	1351	4.99	4.99	+/- 0.55	5.13	+/- 0.57
<i>Cu</i>	4095	---	---	---	---	---
<i>Zn</i>	22790	---	---	---	---	---
<i>Zn</i>	52961	95.01	95.01	+/- 1.38	94.87	+/- 1.38
<i>Total</i>		100.00	100.00		100.00	

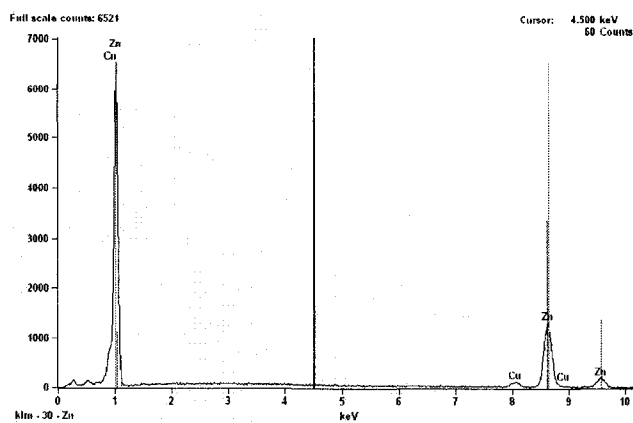
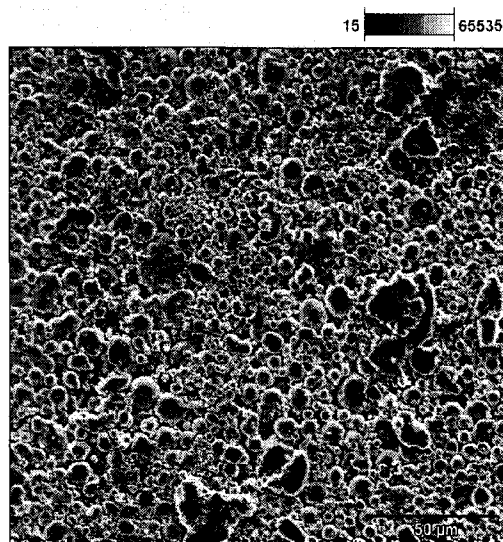


Table 12. Quantitative results of sample (4) – spot 3

<i>Element</i>	<i>Net Counts</i>	<i>Weight %</i>	<i>Norm. Wt. %</i>	<i>Norm. Wt. % Err</i>	<i>Atom %</i>	<i>Atom % Error</i>
<i>Cu</i>	1653	5.82	5.82	+/- 0.55	5.98	+/- 0.56
<i>Cu</i>	4729	---	---	---	---	---
<i>Zn</i>	23488	---	---	---	---	---
<i>Zn</i>	53686	94.18	94.18	+/- 1.37	94.02	+/- 1.36
<i>Total</i>		100.00	100.00		100.00	

- **Sample (5)**



Accelerating Voltage: 20.0 kV Magnification: 500

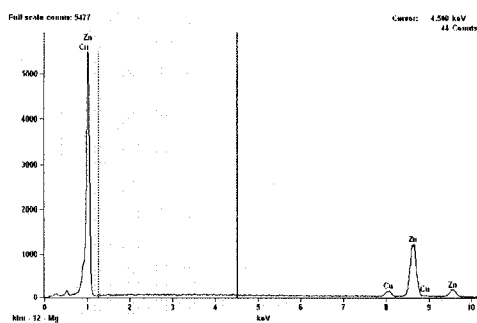


Table 13. Quantitative results of sample (5) – spot 1

<i>Element</i>	<i>Net Counts</i>	<i>Weight %</i>	<i>Norm. Wt. %</i>	<i>Norm. Wt. % Err</i>	<i>Atom %</i>	<i>Atom % Error</i>
<i>Cu</i>	2433	8.08	8.08	+/- 0.53	8.30	+/- 0.55
<i>Cu</i>	4586	---	---	---	---	---
<i>Zn</i>	23067	91.92	91.92	+/- 1.21	91.70	+/- 1.21
<i>Zn</i>	46058	---	---	---	---	---
<i>Total</i>		100.00	100.00		100.00	

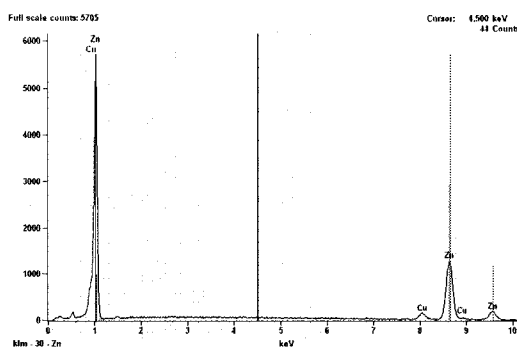


Table 14. Quantitative results of sample (5) – spot 2

<i>Element</i>	<i>Net Counts</i>	<i>Weight %</i>	<i>Norm. Wt. %</i>	<i>Norm. Wt. % Err</i>	<i>Atom %</i>	<i>Atom % Error</i>
<i>Cu</i>	2345	8.55	8.55	+/- 0.59	8.78	+/- 0.61
<i>Cu</i>	5734	---	---	---	---	---
<i>Zn</i>	22986	---	---	---	---	---
<i>Zn</i>	46368	91.45	91.45	+/- 1.45	91.22	+/- 1.44
<i>Total</i>		100.00	100.00		100.00	

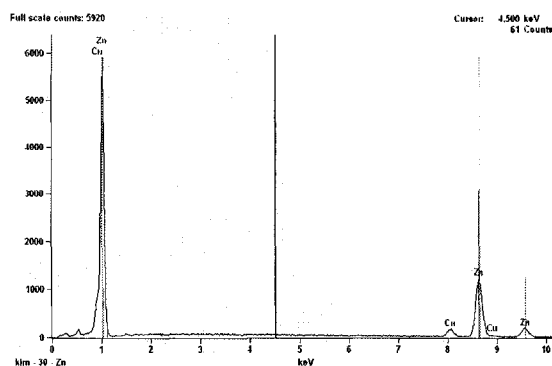
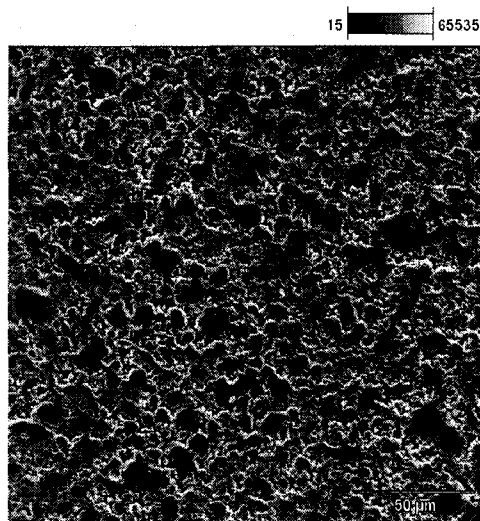


Table 15. Quantitative results of sample (5) – spot 3

<i>Element</i>	<i>Net Counts</i>	<i>Weight %</i>	<i>Norm. Wt. %</i>	<i>Norm. Wt. % Err</i>	<i>Atom %</i>	<i>Atom % Error</i>
<i>Cu</i>	2397	8.30	8.30	+/- 0.57	8.51	+/- 0.58
<i>Cu</i>	5887	---	---	---	---	---
<i>Zn</i>	22902	---	---	---	---	---
<i>Zn</i>	49370	91.70	91.70	+/- 1.42	91.49	+/- 1.41
<i>Total</i>		100.00	100.00		100.00	

- **Sample (6)**



Accelerating Voltage: 20.0 kV Magnification: 500

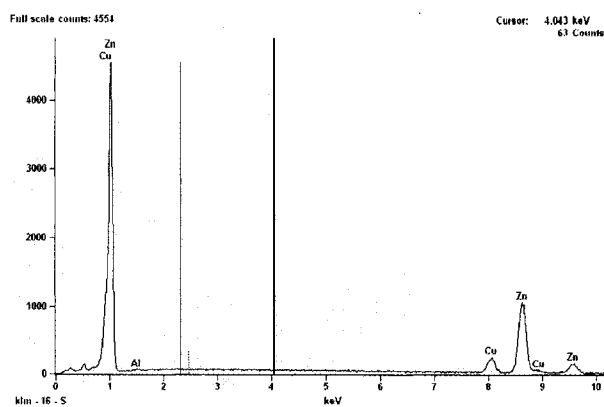


Table 16. Quantitative results of sample (6) – spot 1

<i>Element</i>	<i>Net Counts</i>	<i>Weight %</i>	<i>Norm. Wt. %</i>	<i>Norm. Wt. % Err</i>	<i>Atom %</i>	<i>Atom % Error</i>
<i>Al</i>	274	0.63	0.63	+/- 0.12	1.50	+/- 0.30
<i>Cu</i>	4064	14.19	14.19	+/- 0.62	14.41	+/- 0.63
<i>Cu</i>	8507	---	---	---	---	---
<i>Zn</i>	19210	---	---	---	---	---
<i>Zn</i>	38523	85.19	85.18	+/- 1.57	84.09	+/- 1.55
<i>Total</i>		100.01	100.00		100.00	

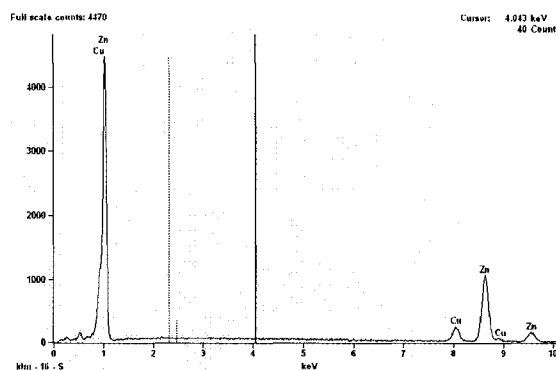


Table 17. Quantitative results of sample (6) – spot 2

<i>Element</i>	<i>Net Counts</i>	<i>Weight %</i>	<i>Norm. Wt. %</i>	<i>Norm. Wt. % Err</i>	<i>Atom %</i>	<i>Atom % Error</i>
<i>Cu</i>	3575	13.20	13.20	+/- 0.65	13.52	+/- 0.67
<i>Cu</i>	8996	---	---	---	---	---
<i>Zn</i>	19743	---	---	---	---	---
<i>Zn</i>	38126	86.80	86.80	+/- 1.62	86.48	+/- 1.61
<i>Total</i>		100.00	100.00		100.00	

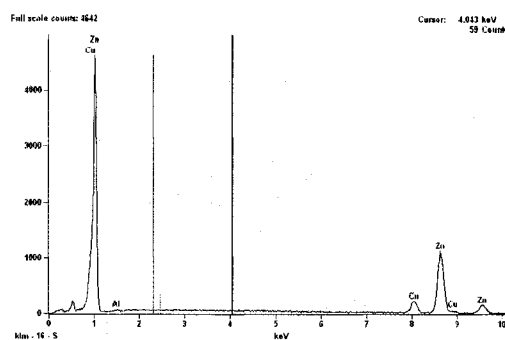
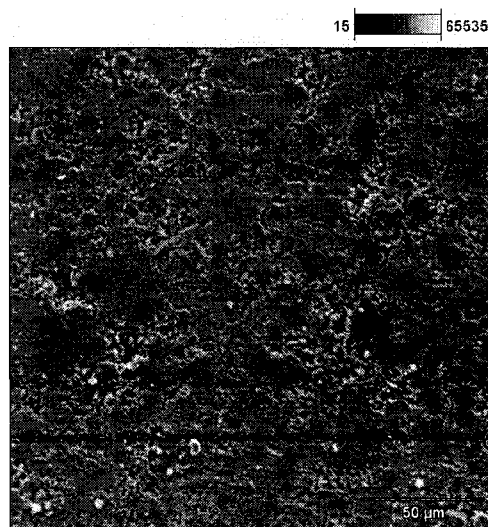


Table 18. Quantitative results of sample (6) – spot 3

<i>Element</i>	<i>Net Counts</i>	<i>Weight %</i>	<i>Norm. Wt. %</i>	<i>Norm. Wt. % Err</i>	<i>Atom %</i>	<i>Atom % Error</i>
<i>Al</i>	282	0.69	0.69	+/- 0.13	1.64	+/- 0.31
<i>Cu</i>	3493	13.03	13.03	+/- 0.65	13.23	+/- 0.66
<i>Cu</i>	8750	---	---	---	---	---
<i>Zn</i>	19503	---	---	---	---	---
<i>Zn</i>	37673	86.28	86.28	+/- 1.62	85.13	+/- 1.60
<i>Total</i>		100.00	100.00		100.00	

- **Sample (7)**



Accelerating Voltage: 20.0 kV Magnification: 500

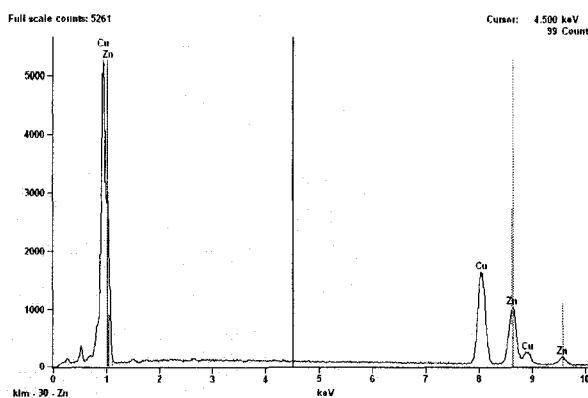


Table 19. Quantitative results of sample (7) – spot 1

<i>Element</i>	<i>Net Counts</i>	<i>Weight %</i>	<i>Norm. Wt. %</i>	<i>Norm. Wt. % Err</i>	<i>Atom %</i>	<i>Atom % Error</i>
<i>Cu</i>	29465	49.26	49.26	+/- 0.59	49.97	+/- 0.60
<i>Cu</i>	45894	---	---	---	---	---
<i>Zn</i>	17836	---	---	---	---	---
<i>Zn</i>	23067	50.74	50.74	+/- 1.89	50.03	+/- 1.86
<i>Total</i>		100.00	100.00		100.00	

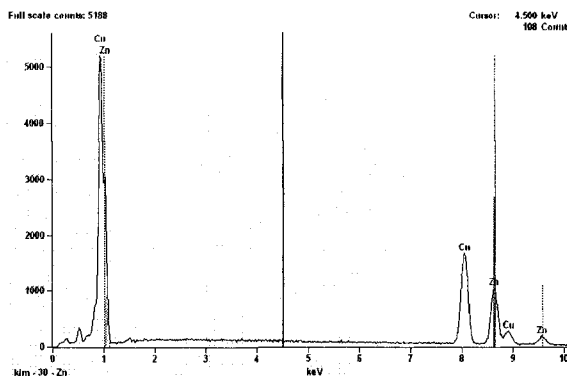


Table 20. Quantitative results of sample (7) – spot 2

<i>Element</i>	<i>Net Counts</i>	<i>Weight %</i>	<i>Norm. Wt. %</i>	<i>Norm. Wt. % Err</i>	<i>Atom %</i>	<i>Atom % Error</i>
<i>Cu</i>	28963	48.31	48.31	+/- 0.59	49.02	+/- 0.59
<i>Cu</i>	45709	---	---	---	---	---
<i>Zn</i>	18040	---	---	---	---	---
<i>Zn</i>	23925	51.69	51.69	+/- 1.87	50.98	+/- 1.84
<i>Total</i>		100.00	100.00		100.00	

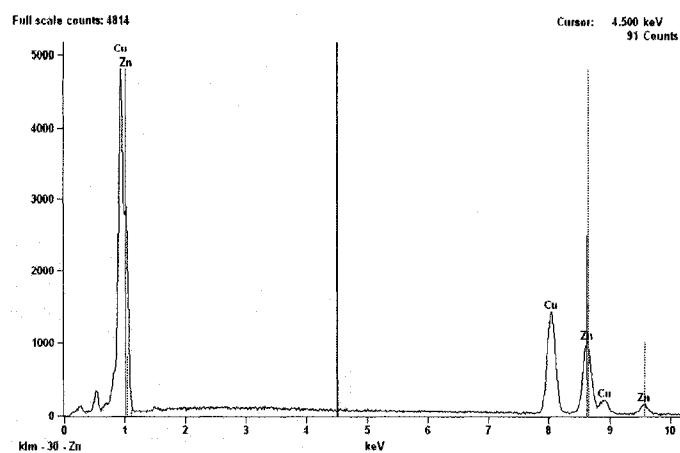


Table 21. Quantitative Results of sample (7) – spot 3

<i>Element</i>	<i>Net Counts</i>	<i>Weight %</i>	<i>Norm. Wt.%</i>	<i>Norm. Wt.% Err</i>	<i>Atom %</i>	<i>Atom % Error</i>
<i>Cu</i>	25071	46.27	46.27	+/- 0.61	46.98	+/- 0.62
<i>Cu</i>	41478	---	---	---	---	---
<i>Zn</i>	17307	---	---	---	---	---
<i>Zn</i>	23257	53.73	53.73	+/- 1.92	53.02	+/- 1.90
<i>Total</i>		100.00	100.00		100.00	

Curriculum Vitae Olodia Ayed Taha Nassef

EDUCATION

- | | | |
|-------------|---|--------------|
| 1991 - 1996 | Cairo University
Physics Department | Cairo, Egypt |
| | <ul style="list-style-type: none"> • MS in Physics | |
| 1987 - 1990 | Cairo University
Physics Department | Cairo, Egypt |
| | <ul style="list-style-type: none"> • BS in Physics, May 1990 | |

PROFESSIONAL CHRONOLOGY

- | | | |
|-------------|--|--|
| 2000 – now | Old Dominion University
Norfolk, VA | |
| | <ul style="list-style-type: none"> • Research Assistant | |
| 1996 – now | National Institute of Laser
Cairo, Egypt | |
| | Enhanced Sciences (NILES) | |
| | <ul style="list-style-type: none"> • Assistant lecturer | |
| 1992 - 1996 | National Institute of Laser
Cairo, Egypt | |
| | Enhanced Sciences (NILES) | |
| | <ul style="list-style-type: none"> • Researcher | |

RESEARCH INTERESTS

Theoretical Studies of Laser Breakdown in Gases.
Study of Laser Induced Breakdown Spectroscopy as an Elemental Technique.

Participation

Summer 1998	NILES	Cairo, Egypt
Second International Conference on Laser Enhanced Sciences and its Applications		
Summer 1994	NILES	Cairo, Egypt
First International Conference on Laser Enhanced Sciences and its Applications		

PUBLICATIONS

O. Ayed Nassef, Hani E. Elsayed-Ali, "Spark discharge assisted laser induced breakdown spectroscopy," *Spectrochim. Acta B* 60, 1564-1572 (2005).

O. Ayed Nassef, Hani E. Elsayed-Ali, "Self-absorption laser induced breakdown spectroscopy," (in preparation).